THE UNIVERSITY OF CHICAGO

SEARCHING FOR SUPERSYMMETRY IN FULLY HADRONIC FINAL STATES WITH THE ATLAS EXPERIMENT

A DISSERTATION SUBMITTED TO
THE FACULTY OF THE DIVISION OF THE PHYSICAL SCIENCES
IN CANDIDACY FOR THE DEGREE OF
DOCTOR OF PHILOSOPHY

DEPARTMENT OF PHYSICS

BY
MATS JOAKIM ROBERT OLSSON

CHICAGO, ILLINOIS
DECEMBER 2018

To my family.

"You must unlearn what you have learned."

— Yoda, The Empire Strikes Back

"If my calculations are correct, when this baby hits 88 miles per hour. . . you're gonna see some serious shit."

— Dr. Emmett Brown, Back to the Future

"Time is an illusion. Lunchtime doubly so."

— Douglas Adams, The Hitchhiker's Guide to the Galaxy

Table of Contents

List of Figures

List of Tables

ACKNOWLEDGMENTS

I am writing this final part of my thesis on my last evening in Chicago (for now), before I fly out to LA to begin a postdoc at UC Irvine. The fact that my life for the past six years, as a graduate student at the University of Chicago, is coming to an end is beginning to sink in. Two things are going through my mind at this time, excitement for the next chapter of my life and an immense sense of gratitude to all the many awesome friends and colleagues—from all around the world—whom I have had the pleasure of getting to know and work with during the past several years.

Finishing my Ph.D. has been a long and sometimes quite challenging endeavor. I am extremely grateful to my awesome Ph.D. advisor David Miller for his tireless support and mentorship during this process. I first started working with David at CERN in 2012, when he was still a postdoc in the UChicago ATLAS group, and I was thrilled to sign up as one of his first graduate students (along with Miles and Giordon) when he got hired as an assistant professor at UChicago in 2013. I would like to thank the "Miller group" postdocs, Reina Camacho and Max Swiatlowski, for all their help with analysis and advice about ATLAS and HEP at large. Thanks also to my fellow "Miller group" graduate students, Giordon Stark and Miles Wu, I have learned a lot from you. Finally, all three of us have now graduated.

Thanks to John Carlstrom, Jim Pilcher, and Carlos Wagner for your support while kindly serving on my thesis committee. Thanks to Mark Oreglia, for supporting me as a student before David got hired, and for your guidance and great sense of humor. Thanks to everyone in the UChicago ATLAS group (faculty, postdocs, students, and staff) for creating a welcoming and open environment well suited to do great work, and have fun at the same time. Thanks to all the fantastic UChicago undergraduate students I have had the privilege to teach over the years, UChicago students ask the best questions. Thanks to everyone else at UChicago who has helped me during the past six years. Thanks to David Axelrod and the

UChicago Institute of Politics for the many interesting events you hosted during my time at the university. I would be remiss if I didn't give a special thanks to Yangyang Cheng. In your own thesis acknowledgement, you wrote how your life is forever different and for the better because of our friendship, I certainly echo the same right back at you!

Thanks to all the excellent people I worked with at CERN, especially in the SUSY, JetEtmiss, and TileCal groups. You are the best colleagues!

Thanks to the many awesome friends I have made in Chicago, Geneva, Japan, and all around the world over the past decade. The list is long, but I think you know who you are :)

Thanks to my closest friends back home. James and Philip for a lifelong friendship, you were an integral part of my childhood and I'm proud to still count you among my closest friends. Let's keep on wakeboarding together every summer. Ruud for the many (mis)adventures we had in Japan and for our close friendship after you moved to Gothenburg to start your wonderful young family. Hans for productive collaboration at Chalmers (not sure I would have gotten to the US without CETAC), and a lasting friendship ever since. The list goes on... I'm privileged to have great friends and I love you all!

Finally, I am forever indebted to my wonderful and supportive family and grandmother back home in Sweden. This thesis is dedicated to you.

ABSTRACT

The Large Hadron Collider (LHC) and its experiments were built to explore fundamental questions of particle physics via proton-proton collisions at unprecedented center-of-mass energies, thus providing a unique environment for testing the Standard Model (SM) at the electroweak scale and searching for signs of new physics beyond the SM (BSM). The discovery of a SM-like 125 GeV Higgs boson by ATLAS and CMS hints of new physics at the electroweak scale—possibly within reach of the LHC—in order to mitigate divergent radiative corrections to the Higgs squared mass. This can systematically be accomplished by the introduction of supersymmetry (SUSY). For the experimentalist, SUSY provides a set of simplified benchmark models, with explicit and testable predictions, which are useful when searching for BSM physics. A large number of BSM searches has been carried out at the LHC. However, no evidence for SUSY has been found. It is therefore important to expand the scope. This thesis presents two ATLAS analyses for SUSY, both utilizing fully hadronic final states. The first analysis searches for the pair production of top squarks (stops), each with R-parity-violating decays into a b- and an s-quark. This analysis was performed using proton-proton collision data with an integrated luminosity of 17.4 fb^{-1} at a center-of-mass energy of 8 TeV. The second analysis searches for electroweak production of a chargino-neutralino pair, decaying into SM-quarks via a W boson and a SM-like 125 GeV Higgs boson, performed using an integrated luminosity of 36.1 fb^{-1} at a center-of-mass energy of 13 TeV. No evidence of an excess beyond the SM background prediction is observed in either search, thus exclusion limits are set at 95% CL. Stops decaying directly to hadronic final states are excluded for masses in the range 100 to 315 GeV. Charginos and neutralinos decaying via Wh to hadronic final states are excluded up to 680 GeV, by far the strongest limits on electroweak SUSY with Wh decays to date. The tools and strategies developed in the searches for SUSY with hadronic final states in this thesis should prove useful in future searches for BSM physics at the LHC.

PREFACE

I feel incredibly fortunate to have joined the ATLAS Collaboration as a PhD student with the University of Chicago group in the summer of 2012, just at the right time to witness the public announcement of the Higgs boson discovery live in the auditorium at CERN. During my PhD, I made significant contributions to ATLAS physics analyses by searching for supersymmetry in new ways, focusing on fully hadronic final states, and utilizing techniques of jet substructure, to gain sensitivity to new physics in previously unexplored regions of phase space. I was the lead analyzer for two SUSY searches with fully hadronic final states. The first one (presented in chapter 8) was an 8 TeV search for R-parity-violating stops [1], and the second (presented in chapter 9) a 13 TeV search for direct production of a chargino and a neutralino decaying via Wh. In both of these searches I did most of the work related to all aspects of the analysis; everything from private sample production for initial sensitivity studies, development of analysis strategy to suppress background, data/MC comparisons, systematics evaluation, HistFitter limit setting, editing of supporting note and paper, etc. In addition to analysis, I have also made significant contributions to ATLAS energy calibration efforts by measuring the calorimeter response to single isolated charged hadrons, E/p , and I took on a leading role in the testing of new hardware for the ATLAS Tile Calorimeter (TileCal) HL-LHC upgrade during four test beam periods at CERN in 2015–2017. My main responsibilities were trigger, beam line elements, and supervising students analyzing hadron beam runs. I have contributed to the ATLAS detector operations and maintenance by spending around 200 hours in the control room at CERN doing shifts, and by serving as the TileCal Data Quality Team Leader. As a side project, I have experimented with Machine Learning, in particular for calorimeter topo-cluster classification in ATLAS. I have spent over a year based at CERN, my longest continuous stay was about 9 months in 2016. Working on the ATLAS experiment in a time of 13 TeV data taking has been the privilege of a lifetime.

CHAPTER 1

INTRODUCTION

The field of particle physics seek answers to an age-old question that has fascinated humans for thousands of years: "What is the world made of?" The goal is to uncover the most fundamental constituents of nature and how they interact. An early answer to this question was proposed by Anaximenes of Miletus [2] (fl. 535 B.C.E)—all forms of matter are obtained by condensing or rarefying the principal element *air*. His theory was conceptually simple, but it was also totally wrong! The introduction of the periodic table of elements by Dimitri Mendeleev in 1869 [3] is a more recent attempt at answering the same question. Mendeelev's periodic table was truly quantitative and in agreement with experimental evidence, however it lacked the conceptual simplicity of Anaximenes theory. The regularities in Mendeleev's table hinted of more fundamental constituents, which were found to be electrons and atomic nuclei. We now know that nuclei are made up of protons and neutrons, which are in turn made up of even more fundamental constituents called quarks. Our current best answer to the question regarding what the world is made of is the Standard Model (SM) of particle physics, a theory which is both conceptually simple[1] and in total agreement with accepted experimental facts, describing all of the visible matter as made up of quarks and leptons, and three of the known four forces in nature—the electromagnetic, weak, and strong interactions (excluding gravity).

Progress in fundamental physics has benefited enormously from an interplay between theory and experiment. Important theoretical developments have often been instigated by empirical data. When developing the classical theory of electromagnetism, James Clerk Maxwell carefully studied the measurements painstakingly performed by Michael Faraday and distilled

1. Although not quite as simple as the best answer physics had to offer the question in 1932, when it was all just protons, neutrons, and electrons.

their implications into an elegant and concise set of mathematical equations, *Maxwell's equations* [4, 5]. Sometimes experimental insights have led to the rejection of established paradigms, even from experiments at the time considered as "failed". The most famous "failed experiment" ought to be the one performed by Albert A. Michelson and Edward W. Morley in 1887 [6]. The Michelson–Morley experiment attempted to measure the relative motion of matter through the stationary *luminiferous aether*[2], by measuring the speed of light in the direction of motion through the aether and in perpendicular directions. However their experiment failed to detect any significant differences. Their *null* result provided the first strong evidence against the established aether theory [9], and instigated a new line of research which ultimately culminated with Einstein's theory of special relativity [10]. New insights may also occur when established theories yield nonsensical predictions in some regime, such was the case with the *ultraviolet catastrophe* at the turn of the 20$^{\text{th}}$ century, when classical statistical mechanics predicted that the total power radiated by a hot object (*blackbody spectrum* for the emitted electromagnetic radiation) diverges towards infinity[3]. Max Planck managed to avoid the ultraviolet catastrophe and fit the experimental data by assuming that electromagnetic radiation is *quantized*[4], which he himself later described as an "act of desperation" [11]. However, this act is widely recognized as the birth of the theory of quantum mechanics.

The Standard Model is a product of fruitful interplay between experimental discoveries and theoretical insights over the past century, culminating with the discovery of its final missing piece, the Higgs boson, at the Large Hadron Collider (LHC) in 2012 [12, 13]—almost 50

2. The *luminiferous aether* was assumed to exist for most of the 19$^{\text{th}}$ century as the medium for transmitting light (as electromagnetic waves). Aether theories had been around since long before the 19$^{\text{th}}$ century however, Isaac Newton suggested an aether as a medium for transmitting both gravity and light [7]. The concept of an aether permeating space even dates back to Aristotle [8].

3. According to Rayleigh-Jeans Law: $B_\nu = \frac{2\nu^2 k_{\text{B}} T}{c^2}$, which accurately predicts experimental results at low frequencies, but it radically diverges towards infinity at higher frequencies.

4. $E = h\nu$, where ν is the frequency of the radiation, and h is what's now called *Planck's constant*, which Planck adjusted to fit the data.

years after it was first predicted by Peter Higgs and others in 1964 [14, 15, 16]. However, there are still many open questions in fundamental physics not addressed by it. There are good reasons to believe that the SM is an effective field theory only valid up to a certain energy scale. Specifically, because of electroweak symmetry breaking the square of the Higgs boson mass parameter (m_H^2) is sensitive to higher order quantum corrections, which would destabilize the SM, unless there is either new physics or significant fine-tuning involved. Furthermore, the indirect experimental evidence of Dark Matter (DM) from cosmological observations is among the most striking evidence for beyond-the-SM-physics (BSM). The LHC experiments were designed to test the SM at center-of-mass energies of up to 14 TeV, the highest energy scales every achieved in a controlled laboratory experiment. There is a large volume of publications in theoretical physics proposing various extensions to the SM. One of the most prominent ideas is Supersymmetry (SUSY), which proposes a solution to the hierarchy problem by introducing a new symmetry such that for each boson (fermion) in the SM, there exists a fermionic (bosonic) superpartners. It is a very intriguing idea for which there is not yet any experimental evidence. However, the LHC has only collected a tiny percentage of the data it is scheduled to collect during its lifetime. Like Faraday, Michaelson–Morley, and many other physicists who have come before us, we must painstakingly gather data from our experiments. New discoveries could very well end up confirming SUSY and/or some other proposed extension(s) of the SM. We may also discover something totally unexpected, which could lead us down a whole new path. Even a non-discovery (i.e. "*just the Standard Model 125 GeV Higgs and nothing new*" scenario) could ultimately prove to be just as important for setting a new course (as was the case with the outcome of Michelson and Morely's experiment). So far most searches for SUSY focus on scenarios such as the minimal supersymmetric Standard Model (MSSM), in which R-parity (baryon and lepton number) is conserved. SUSY particles are required to be produced in pairs and decay to a neutral and stable lightest supersymmetric particle (LSP), which escapes detection and

is often considered a promising DM candidate. Thus, common search signatures include significant missing transverse momentum ($E_{\mathrm{T}}^{\mathrm{miss}}$), as a proxy for the LSP, together with zero or more leptons and/or jets. A large number of searches for SUSY with R-parity conservation have been carried out by the ATLAS and CMS experiments, however thus far no evidence for SUSY has been found. With the strong exclusion limits placed on RPC SUSY scenarios, it is important to expand the scope. The strong constraints placed on MSSM scenarios can be relaxed to allow for either lepton- or baryon-number-violating-couplings. In such R-parity violating (RPV) scenarios the LSP is allowed to decay directly into SM particles, and thus the primary challenge in searches for RPV SUSY final states is to find suitable substitutes for the large $E_{\mathrm{T}}^{\mathrm{miss}}$ signature of canonical RPC SUSY searches.

This thesis presents a search [1] for RPV SUSY with pair-produced stop squarks, each decaying into a b- and an s-quark, leading to four quarks in the final state ($\tilde{t}\tilde{t}^{*} \rightarrow \bar{b}\bar{s}bs$). The search used the 8 TeV dataset collected by ATLAS in 2012. The final state was particularly challenging to distinguish from SM background, as there is no $E_{\mathrm{T}}^{\mathrm{miss}}$, and thus multijet final states tend to overwhelm the signal in a four-jet topology. The best constraints on this process at the time left a gap between $\sim 100 - 200$ GeV (the Tevatron excluded light-stops up to 90 GeV and CMS excluded stops in the range $200 - 385$ GeV). A key objective of our analysis was to close this gap, which we ultimately accomplished by excluding light stops in the range $100 - 315$ GeV. The two main challenges were overcoming the huge contributions from the QCD multijet background and maintaining high trigger efficiency for jets corresponding to final states with low-mass-stops down to 100 GeV. This was accomplished by utilizing a trigger with a relatively low jet-p_{T}/jet-HT trigger, and noting that for $m_{\tilde{t}} \approx 100 - 300$ GeV, the initial stop transverse momentum spectrum p_{T} extends significantly into the range for which $p_{\mathrm{T}} \gg m_{\tilde{t}}$, thus a boosted approach becomes feasible (the stops receive a boost from ISR). This thesis also presents a novel search for SUSY with direct electroweak pair production of a chargino and a neutralino, based on 36.1 fb^{-1} of $\sqrt{s} =$

13 TeV proton-proton collision data. It is possible that direct pair production of charginos and neutralinos dominate if the superpartners of the gluon and quark are heavier than a few GeV. Specifically, I am focusing on a scenario with direct production of a chargino and a neutralino, decaying via Wh, into SM particles and the lightest neutralino (LSP) which is stable (i.e. R-parity is conserved). I have been leading the search for the hadronic final state with four jets and $E_{\mathrm{T}}^{\mathrm{miss}}$. This is the first fully hadronic electroweak Wh search at the LHC, and it is proven to be extremely promising for targeting the high mass chargino/neutralino phase-space, significantly increasing the exclusion limits compared to previous searches.

The thesis is organized as follows: Chapter 2 provides an introduction to the Standard Model, including a brief historical overview, description of its mathematical formulation, and QCD physics relevant in collider physics and hadronic final states. The chapter is concluded with a discussion of some of the main limitations of the SM, and motivation for beyond-the-SM (BSM) physics. Chapter 3 introduces supersymmetry (SUSY), how to search for it at colliders, and the status of ATLAS SUSY searches thus far. Chapter 4 gives an overview of the design and operations of Large Hadron Collider (LHC), the machine which accelerates and collides protons at unprecedented energies, and chapter 5 then describes the ATLAS detector, the instrument we use to study the products of proton–proton collisions. Chapter 6 provides a brief introduction to the methods and tools used for simulating particle physics events at the LHC, as well as the ATLAS event reconstruction. Chapter 7 Provides an introduction to hypothesis testing when searching for new physics at the LHC. Chapter 8 presents the analysis strategy and results of the search for R-parity violating stops with a fully hadronic final state with the ATLAS detector at 8 TeV, where innovative jet reconstruction techniques were used to gain sensitivity for measuring signals in a huge QCD background. Finally, the analysis strategy and results of the search for SUSY with electroweak production of a chargino and a neutralino, decaying via Wh into fully hadronic final states, is presented in Chapter 9. The results are summarized in Chapter 10, which also includes a discussion of

possible extensions of these searches with the full LHC Run II dataset, and presents some thoughts on the future of the LHC program and its planned upgrades. Appendix A provides additional material for the electroweak Wh search (which is presented in chapter 9).

CHAPTER 2

THE STANDARD MODEL OF PARTICLE PHYSICS

This chapter provides an introduction to the Standard Model, a quantum field theory that describes all the known fundamental matter and force carrying particles in nature, with the exception of gravity.

This chapter is organized as follows: Section 2.1 gives a brief introduction to the SM in a historical context. Section 2.2 describes the mathematical structure of Quantum Chromodynamics (QCD), the electroweak theory, and spontaneous symmetry breaking via the Higgs mechanism. Section 2.3 describes concepts in QCD relevant to collider physics and the hadronic final states studied in this thesis. Finally, some of the main limitations of the SM are discussed in section 2.4.

2.1 Overview and Historical Background

The unification of all fundamental forces in nature is a longstanding goal in particle physics. The Standard Model (SM) is currently the most successful theory we have on the path towards achieving this goal, it unifies quantum mechanics and special relativity into a quantum field theory describing known fundamental particles, the *quarks* and the *leptons*[1], and their interactions mediated via the *electromagnetic*, *weak*, and *strong* force. The theory consists of the Glashow-Weinberg-Salam theory of electroweak interactions, describing the electromagnetic and weak nucelar forces, and Quantum Chromodynamics, which describes the strong nuclear force. An overview of the SM particles and their interactions is shown in fig. 2.1.

1. *Hadrons* (from the Greek *adros* meaning *bulky*) are particles composed of quarks. The protons and neutrons that atomic nuclei are made of belong to this family. On the other hand, *leptons* are particles that are not made of quarks. Electrons and muons are examples of leptons (from the Greek *leptos* meaning *thin*).

The quarks and leptons (matter particles) are known as *fermions*, which have spin-$\frac{1}{2}$ and thus obey Fermi-Dirac statistics. The force carriers have integer spin and thus obey Bose-Einstein statistics. Both the fermions and bosons have anti-particles, which have the same mass but carry opposite charge. The electromagnetic, weak, and strong force are mediated by the *photon* (γ), *intermediate vector bosons* ($W^{\pm}/Z$), and *gluons* (g), respectively. Finally, interactions with the *Higgs field* (H) is what gives all massive particles their mass.

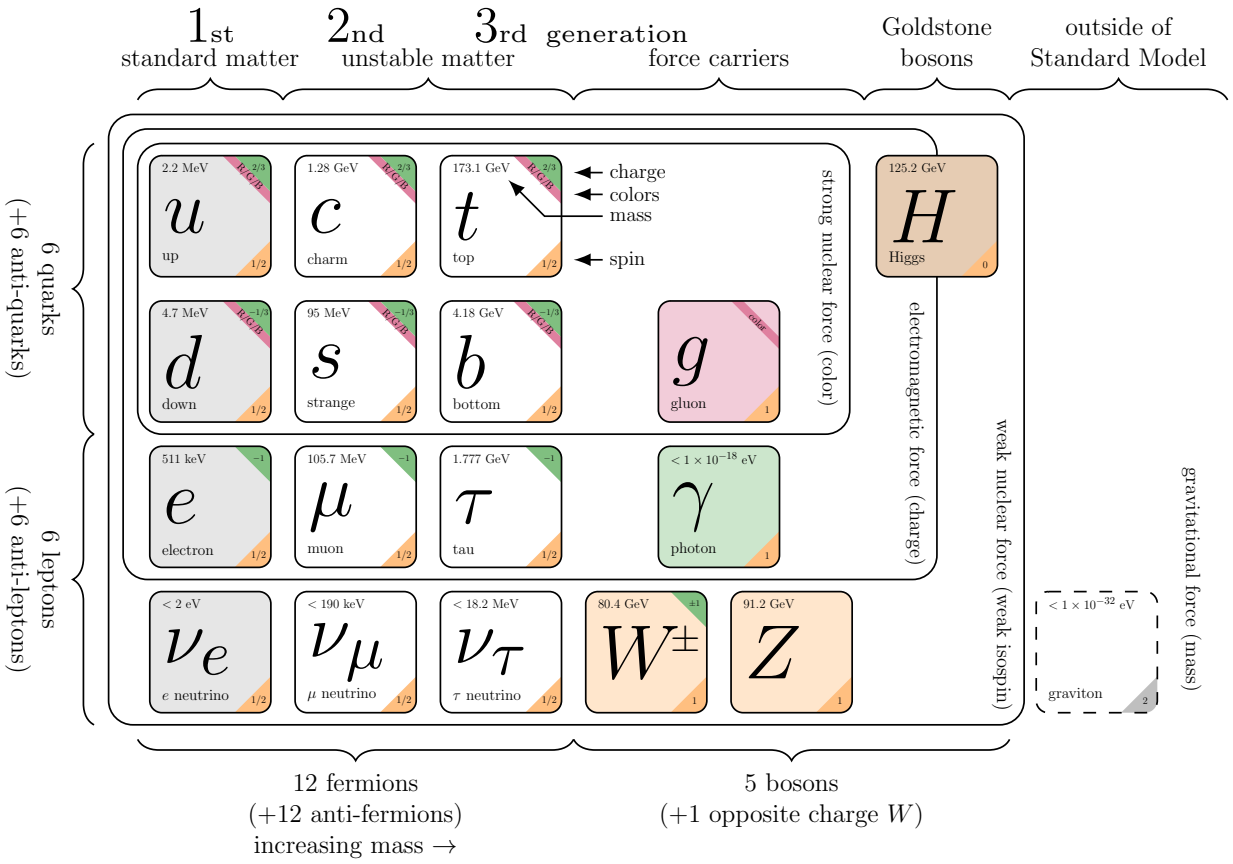

Figure 2.1: Summary of the SM particle content. The box for each particle includes its name, symbol, mass, charge, and spin (and color charge in the case of the quarks). The interactions with the strong, electromagnetic, and weak force is indicated by a set of larger boxes encapsulating the particles affected, as well as the conserved quantities associated with each force (color, charge, weak isospin, for the strong, electromagnetic, and weak force, respectively). Gravity is represented by the hypothetical *graviton*, which falls outside the SM model. Diagram created with TikZ [17], courtesy of [18]. Masses and constraints were taken from the Particle Data Group (PDG) [19].

The Standard Model was conceived in the 1960s, with major contributions by Sheldon

Glashow [20], Steven Weinberg [21], and Abdus Salam [22], who shared the 1979 Nobel Prize in Physics *"for their contributions to the theory of the unified weak and electromagnetic interaction between elementary particles, including, inter alia, the prediction of the weak neutral current"* [23]. Crucial to the Standard Model is the Higgs mechanism, which describes how the elementary particles acquire their masses by interaction with the Higgs boson. The consequences of a non-relativistic Higgs mechanism in particle physics were first discussed in 1962 by Philip Warren Anderson [24]. A relativistic Higgs model was presented independently in 1964 by Peter Higgs [14], Robert Brout and Francois Englert [15], and Gerald Guralnik, C. R. Hagen and Tom Kibble [16]. With discovery of the Higgs boson by the ATLAS [12] and CMS [13] collaborations at the LHC, all the particles predicted by the SM had finally been discovered. However, there are still many open questions in fundamental physics not addressed by it (such as the nature of *dark matter*, or the *hierarchy problem*), this is the topic of section 2.4 and chapter 3.

The predictions of the SM has held up to rigorous experimental testing at the highest energies available in the laboratory over the past several decades. It manages to explain all known physics (except gravity) listed in the 1808 pages of the 2016 edition of the PDG *Review of Particle Physics* [25] using only $\sim$ 19 free parameters[2]. Some observables have been determined with a remarkable accuracy. Experimental results and Quantum Electrodynamics (QED) theory have determined the *fine structure constant* (α), which characterizes the strength of the electromagnetic interaction, to $\alpha = 137.035999084(51)$ [0.37 ppb] [26]. At the LHC, many SM precision measurements for a large variety of final states have been performed, all in excellent agreement with the SM prediction, as summarized in fig. 2.2.

2. Nine quark and lepton masses (excluding the neutrinos), four Cabibbo-Kobayashi-Maskawa (CKM) matrix parameters (three mixing angles and one CP violation phase), three gauge couplings (g', g, g_s), the QCD vacuum angle, the Higgs vacuum expectation value, the Higgs mass.

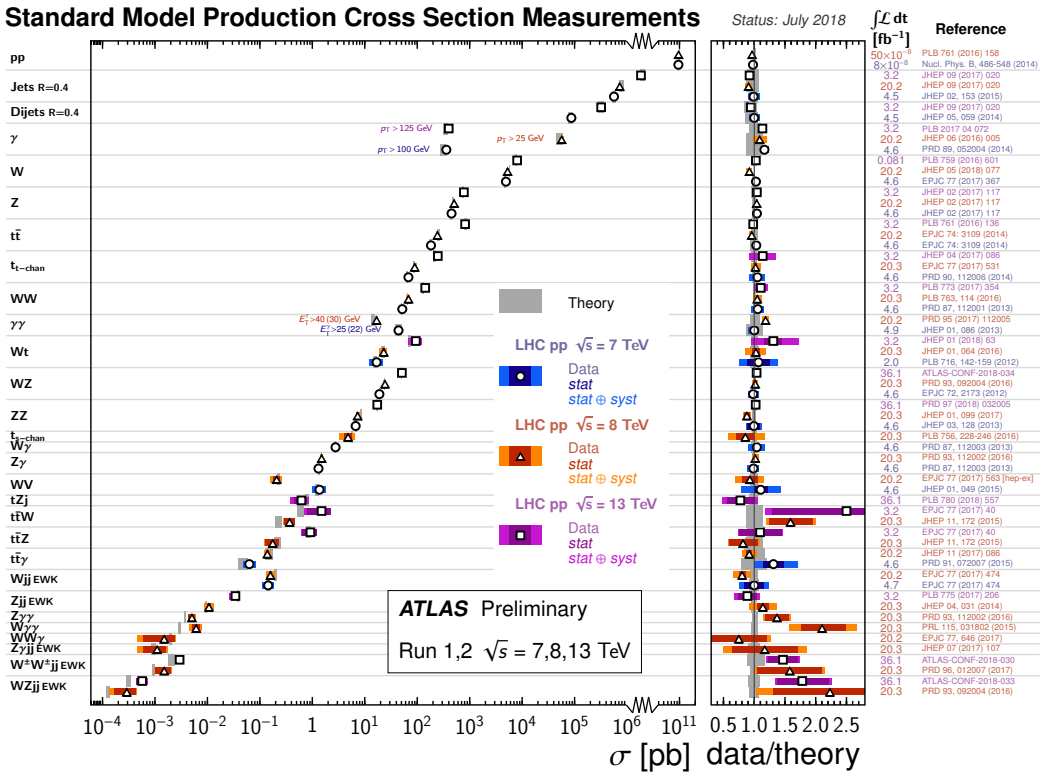

Figure 2.2: Summary of several Standard Model total and fiducial production cross section measurements by the ATLAS Collaboration at 7, 8, and 13 TeV. The agreement between the observed value and theoretical prediction (in gray) is excellent across all the various channels, spanning almost 15 orders of magnitude. [27]

2.2 Mathematical Formulation

In the Standard Model, QED and the theory of weak interactions are unified into the electroweak theory, which is then grouped together with QCD into an internally consistent quantum field theory, with the following gauge group:

$$SU(3)_C \otimes SU(2)_L \otimes U(1)_Y, \tag{2.1}$$

where $SU(3)_C$ is the gauge group of strong interaction (QCD), mediated by the eight gluons between color charged (C) particles, and $SU(2)_L \otimes U(1)_Y$ is the gauge group of electroweak

theory that is spontaneously broken to the $U(1)_Q$ subgroup of electromagnetism:

$$SU(2)_L \otimes U(1)_Y \rightarrow U(1)_Q. \tag{2.2}$$

Here, the subscript L indicates a coupling only to *left-handed* fermions. Y is the *hypercharge*[3], which is related to the electric charge via $Q = I_3 + \frac{Y}{2}$, where I_3 is the *weak isospin* [29].

Below we will cover the mathematical structure of the SM, the gauge group and the covariant derivative, the Lagrangian of QCD and the electroweak theory, electroweak symmetry breaking, Higgs and Yukawa interactions, transformation from gauge to mass eigenstates, and the gauge currents. [19, 30, 29, 31].

The Standard Model is a chiral gauge theory, meaning that the left-handed and right-handed chiralities transform differently under the gauge group.[4] The theory contains:

- left-handed fermion doublets for quarks, $Q_L^f = \begin{pmatrix} u_L^f \\ d_L^f \end{pmatrix}$ and leptons, $L_L^f = \begin{pmatrix} \nu_L^f \\ e_L^f \end{pmatrix}$;
- right-handed fermion singlets for quarks, u_R^f and d_R^f and leptons, e_R^f (ν_R^f);
- a complex scalar doublet (Higgs), $\phi = \begin{pmatrix} \phi^+ \\ \phi^0 \end{pmatrix}$;

3. $Y \equiv B+S$, where B denotes the *baryon* number and S is a property called *strangeness*. In the so-called *Eightfold Way*, Murray Gell-Mann arranged the baryons (which consists of three quarks, e.g. protons or neutrons) and mesons (consisting of two quarks, e.g. pions) into geometrical patterns, according to their charge and strangeness [28].

4. In this thesis we use the Weyl basis for describing spinors, which is more convenient than the Dirac basis, since there is no natural correspondence between left-handed and right-handed fermion fields in the Standard Model. Weyl spinors are related to the Dirac spinors as follows: [30] $\psi_R = P_{R/L}\psi = \frac{1}{2}(1 \pm \gamma^5)\psi$. The Weyl basis is also convenient to use for the fields in supersymmetry, as we shall see chapter 3. [32]

- gluon and electroweak gauge fields, G^A_μ, W^a_μ, B_μ;

where $f = 1, 2, 3$ is a generation index. In the Standard Model the right-handed neutrinos ν^f_R does not exist, but they are needed in some extensions. The transformation properties and hypercharges (Y_ψ) for the fermions, and the Higgs scalar (Y_ϕ), under the gauge group are given in table 2.1. Only the quarks (Q_L, u_R, and d_R) interact with the strong force, mediated by the gluon gauge field G^A_μ, and thus transform under the fundamental representation[5] of the $SU(3)_C$ gauge group. The left-handed fermion fields and the Higgs field transform under the fundamental representation of $SU(2)_L$[6], and all the fields (except ν_R) are charged under $U(1)_Y$ (hypercharge) [29].

From table 2.1 we can construct a covariant derivative for the matter fields. A general covariant derivative for the Standard Model can be written as:

$$D_\mu = (\partial_\mu - ig_s G^A_\mu T^A - igW^a_\mu \tau^a - ig' Y B_\mu), \tag{2.3}$$

where $T^A = \frac{1}{2}\lambda^A$ and $\tau^a = \frac{1}{2}\sigma^a$ are the generators of $SU(3)$ and $SU(2)$, respectively. The λ^A's are the Gell-Mann matrices, and σ^a's are the Pauli matrices. For example, the covariant derivative for left handed-quarks becomes:

$$D_\mu Q_L = (\partial_\mu - ig_s G^A_\mu T^A - igW^a_\mu \tau^a - i\frac{1}{6} g' B_\mu) Q_L, \tag{2.4}$$

5. The *fundamental* representation of $SU(3)$ is a set of eight linearly independent traceless hermitian 3×3 matrices (hence eight *gluons*), which generate the $SU(3)$ gauge group. These matrices are commonly referred to as the *Gell-Mann matrices*, after Murray Gell-Mann (Table I. in Ref. [33]). In this section the $SU(3)$ generators are written as $T^A = \frac{1}{2}\lambda^A$ (where $A = 1, \ldots, 8$). When a quark interacts with a gluon, they encode how the color of the quark is rotated in the $SU(3)$ space. [29, 19]

6. The generators of $SU(2)$ are written as $\tau^a = \frac{1}{2}\sigma^a$ (with $a = 1, 2, 3$) where σ^a are the *Pauli matrices*.

Symmetry group		$SU(3)_C$	$SU(2)_L$	$U(1)_Y$
Gauge field		G^A_μ	W^a_μ	B_μ
Coupling		g_s	g	g'
Quarks	$Q^f_L = \begin{pmatrix} u^f_L \\ d^f_L \end{pmatrix}$	**3**	**2**	1/6
	u^f_R	**3**	**1**	2/3
	d^f_R	**3**	**1**	$-1/3$
Leptons	$L^f_L = \begin{pmatrix} \nu^f_L \\ e^f_L \end{pmatrix}$	**1**	**2**	$-1/2$
	e^f_R	**1**	**1**	-1
	(ν^f_R)	**1**	**1**	0
Higgs	$\phi = \begin{pmatrix} \phi^+ \\ \phi^0 \end{pmatrix}$	**1**	**2**	1/2

Table 2.1: The field content (using a Weyl spinor basis) and field transformations under the gauge group in the Standard Model. The notation **3** and **2** indicates that the field transforms under the fundamental representation of the $SU(3)C$ and $SU(2)$ gauge group, respectively, and **1** means that the field does not transform under the gauge group. The three generations of particles in the Standard Model are denoted by $f = 1, 2, 3$.

and similarly for the Higgs:

$$D_\mu \phi = (\partial_\mu - igW^a_\mu \tau^a - i\frac{1}{2}g' B_\mu)\phi, \tag{2.5}$$

where g_s is the coupling constant for the strong interaction, g and g' are coupling constants for the electroweak interactions. Furthermore, the fields in table 2.1 come in three generations (as shown in fig. 2.1), thus we can add a generation index to all of them. To illustrate how many objects we have, take Q_L as an example:

$$Q_L = Q_L^{f=1,2,3}{}_{\alpha=1,2,c=1,2,3,i=1,2}(x) \tag{2.6}$$

For any given f, α, c, i this is a Grassmann number at one point in space-time, where f is a generation index (three generations of fermions), α is a Weyl index (two-component spinor), c is a color index of $SU(3)$ (R, G, B), and i is an index of $SU(2)$ (two independent eigenstates, e.g. spin up/down). The covariant derivative for Q_L in eq. (2.4) with all the indices explicitly written becomes:

$$\begin{aligned}(D_\mu Q_L)^f_{\alpha,c,i} = \partial_\mu Q^f_{L\alpha,c,i} - ig_s G^A_\mu (T^A)^{c'}_c Q^f_{L\alpha,c',i} \\ - igW^a_\mu (\tau^a)^j_i Q^f_{L\alpha,c,j} - ig' B_\mu \frac{1}{6} Q^f_{L\alpha,c,i}.\end{aligned} \tag{2.7}$$

2.2.1 The Standard Model Lagrangian

The Standard Model Lagrangian density can be compactly written as:

$$\begin{aligned}\mathcal{L}_{\text{SM}} = \quad & -\tfrac{1}{4} F_{\mu\nu} F^{\mu\nu} && \text{(the gauge field kinetic energies and self-interaction terms)} \\ & + i\bar{\Psi} \not{D} \Psi && \text{(fermion kinetic energies and interactions with } W^\pm,\ Z,\ \gamma) \\ & + \Psi_i y_{ij} \Psi_j \phi + h.c. && \text{(Yukawa interactions, i.e. fermionic masses and couplings to Higgs)} \\ & + |D_\mu \phi|^2 - V(\phi) && (W^\pm,\ Z,\ \gamma \text{ and Higgs masses and couplings}),\end{aligned} \tag{2.8}$$

where the different terms are explained in detail below.

The Gauge Fields

The gauge field kinetic energy and self-interactions are given by:

$$\mathcal{L}_{\text{gauge}} = -\frac{1}{4}F_{\mu\nu}F^{\mu\nu} = \underbrace{-\frac{1}{4}G^A_{\mu\nu}G^{\mu\nu A}}_{\text{QCD}} \underbrace{-\frac{1}{4}W^a_{\mu\nu}W^{\mu\nu a} - \frac{1}{4}B_{\mu\nu}B^{\mu\nu}}_{\text{electroweak theory}}, \tag{2.9}$$

where

$$G^A_{\mu\nu} = \partial_\mu G^A_\nu - \partial_\nu G^A_\mu - g_s f_{ABC} G^B_\mu G^C_\nu \tag{2.10}$$

is the gauge field strength tensor for the gluon fields $G^{A=1,\ldots,8}_\mu$, and the structure constants f_{ABC} $(A, B, C = 1, \ldots, 8)$ are defined by the commutation relation:

$$[\lambda^A, \lambda^B] = 2i f_{ABC} \lambda^C, \tag{2.11}$$

where λ^A are the $SU(3)$ Gell-Mann matrices. QCD has a property called *asymptotic freedom*, which means that the running coupling constants become weak at high energies or short distances (more about that in section 2.3.1). The QCD gauge terms in the Lagrangian eq. (2.10) lead to the three and four-point gluon self-interactions in fig. 2.3. The QCD theory is essential for understanding the physics of hadron colliders and hadronic final states, this is explained in more detail in section 2.3.

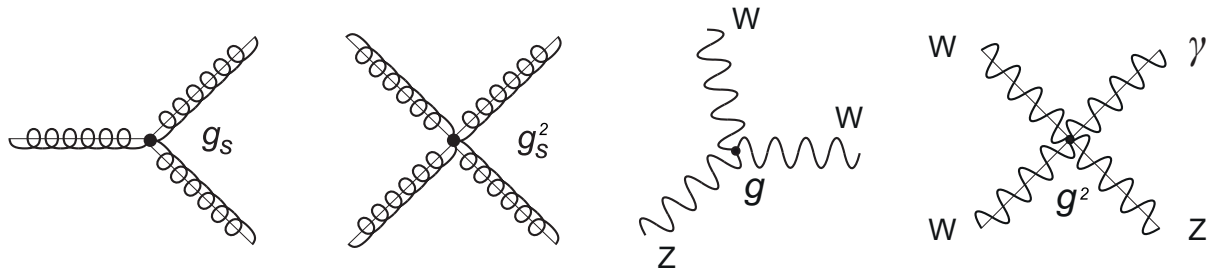

Figure 2.3: Example of some interactions between gauge bosons in $\mathcal{L}_{\text{gauge}}$.

For the electroweak theory we have:

$$W^a_{\mu\nu} = \partial_\mu W^a_\nu - \partial_\nu W^a_\mu - g\epsilon_{abc} W^b_\mu W^c_\nu$$
$$B_{\mu\nu} = \partial_\mu B_\nu - \partial_\nu B_\mu, \tag{2.12}$$

where $W^{i=1,2,3}_\mu$ and B_μ are the $SU(2)$ and $U(1)$ gauge fields respectively. The structure constants are given by the totally antisymmetric symbol ϵ_{abc} $(a, b, c = 1, 2, 3)$, satisfying the commutation relation:

$$[\sigma^a, \sigma^b] = 2i\epsilon_{abc}\sigma^c, \tag{2.13}$$

where σ^a are the Pauli matrices, which generate $SU(2)$. The $SU(2)$ fields also have three and four-point self-interactions, two such examples are shown in fig. 2.3.

The Fermions

The fermionic gauge interactions and kinetic terms are governed by:

$$\begin{aligned}\mathcal{L}_\mathrm{f} = i\bar{\Psi}\not{D}\Psi = {} & i(\bar{Q}^f_L)^{c,i}\ \gamma^\mu (D_\mu Q^f_L)_{c,i} + i(\bar{u}^f_R)^c\ \gamma^\mu D_\mu (u^f_R)_c + i(\bar{d}^f_R)^c\ \gamma^\mu D_\mu (d^f_R)_c \\ & + i(\bar{L}^f_L)^i\ \gamma^\mu D_\mu (L^f_L)_i + i\bar{e}^f_R\ \gamma^\mu D_\mu e^f_R + \left(i\bar{\nu}^f_R\ \gamma^\mu D_\mu \nu^f_R\right),\end{aligned} \tag{2.14}$$

where we have summed over generation index f, color index c, and weak index i, with the Weyl index α suppressed, using a covariant derivative as defined in eq. (2.3) and indices from eq. (2.7). Keep in mind that the terms in the covariant derivative change for each field, e.g. only quarks are colored, as represented here by the index c, and transform under $SU(3)$. The correct form of any covariant derivative can be read from table 2.1. This part of the Lagrangian gives rise to interactions between gauge bosons and fermions, a few examples are given in fig. 2.4.

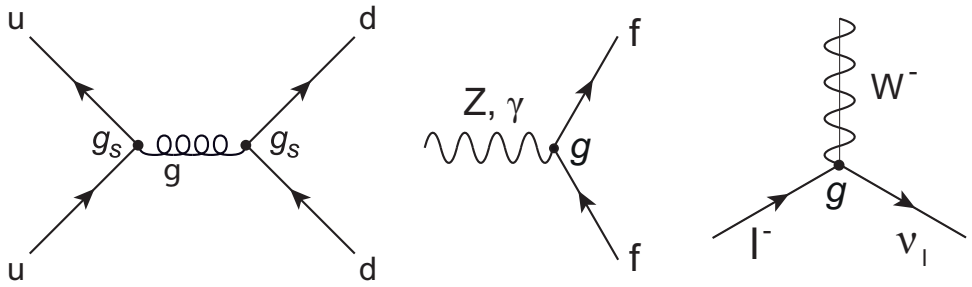

Figure 2.4: Example of interactions induced by $\mathcal{L}_{\rm f}$.

The Yukawa Interactions

The Yukawa terms are responsible for giving mass to all the fermions, by coupling them to the Higgs boson as in the first diagram of fig. 2.5.

$$\begin{aligned}\mathcal{L}_{\rm Yukawa} = \Psi_i y_{ij} \Psi_j \phi + h.c. = &- y^{(d)}_{ij} (\bar{Q}^i_L)^a \phi_a d^j_R \\ &- y^{(u)}_{ij} \epsilon_{ab} (\bar{Q}^i_L)^a \phi^{\dagger b} u^j_R \\ &- y^{(e)}_{ij} (\bar{L}^i_L)^a \phi_a e^j_R \\ &- \left(y^{(\nu)}_{ij} \epsilon_{ab} (\bar{L}^i_L)^a \phi^{\dagger b} \nu^j_R \right) \\ &+ h.c.\end{aligned} \tag{2.15}$$

The couplings in eq. (2.15) are the only possible gauge invariant terms. The Hermitian conjugate ($h.c.$) is needed since the Lagrangian must be real-valued.

The Higgs Field and Scalar Potential

The scalar part of the Lagrangian in eq. (2.8) is given by:

$$\mathcal{L}_\phi = |D_\mu \phi|^2 - V(\phi) = (D^\mu \phi)^\dagger (D_\mu \phi) - V(\phi), \tag{2.16}$$

where $\phi = \begin{pmatrix} \phi^+ \\ \\ \phi^0 \end{pmatrix}$ is a complex Higgs scalar, which transforms under the fundamental representation of $SU(2)$ with a $U(1)$ hypercharge $Y_\phi = +\frac{1}{2}$. The scalar Higgs potential is given by:

$$V(\phi) = +\mu^2 \phi^\dagger \phi + \lambda (\phi^\dagger \phi)^2. \tag{2.17}$$

The Higgs couples to all the fermions, the $W^\pm$ and Z^0 vector bosons, and also to itself by the cubic and quadratic self-interactions in fig. 2.5.

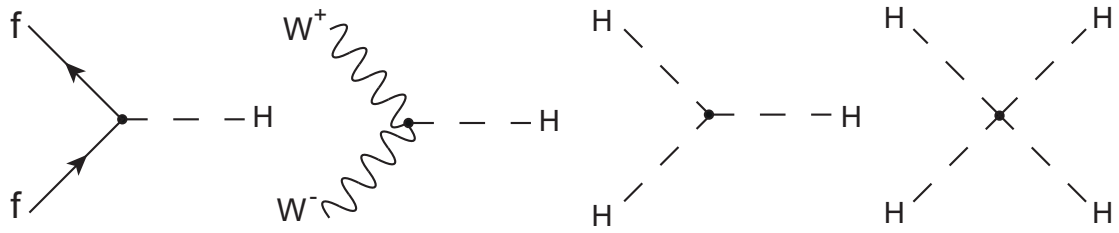

Figure 2.5: Example of interactions with the Higgs boson in $\mathcal{L}_{\text{Yukawa}}$ and $\mathcal{L}_\phi$.

The physical implications of the scalar part of the SM Lagrangian in eq. (2.16) will be described in more detail in the following sections.

2.2.2 *Spontaneous Symmetry Breaking*

We start by investigating how the gauge group of the electroweak theory gets broken, and explain how the particles in the Standard Model acquire mass. We know from experiment that the fermions (most likely including even the neutrinos) and gauge bosons of weak interaction have mass. However, gauge invariance and renormalizability does not allow for bare mass terms in the Lagrangian for gauge bosons or chiral fermions. The solution in the Standard Model is to introduce the concept of spontaneous symmetry breaking of the gauge invariance, which preserves renormalizability. Basically, what it means is that the lowest energy state (vacuum) is not gauge invariant and induces masses for the particles propagating through it. To find the lowest energy solution of the classical potential, we minimize the scalar Higgs potential $V(\phi)$. As introduced in eq. (2.17), the scalar potential is given by:

$$V(\phi) = +\mu^2\phi^\dagger\phi + \lambda(\phi^\dagger\phi)^2. \tag{2.18}$$

The form of the potential is restricted to due to $SU(2) \times U(1)$ gauge invariance and renormalizability. The complex Higgs doublet ϕ can be written as: [31]

$$\phi = \begin{pmatrix} \phi^+ \\ \\ \phi^0 \end{pmatrix} = \begin{pmatrix} \frac{1}{\sqrt{2}}(\phi_1 - i\phi_2) \\ \\ \frac{1}{\sqrt{2}}(\phi_3 - i\phi_4) \end{pmatrix}, \tag{2.19}$$

where $\phi_{i=1,2,3,4} \in \mathbb{R}$. Writing the Higgs potential in this basis we get:

$$V(\phi) = \frac{1}{2}\mu^2\left(\sum_i \phi_i^2\right) + \frac{1}{4}\lambda\left(\sum_i \phi_i^2\right)^2. \tag{2.20}$$

Since this is $O(4)$ invariant, we can choose an axis in four-dimensional space where $\langle 0|\phi_i|0\rangle = 0$ for $i = 1, 2, 4$ and $\langle 0|\phi_3|0\rangle = v$. eq. (2.20) reduces to:

$$V(\phi) \to V(\phi_0) = \frac{1}{2}\mu^2 v^2 + \frac{1}{4}\lambda v^4, \tag{2.21}$$

where

$$\phi_0 = \begin{pmatrix} 0 \\ \\ v \end{pmatrix}. \tag{2.22}$$

We now minimize eq. (2.21) with respect to v. Spontaneous symmetry breaking occurs when $\mu^2 < 0$, and vacuum stability forces $\lambda > 0$. We consider two cases:

- For $\mu^2 > 0$ the minimum occurs at $v = 0$ and the symmetry remains unbroken.
- For $\mu^2 < 0$ the symmetric point $v = 0$ is unstable and the minimum occurs at

$$v = \sqrt{-\mu^2/\lambda}, \tag{2.23}$$

  which breaks the $SU(2) \times U(1)$ gauge symmetry.

The two solutions are illustrated in fig. 2.6. This is the classical result, the quantum theory can be obtained by considering fluctuations around the classical minimum, i.e.[7]

$$\phi = \phi_0 + \phi' = \frac{1}{\sqrt{2}} \begin{pmatrix} 0 \\ \\ v + H \end{pmatrix} \tag{2.24}$$

7. In the so-called *unitary gauge*, where the scalar fields responsible for the Higgs mechanism transform into a basis in which their Goldstone boson disappears (i.e. minimal degrees of freedom). [31]

where ϕ' are quantum fields with zero vacuum expectation value (VEV), and H is an Hermitian field that will turn out to be the physical Higgs scalar boson. With ϕ as in eq. (2.24)

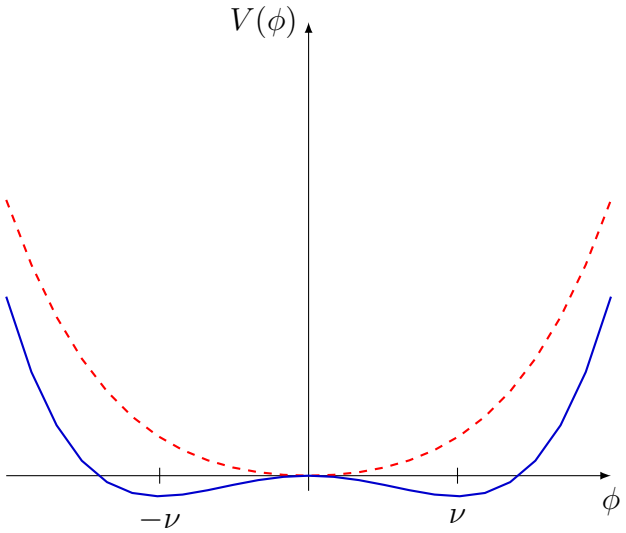

Figure 2.6: The Higgs potential for $\mu > 0$ (dashed line) and $\mu < 0$ (solid line). Image created with TikZ [17].

and the covariant derivative in eq. (2.5), the scalar kinetic energy becomes:

$$\begin{aligned}(D_\mu\phi)^\dagger D^\mu\phi &= \frac{1}{2}(0,v)\left(gW_\mu^a\tau^a+\frac{1}{2}g'B_\mu\right)\left(gW^{\mu b}\tau^b+\frac{1}{2}g'B^\mu\right)\begin{pmatrix}0\\ \\ v\end{pmatrix}+\text{H terms}\\ &= \frac{v^2}{8}\left(g^2\left(W_\mu^1+iW_\mu^2\right)\left(W^{1\mu}-iW^{2\mu}\right)+\left(-gW_\mu^3+g'B_\mu\right)^2\right)+\text{H terms}\\ &\to M_W^2W^{\mu+}W_\mu^- + \frac{M_Z^2}{2}Z^{0\mu}Z_\mu^0+\text{H terms},\end{aligned} \tag{2.25}$$

where we have omitted the kinetic energy and gauge interactions terms of the physical Higgs boson. Thus, three of the generators of $SU(2)\times U(1)$ are broken giving rise to massive gauge

bosons:

$$W_\mu^\pm = \frac{1}{\sqrt{2}}\left(W_\mu^1 \mp W_\mu^2\right)$$
$$Z_\mu^0 = -\sin\theta_W B_\mu + \cos\theta_W W_\mu^3. \tag{2.26}$$

The vacuum carries no electric charge since $Q\phi_0 = (\tau^3 + Y)\phi_0 = 0$, and thus the $U(1)_Q$ of electromagnetism is not broken ($Q = \tau^3 + Y$ is the electric charge operator, where τ^3 is the third generator of $SU(2)$ and $Y = \frac{1}{2}\mathbf{1}_{2\times 2}$). In terms of the gauge group this can be written as $SU(2) \otimes U(1)_Y \to U(1)_Q$. Thus, the photon,

$$A_\mu = \cos\theta_W B_\mu + \sin\theta_W W_\mu^3, \tag{2.27}$$

remains massless. The masses of the gauge bosons are (numerical values from PDG, using the $\overline{\text{MS}}$-definition [19]):

$$M_W = \frac{gv}{2} = 80.379 \pm 0.012 \text{ GeV}$$
$$M_Z = \sqrt{g^2 + g'^2}\frac{v}{2} = \frac{M_W}{\cos\theta_W} = 91.1876 \pm 0.0021 \text{ GeV}, \tag{2.28}$$

where

$$\tan\theta_W \equiv \frac{g'}{g} \Rightarrow \sin^2\theta_W = 1 - \frac{M_W^2}{M_Z^2} = 0.23122(4) \tag{2.29}$$

is the weak (Weinberg) mixing angle.

The Higgs and Yukawa Interactions

By keeping the H terms in eq. (2.25) the full Higgs Lagrangian becomes (in the unitary gauge):

$$\begin{aligned}\mathcal{L}_\phi &= (D_\mu\phi)^\dagger D^\mu\phi - V(\phi) \\ &= M_W^2 W^{\mu+}W_\mu^- \left(1+\frac{H}{v}\right)^2 + \frac{M_Z^2}{2} Z^{0\mu} Z_\mu^0 \left(1+\frac{H}{v}\right)^2 \\ &+ \frac{1}{2}(\partial_\mu H)^2 - V(\phi). \end{aligned} \tag{2.30}$$

This equation incorporates the W and Z mass terms as well as the ZZH^2, $W^+W^-H^2$, ZZH, and W^+W^-H interactions. The last line is the canonical Higgs kinetic energy and the potential, which becomes (in unitary gauge):

$$V(\phi) = -\frac{\mu^4}{4\lambda} - \mu^2 H^2 + \lambda v H^3 + \frac{\lambda}{4} H^4, \tag{2.31}$$

after the symmetry breaking. The first term in eq. (2.31) is a constant, the second term represents a tree-level mass:

$$M_H = \sqrt{-2\mu^2} = \sqrt{2\lambda} v \tag{2.32}$$

for the Higgs boson. Since the quadratic coupling λ is unknown, M_H cannot be predicted from the theory[8]. The third and forth terms in $V(\phi)$ are the induced cubic and quadratic interactions of the Higgs scalar.

After the spontaneous symmetry breaking, where ϕ gets its VEV eq. (2.24), in unitary gauge

8. Which is why the 2012 discovery [12, 13] at the LHC was such a big deal.

the Yukawa terms (2.15) become

$$\begin{aligned}\mathcal{L}_{\text{Yukawa}} \to & -y_{ij}^{(d)}\bar{d}_L^i\left(\frac{v+H}{\sqrt{2}}\right)d_R^j - y_{ij}^{(u)}\bar{u}_L^i\left(\frac{v+H}{\sqrt{2}}\right)u_R^j \\ & - y_{ij}^{(e)}\bar{e}_L^i\left(\frac{v+H}{\sqrt{2}}\right)e_R^j - \left(y_{ij}^{(\nu)}\bar{\nu}_L^i\left(\frac{v+H}{\sqrt{2}}\right)\nu_R^j\right) + h.c. \\ & = \bar{u}_L(M^{(u)} + h^{(u)}H)u_R + (d, e, \nu)\text{ terms} + h.c. \end{aligned} \tag{2.33}$$

where $\bar{u}_L = (\bar{u}_{1L}, \bar{u}_{2L}, \bar{u}_{3L})$, with a similar definition for u_R and for the d, e, and ν's. $M^{(x)} = y_{ij}^{(x)}v/\sqrt{2}$ is the fermion mass matrix induced by the spontaneous symmetry breaking, and $h^{(x)} = M^{(x)}/v$ is the Yukawa coupling matrix. However, in general $M^{(x)}$ is not diagonal or Hermitian, so in order to identify the physical fields, M needs to be diagonalized. Thus, for every flavour (u_L^i, d_L^i, e_L^i, ν_L^i, u_R^i, d_R^i, e_R^i, and, ν_R^i) find a unitary matrix and rotate, i.e $u_L^i \to \mathrm{U}_{ij}^{(u)\dagger}u_L^j$, $u_R^i \to \mathrm{W}_{ij}^{(u)\dagger}u_R^j$, and analogously for $d_{L,R}$, $e_{L,R}$, and $\nu_{L,R}$. This is just a field redefinition, a change of variables inside the Lagrangian, and does not change the physics. The matrices $\mathrm{U}^{(x)}$ and $\mathrm{W}^{(x)}$ must be unitary, in order for the kinetic terms to be invariant, e.g. $\bar{u}_L \not{D} u_R \to \bar{u}_L \underbrace{\mathrm{U}^{(u)}\mathrm{U}^{(u)\dagger}}_{=1} \not{D} u_R$.

For the u-type quark masses we get,

$$\mathrm{U}^{(u)}M^{(u)}\mathrm{W}^{(u)\dagger} = M_D^{(u)} = \begin{pmatrix} m_u & 0 & 0 \\ 0 & m_c & 0 \\ 0 & 0 & m_t \end{pmatrix}, \tag{2.34}$$

a diagonal matrix with eigenvalues equal to the physical masses. The down quarks, charged leptons, and the neutrinos are diagonalized in analogous fashion. Thus, if the matrices U and W are unitary, we have diagonal mass terms and the kinetic terms remain invariant.

When rotating to the mass eigenstates we can write ($\psi_L'^i = \mathrm{U}_{ij}^{(\psi)}\psi_L^j$, $\psi_R'^i = \mathrm{W}_{ij}^{(\psi)}\psi_R^j$, etc., where $\psi' = u', d', e', \nu'$ represents the mass eigenstates of the fermion fields)

$$\begin{aligned}\mathcal{L}_{\text{Yukawa}} &= -\sum_{i=1}^{3} m_{(\psi')}^i \bar{\psi}'^i_L \psi'^i_R \left(1 + \frac{H}{v}\right) + h.c. \\ &= -\sum_{i=1}^{3} m_{(\psi')}^i \bar{\psi}'^i_L \psi'^i_R \left(1 + \frac{g}{2M_W} H\right) + h.c.,\end{aligned} \tag{2.35}$$

where the sum is over all the left- and right-handed fermion pairs[9]. Note that the physical Higgs boson couples to the i^{th} fermion with the strength $gm_i/2M_W$, which is very small except for the top quark.

The Gauge Currents

The fermion kinetic and interaction terms of the SM Lagrangian eq. (2.14) can be rewritten as couplings of fermionic currents to the physical gauge bosons. First, the covariant derivative eq. (2.3) of the electroweak interaction becomes

$$\begin{aligned}D_\mu &= \partial_\mu - igW_\mu^a \tau^a - ig' Y B_\mu \\ &= \partial_\mu - \frac{g}{\sqrt{2}}\left(W_\mu^+ \tau^+ + W_\mu^- \tau^-\right) - i\frac{g}{\cos\theta_W} Z_\mu^0 \left(\tau^3 - \sin^2\theta_W Q\right) - ieA_\mu Q\end{aligned} \tag{2.36}$$

with the definitions, $e \equiv \frac{gg'}{\sqrt{g^2+g'^2}}$, $Q \equiv \tau^3 + Y$ and $\tau^\pm = \frac{1}{2}(\sigma^1 \pm i\sigma^2)$.

9. At the weak scale $v = 2M_W/g \simeq (\sqrt{2}G_F)^{-1/2} \simeq 246\,\text{GeV}$ [31].

Second, eq. (2.14) is rewritten as:

$$\begin{aligned}\mathcal{L}_{\rm f} &= i\bar{Q}_L^f \not{D} Q_L^f + i\bar{u}_R^f \not{D} u_R^f + i\bar{d}_R^f \not{D} d_R^f + \bar{L}_L^f \not{D} L_L^f + \bar{e}_L^f \not{D} e_L^f \\ &= \text{kinetic terms} + g\left(W_\mu^+ \mathcal{J}_{W^+}^\mu + W_\mu^- \mathcal{J}_{W^-}^\mu + Z_\mu^0 \mathcal{J}_{Z^0}^\mu\right) \\ &+ eA_\mu \mathcal{J}_{\rm em}^\mu + g_s G_\mu^A \mathcal{J}_{\rm QCD}^{A\mu},\end{aligned} \tag{2.37}$$

where the charged currents for the $W_\mu^\pm$ are given by:

$$\begin{aligned}\mathcal{J}_{W^+}^\mu &= \frac{1}{\sqrt{2}}\left(\bar{\nu}_L^f \gamma^\mu e_L^f + \bar{u}_L^f \gamma^\mu d_L^f\right) \\ \mathcal{J}_{W^-}^\mu &= \frac{1}{\sqrt{2}}\left(\bar{e}_L^f \gamma^\mu \nu_L^f + \bar{d}_L^f \gamma^\mu u_L^f\right),\end{aligned} \tag{2.38}$$

and the weak neutral current becomes:

$$\mathcal{J}_{Z^0}^\mu = \frac{1}{\cos\theta_W} \sum_\psi \bar{\psi}\gamma^\mu \left(\tau^3 - \sin^2\theta_W\right)\psi, \tag{2.39}$$

where $\psi = \nu_L, \nu_R, e_L, e_R, \ldots$ (the sum is over all the fermions). The two last terms of eq. (2.37) are the electromagnetic current:

$$\mathcal{J}_{\rm e.m.}^\mu = -\bar{e}^f \gamma^\mu e^f + \frac{2}{3}\bar{u}^f \gamma^\mu u^f - \frac{1}{3}\bar{d}^f \gamma^\mu d^f, \tag{2.40}$$

and the strong current:

$$\mathcal{J}_{\rm QCD}^{\mu A} = \bar{u}^f \gamma^\mu T^A u^f + \bar{d}^f \gamma^\mu T^A d^f, \tag{2.41}$$

where for the last currents, which are *vector like*, we revert to the Dirac notation $\bar{\psi}\gamma^\mu\psi = \bar{\psi}_L\gamma^\mu\psi_L + \bar{\psi}_R\gamma^\mu\psi_R$.

However, we are still in the gauge eigenstates, and to get the mass eigenstates we have to perform the U,W rotation. The kinetic terms and the currents, $\mathcal{J}_{\rm e.m.}^\mu$, $\mathcal{J}_{Z^0}^\mu$, and $\mathcal{J}_{\rm QCD}^{\mu A}$, are

unchanged (since they only include terms of the same flavor with the same coefficients and the U,W matrices are unitary). The charged currents become

$$\begin{aligned}\mathcal{J}^{\mu}_{W^+} &\to \frac{1}{\sqrt{2}}\left(\bar{\nu}^i_L\gamma^\mu \mathrm{U}^{(\nu)}_{ik}\mathrm{U}^{(e)\dagger}_{kj}e^j_L + \bar{u}^i_L\gamma^\mu \mathrm{U}^{(u)}_{ik}\mathrm{U}^{(d)\dagger}_{kj}d^j_L\right)\\ \mathcal{J}^{\mu}_{W^-} &\to \frac{1}{\sqrt{2}}\left(\bar{e}^i_L\gamma^\mu \mathrm{U}^{(e)}_{ik}\mathrm{U}^{(\nu)\dagger}_{kj}\nu^j_L + \bar{d}^i_L\gamma^\mu \mathrm{U}^{(d)}_{ik}\mathrm{U}^{(u)\dagger}_{kj}u^j_L\right).\end{aligned} \tag{2.42}$$

Note that there is no W dependence, since the charged currents depend only on left-handed fields. In eq. (2.42) we have the rotation matrix $\mathrm{U}^{(\nu)}$ for the neutrinos, which follows from the Yukawa term for the neutrinos in eq. (2.33). However, in the Standard Model neutrinos are normally assumed to be massless, i.e. there is no need for the $\mathrm{U}^{(\nu)}$, so we can take it out. Because it is always possible to redefine a field by an overall rotation, we can take $\nu_j \to \mathrm{U}^{(e)\dagger}_{ji}\nu_i$. Thus, $\mathrm{U}^{(e)}$ also disappears. It is common to define $V_{\mathrm{CKM}} = \mathrm{U}^{(u)}\mathrm{U}^{(d)\dagger}$, which is the famous CKM matrix. If the neutrinos are not taken as massless we can make a similar definition[10] for the leptonic part, $\mathrm{V}_{\mathrm{PMNS}} = \mathrm{U}^{(\nu)}\mathrm{U}^{(e)\dagger}$, the Pontecorvo-Maki-Nakagawa-Sakata (PMNS) matrix.

10. The definition is exactly the same except in the case of a Majorana mass for ν_R.

The Lagrangian in Mass Eigenstates

After the spontaneous symmetry breaking and the rotation from gauge to mass eigenstates, the SM Lagrangian (2.8) can be summarized as

$$\begin{aligned}\mathcal{L} = \mathcal{L}_{\text{gauge}} &+ \sum_i \bar{\psi}_i \left(i\partial\!\!\!/ - m_i - \frac{m_i H}{v} \right) \psi_i \\ &+ g \left(\mathcal{J}^\mu_{W^+} W^+ + \mathcal{J}^\mu_{W^-} W^- + \mathcal{J}^\mu_{Z^0} Z^0_\mu \right) + e A_\mu \mathcal{J}^\mu_{\text{e.m.}} + g_s G^A_\mu \mathcal{J}^{A\mu}_{QCD} \\ &+ M_W^2 W^+_\mu W^{-\mu} + \frac{1}{2} M_Z^2 Z^0_\mu Z^{0\mu} \\ &+ -\frac{\mu^4}{4\lambda} - \mu^2 H^2 + \lambda v H^3 + \frac{\lambda}{4} H^4\end{aligned} \tag{2.43}$$

2.3 QCD and Collider Physics

Quantum Chromodynamics (QCD) is the theory of the strong force. In the previous section we have seen how the interactions between quarks and gluons can be derived from the SM Lagrangian, eq. (2.8). In this section, we shall look into the relevance the QCD theory for collider physics and the hadronic final states probed in this thesis. Section 2.3.1 briefly discusses renormalization, asymptotic freedom, confinement, and running gauge couplings. Section 2.3.2 describes parton distribution functions. Section 2.3.3 describes parton shower and hadronization.

2.3.1 Renormalization, Asymptotic Freedom, and Confinement

In quantum field theories, such as QCD, the initial and final state of any interaction are connected via the so-called *S-matrix* (scattering matrix)[11], which gives the probability for an

11. The S-matrix is a unitary matrix connecting the input and output states in a Hilbert space. [30]

interaction to happen. The simplest *leading order* (LO) processes, such as $2 \to 2$ scattering, include only tree-level diagrams. More complicated processes, such as *next-to-leading order* (NLO), also involve virtual particles. Examples of LO and NLO processes are shown in fig. 2.7. While diagrams up to arbitrary high order are allowed in principle, calculations beyond NLO or NNLO (next-to-next-to-leading order) are extremely challenging.

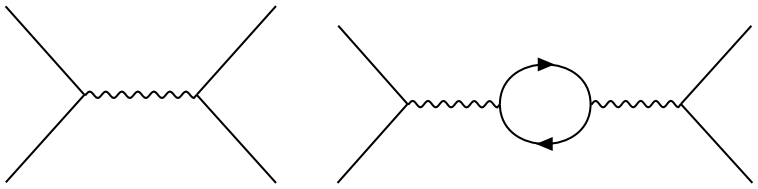

Figure 2.7: Example of leading order (left) and next-to-leading order (right) processes.

For many processes, higher order perturbative expansions of the S-matrix gives rise to loop diagrams which lead to divergent integrals, as the momentum in the loop is integrated over all possible values[12], such as the examples shown in fig. 2.8. The solution to get rid of these divergences is a set of schemes, *renormalization*, to reformulate the theory in such a way as to keep the integrals finite. In a nutshell this means setting the energy scale in so that the infinite integrals in the loops are cut off from any calculation of physical observables [30].

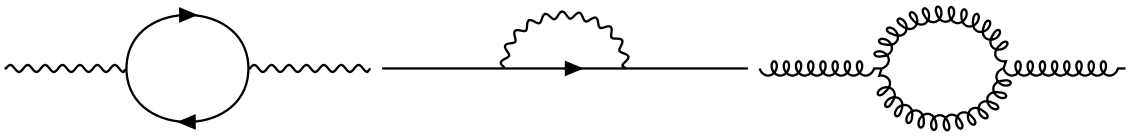

Figure 2.8: Example of loop diagrams which give rise to divergent integrals in QFT.

An interesting consequence of renormalization is that coupling "constants" associated with gauge fields—such as $\alpha_s \equiv \frac{g_2^2}{4\pi}$ in QCD, or $\alpha \equiv g$ in QED (i.e. the fine structure constant)—are not really that constant. Rather, they are only constant after first fixing the renormalization scale. The value of α_s constant at some arbitrary energy scale Q, relative to a reference

12. Analogous to the story of diverging radiated power in the *blackbody* spectrum from a hot object in the introduction, although the specific problem and solution are of course different here.

energy scale μ is given by: [29]

$$\alpha_s(Q^2) = \frac{\alpha_s(\mu^2)}{1 + \frac{\alpha_s(\mu^2)}{12\pi}(33 - 2n_f)\log\left(\frac{Q^2}{\mu^2}\right)}, \tag{2.44}$$

where n_f is the number of flavours in the theory, thus $n_f = 6$ in the SM (six quarks flavours). From eq. (2.44) it is clear that α_s decreases logarithmically as the energy scale Q^2 increases (or as the distance scale decreases), relative to the reference scale μ^2. As Q^2 goes to infinity, α_s goes to zero, this is referred to as *asymptotic freedom*. On the other hand, for sufficiently small Q^2 the coupling becomes large ($\alpha_s \gg 1$), and the perturbation theory does not work anymore, since higher order terms diverge (contributing more and more to the perturbation expansion) [34, 35]. The Q^2 scale at which this happens is often denoted by Λ, and eq. (2.44) is re-written as:

$$\alpha_s(Q^2) = \frac{12\pi}{(33 - 2n_f)\log\left(\frac{Q^2}{\Lambda^2}\right)}, \tag{2.45}$$

where the cut off scale Λ (at which perturbation theory breaks down) is of the order 0.1 to 0.5 GeV [29]. With Q^2 at the Z-pole[13], $\alpha_s = 0.1181(11)$ [19], thus we may safely apply perturbation theory in this regime. The breakdown of the perturbation theory for α_s at low Q^2 implies that transition to a new regime has occurred[14] Indeed, this leads to the confinement of quarks and gluons, i.e. neither quarks nor gluons are ever observed free, only in bound states [36]. In contrast, the QED coupling α,

$$\alpha(Q^2) = \frac{\alpha(\mu^2)}{1 - \frac{\alpha(\mu^2)}{3\pi}\log\left(\frac{Q^2}{\mu^2}\right)}, \tag{2.46}$$

becomes smaller at higher energies, thus higher order corrections in the perturbation theory

13. Scale of the Z boson mass

14. Although there is no known theoretical mechanism to explain the transition to this state, the existence of jets and the fact that colored particles have never been observed suggest that confinement is a reality.

contributes less and less.

2.3.2 Parton Distribution Functions

What's inside the proton? The answer to this question is that it depends on at what energy scale the proton is being probed. The quarks inside the proton (and all other hadrons) are bound together by gluons, which can split into virtual quark/anti-quark pairs. These virtual quarks are referred to as a *sea* of partons (*udd* are known as valence partons). While QCD scattering at higher energies can be calculated with perturbation theory via matrix element calculations for the relevant process, the partons within the proton are in the non-perturbative regime. Fortunately, the cross section of the $2 \to n$ body parton hard-scattering process (i.e. the actual collision) can be factorized from the non-perturbative components using the QCD factorization theorem [37].

The probability of finding a parton of a given flavor, from the proton interacting at a momentum-scale Q^2, with momentum fraction x is parametrized by a probability density known as a *parton distribution function* (PDF) [38]. Example PDF sets at two different momentum scales ($Q^2 = 10$ GeV^2 (left) and $Q^2 = 10^4$ GeV^2) are shown in fig. 2.9. At lower Q^2, the PDF set is dominated by the up/down-quarks and gluons. However, at higher Q^2 a sea of c, s, and b quarks participate in interactions. Many different PDF sets are available and used in the Monte Carlo event simulations crucial for LHC precision measurements and searches (such as the analyses presented in chapter 8 and chapter 9). Two PDF sets in common use at the LHC are NNPDF [39] and MMHT14 [40], both are at Next-to-Next-to-Leading Order (NLO).

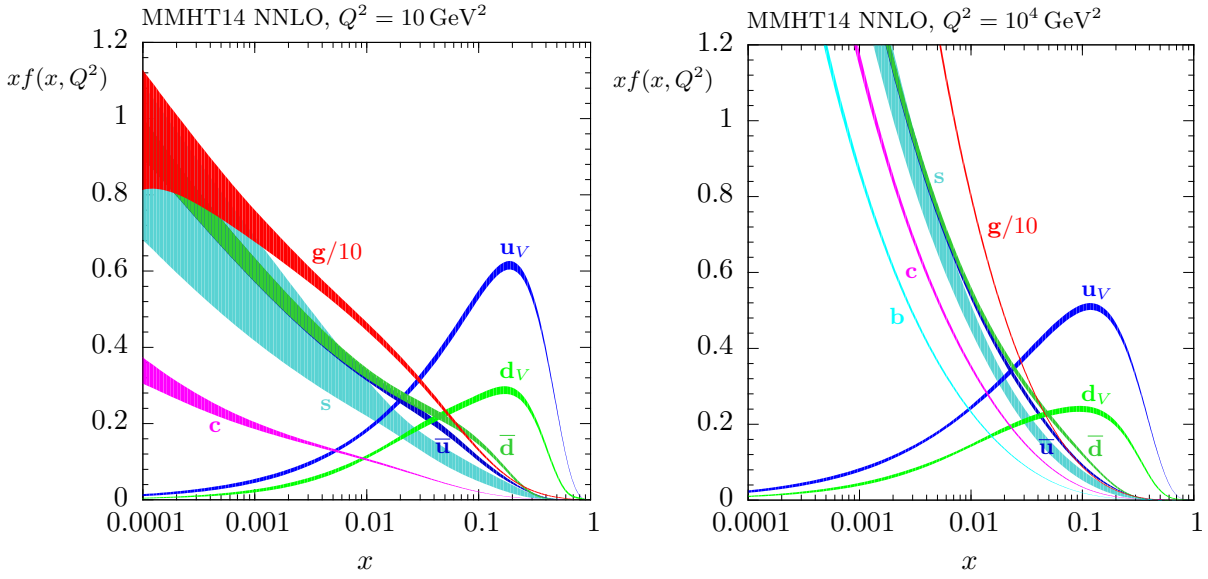

Figure 2.9: The MMHT14 NNLO parton distribution functions, evaluated at energy scales of $Q^2 = 10$ GeV^2 (left) and $Q^2 = 10^4$ GeV^2 (right), are shown for several flavours. Uncertainty bands are plotted at 68% CL. [40]

2.3.3 Parton Shower and Hadronization

As discussed in the previous section, the hard-scatter collisions at the LHC are taking place at the parton level. Confinement implies that free quarks and gluons produced in the collisions, or in the decays of other particles, will use some of their kinetic energy to create partners in order to form bound states. This process is referred to as hadronization. However, before hadronization happens, the high energy partons coming from the hard-scatter collisions will radiate gluons (via QCD) and photons (via QED). Since gluons also carry color charge they can in turn radiate partons, leading to showers of particles known as jets. At high energies the probability of a single parton to split into two daughter particles depends on the energy of the daughter particles and a splitting scale μ, according to the DGLAP (Dokshitzer-Gribov-Lipatov-Altarelli-Parisi) formalism [41, 42, 43]. The splitting will continue on each of the daughter particles until energies are low enough for hadronization, around $\mu_{\mathrm{min}} \sim 1$ GeV^2. This the processes of parton showering and hadronization are summarized in fig. 2.10.

The process of hadronization is non-preturbative and highly complicated. Two commonly used approaches for approximating it are known as the *cluster model* [44], and the *Lund string model* [45]. The cluster model starts with the non-perturbative splitting of gluons into colorless $q\bar{q}$ pairs, which are clustered and analyzed to predict daughter hadrons. The Lund string model forms narrow tubes (or strings) of strong color fields from gluons which are attracted to each other via the gluon self-interactions. Both models are applied in the event simulations in this thesis, via the PYTHIA simulator [46] which uses the string model, and the HERWIG++ simulator [47] which uses the cluster model. An illustration comparing the phenomenology of the cluster and string hadronization models are shown in fig. 2.11.

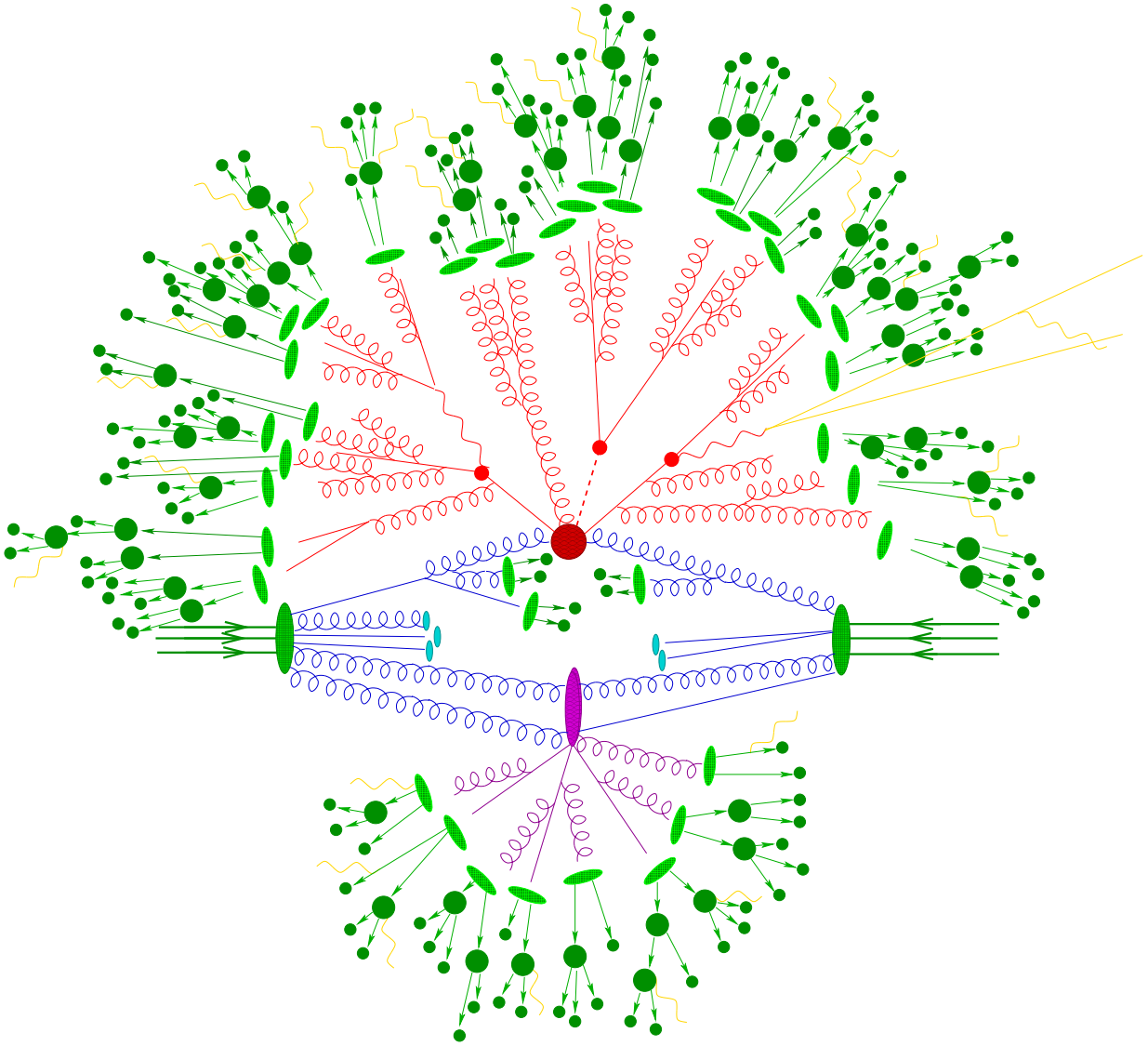

Figure 2.10: Illustration of a typical Monte Carlo event simulation of a proton-proton collision at the LHC. The most energetic (and thus often the most interesting) final state particles originate from interactions with large momentum transfers from the primary hard scatter interaction (red blob in the middle). Secondary interactions involves smaller momentum transfers which lead to lower energy (less interesting) decay products (purple). Higher energy partons shower according to perturbative QCD via processes such as gluon splitting (red). Lower energy partons form hadrons, via a process called hadronization, into various quasi-stable baryons and mesons (green). [48]

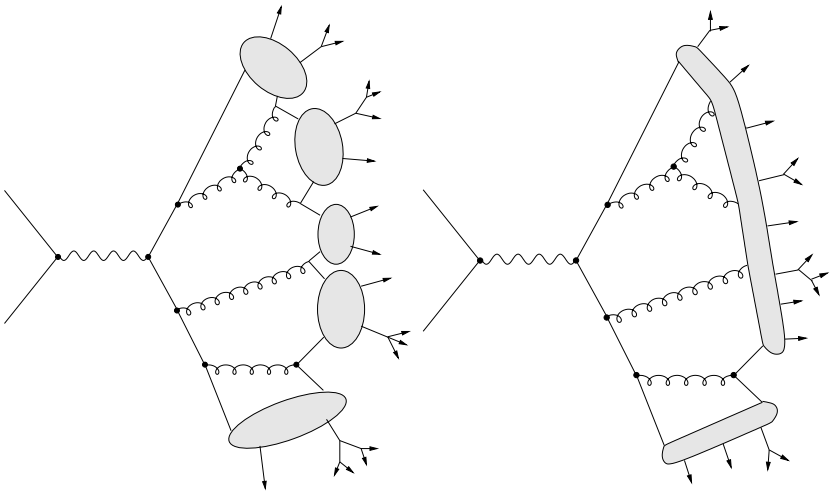

Figure 2.11: An illustration of the cluster (left) and string (right) hadronization models. [44]

2.4 Problems with the Standard Model

After describing the extraordinary success of the Standard Model in the previous chapters, we shall now discuss some of its main shortcomings. First, there are several cases where the Standard Model fails to provide a sufficient explanation for experimentally observed phenomena (section 2.4.1). Second, there are structural issues with the theory itself, i.e. the so-called *hierarchy problem*, which follow from higher order interactions of the Higgs boson with heavy fermions and gauge bosons (section 2.4.2).

2.4.1 Observational Hints of Physics Beyond the Standard Model

Among the most striking examples of existence of physics beyond the SM (BSM) is the presence of a significant amount of a mysterious substance known as DM[15], since its presence has only been inferred via gravitational effects in cosmological observations, such as analysis

15. Since it does not interact electromagnetically, it does not emit light, hence the name *dark matter*.

of galactic rotation curves (illustrated in fig. 2.12) [49, 50], gravitational lensing [51, 52], and measurements of the cosmic microwave background radiation [53]. Measurements like these strongly suggest that there must be a source of mass which makes up approximately 85% of the mass in the universe. The SM does not provide a viable candidate to account for the abundance of DM in the universe. A dark matter candidate could not carry electromagnetic charge, nor is it believed to interact via the strong force, which only leaves the weak interactions as an option (besides its known gravitational interaction). The only SM particles that would be potential DM candidates are the neutrinos, however the small mass of the known neutrinos makes them too *hot* (fast) to lump together and form the dense dark matter structures needed to hold galaxies and galaxy clusters together [54, 55].

In addition to open question about the nature of dark matter, the SM does not provide an sufficient explanation for the asymmetry between matter and antimatter in the universe. Although part of this asymmetry can be accounted for via processes that violate charge-parity (CP) conservation in the SM, it is an open question whether these parameters are sufficient to account for the observed matter-antimatter asymmetry [56]. The SM also does not account for the known phenomena of neutrino oscillations, although that could be included with only minor modifications to the current theory (such as incorporating the PMNS matrix, analogously to the CKM mixing matrix for the quark sector) [57].

2.4.2 Structural Problems with the Theory

As described in section 2.2.2, the Higgs field is responsible for generating masses for the W, Z, and fermions. However, these interactions go both ways. Since the Higgs boson couples to all massive bosons (via the gauge interactions) and fermions (via the Yukawa interactions), the *bare* Higgs mass receives perturbative corrections from higher order loop diagrams terms, as shown in fig. 2.13.

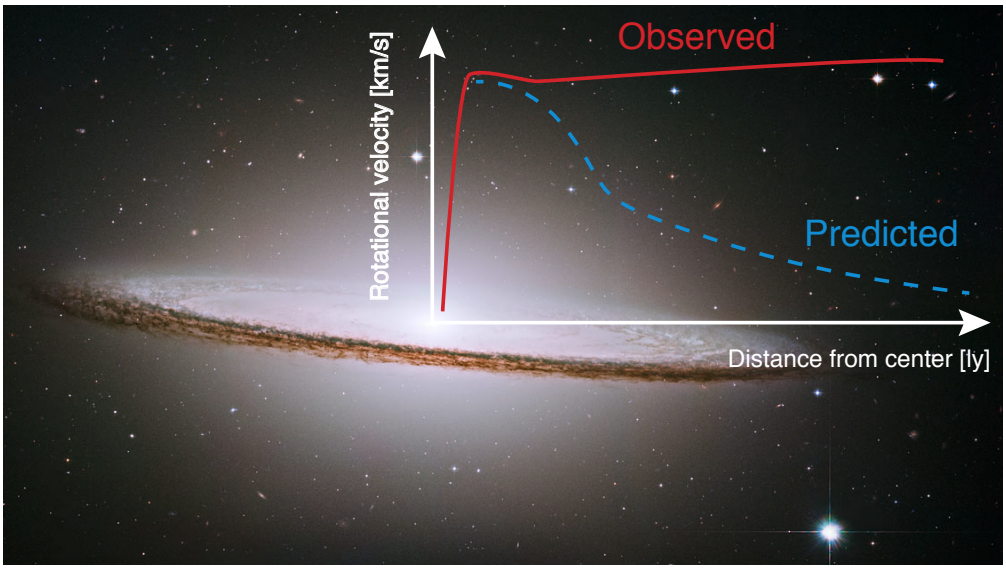

Figure 2.12: Illustration of galactic rotational velocity (in km/s) as a function of the distance from the center of the galaxy. The red (blue) curve illustrate what the observed (predicted) curve typically looks like. Image of the Sombrero Galaxy by the Hubble Space Telescope. [58]

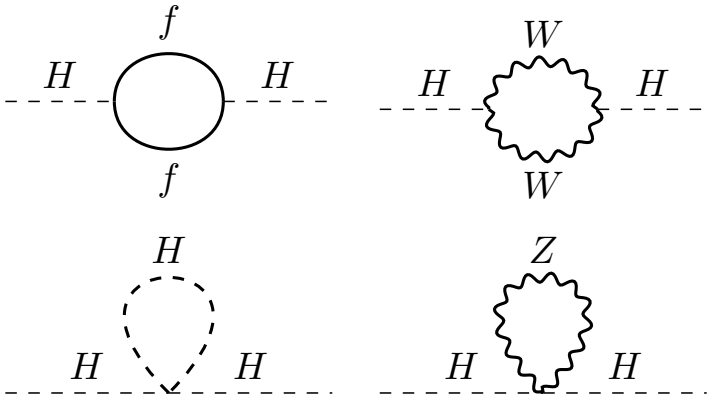

Figure 2.13: Examples of higher order loop correction diagrams to the Higgs mass. The largest correction comes from the top quark. [31]

The largest corrections involve higher order interactions with the top quark, as follows:

$$m_H^2 = \left(m_H^2\right)_{bare} + \Delta m_H^2, \tag{2.47}$$

where the correction is given by:

$$\Delta m_H^2 = -\frac{|y_T|^2}{8\pi^2}\Lambda_{\text{UV}}^2 + \ldots, \tag{2.48}$$

where y_T is the Yukawa coupling for the top quark, and Λ_{UV} is the high-energy cutoff of the theory [31, 32]. It is clear from eq. (2.48) that this correction diverges quadratically with the cutoff scale (Λ_{UV}^2). The implication of this is that if the SM is really the only theory up to the Planck scale (where the effects the SM forces and general relativity can no longer be considered separately, and effects of quantum gravity are expected to dominate), then $\Lambda_{\text{UV}}^2 \sim M_{\text{Planck}} = 1.22 \times 10^{19}$ GeV [19, 32] (as illustrated in fig. 2.14). Given that the observed Higgs boson mass of 125 GeV [12], the only way to reconcile this is to set the *bare* Higgs mass to a value such as the discrepancy between $\left(m_H^2\right)_{bare}$ and the correction Δm_H^2 precisely cancel to 125 GeV. This means that, unless there is some way for the terms in Δm_H^2 to cancel each other out, the bare mass would have to be defined to a precision of about 1 part in 10^{19}, which seems absurd[16]. As we shall see in the next chapter, supersymmetry proposes an elegant solution to this problem.

16. Such "lucky" cancellation of terms is what physicists consider both "ugly" and improbable, hence the motivation for *naturalness*. [31]

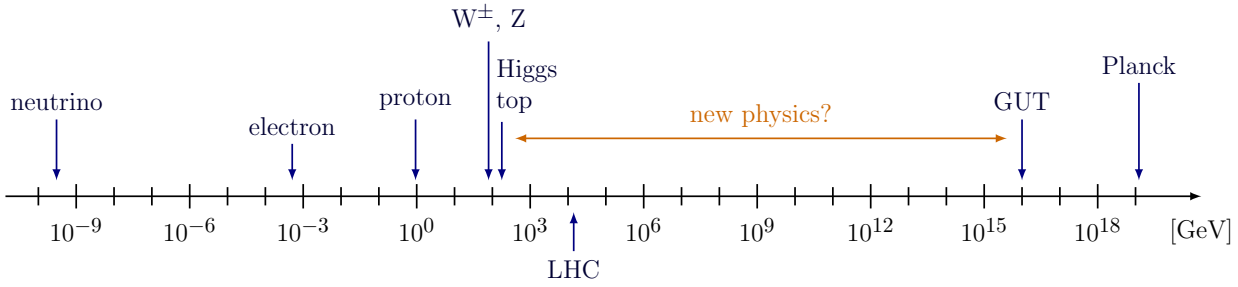

Figure 2.14: There are almost 10^{16} orders of magnitude between the low-TeV scale, within reach of the LHC, and the Planck-scale (then there is the so-called GUT-scale around 10^{16} GeV, which will be discussed in chapter 3 about supersymmetry). Does new physics hide somewhere in this range? Diagram created with TikZ [17], courtesy of [59].

2.5 Conclusion

The Standard Model is a theory of the quarks, leptons, and gauge fields which describe nature, with remakable accuracy, at the most fundamental scale known to modern science. It combines the theory of strong interactions (QCD) with the electroweak theory into a coherent quantum field theory. Central to the theory is the concept of local gauge invariance, the $SU(3)_C \otimes SU(2)_L \otimes U(1)_Y$ symmetry group, and the Higgs field. It is the product of a decades long interplay between theoretical and experimental advancements. So far the Standard Model is in agreement with experiment at the highest energy scales, a remarkable achievement. Despite its success, it is clear that the Standard Model cannot be the final theory of nature. There are some theoretical problems with the model at high energy scales (i.e. the hierarchy problem) and there are observed phenomena which it does not provide an explanation for, such as dark matter.

CHAPTER 3

SUPERSYMMETRY

This chapter introduces supersymmetry (SUSY), a very popular theoretical framework for both the theorist and experimentalist. For the theorist, SUSY is helpful when trying to understand how some of the biggest open questions in physics might fit together in a cohesive mathematical formalism. For the experimentalist, SUSY provides a set of very useful benchmark scenarios when searching for physics beyond the Standard Model.

This chapter is organized as follows: Section 3.1 gives a brief introduction to SUSY, with an emphasis on the big open questions in physics that it is attempting to address. Section 3.2 provides a brief overview of SUSY phenomenology, focusing on its minimal extension of the SM physics, the so-called Minimal Supersymmetric Standard Model (MSSM), the particle spectrum, the electroweak sector, and an important symmetry known as R-parity. Section 3.3 discusses the topics most relevant when searching for SUSY at the LHC, such as *simplified models*, how to produce SUSY at hadron colliders. Section 3.3 concludes with a summary of recent ATLAS results.

3.1 SUSY in a Nutshell

As was discussed in section 2.4, despite its extraordinary success, there are open questions in physics that the Standard Model does not address. Two important such examples are the *dark matter* problem and the *hierarchy problem*, the first is strongly backed by experimental data from cosmological experiments [49, 50, 51, 52, 53], and the latter by strong theoretical arguments [32, 31].

Supersymmetry (SUSY) is an especially alluring theoretical extension of the SM [60, 61,

62, 63, 64, 65, 32], given its potential to resolve all three of these important open questions by introducing new partners, called *superpartners* or (*sparticles*)[1], of the known bosons and fermions that share the same mass and internal quantum numbers in the case that the supersymmetry is unbroken. Before the spontaneous symmetry breaking in SUSY , a supersymmetric transformation operator (denoted by Q) turns a bosonic state into a fermionic state, and vice versa: [32]

$$Q_{\text{SUSY}} \,|\text{Boson}> \;\rightarrow\; |\text{Fermion}>, \qquad Q_{\text{SUSY}} \,|\text{Fermion}> \;\rightarrow\; |\text{Boson}> \tag{3.1}$$

However, given the lack of observation of superpartners of this kind, SUSY must be a broken symmetry and the mass scale of the supersymmetric particles is as yet undetermined. Theoretical and experimental arguments suggest that the SM is an effective theory valid up to a certain energy scale. The observation by the ATLAS and CMS collaborations of a particle consistent with the SM Higgs boson [66, 67, 68, 69] has brought renewed attention to the mechanism of electroweak symmetry breaking and the hierarchy problem [70, 71, 72, 73], since the Higgs boson mass is strongly sensitive to quantum corrections from physics at very high energy scales and demands a high level of fine-tuning. In particular, as was discussed in section 2.4.2, the largest quantum corrections to the Higgs comes from its higher order interactions with the top quark, such as the loop diagram shown in fig. 3.1. SUSY offers an

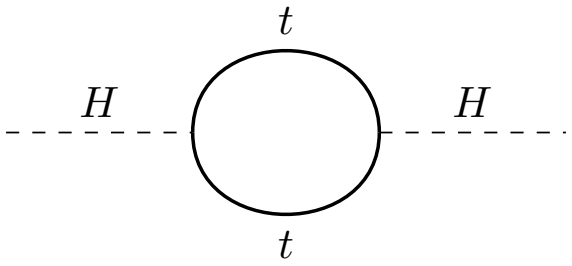

Figure 3.1: Loop correction to the Higgs squared mass from the top quark. [32]

1. The SUSY nomenclature is quite amusing. Fermion names are prefixed by the letter *s*, i.e. *sfermions*, *squarks*, *sleptons*, *stops*, *selectrons*, etc. Boson names receive an *ino*-suffix, e.g. *Wino*, *Bino*, *Higgsino*, etc.

elegant solution to the hierarchy problem [70, 71, 72, 73], as both the familiar SM particles and the new superpartners couple to the same Higgs sector[2]. It turns out that superpartners, because of the symmetry with their SM counterparts, couple to the Higgs with the exact same Yukawa couplings, but with an opposite sign. This leads to a cancellation of all higher order corrections to the Higgs mass in eq. (2.48)[3]. The possibility of a supersymmetric dark matter candidate [74, 75] is related closely to the preservation of R-parity [76]. Under the R-parity conservation hypothesis, the lightest supersymmetric particle (LSP) is stable. If the LSP is weakly interacting, it may provide a viable DM candidate. The nature of the LSP is defined by the mechanism that spontaneously breaks supersymmetry and the parameters of the chosen theoretical framework. Finally, in the context of the Minimal Supersymmetric Standard Model the running gauge couplings intersect at an energy of about 10^{16} GeV, as shown in fig. 3.2, offering the alluring possibility of unifying all the fundamental forces in the SM in to a Grand Unified Theory [32, 77].

3.2 SUSY Phenomenology

Writing down the MSSM Lagrangian can be a bit cumbersome, as it usually is done by first introducing a few new mathematical concepts, such as *supercoordinates*, *superfields*, and *superspace* integration and differentiation, which provide a powerful framework for understanding the structure of supersymmetric theories. However, for the sake of brevity and to focus on what is of most relevance for the SUSY searches presented in chapters 8 and 9, these techniques will be skipped over[4].

2. In SUSY there are four Higgses, organized into two supermultiplets, as shown in table 3.1

3. There are some important caveats to this after supersymmetry is broken, more about that in section 3.2

4. The interested reader may find an introduction in Refs. [32, 55]

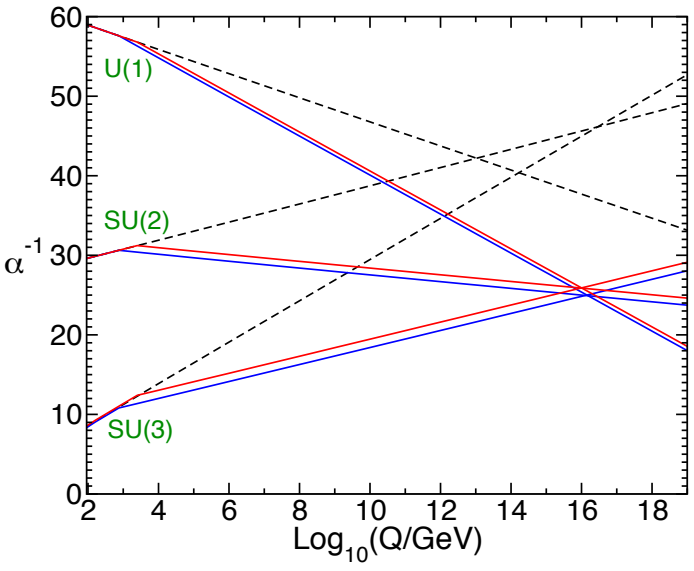

Figure 3.2: Running of the inverse gauge couplings α^{-1}(Q) in the SM (dashed lines) and MSSM (solid lines). In the MSSM, the gauge coupling constants met at an energy scale of about $Q \simeq 10^{16}$ GeV. [32]

3.2.1 The Minimal Supersymmetric Standard Model

This section introduces the phenomenology of SUSY in the context of the Minimal Supersymmetric Standard Model (MSSM). Before the supersymmetry breaking, the SUSY particles are naturally written in terms of supermultiplets, which are combinations of fermions and bosons. The supermultiplets of the MSSM are listed in table 3.1, organized according to their transformation properties under the usual SM gauge group, $SU(3)_C \otimes SU(2)_L \otimes U(1)_Y$, and their spin (similar to the SM fields in table 2.1). The list includes all the familiar fermions and bosons in the SM and their superpartners, which differ by spin-1/2. In addition, two Higgs superfields are required (denoted by H_u and H_d) in order to construct a minimal extension of the SM which gives mass to all particles[5]. The Standard Model Higgs boson (often denoted by h^0) would be a linear combination of H_u^0 and H_d^0.

5. One reason for this is that if there were only one Higgs chiral supermultiplet, the electroweak gauge symmetry would suffer a so-called *gauge anomaly*, which would make it inconsistent as a quantum theory. [32]

If SUSY was an unbroken symmetry in nature, then the superpartners of the quarks and leptons would have exactly the same masses as their SM counterparts, e.g. there would be left/right-handed *selectrons* with the same mass as the electron, and there would also be a massless *gluino* and a *photino*. If such particles existed they would have been very easy to detect, thus the lack of experimental evidence clearly suggests that if SUSY exists it must be a *broken symmetry* (in the vacuum state where our universe presently resides). Thus, any realistic phenomenological model must contain a mechanism for spontaneous supersymmetry breaking [32]. Before the breaking supersymmetry is an exact symmetry, which means that the Lagrangian of the MSSM supermultipets must be invariant under SUSY transformations (but the broken vacuum state is not). The Lagrangian which contains all gauge and Yukawa interactions invariant under supersymmetry takes the general form:

$$\mathcal{L}_{\text{SUSY}} = \mathcal{L}_{\text{kinetic}} + \mathcal{L}_{\mathcal{W}}, \tag{3.2}$$

where the first term is the standard kinetic term and the second term is the Lagrangian of the SUSY *superpotential*, which includes the supermultiplets in table table 3.1. The MSSM superpotential only contains terms that are renormalizable, invariant under supersymmetry, and respects another symmetry known as R-parity, which prevents terms that violate baryon or lepton number conservation [32]. R-parity is an important concept in the searches presented in this thesis (in particular the R-parity violating search in chapter 8), and it will be introduced in section 3.2.3. The superpotential is given by:

$$\mathcal{W}_{\text{MSSM}} = \bar{u}\mathbf{y_u}QH_u - \bar{d}\mathbf{y_d}QH_d - \bar{e}\mathbf{y_e}LH_d + \mu H_u H_d, \tag{3.3}$$

where $\mathbf{y_u}$, $\mathbf{y_d}$ and $\mathbf{y_e}$ are the Yukawa couplings (represented by 3×3 matrices). After the

supersymmetry breaking, the effective Lagrangian can be written as:

$$\mathcal{L} = \mathcal{L}_{\text{SUSY}} + \mathcal{L}_{\text{soft}}, \tag{3.4}$$

where all the terms that violate supersymmetry are included in $\mathcal{L}_{\text{soft}}$. So what form does $\mathcal{L}_{\text{soft}}$ take? Unbroken supersymmetry guarantees the cancellation of divergent terms in the quadratic Higgs mass term in eq. (2.48) to all orders in perturbation theory, since the superpartners give rise to contributions of equal magnitude but opposite sign. In order for SUSY to still resolve the hierarchy problem after the supersymmetry-breaking, it is important that $\mathcal{L}_{\text{soft}}$ only contains terms of positive mass dimension (commonly referred to as *soft*). This means in particular that dimensionless supersymmetry-breaking couplings should be absent. [32]. Figure fig. 3.3 shows the one-loop corrections to Higgs squared mass from the top quark and stop squark, two particles that contribute heavily to the renormalization of the Higgs squared mass. Due to supersymmetry the top and stop contributions have opposite sign, and thus cancel to a value proportional to the mass of the top quark and stop squarks involved: [32]

$$\Delta m_{h^0}^2 = \frac{3}{4\pi} \cos^2 \alpha y_t^2 m_t^2 \ln(m_{\tilde{t}_1} m_{\tilde{t}_2}), \tag{3.5}$$

where α is a mixing angle in the SUSY Higgs sector, and y_t is the top Yukawa coupling. Thus, it seems like the contribution of $\Delta m_{h^0}^2$ to the bare SM Higgs mass in eq. (3.5) is finite, and depends on the mass of the stops. However, the situation is complicated by the fact that the stop also is a scalar particle and thus its mass also receives corrections, similarly to the Higgs [78]. The gluino coupling to the stop is especially strong due to its large color charge.

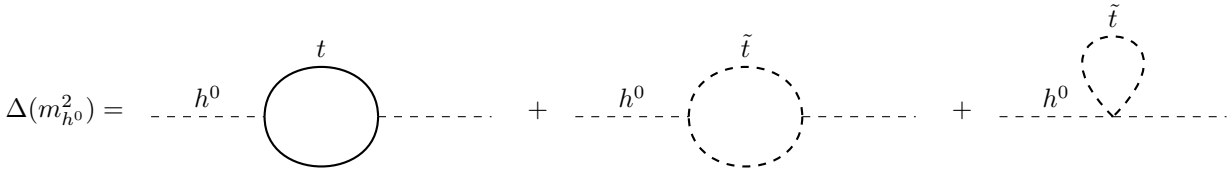

Figure 3.3: Diagrams representing the top and stop one-loop corrections to Higgs squared mass. Terms in $\mathcal{L}_{\text{soft}}$ can lead to an incomplete cancellation and thus a large positive correction to $m_{h^0}^2$ in the limit of heavy stops. [32]

Names		Spin-0	Spin-1/2	Spin-1	$SU(3)_C$	$SU(2)_L$	$U(1)_Y$
Chiral supermultiplets							
Squarks, Quarks	$Q =$	$\begin{pmatrix} \tilde{u}_L \\ \tilde{d}_L \end{pmatrix}$	$\begin{pmatrix} u_L \\ d_L \end{pmatrix}$	–	**3**	**2**	1/6
(×3 families)	$\bar{u} =$	$\tilde{u}_R^*$	$u_R^\dagger$	–	$\bar{\mathbf{3}}$	**1**	−2/3
	$\bar{d} =$	$\tilde{d}_R^*$	$d_R^\dagger$		$\bar{\mathbf{3}}$	**1**	1/3
Sleptons, Leptons	$L =$	$\begin{pmatrix} \tilde{\nu} \\ \tilde{e}_L \end{pmatrix}$	$\begin{pmatrix} \nu \\ e_L \end{pmatrix}$	–	**1**	**2**	−1/2
(×3 families)	$\bar{e} =$	$\tilde{e}_R^*$	$e_R^\dagger$	–	**1**	**1**	1
Higgs, Higgsinos	$H_u =$	$\begin{pmatrix} H_u^+ \\ H_u^0 \end{pmatrix}$	$\begin{pmatrix} \tilde{H}_u^+ \\ \tilde{H}_u^0 \end{pmatrix}$	–	**1**	**2**	+1/2
	$H_d =$	$\begin{pmatrix} H_d^0 \\ H_d^- \end{pmatrix}$	$\begin{pmatrix} \tilde{H}_d^0 \\ \tilde{H}_d^- \end{pmatrix}$	–	**1**	**2**	−1/2
Gauge supermultiplets							
Gluino, Gluon	–	–	$\tilde{g}$	g	**8**	**1**	0
Winos, W bosons	–	–	$\tilde{W}^\pm, \tilde{W}^0$	$W^\pm, W^0$	**1**	**3**	0
Bino, B boson	–	–	$\tilde{B}^0$	B^0	**1**	**1**	0

Table 3.1: The chiral- and gauge- *supermultiplets* in the MSSM, using a Weyl spinor basis, just as we did in table 2.1 for the SM fields (suppressing the generation index f). In SUSY it is convenient to write all field terms as left-handed Weyl spinors, hence the bar over the otherwise right-handed fields (i.e. $\bar{u}$, $\bar{d}$, $\bar{e}$). The gauge group in the MSSM is the same as in the SM, $SU(3)_C \otimes SU(2)_L \otimes U(1)_Y$, hence the strong, and electroweak gauge couplings are also the same.

3.2.2 SUSY and Electroweak Symmetry Breaking

The electroweak symmetry breaking in SUSY occurs analogously to what was described in section 2.2.2, for the SM. However, the calculations are slightly more complicated due to the two complex Higgs doublets, H_u and H_d, rather than just one in the SM[6]. Due to the nature of the Yukawa couplings in the Higgs sector, it is not possible to simultaneously diagonalize the gauge and the mass eigenstates. The mass eigenstates and mixing of the superpartners is of course of great interest to experimentalists. For the searches presented in this thesis, the electroweak and stop mass eigenstates introduced below are of particular importance. Table 3.2 list the particles of the MSSM, both in their gauge and mass eigenstates.

The Neutralino and Chargino Mass Eigenstates

The neutral higgisnos ($\tilde{H}_u^0,\ \tilde{H}_d^0$) and gauginos ($\tilde{B},\ \tilde{W}^0$) combine to form four neutral mass eigenstates called *neutralinos*, which are labelled in ascending order according to their mass: $m_{\tilde{\chi}_1^0} < m_{\tilde{\chi}_2^0} < m_{\tilde{\chi}_3^0} < m_{\tilde{\chi}_4^0}$. The lightest neutralino is usually assumed to be the LSP, unless R-parity is violated (or unless a lighter gravitino is included). Similarly, the charged higgsinos ($\tilde{H}_u^+,\ \tilde{H}_d^+$) and winos ($\tilde{W}^\pm$) mix to form two mass eigenstates of charge ± 1 called *charginos*, which are ordered as: $m_{\tilde{\chi}_1^\pm} < m_{\tilde{\chi}_2^\pm}$. For example, in the case of the neutralino masses, the Lagrangian in the gauge-eigenstate basis can be written as:

$$\mathcal{L}_{\text{neutralino}} = \frac{1}{2}(\psi^0)^T \boldsymbol{M}_{\tilde{\chi}^0}\psi^0 + h.c., \tag{3.6}$$

6. For detailed calculations of the electroweak symmetry breaking in the MSSM see Ref. [32].

where $\psi^0 = (\tilde{B},\ \tilde{W}^0,\ \tilde{H}_d^0, \tilde{H}_u^0)$, and

$$\boldsymbol{M}_{\tilde{\chi}^0} = \begin{pmatrix} M_1 & 0 & -c_\beta s_W m_Z & s_\beta s_W m_Z \\ 0 & M_2 & c_\beta c_W m_Z & -s_\beta c_W m_Z \\ -c_\beta s_W m_Z & c_\beta c_W m_Z & 0 & -\mu \\ s_\beta s_W m_Z & -s_\beta c_W m_Z & -\mu & 0 \end{pmatrix}. \tag{3.7}$$

Here the two[7] mixing angles have been abbreviated as: $s_k \equiv \sin\theta_k$ and $c_k \equiv \cos\theta_k$. The entries M_1 and M_2 comes from $\mathcal{L}_{\text{soft}}$ [32]. This matrix can be diagonalized to obtain the neuralino mass eigenstates listed above. The procedure is similar for the charginos.

The Stop Mass Eigenstates

There is also a mixing taking place for squarks and sleptons, specifically the mass eigenstates for the stops is obtained as follows:

$$\begin{pmatrix} \tilde{t}_1 \\ \tilde{t}_2 \end{pmatrix} = \begin{pmatrix} c_{\tilde{t}} & -s_{\tilde{t}^*} \\ s_{\tilde{t}} & c_{\tilde{t}} \end{pmatrix} \begin{pmatrix} s_{\tilde{t}} \\ c_{\tilde{t}} \end{pmatrix}, \tag{3.8}$$

where $c_{\tilde{t}}$ and $s_{\tilde{t}}$ are mixing angles incorporating terms in Yukawa couplings and soft breaking terms which mix left/right-handed stops. [32]

7. Since there are two Higgs doublets in the MSSM, we now have two mixing angles

Names	Spin	P_R	Gauge Eigenstates	Mass Eigenstates
Higgs bosons	0	+1	$H_u^0, H_d^0, H_u^+, H_d^-$	$h^0, H^0, A^0, H^\pm$
squarks	0	-1	$\tilde{u}_L, \tilde{u}_R, \tilde{d}_L, \tilde{d}_R$	(same)
			$\tilde{s}_L, \tilde{s}_R, \tilde{c}_L, \tilde{c}_R$	(same)
			$\tilde{t}_L, \tilde{t}_R, \tilde{b}_L, \tilde{b}_R$	$\tilde{t}_1, \tilde{t}_2, \tilde{b}_1, \tilde{b}_2$
sleptons	0	-1	$\tilde{e}_L, \tilde{e}_R, \tilde{\nu}_e$	(same)
			$\tilde{\mu}_L, \tilde{\mu}_R, \tilde{\nu}_\mu$	(same)
			$\tilde{\tau}_L, \tilde{\tau}_R, \tilde{\nu}_\tau$	$\tilde{\tau}_1, \tilde{\tau}_2, \tilde{\nu}_\tau$
neutralinos	1/2	-1	$\tilde{B}^0, \tilde{W}^0, \tilde{H}_u^0, \tilde{H}_d^0$	$\tilde{\chi}_1^0\ \tilde{\chi}_2^0\ \tilde{\chi}_3^0\ \tilde{\chi}_4^0$
charginos	1/2	-1	$\tilde{W}^\pm, \tilde{H}_u^+, \tilde{H}_d^-$	$\tilde{\chi}_1^\pm, \tilde{\chi}_2^\pm$
gluino	1/2	-1	$\tilde{g}$	(same)
goldstino (gravitino)	$\frac{1}{2}$ $\frac{3}{2}$	-1	$\tilde{G}$	(same)

Table 3.2: The SUSY particles in the MSSM, both in their gauge and mass eigenstates. [32]

The Gluino

Since the gluino is a color octet (superpartner of the gluon) it cannot mix with the other particles in the MSSM. [32]

3.2.3 R-Parity (Violation)

R-parity (R_p) is a discrete symmetry that explicitly forbids all the terms in eq. (3.10). It is defined as: [79]

$$R_p = (\mathbf{1})^{3B+L+2S}, \tag{3.9}$$

where B denotes the baryon number, L the lepton number, and S the spin of the particle. All SM particles have $R_p = 1$, while supersymmetric particles have $R_p = -1$. If R-parity is conserved, then superpartners can only be produced in pairs and the LSP is stable, thus providing a possible DM candidate. R-parity in the context of ATLAS searches is discussed in section 8.1.

In the Standard Model there are no interactions that violate baryon- and lepton number. However, in the MSSM it is possible to write down the following renormalizable terms which violate either baryon number, lepton number, or both simultaneously: [32]

$$\mathcal{W}_{\not{R}_p} = \frac{1}{2}\lambda^{ijk} L_i L_j \bar{e}_k + \lambda'^{\,ijk} L_i Q_j \bar{d}_k + \frac{1}{2}\lambda''^{\,ijk} \bar{u}_i \bar{d}_j \bar{d}_k + \kappa^i L_i H_u, \tag{3.10}$$

where i, j, k are generation indices, and the λ's are Yukawa couplings (different from the Yukawa couplings in eq. (3.4)). The last term can be removed by a change of gauge by rotating the L and H superfields so it is often ignored [79]. There is no obvious theoretical constrain to remove any of the other terms. The most concerning fact about R-parity violation (RPV) is that the combination of both lepton- and baryon-number terms in eq. (3.10)

can lead to the possibility of rapid proton decay, an example is shown in fig. 3.4. Using dimensional arguments the decay rate of this process can be estimated as: [79]

$$\Gamma(p \to e^+\pi^0) \approx \frac{\lambda'^{\,2}_{11k}\lambda''^{\,2}_{11k}}{16\pi^4 \tilde{m}^4_{d_k}} M^5_{\text{proton}}. \tag{3.11}$$

By inserting experimental constraints on the proton decay of $\tau(p \to e\pi) > 10^{32}$ years [19] into eq. (3.11), an upper limit on the product of the λ'_{11k} and λ''_{11k} Yukawa couplings as:

$$\lambda'_{11k} \times \lambda''_{11k} \lesssim 2 \times 10^{-23} \left(\frac{m_{\tilde{q}}}{100 \text{ GeV}}\right), \tag{3.12}$$

where $m_{\tilde{q}}$ is a typical squark mass [80].

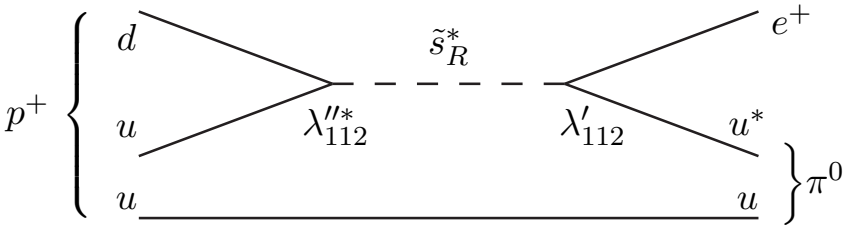

Figure 3.4: Example of a diagram which contributes to rapid proton decay if R-parity is violated for both λ' and λ'' terms. In the diagram shown a squark acts as a mediator for the $p \to e\pi^0$ process. [32]

3.3 Searching for SUSY at Hadron Colliders

This section provides a brief overview of how SUSY is being searches for at hadron colliders, such as the LHC. Due to the large space of free parameters in models[8] like the MSSM, searches are performed using *simplified models*. Common assumptions that go into these simplified models are discussed below in section 3.3.1. Then there is the question of how

8. There are 105 new free parameters in the MSSM, interpreting the results of a SUSY search with that many free parameters is not feasible.

to actually produce SUSY particles in the collisions at the LHC (assuming they exist at an energy scale that is within reach), and how they might decay, this is discussed in section 3.3.2. Finally, a brief status update is given on the latest SUSY results from ATLAS and CMS (as of 2018) in section 3.3.3.

3.3.1 Simplified Models

A *simplified model* in the context of SUSY searches at the LHC is defined by an effective Lagrangian, which only includes the interactions of a small number of parameters directly related to a particular set of collider observables at the TeV-scale. In such simplified models, the other SUSY particles are assumed to be heavy and thus can be decoupled using an Effective Field theory approach [81]. For the experimentalist, this usually means a small number of masses and cross sections to look for (and compare with SM predictions). The specific choices made when defining a simplified model vary depending on the search. However, in order to mitigate the hierarchy problem (and rescue naturalness), light stops are required to keep $\Delta m^2_{h^0}$ in eq. (3.5) low. Light gluinos are also desired in order to keep the radiative corrections to the stop mass low.

3.3.2 SUSY Production at the LHC

Assuming supersymmetry in the context of the MSSM (or closely related SUSY extension of the SM), SUSY particles can be produced in several ways. For a hadron collider, such as the LHC, strong production via interactions with SM quarks or gluons is expected to yield the largest production cross sections. Direct production of charginos and neutralinos is of course also a possibility[9], however such production could only occur via the electroweak interaction

9. In fact, searching for SUSY with electroweak production has constituted the bulk of my thesis, which is presented in chapter 9.

(since charginos and neutralinos does not interact via the strong force), and would thus have significantly less production cross section compared to superpartners produced via the strong interaction. However, given that we have no idea what the SUSY mass-hierarchy looks like, there is certainly a possibility that the strongly-coupled SUSY particles are too massive to be directly produced at the LHC. In that case SUSY may still be accessible via direct electroweak production. If R-parity is conserved, SUSY particles are required to be produced in pairs. In R-parity-violating scenarios, the RPV interactions could contribute to production (e.g. resonant single stop production), however these interactions are often vanishingly small and thus neglected in LHC analyses (such as in the case of the RPV stop search presented in chapter 8). Figure 3.5 shows the simulated pair-production cross section for various scenarios with both strong and electroweak production.

Example diagrams for SUSY pair-production channels considered in LHC searches are shown in fig. 3.6. Figure 3.7a shows the leading order diagram which contribute to the RPV stop search presented in chapter 8, and fig. 3.7b shows the leading order diagrams which contribute to the electroweak Wh search presented in chapter 9. Diagrams showing the decays into fully hadronic final states are shown in fig. 3.8.

3.3.3 Status of SUSY Searches at the LHC as of 2018

The most recent results from SUSY searches at the LHC are available via the ATLAS [83] and CMS [84] websites. Figure 3.9 summarizes the mass reach of ATLAS SUSY searches.

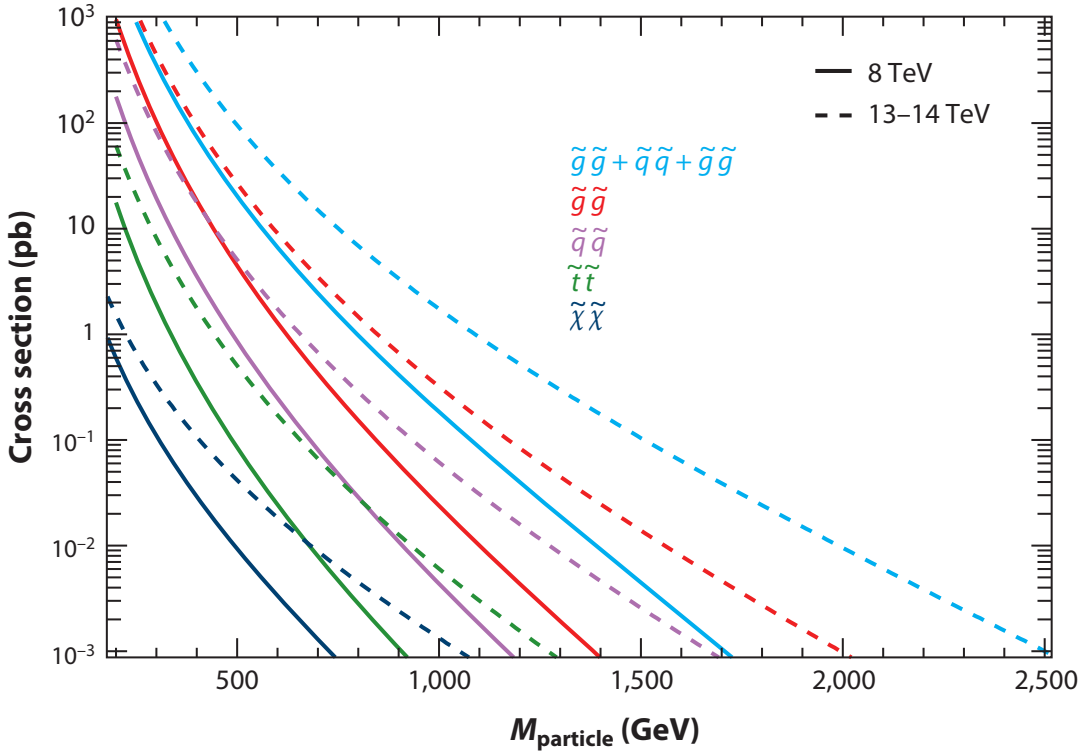

Figure 3.5: Simulated production cross section as a function of mass for sparticles at 8 TeV and 13 – 14 TeV. Gluinos have the highest production cross section due to the strong coupling constant. Direct chargino and neutralino production has significantly lower cross section, since it depends on the weak coupling constant. There is a significant increase in the production cross section with the increase in energy for all processes. The electroweak pair production is sensitive to mixing, and the Higgsino cross section is about an order of magnitude lower than the pure wino case. [82]

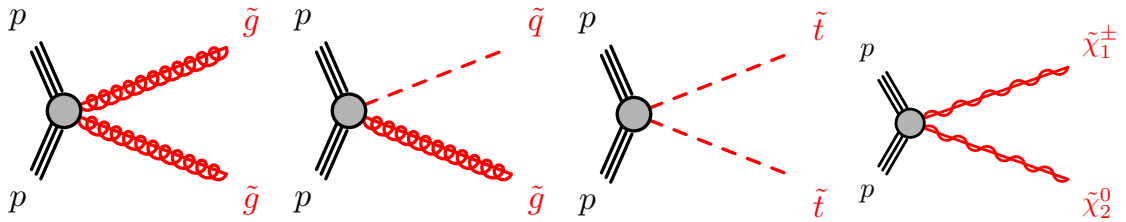

Figure 3.6: Example Feynman diagrams for SUSY pair-production channels at the LHC; (a) $\tilde{g}\tilde{g}$, (b) $\tilde{q}\tilde{g}$, and (c) $\tilde{t}\tilde{t}$, at the strong scale; and (d) $\tilde{\chi}_1^{\pm}\tilde{\chi}_2^0$ at the electroweak scale. The dashed red lines represent the SUSY processes.

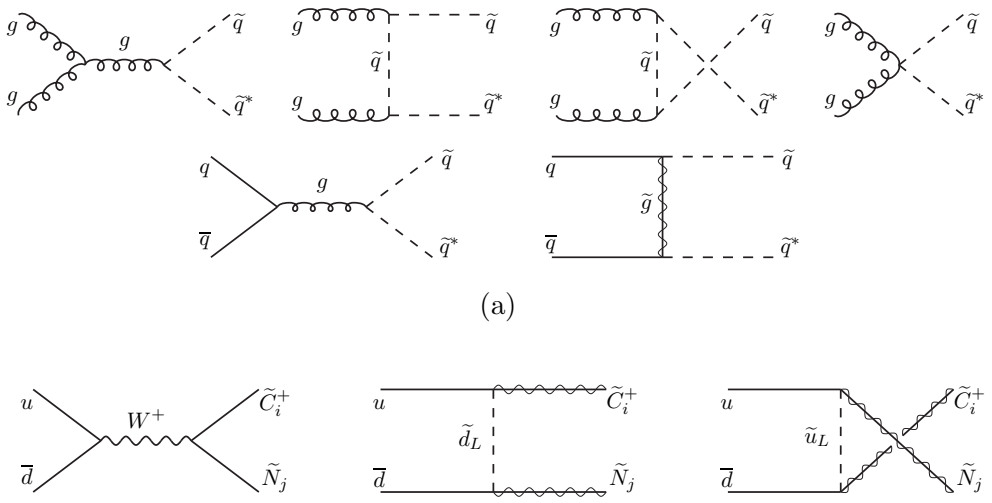

Figure 3.7: Detailed Feynman diagrams for the pair-production processes relevant for (a) the $\tilde{t}\tilde{t}^*$ channel in chapter 8, and (b) the chargino-neutralino channel in chapter 9. [32]

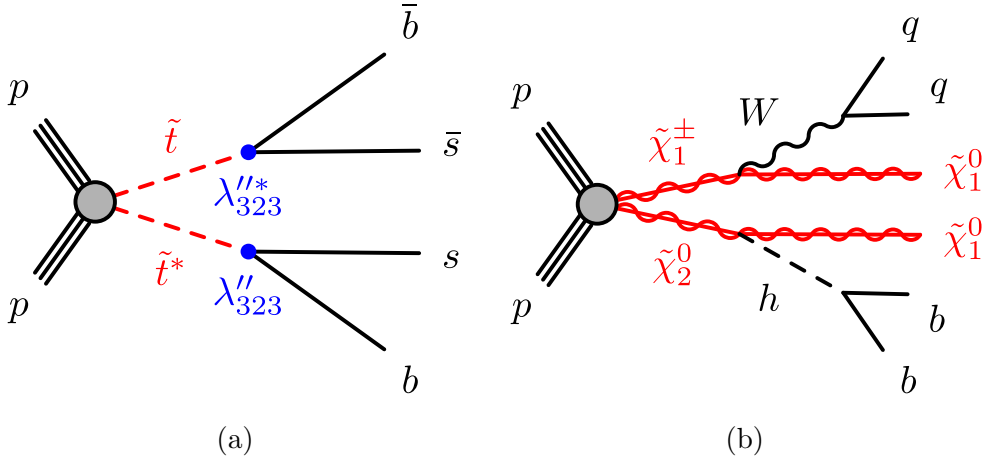

Figure 3.8: Example Feynman diagrams for SUSY pair-production with decays into fully hadronic final states: (a) the R-parity violating stop process chapter 8. (b) the chargino-neutralino production with R-parity conserving decays presented in chapter 9. The solid black lines represent Standard Model particles, the dashed red lines represent the SUSY processes, and the blue points represent RPV vertices labelled by the relevant coupling.

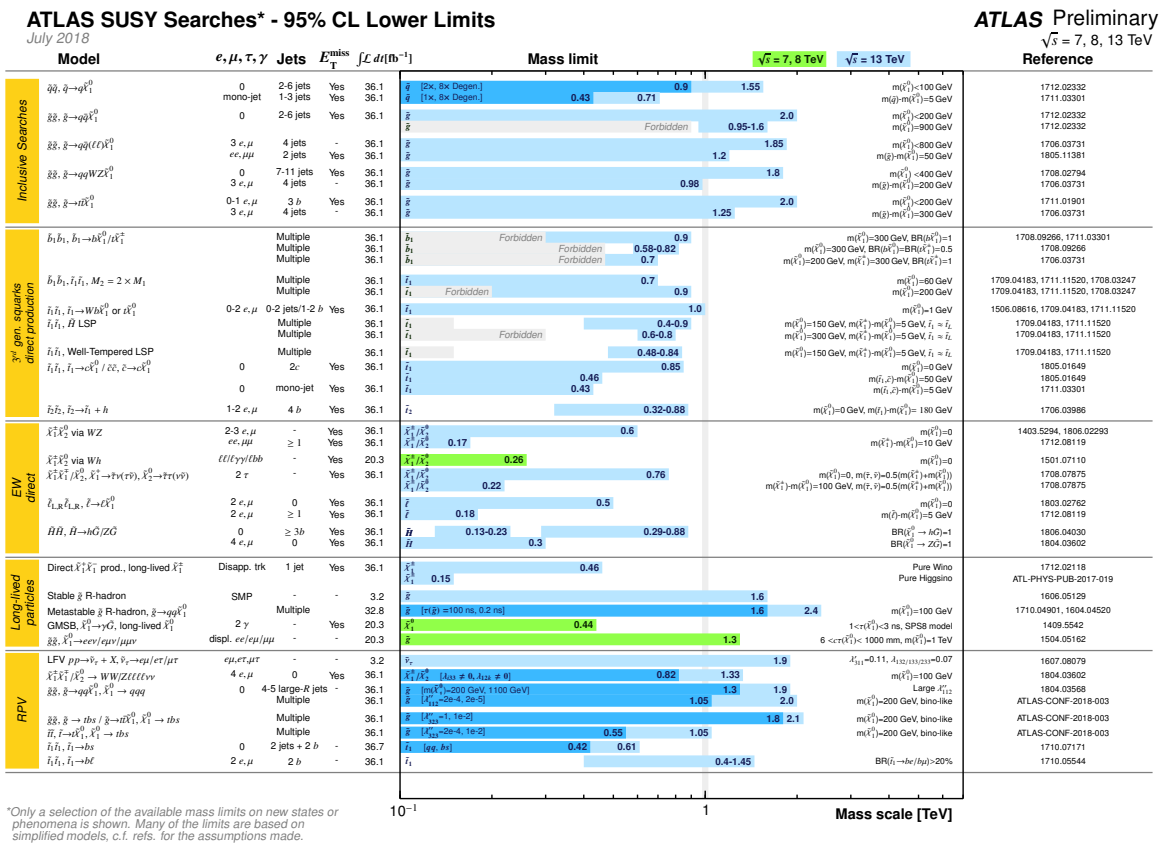

Figure 3.9: Summary of mass reach of the ATLAS searches for Supersymmetry. A representative selection of the available search results is shown. Results are quoted for the nominal cross section in both a region of near-maximal mass reach and a demonstrative alternative scenario, in order to display the range in model space of search sensitivity. Some limits depend on additional assumptions on the mass of the intermediate states, as described in the references provided in the plot. [83]

3.4 Conclusion

Supersymmetry is an extension of the Standard Model that fundamentally relates fermions and bosons. It is an especially alluring theoretical possibility given its potential to solve the hierarchy problem and to provide a dark matter candidate. The observation of a 125 GeV SM like Higgs boson at the electroweak scale hints that supersymmetric particles may show up at the TeV-scale in order to resolve the hierarchy problem, and prevent excessive fine-tuning. There is also the possibility of the lightest supersymmetric particle as a candidate for the hitherto mysterious dark matter. There is also the (more speculative) possibility for SUSY to provide unification of the gauge groups into a Grand Unified Theory at some very high energy scale. When searching for new physics at the LHC, simplified *effective field theories* provide powerful benchmarks to compare against the predictions of the SM. At hadron colliders, sparticles could be produces in pairs from parton collisions of either electroweak or QCD strength. No evidence for SUSY has been found to date, however there are still good reasons to be hopeful it may show up at the LHC, as there is more phase space to explore.

CHAPTER 4

THE LARGE HADRON COLLIDER

This chapter begins with a brief introduction to the Large Hadron Collider (LHC) and the accelerator complex at CERN in Section 4.1, followed by a review of the design and performance goals of this remarkable machine in Section 4.2, including a discussion of luminosity and pile-up; and a summary of LHC operations and the datasets used in this thesis, recorded at $\sqrt{s} = 8$ TeV (2012) and $\sqrt{s} = 14$ TeV (2015–2016), in Section 4.3. For detailed technical information about the LHC, see Refs. [85, 86, 87]. For the layman, the official "LHC Guide" by CERN should be a pleasant read [88].

4.1 Overview

The LHC is a 26.7 km long superconducting proton–proton (pp) synchrotron, the largest and most powerful in history, thus far[1]. The accelerator was built and is operated by the the European Organization for Nuclear Research (CERN) and an international collaboration of universities and national labs, involving thousands of scientists and engineers from all over the globe. It is located in a tunnel, previously occupied by Large Electron Positron Collider (LEP) [90], about 100 m beneath the idyllic landscape near the border of France and Switzerland, just outside the city of Geneva. The decision to locate the LHC underground was made mainly because it is cheaper to excavate a tunnel rather than acquire the land to build at the surface, it also reduces the impact on the landscape to a minimum [88]. The LHC

1. While, at present, the international particle physics community is focused on the LHC and its High-Luminosity LHC (HL-LHC) upgrade, several options for post-LHC colliders are currently undergoing feasibility studies, including facilities such as ILC in Japan; CEPC–SPPC in China; CLIC, FCC, and HE-LHC in Europe. [89]

accelerates two beams of protons[2] in opposite directions and is designed to deliver collisions at unprecedented center-of-mass energies up to $\sqrt{s} = 14$ TeV (7 TeV per beam) at a rate of 10^{34} cm^{-2}s^{-1}. The protons are then moving at 99.9999991%[3] the speed of light, going around the ring more than 11 000 times per second. The proton beams are steered to collide at four fixed interaction points, corresponding to the location of four cathedral-sized main experiments; A Large Ion Collider Experiment (ALICE) [92], A Toroidal LHC ApparatuS (ATLAS) [93], Compact Muon Solenoid (CMS) [94], and The Large Hadron Collider beauty (LHCb) [95]. There are also a few smaller experiments, such as LHC forward (LHCf) [96], TOTal Elastic and diffractive cross section Measurement (TOTEM) [97], and Monopole and Exotics Detector at the LHC (MoEDAL) [98], located close to the ATLAS, CMS, and LHCb interaction points, respectively. An illustration of the LHC ring is shown in fig. 4.1.

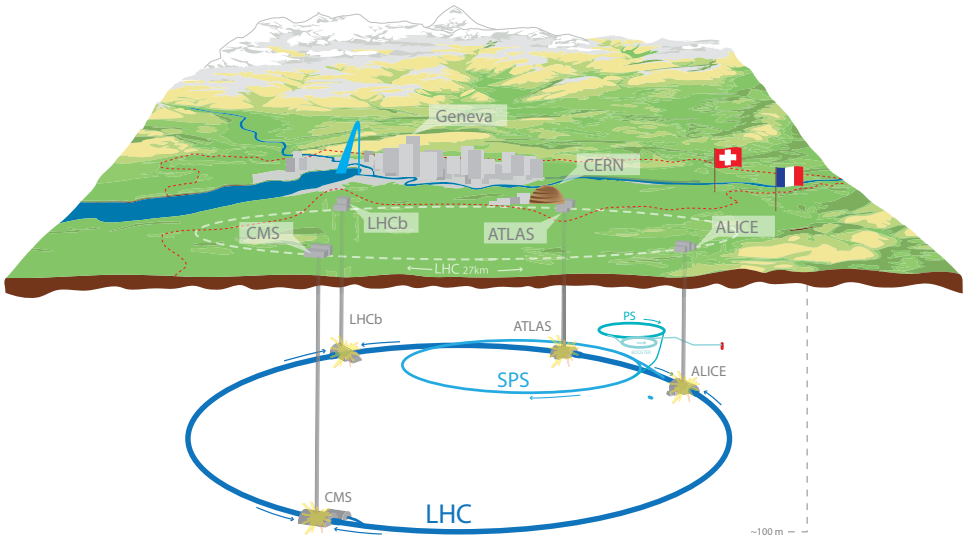

Figure 4.1: Overall schematic view of the LHC, including the four main experiments; ALICE, ATLAS, CMS, and LHCb. The experiments are located about 100 m below the French-Swiss border. Copyright CERN [99].

2. The LHC also collides ultra-relativistic heavy (Pb) ions, with an energy of 2.8 TeV per nucleon and peak luminosity of 10^{27} cm^{-2}s^{-1}[85], in order to study strongly interacting matter under extreme conditions of high temperature and energy density. For an overview, see Ref. [91].

3. $\beta = \sqrt{1 - 1/\gamma^2} = \sqrt{1 - (m_p/(7\text{ TeV}))^2}$

The high energy protons that ultimately collide in the LHC are first accelerated by a succession of particle accelerators to increasingly higher energies [100]. An illustration is shown in fig. 4.1. The protons begin their journey in a simple bottle of hydrogen gas. Hydrogen atoms are stripped of their electrons by an electric field to yield protons, which are then accelerated by Linac 2 to 50 MeV, the first step in a chain of particle accelerators with successive higher energies. The beam of protons is then injected into the Proton Synchrotron Booster (PSB), which accelerates them to 1.4 GeV for injection into the Proton Synchrotron (PS), which further accelerates the beam to 25 GeV. Next, the beam is sent to the Super Proton Synchrotron (SPS) where it is accelerated to 450 GeV. Finally, the protons are transferred into the LHC, which is designed to accelerate protons up to 7 TeV[4].

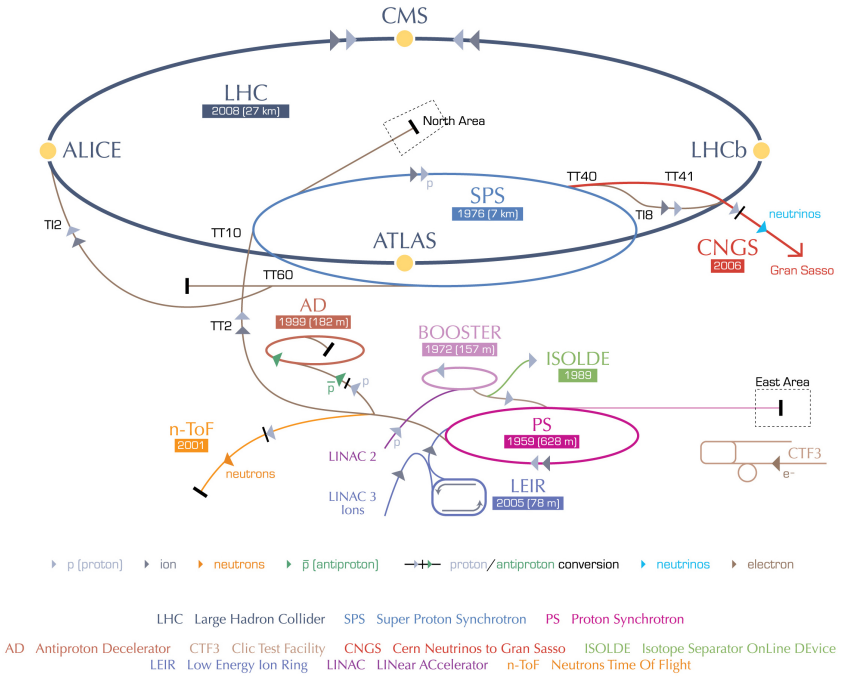

Figure 4.2: Illustration of the chain of particle accelerators at CERN, where successive machines boosts the particles to higher and higher energies before injection into the LHC (dark gray line). Particles are also delivered to a whole set of smaller experiments, e.g. ISOLDE [101], AD [102], CNGS [103], and the test beam facilities at CERN's North Area. Copyright CERN [104].

4. Since 2015 the LHC as operated at an energy of 6.5 GeV per proton (13 TeV collision energy).

The LHC consists of two beam pipes (see fig. 4.3), in one the particles circulate clockwise, while in the other they circulate counterclockwise. Filling each ring of the LHC takes 4 minutes and 20 seconds, it then takes about 20 minutes for the protons to reach their maximum energy [100].

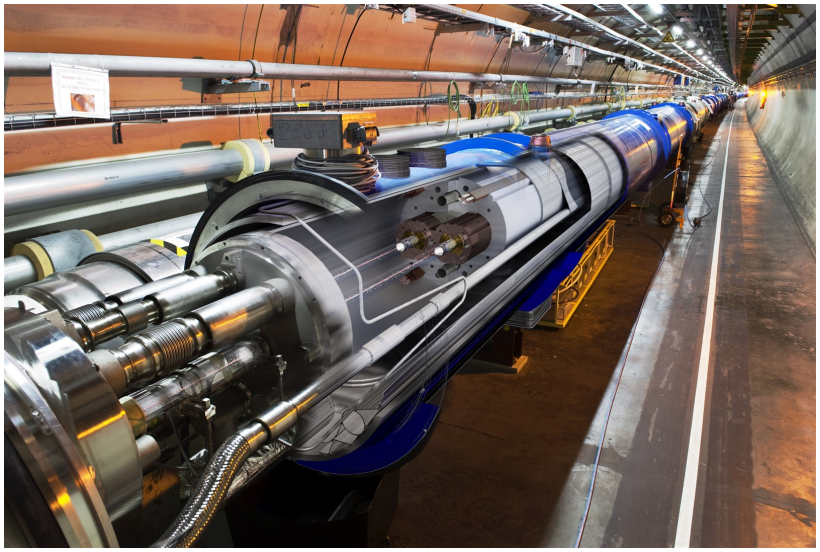

Figure 4.3: Photo of LHC dipole magnets in the tunnel, overlaid with a 3-dimensional illustration of the two proton beams inside the magnet. Copyright CERN [105].

4.2 Machine Design and Performance Goals

In this section we shall take a closer look at the machine design and performance goals of the LHC, and why it was designed that way. Let us begin with a brief discussion of particle synchrotrons. A particle accelerator uses electromagnetic fields to accelerate charged particles. Among the most important design decisions when designing a particle accelerator are:

- colliding beam or fixed target experiment,
- linear or circular accelerator,

- e^+e^- vs. pp (if colliding beams).

The advantage of a collider, over a fixed target experiment, is that the energy available (e.g. to make new particles) is the sum of the colliding beams, $E_{\text{available}} = E_{\text{beam},1} + E_{\text{beam},2}$ (e.g. 7 TeV + 7 TeV for the LHC). For a fixed target experiment, the available energy is only proportional to $E_{\text{available}} = \sqrt{E_{\text{beam}}}$.

In a linear accelerator the particles can be accelerated only once, and particles that do not interact are lost forever. Thus, a linear accelerator generally will have a significantly lower luminosity, compared to a circular accelerator (more about luminosity in the next section). In a circular accelerator particles often can remain in the accelerator for many hours, and thus can be accelerated at each turn. A particle of charge e, moving with velocity $\vec{v}$ in the presence of an electric field $\vec{E}$ and a magnetic field $\vec{B}$, experiences a Lorentz force (in Gaussian units),

$$\vec{F} = e(\vec{E} + \frac{\vec{v}}{c} \times \vec{B}) \tag{4.1}$$

If the particle is moving in a circular orbit of radius ρ, then this force is also given by,

$$F = ma = \frac{mv^2}{\rho}. \tag{4.2}$$

Assuming $v \perp B$, $E = 0$, and re-arranging eq. (4.1) and eq. (4.2), we can write [106]

$$\frac{1}{\rho}\ [\text{m}^{-1}] = \frac{|B\ [\text{T}]|}{\beta E\ [\text{GeV}]}. \tag{4.3}$$

In a particle synchrotron (such as the LHC) the bending radius ρ is fixed. Thus, as the energy of the beam increases, the magnetic field must increase linearly in order to keep the beam inside the ring (c.f. cyclotron, which accelerates particles along an outward spiral path). From eq. (4.3) (i.e. $E \propto B\rho$), it is also clear that in order to increase the energy of the particle beam in a synchrotron, one either has to build an accelerator with a larger

radius or install more powerful magnets.

Another critical decision to make when designing a particle accelerator, is what type of particles to accelerate. Common choices are e^+e^- (LEP) [90], $p\bar{p}$ (Tevatron) [107], and pp (LHC) [85]. The advantage of an e^+e^- collider is that the physical processes resulting from the collisions are generally significantly cleaner than in a $p\bar{p}$ or pp collider, which allows for higher precision measurements. However, the energy reach of e^+e^- colliders is severely limited by synchrotron radiation, as the electrons/positrons lose energy at a rate $(m_p/m_e)^4 \approx 10^{13}$ times higher than protons do[5].

The LHC ring is made up of 1232 dipole magnets, which generate a magnetic field of 8.3 T. As indicated by eq. (4.3), the energy of the beam is limited by the magnetic field of the dipole magnets. These magnets are constructed from superconducting NbTi wires operated at 1.9K (cooled by superfluid helium), with a current of 11850 A flowing through the wires. In addition to the dipole magnets, the LHC also contains 852 quadrupole magnets for focusing the beam, and an additional 7000 smaller correction magnets (sextupole, octupole, etc.) are used for shaping of the beam. Particles are accelerated by a gradient of 5 MV/m at 400 MHz, by 8 superconducting RF cavities per beam. The LHC is segmented into eight sections (*octants*), where Octant 1 contains the collision point for ATLAS (near the CERN main campus), and Octant 5 contains the collision point for CMS (in the French countryside). Each octant consists of a straight *insertion* segment where particles collide, and one half of an arc segment on either side of the insertion. For an illustration, see fig. 4.4 [85].

Particles in the LHC are accelerated in bunches. When operating at full design luminosity (10^{34} cm^{-2}s^{-1}), each beam of the LHC contains 2808 bunches, with about 10^{11} protons per bunch. This corresponds to a spacing between bunches of 25 ns.

5. The power radiated by a particle accelerated in a circular collider goes as m^{-4} (since $P = \frac{e^2 a^2 \gamma^4}{6\pi\epsilon_0 c^3}$, where $a \perp v$ of a charged particle e, and $E = \gamma mc^2$).

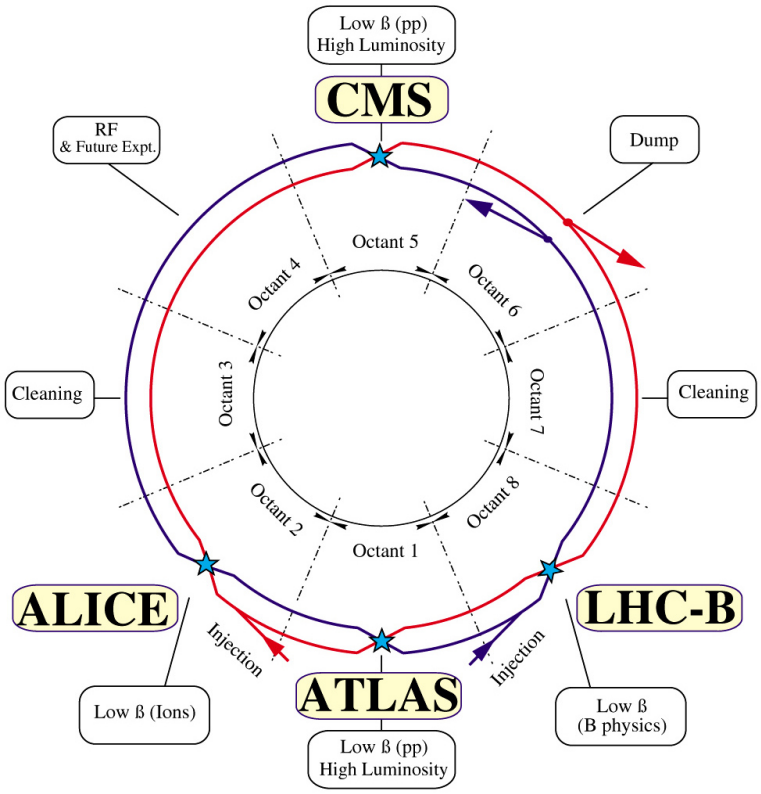

Figure 4.4: Underground layout of the LHC. Copyright CERN [108].

The total number of events N_{event} of a particular type is given by the product of the integrated luminosity L_{int} and the cross section σevent for that type of event,

$$N_{\text{event}} = L_{\text{int}}\sigma_{\text{event}}, \tag{4.4}$$

where the L_{int} is given by the integral of the instantaneous luminosity L,

$$L_{\text{int}} = \int L dt \tag{4.5}$$

For a circular collider, the instantaneous luminosity L can be defined as

$$L = \frac{N_b^2 n_b f_{\text{rev}} \gamma}{4\pi\epsilon_n \beta^*} F, \tag{4.6}$$

where N_b is the number of particles per bunch, n_b is the number of bunches per beam, f_{rev} is the frequency at which particles orbit the ring, γ is the Lorentz factor, β^* is the beta function at the collision point, and ϵ_n is the normalized transverse beam emittance. Finally, F is a factor due to the crossing angle at the interaction point,

$$\left(1 + \left(\frac{\theta_c \sigma_z}{2\sigma^*}\right)^2\right)^{-1/2}, \tag{4.7}$$

where θ_c is the full crossing angle at the interaction point, σ_z is the RMS bunch length, and σ^* is the transverse RMS beam size at the interaction point[6].

Searching for rare physics events at the LHC therefore require both high energies and high luminosities.

4.3 Operations 2012-2018

The operation of the LHC has been a tremendous success, with a delivered integrated luminosity (from pp collisions) to ATLAS and CMS of about 20 fb^{-1} at $\sqrt{s} = 8$ TeV in Run I (2012), and about 36 fb^{-1} at $\sqrt{s} = 14$ TeV during the first two years of operation in Run II (2015–2016). See fig. 4.5 for 2015–2016 Run II results. The analysis presented in chapter 8 is based on the 2012 ATLAS $\sqrt{s} = 8$ TeV dataset, and the analysis presented in chapter 9 is based on the 2015–2016 ATLAS $\sqrt{s} = 13\,\text{TeV}$ dataset. However, since then the LHC has delivered significant additional luminosity. As of May 2018, the LHC has delivered over 80 fb^{-1} at $\sqrt{s} = 13\,\text{TeV}$, and it is expected to deliver well over 100 fb^{-1} before Run II ends in late-2018. The rate of interesting physics events is significantly lower than the total event rate, thus interesting events are going to be embedded in other collisions, so-called *pile-up*. The average pile-up profiles for the 2015 and 2016 LHC runs are shown in fig. 4.6. In 2016,

6. Equation (4.7) assumes round beams, with $\sigma_z \ll \beta$, with equal parameters for both beams

the LHC reached a peak luminosity of approximately 1.4×10^{34} cm^{-2}s^{-1} (1.4 times the LHC design luminosity), as shown in fig. 4.7.

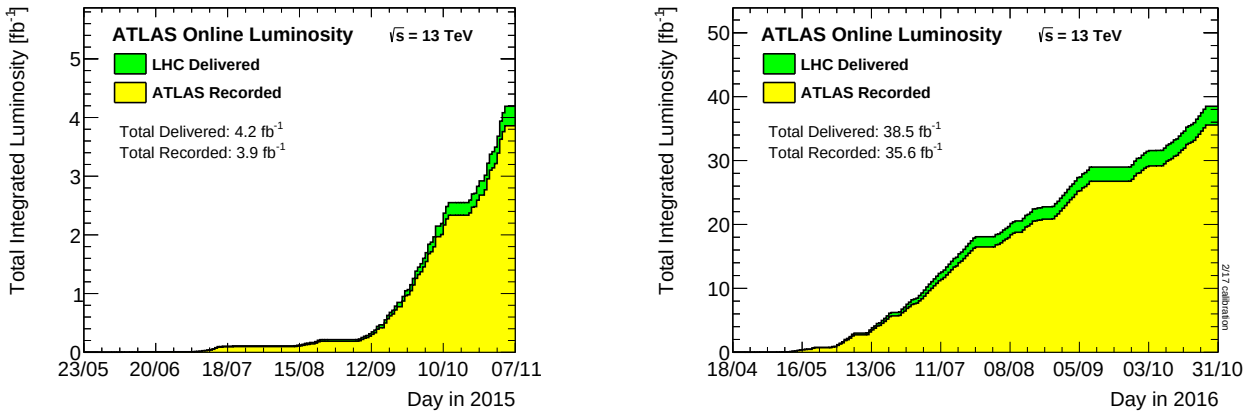

(a) 2015 (b) 2016

Figure 4.5: Cumulative luminosity versus time delivered to (green) and recorded by ATLAS (yellow) during stable beams for pp collisions at 13 TeV centre-of-mass energy in (a) 2015, and (b) 2016. The delivered luminosity accounts for luminosity delivered from the start of stable beams until the LHC requests ATLAS to put the detector in a safe standby mode to allow for a beam dump or beam studies. The recorded luminosity reflects the DAQ inefficiency, as well as the inefficiency of the so-called warm start: when the stable beam flag is raised, the tracking detectors undergo a ramp of the high-voltage and, for the pixel system, turning on the preamplifiers. Shown is the luminosity as determined from counting rates measured by the luminosity detectors. These detectors have been calibrated with the use of the van-der-Meer beam-separation method, where the two beams are scanned against each other in the horizontal and vertical planes to measure their overlap function. The luminosity shown represents the preliminary 13 TeV luminosity calibration based on van-der-Meer beam-separation scans in 2016. Copyright CERN [109].

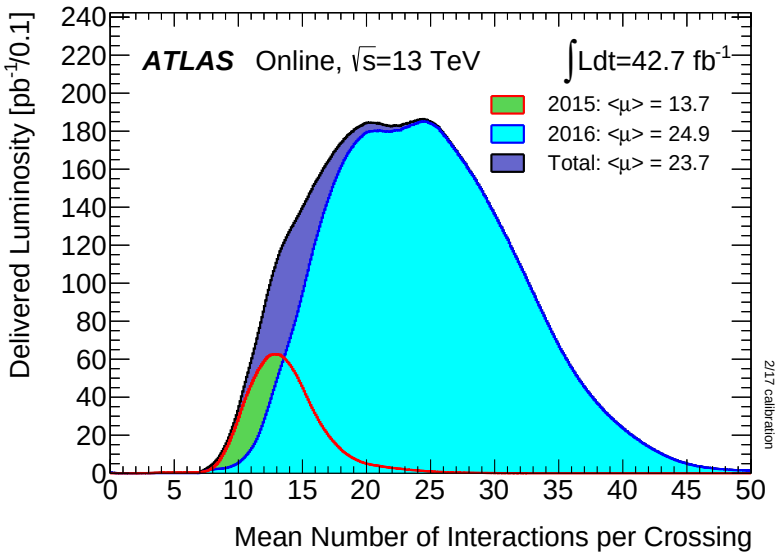

Figure 4.6: Average pile-up profiles for the 2015 and 2016 LHC runs. Copyright CERN [109].

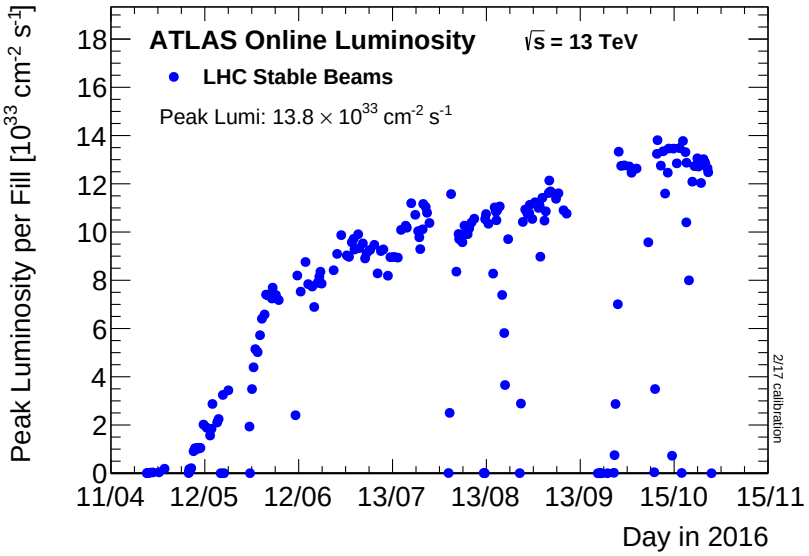

Figure 4.7: The peak instantaneous luminosity delivered to ATLAS during stable beams for pp collisions at 13 TeV centre-of-mass energy is shown for each LHC fill as a function of time in 2016. The luminosity is determined using counting rates measured by the luminosity detectors, and is based on a preliminary analysis of van-der-Meer beam-separation scans during 2016. Copyright CERN [109].

4.4 Conclusion

The LHC is the largest and most complex scientific project ever attempted. It is a particle synchrotron designed to collide protons at center-of-mass energies up to 14 TeV at an instantaneous luminosity of 10^{34} $\mathrm{cm}^{-2}\mathrm{s}^{-1}$. The collisions happens at four interaction points that are surrounded by four primary experiments; ALICE, ATLAS, CMS, and LHCb. The operation of the LHC has been excellent thus far, with a delivered integrated luminosity to ATLAS and CMS of about 20 fb^{-1} at $\sqrt{s} = 8$ TeV in Run I (2012), and about 36 fb^{-1} at $\sqrt{s} = 13\,\mathrm{TeV}$ during the first two years of operation in Run II (2015–2016). As of May 2018, the LHC has delivered over 80 fb^{-1} at $\sqrt{s} = 13\,\mathrm{TeV}$, and it is expected to deliver well over 100 fb^{-1} before Run II ends in late-2018.

CHAPTER 5

THE ATLAS EXPERIMENT

An introduction to the ATLAS detector and the basic design principles of general purpose detectors is given in section 5.1. More information about the design, commissioning, and performance of the ATLAS detector can be found in Refs. [93, 110, 111, 112, 113]. The rest of the chapter is organized as follows: The ATLAS magnets are described in section 5.2. Section 5.3 describes the Inner Detector (ID). Section 5.4 describes the electromagnetic and hadronic calorimeters. Section 5.5 describes the muon spectrometer. Section 5.6 very briefly describes the forward detectors. Finally, the trigger system is described in section 5.7.

5.1 Overview

The LHC was designed with two high-luminosity interaction points at opposite sides of the ring [114]; two general purpose detectors, ATLAS [93] and CMS [94], were built around the LHC beam pipe at these points. ATLAS is located approximately 100 m beneath the ground at LHC Point 1 (i.e. in the first octant of the LHC, see fig. 4.4) just next to the main CERN campus in Meyrin, Switzerland. CMS is located at LHC Point 5 at the opposite side of the LHC ring, beneath the French countryside.

The purpose of particle detectors is to reconstruct the physics of the secondary particles produced in collision events, and to measure their spatial positions, charges, momenta, and energies. Both ATLAS and CMS are able to accurately reconstruct events from pp collisions at unprecedented energies up to $\sqrt{s} = 14$ TeV with a bunch spacing of 25 ns (40 million collision events second), a highly challenging task which requires sophisticated sub-detectors, rapid trigger electronics, high-bandwidth readout architecture, and clever reconstruction al-

gorithms in order to record and reconstruct interesting events. Reconstruction of collision events is the main topic of chapter 6. Particles are measured indirectly through their interactions with matter in the detector, as shown schematically in fig. 5.1. Modern general purpose detectors (such as ATLAS and CMS) are built to be hermetic (with nearly 4π radians of solid angle coverage around the central collision point) and have the following characteristics in common:

1. Tracking system for measuring the momentum of charged particles (such as electrons and charged hadrons).

2. Strong magnets for bending trajectories (tracks) of charged particles in order to measure their electric charge.

3. Calorimeter system to accurately measure the energy and position of electrons, photons, and hadrons.

4. Muon spectrometer to precisely reconstruct muons.

5. Rapid trigger and high-bandwidth readout system for identifying and recording interesting physics events.

Among the particles in the SM, only neutrinos escape detection, as they interact with matter only via the weak force. The presence of neutrinos can be inferred indirectly from the lack of momentum conservation in the transverse plane (more about that in chapter 6).

The ATLAS detector is a dense object of steel and sophisticated electronics, about the size of a cathedral. Shown in fig. 5.2, it is 44 m long, stands 25 m tall, and weights approximately 7000 tonnes. The detector is symmetric with respect to the interaction point, and consists of separate sub-detectors in an onion-layer configuration. Particles produced in the collisions interact in different ways (depending on the type of particle and its kinematic properties)

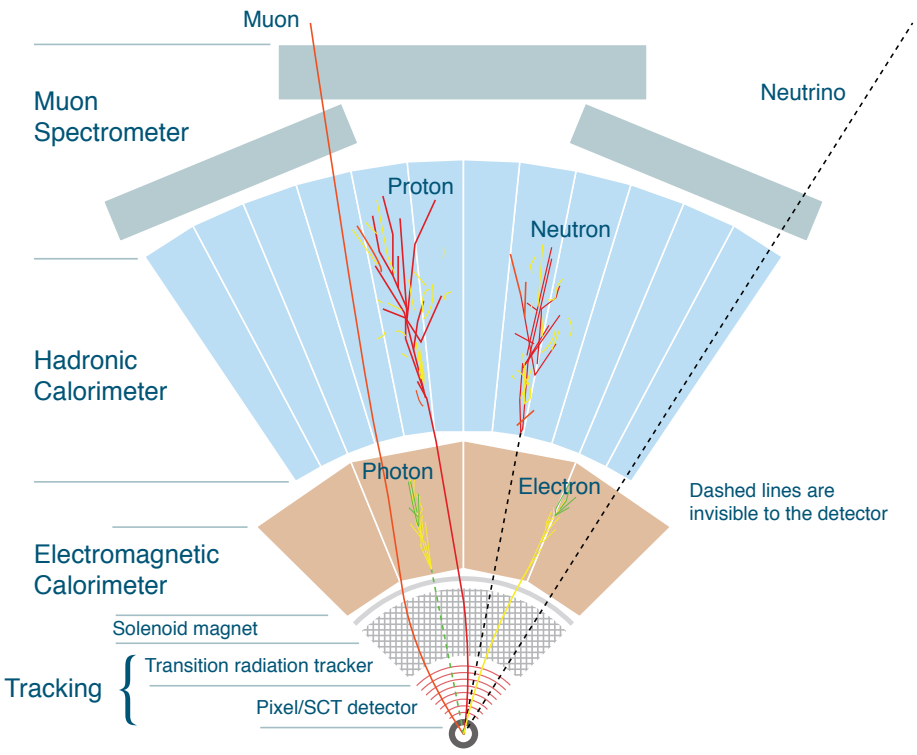

Figure 5.1: Illustration of particles propagating through different layers of the ATLAS detector. Charged particles leaves traces in the inner detector, which are reconstructed as tracks. The calorimeters measure the energy of particles; the electromagnetic (EM) calorimeter primarily detects electrons and photons; the hadronic calorimeter primarily detects hadrons. Muons do leave tracks, but escape detection in the calorimeters, thus special set of muon detectors surround the calorimeter. Neutrinos escape undetected. The image was created with Adobe Illustrator.

and may pass through several layers of sub-detectors. Each sub-detector system is designed to be sensitive to different types of particles. Closest to the interaction point (covering up to $|\eta| < 2.5$) is the inner detector; composed of sub-detectors made of the concentric silicon Pixel Detector, the Semiconductor Tracker (SCT), and the Transition Radiation Tracker (TRT). Tracks, reconstructed from hits in the inner detector, can be used to identify the point of collision, and measure semi-long-lived particles whose decays are displaced from the origin (e.g. b-quarks). The inner detector is immersed in a magnetic field from a 2 T solenoid. Outside the solenoid, immersed in a liquid nitrogen cryostat, sits a lead-Liquid Argon Calorimeter (LAr) EM calorimeter, with excellent resolution for measuring energy

deposits from electrons and photons (and hadrons, to a lesser extent) up to $|\eta| < 3.2$. Next is a hadronic calorimeter, built to stop and measure remaining hadrons. The central (barrel) region, $|\eta| < 1.7$, is covered by the Tile Calorimeter (TileCal), composed of steel and scintillating-tile absorbers. The forward region is covered by the copper-LAr Hadronic End-Cap (HEC) (up to $|\eta| < 3.2$) and the tungsten-LAr Forward Calorimeter (FCal) (up to $|\eta| < 4.9$). The calorimeter is surrounded by the superconducting air-core toroid magnets, and the muon spectrometer; which is composed of the Monitored Drift Tubes (MDTs), Resistive Plate Chambers (RPCs), Thin Gap Chambers (TGCs) and Cathode Strip Chambers (CSCs) subsystems.

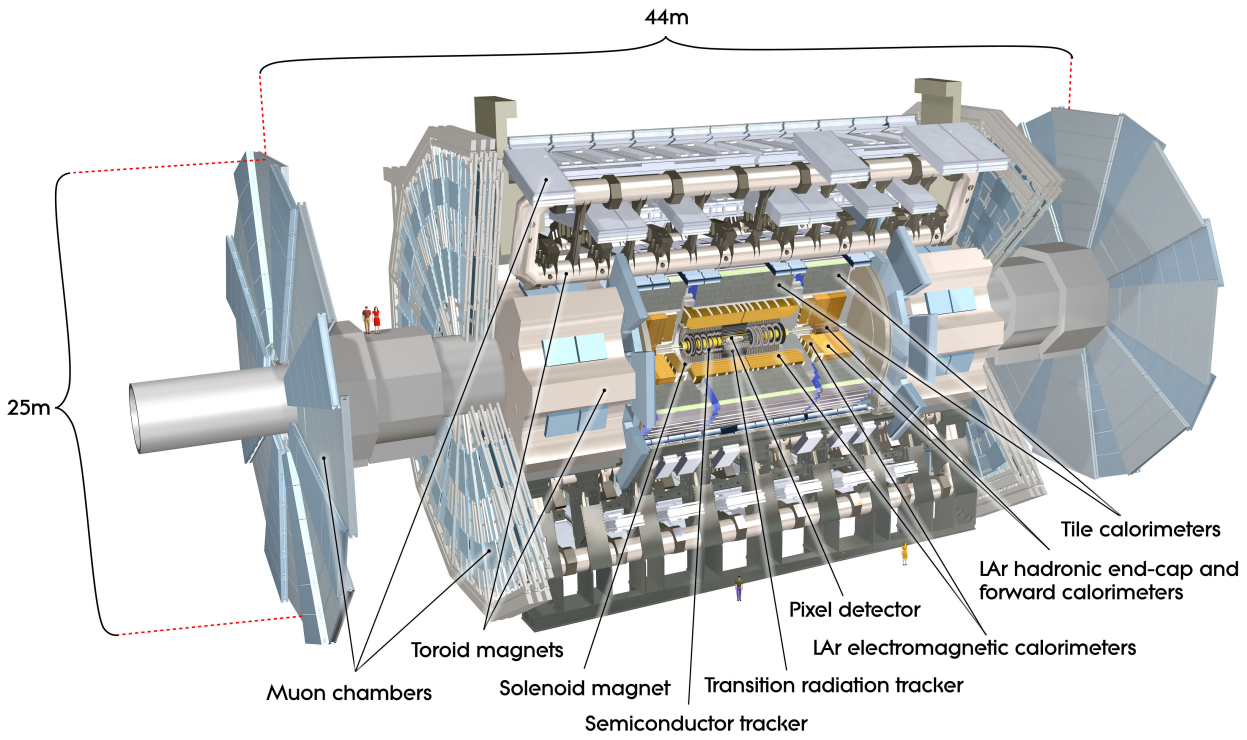

Figure 5.2: Overall view of the main components of the ATLAS detector, showing its main subsystems. Copyright CERN [115].

5.1.1 *Coordinate system*

The ATLAS collaboration uses a common right-handed coordinate system, with the nominal interaction point at its origin [93], the z-axis along the beam line, and the x-y plane is transverse to the beam. The positive x-axis is defined as pointing from the interaction point towards the center of the LHC and the positive y-axis is defined as pointing upwards. The positive z-axis is pointing eastward, towards Geneva. The A-side (C-side) of the detector is defined as that with positive (negative) z. The azimuthal angle ϕ is measured around the beam axis, and the polar angle θ is the angle from the beam axis towards the x-y plane. The ATLAS coordinate system in relation to the LHC ring is illustrated in fig. 5.3.

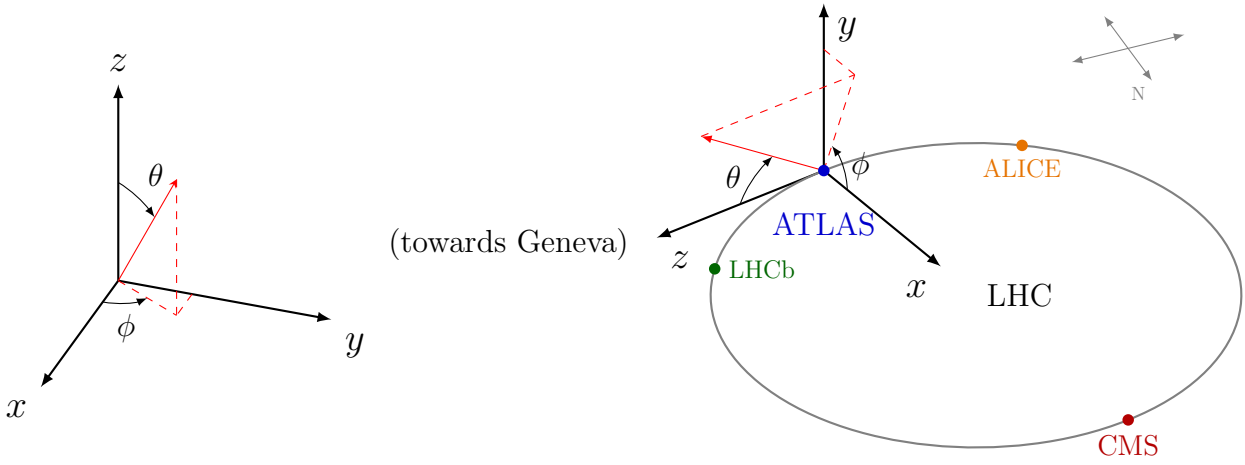

Figure 5.3: The ATLAS coordinate system. Image created with TikZ [17].

Pseudorapidity[1] is defined as

$$\eta \equiv -\ln\left[\tan\frac{\theta}{2}\right], \tag{5.1}$$

where θ is the polar angle (see fig. 5.4). The transverse momentum p_{T}, the transverse energy E_{T}, and the missing transverse energy $E_{\mathrm{T}}^{\mathrm{miss}}$ are defined in the x-y plane unless

1. Pseudorapidity is conventionally used in coordinate systems for hadron collider physics, it is equivalent to rapidity in the limit where the mass of the particle is negligible. Unlike the polar angle θ, rapidity is Lorenz invariant under boosts along the longitudinal axis. Rapidity is defined as $y = 1/2 \ln\left[(E + p_z)(E - p_z)\right]$.

stated otherwise. The distance in the pseudorapidity-azimuthal angle space is defined as $\Delta R = \sqrt{\Delta\eta^2 + \Delta\phi^2}$.

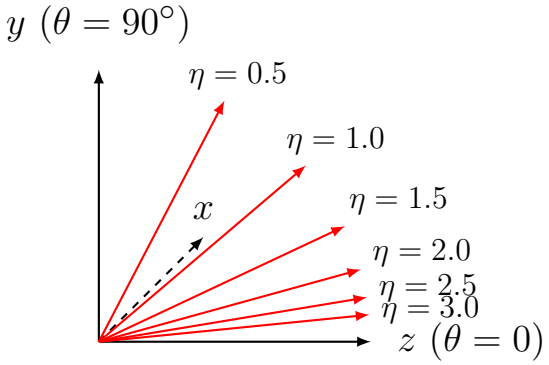

Figure 5.4: Pseudorapidity in the y-z plane overlaid on the ATLAS coordinate system. Red lines are drawn for $\eta = 0.5, 1.0, 1.5, 2.0, 2.5, 3.0$. Image created with TikZ [17].

5.2 Magnets

The momenta of charged particles can be measured from their bending in a magnetic field, according to the Lorenz force law,

$$\frac{d\vec{p}}{dt} = q(\vec{E} + \vec{v} \times \vec{B}), \tag{5.2}$$

where $\vec{p}$ is the particle 4-momentum, q is the charge, $\vec{v}$ is the velocity, $\vec{E}$ is the electric field, and $\vec{B}$ is the magnetic field. The ATLAS magnet system consists of a central solenoid, a barrel toroid, and two end-cap toroids [93]. The ATLAS magnets are shown in fig. 5.5. The central solenoid provides a magnetic field of 2 T (at a current of 7.730 kA) along the z-axis, so that the momentum of charged particles in the inner detector can be measured in the transverse direction. Since the magnetic field is only in the z-direction, the force does not do any work, it just changes the azimuthal direction (the bending is proportional to $\vec{v} \times \vec{p}$). One of the design goals of the ATLAS detector was to minimize the amount of material (radiation

lengths) that particles can interact with before reaching the calorimeter, to this end the solenoid windings and the LAr ECal share a common vacuum vessel. The solenoid magnet windings consist of an Al-stabilized NbTi conductor. The solenoid is 5.8 m long and occupies the space between 2.46 to 2.56 m. Its mass is 5.4 tonnes and the stored energy is 40 MJ. The barrel and end-cap toroids are tasked with bending particles in a direction perpendicular to that of the solenoid, which allows for independent measurement of the charge particle tracks. The field is not constant, thus the bending direction is more complicated than for the solenoid [116]. The magnetic field generated by the toroids is approximately 0.5 T and 1 T in the central and end-cap regions of the muon system, respectively. The barrel coils consist of a Al-stabilized Nb/Ti/Cu conductor and are supported by eight inner and eight outer rings of struts, as can be seen in fig. 5.5b. It is 25.3 m long and its inner (outer) diameter is 9.4 m (20.1 m). The end-cap toroids are designed to bend muons interacting in the end-cap of the muon spectrometer. These are mostly made of an Al alloy and weight 240 tonnes, among some of the heaviest objects in the ATLAS cavern.

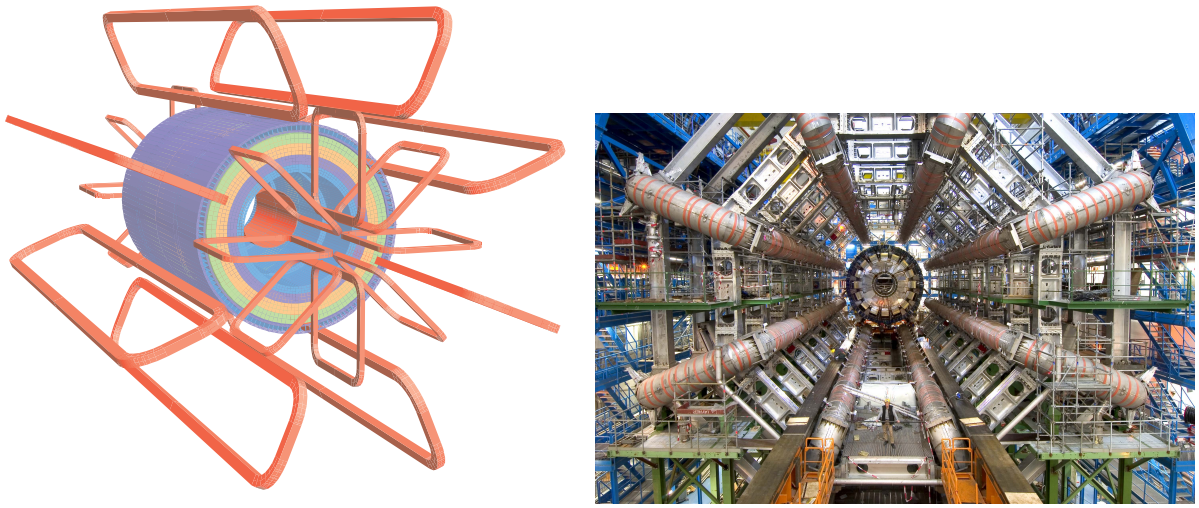

(a) (b)

Figure 5.5: (a) Illustration of the ATLAS solenoid and toroid magnets. (b) A photo of the ATLAS barrel toroids. Copyright CERN [93].

5.3 The Inner Detector

The ID [93, 117] is designed to measure the direction, momentum, and charge of charged particles produced in the collisions. It is located at the center of the experiment, surrounding the collision point, and covering the range up to $|\eta| < 2.5$. A charged particle traversing the ID interacts primarily electromagnetically, either with silicon semiconductors in the Pixel Detector (section 5.3.1) and the SCT (section 5.3.2), or with gas filled straw drift tubes in the TRT (section 5.3.3), leaving hits in the cells of different layers of the sub-detectors that can be combined by a dedicated tracking algorithm to form tacks. A magnetic field of 2 T is provided by the solenoid magnet (as described in section 5.2). The high granularity of the ID provides tracks with excellent spatial and momentum resolution. This is crucial, since approximately 1000 particles emerge from the collision point each 25 ns within the volume of the ID. It is capable of measuring tracks with momenta as low as $p_{\mathrm{T}} = 500$ MeV (below 500 MeV, charged particles do not cross the full ID). Track reconstruction is described in greater detail in chapter 6. The Pixel, SCT, and TRT sub-detectors all have cylindrical geometry; segmented into concentric barrel layers, centered on the interaction point; and end-cap disks perpendicular to the beam line, at either end of the barrel. The whole ID is contained within a cylindrical envelope of length ± 3512 mm and radius ± 1150 mm. The overall layout is shown in fig. 5.6, and a cutaway view of the sensors and structural elements in the barrel and end-cap regions are shown in fig. 5.7. A cross-sectional schematic in the r-z plane is shown in fig. 5.8.

The close proximity to the primary interactions means that the ID in general, and the Pixel detector in particular, is exposed to high levels of radiation, which severely degrades the electronics over time. The initial three layers of the Pixel detector were designed to sustain radiation damage resulting from 300 fb^{-1}, and the design requirements of the IBL assumed an integrated luminosity of 550 fb^{-1}, at a peak luminosity of 3×10^{34} cm^{-2}s^{-1}. The entire

tracking system of the ATLAS detector going to be replaced after the end of Run II (during the LHC Phase II shutdown) with an all-silicon tracker named the Inner Tracker (ITk), designed to cope with the high radiation environment of the HL-LHC [118]

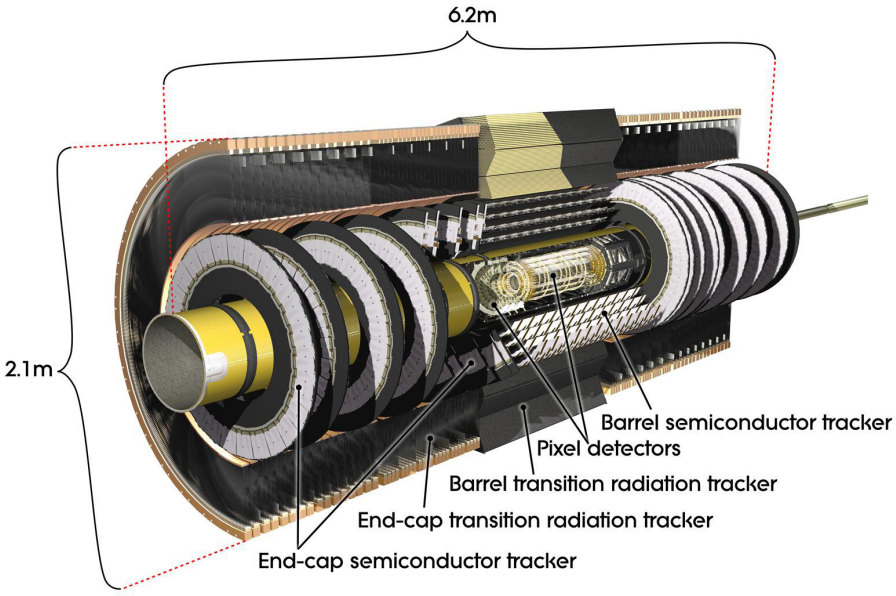

Figure 5.6: The ATLAS ID with sub-detectors and dimensions marked out. Copyright CERN [93].

5.3.1 Pixel Detector

The Pixel detector [93, 120] is installed closest to the interaction point. The Pixel sensors are doped silicon semiconductors which generate electron-hole pairs that are collected and by an applied electric field. Given that the density of particles produced in the collisions is higher near interaction point, the Pixel detector has the finest granularity by far. It consists of 80.4 million independent Pixel channels, with a minimum size in $R-\phi\times z$ of 50×400 μm, which provides a intrinsic accuracy of 10 μm in R-ϕ and 115 μm in z (R) for the barrel (end-cap) detectors. In Run I the Pixel detector consisted of three individual layers parallel to the z direction. During the shutdown period in 2014 a new innermost Pixel layer, the Insertable

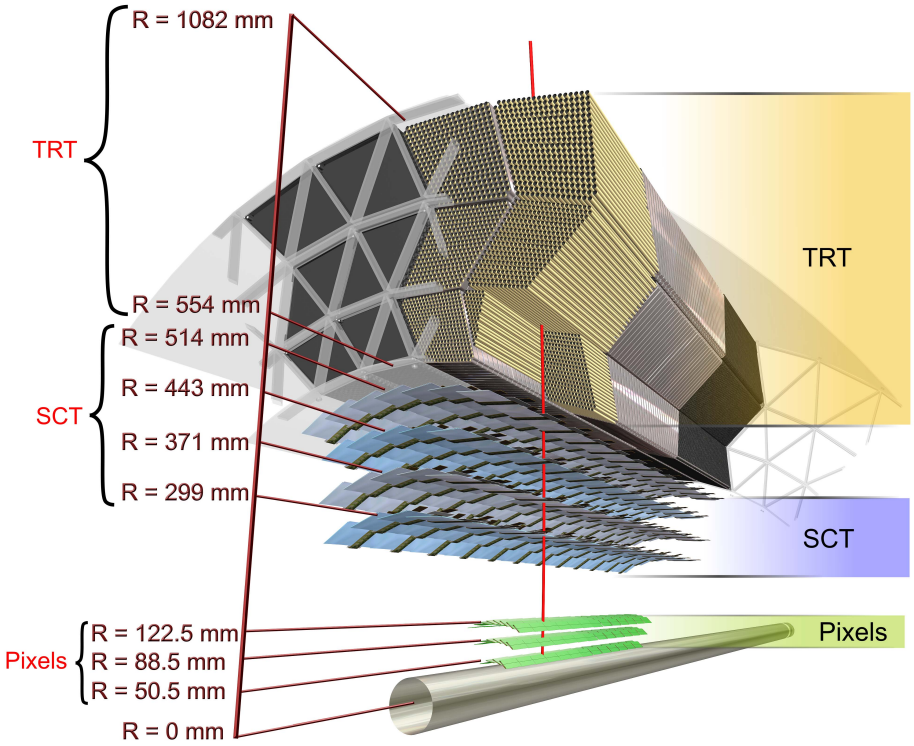

(a)

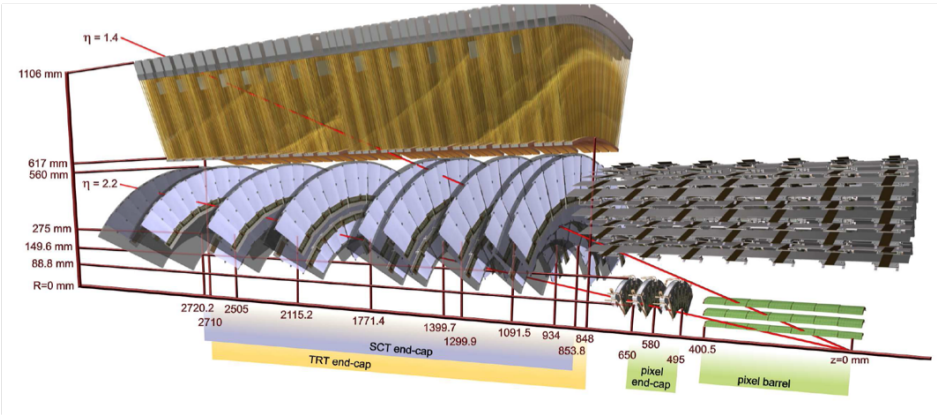

(b)

Figure 5.7: Cutaway view of the of the ATLAS ID in the (a) radial-, and (b) longitudinal direction. A Copyright CERN [93].

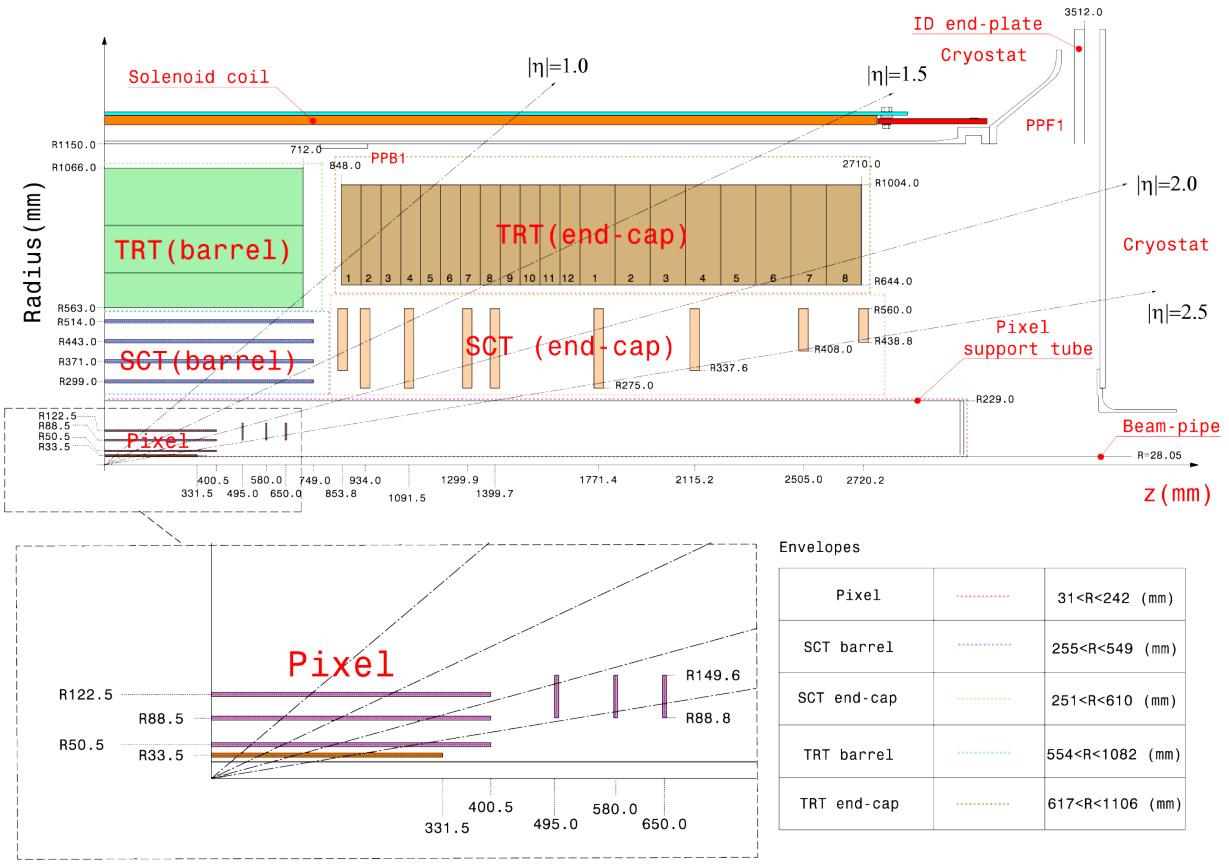

Figure 5.8: A cross-sectional schematic of a quarter of the major ID subsystems in the r-z plane. The bottom panel shows a magnified view of the Pixel detector. The innermost layer of the Pixel detector (IBL) was added for Run II, together with a new beam pipe. Copyright CERN [119].

B-Layer (IBL), was installed in order to improve tracking robustness and precision [121, 119]. The placement of the Pixel detector so close to the beam line[2] makes it possible to very accurately measure the location of both primary vertices (i.e. locations of pp collisions) and displaced secondary vertices (decays of particles with long lifetimes, such as B-hadrons). The Pixel detector provides coverage for $|\eta| < 2.5$, with up 4 four independent measurements of a particle tracks (i.e. one hit for each layer).

2. The IBL sits only 31 mm from the center of the beam pipe [120].

5.3.2 Semiconductor Tracker

The SCT [122, 93] surrounds the Pixel detector. Similarly to the Pixel detector, it operates with doped silicon semiconductor sensors. The SCT is segmented into four cylindrical barrel layers and two end-caps, each with nine circular disk layers. It has 6.3 million readout channels and contains 4088 modules, each consisting of a two pairs of rectangular 64 mm silicon microstrip sensors glued back-to-back at an angle of 40 mrad relative to each other. The mean pitch of the silicon strips is approximately 80 μm. This gives the SCT an intrinsic precision of 17 μm in R-ϕ and 580 in z for the barrel and 17 μm in R-ϕ and 580 in R for the end-cap layers [93]. The SCT covers up to $|\eta| < 2.5$.

5.3.3 Transition Radiation Tracker

The TRT [93, 123] is located outside the SCT and is the largest sub-detector in the ID. Unlike the Pixel and SCT detectors, which use silicon sensors, the TRT is composed of 4 mm diameter straw drift tubes that provide about 36 hits per track. Particles traversing the straw tubes are detected by interacting with the gas in the tube which creates ion/electron pairs. The electrons are accelerated by an electrical field though the gas in the tubes, colliding with other atoms and creating an avalanche of electron/ion pairs, which greatly amplifies the initial signal. The electric field is generated from a potential difference of 1530 V between the exterior of the tube (cathode) and a center wire (anode). The position of the particle in the straw can be determined from the time of arrival of the signal to the anode wire, given that the drift velocity is known. The total number or readout channels is nearly $351,000$. The intrinsic accuracy of the TRT is 130 μm in R-ϕ [93]. The TRT is also able to identify electrons via emission of transition X-rays [124]. The TRT covers the range $|\eta| < 2.0$.

5.4 Calorimetry

The ATLAS calorimeter system measures the energy of all SM particles except muons and neutrinos [93]. It is also important for stopping particles (besides muons and neutrinos) from entering the muon spectrometer. It is located outside the ID and the solenoid and provides near-hermetic coverage up to $|\eta| < 4.9$. The calorimeters are the only detectors able to measuring neutral particles, and are thus crucial for the reconstruction of hadronic final states (e.g. jets). This section focuses on the hardware design of the calorimeter system. The reconstruction of hadronic final states are covered in detail in chapter 6. The calorimeter system thus consists of several sub-detectors: the LAr EM calorimeter (barrel and end-cap), the hadronic TileCal (barrel and extended barrel), the LAr HEC, and the LAr FCal. A cutaway view of the ATLAS calorimeter system is shown in fig. 5.9.

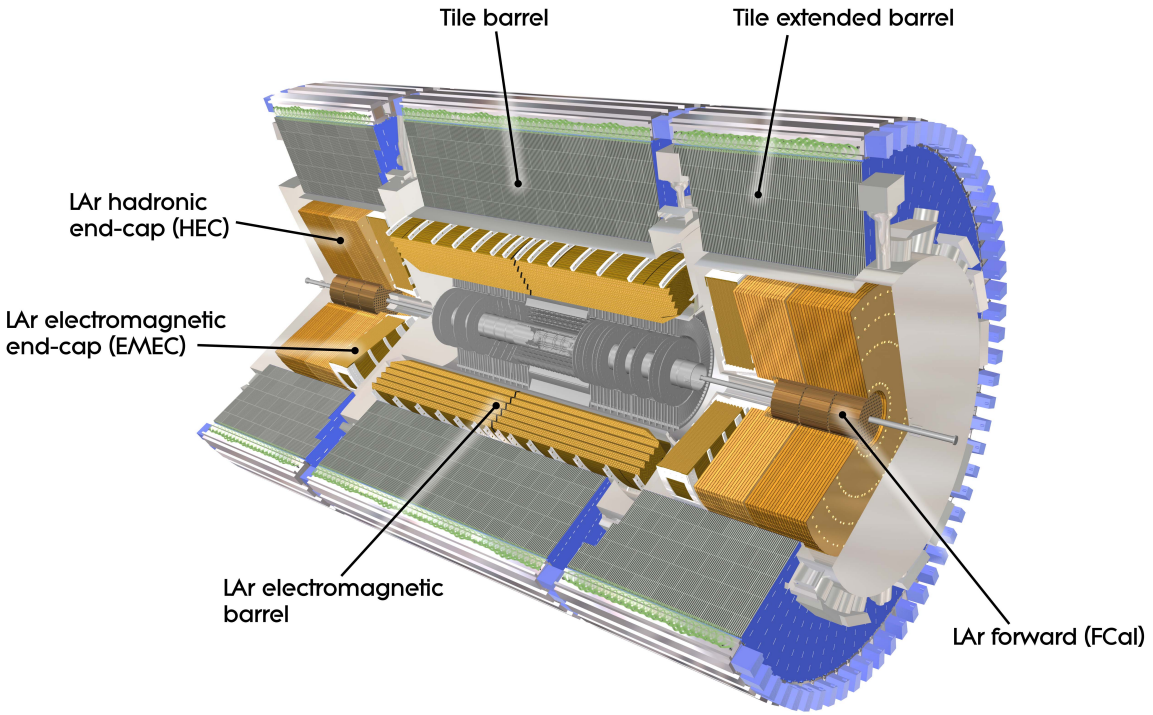

Figure 5.9: A cutaway view of the ATLAS calorimeter system, all the major sub-detectors are shown. Copyright CERN [93].

The techniques used for calorimetry varies based on which physics processes are dominant in different regions of the detector. All calorimeter sub-detectors are *sampling* and *non-compensating*. Sampling means that the detectors are made with alternating layers of active readout (via ionization or scintillation) and high-density passive absorber material (e.g. steel, lead, or copper). Particles propagating through the calorimeter will interact with atoms in the dense absorber material, spawning a cascade of daughter particles of lower energy, which are more easily measured in the active layers. Non-compensating means that not all energy is measured in the passive layers, hence the energy measured in the active layers is less than the actual energy of the particles entering the calorimeter. Although the unmeasured energy can be corrected for in the energy calibration, there is a price to pay in terms of energy resolution.

5.4.1 The Electromagnetic Calorimeter

The high granularity EM calorimeter [93, 125] is designed for precision measurements of electrons and photons. It is divided into one barrel ($|\eta| < 1.475$ and two end-caps ($|1.375 < |\eta| < 3.2$), each housed in a separate cryostat. The EM calorimeter is composed of passive lead absorbers with LAr as the active material. The absorbers are designed to promote electromagnetic showers – primarily from photons and electrons – and provide a large number of radiation lengths to absorb the energy of particles traversing the detector. Particles produced in the electromagnetic showers in the passive lead absorbers ionize the liquid argon in the active layers, creating ions and free electrons. An electric field drifts the free electrons to one side of the detector, where they can be measured. The absorbers are arranged in a special *accordion-shaped* geometry, designed to provide fast readout and uniform coverage in ϕ. The EM barrel is segmented into 3 layer with different granularity in η and ϕ, a schematic is shown in fig. 5.10. The first layer provides especially fine segmentation in η which is helpful

for separating showers initiated by electrons or photons from showers initiated by neutral pions. In order to correct for the energy lost by particles in the EM calorimeter, a LAr presampler detector covers the region of $|\eta| < 1.8$. Including the presampler, the LAr EM calorimeter has over 170,000 readout channels [93].

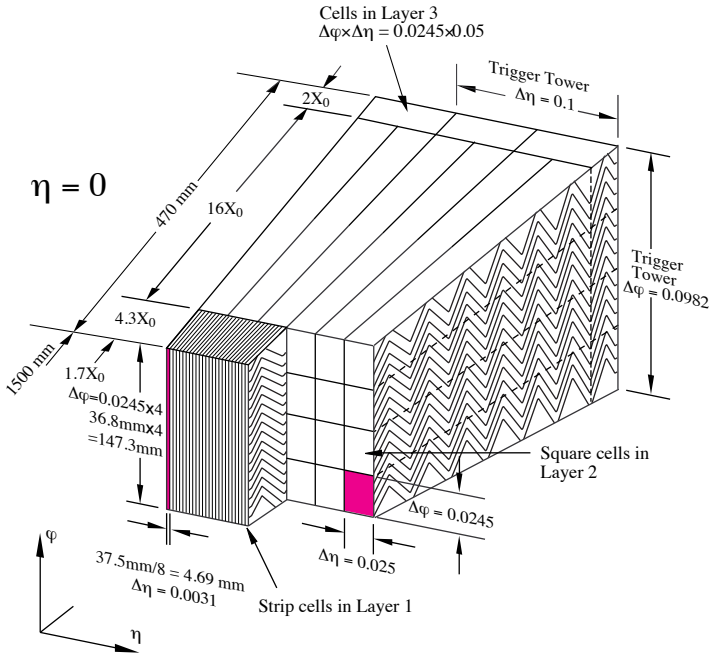

Figure 5.10: Schematic showing a module in the LAr EM calorimeter barrel. The granularity of the cells in η and ϕ is shown for all three layers. The characteristic accordion-shape of the absorbers is indicated in the sketch. Copyright CERN [93].

5.4.2 The Hadronic Calorimeter

The hadronic calorimeter has coarser granularity, which is sufficient to measure the energy of hadrons. It consists of three sub-detectors: the TileCal (barrel and end-cap), the LAr HEC; and the LAr FCal [93]. TileCal [126] is placed directly outside the EM calorimeter and it covers the most central region, the barrel covers up to $|\eta| < 1.0$, and the end-cap covers the range $0.8 < |\eta| < 1.7$. It uses steel plates as absorbers and scintillating plastic tiles as the

active material. Analogously to the EM calorimeter, the steel absorbers promote particle showers of lower energy particles. These particles then pass through the plastic scintillator layers, where organic molecules are excited by the ionizing radiation, and emit scintillating light. The light produced in the scintillators is transmitted by wavelength shifting fibers[3] to photomultiplier tubes (PMTs), which converts the incoming light to an amplified electrical signal. In total, there are approximately 10,000 PMTs in TileCal, which are measured and digitized every 25 ns. The TileCal barrel is 5.8 m long and the extended barrels are 2.6 m long, each is composed of 64 wedge-shaped modules with size $\phi \approx 0.1$. A schematic of a tile module is shown in fig. 5.11. TileCal contains three independent layers, as illustrated in fig. 5.12. The resolution in $\Delta\eta \times \Delta\phi$ of the first two layers is approximately 0.1×0.1 and 0.2×0.1 for the third layer.

The HEC covers $1.5 < |\eta| < 3.2|$ and has a design similar to the EM calorimeter, but with alternating layers of liquid-argon and copper (instead of lead) in a flat geometry. The two forward calorimeters covers $3.1 < |\eta| < 4.9$ and provide both electromagnetic and hadronic energy measurements. Each FCal is composed of three modules, the innermost module uses copper as the absorber material, tungsten is used in the other two. Liquid-argon is used as the active material in all three modules. The HEC and FCal has about 9000 readout channels in total [93].

3. A wavelength sifting material absorbs higher frequency (energy) photons and emits multiple lower frequency (energy) photons.

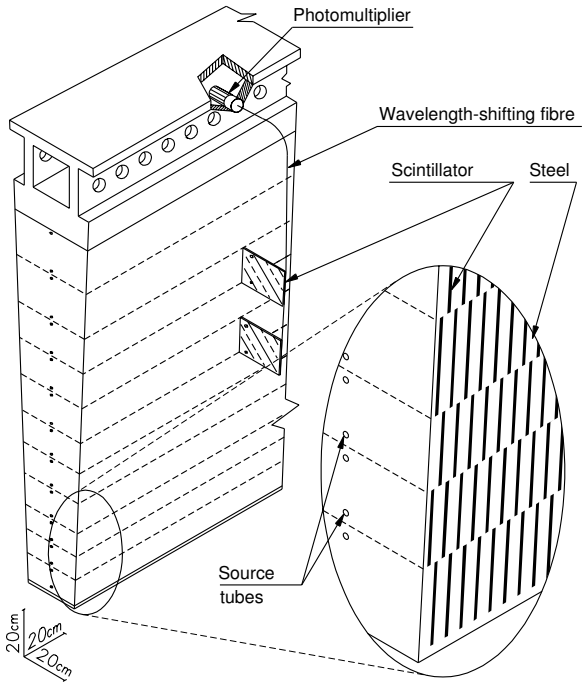

Figure 5.11: Schematic showing the integration of steel absorbers and optical readout (i.e. tiles, fibers, and photomultipliers) in TileCal. Copyright CERN [93].

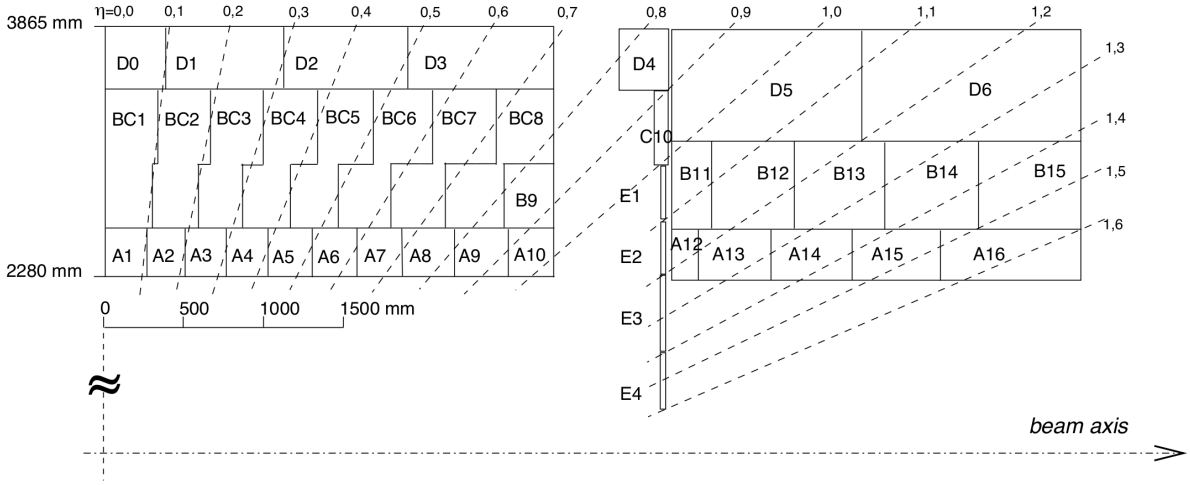

Figure 5.12: Segmentation of TileCal the central and extended barrel modules in depth and η into the so-called A-, BC-, and D-cells. TileCal is symmetric along the beam axis about the interaction point. Copyright CERN [93].

5.5 The Muon Spectrometer

The muon spectrometer [93, 127] forms the outermost part of the ATLAS detector. It is designed to measure the momentum of charged particles escaping the barrel and end-cap calorimeters in the range $|\eta| < 2.7$. It also triggers on muons in the range $|\eta| < 2.4$. The muon system is divided into the barrel-, end-cap-, and transition region, based on which set of toroid magnets are providing the bending; the barrel toroid in the range $|\eta| < 1.4$; the two smaller end-cap toroids in the range $1.6 < |\eta| < 2.7$; and a combination of barrel and end-cap fields in the transition region of $1.4 < |\eta| < 1.6$. Although the muon spectrometer is capable of reconstructing tracks independently, tracks measured in the muon spectrometer are typically combined with tracks measurements in the ID, thus improving the momentum resolution. Since the toriods bend charged particle tracks in a direction perpendicular to the solenoid, the track measurements from the muon spectrometer and the ID are largely independent. The muon spectrometer consists of several subsystems, as shown in fig. 5.13. Most of the $|\eta|$ range is covered by the MDTs. At large pseudorapidities of $2.0 < |\eta| < 2.7$, CSCs are used. The muon trigger system consists of TGCs and RPCs. In the barrel region, the chambers are arranged in three concentric cylindrical layers around the z-axis. In the transition and end-cap regions the chambers are arranged in three wheels, perpendicular to the z-axis. The arrangement of the subsystems are shown in fig. 5.14 .

5.6 Forward Detectors

Several smaller forward detectors provide additional information for luminosity measurements and for the ATLAS trigger system [93, 128]. Luminosity measurements can be performed by several detectors and are critical for physics searches and for understanding detector conditions. LUminosity Cherenkov Integrating Detector (LUCID) is dedicated to online

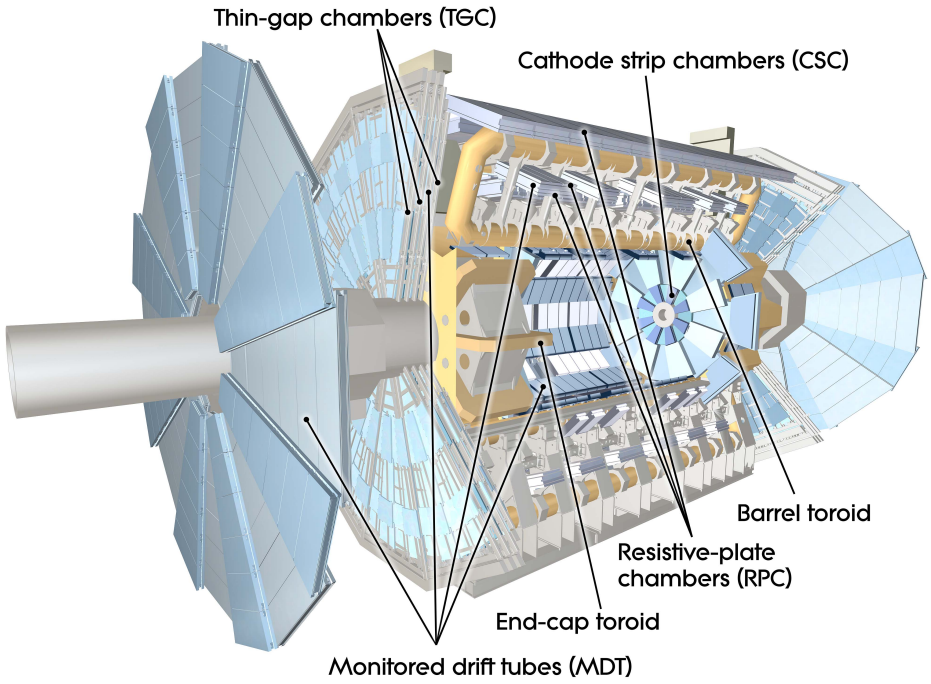

Figure 5.13: Cutaway view of the ATLAS muon spectrometer. Copyright CERN [93].

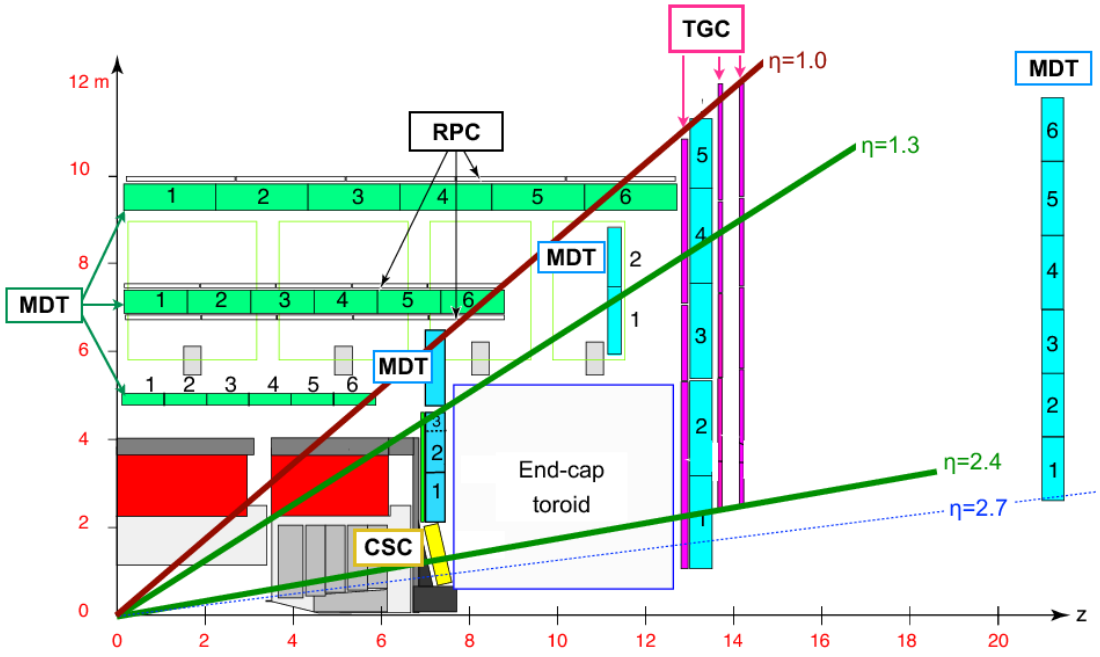

Figure 5.14: Cross-sectional view of the ATLAS muon spectrometer in the y-z plane (bending plane of the toroid magnets). The dashed lines illustrate trajectories of muons of high momentum, which typically traverse three muon stations. Copyright CERN [93].

luminosity monitoring. It consists of two detectors located in the far forward region at ±17 m. It measures the pp inelastic cross section which is used to determine the luminosity. The Absolute Luminosity For ATLAS (ALFA) [129] measures the elastic pp cross section at very small angles, which is used to determine the total pp cross section and luminosity in the LHC. It consists of four so-called Roman Pot stations, located about ±240 m from the ATLAS interaction point. The ATLAS Forward Proton Detector (AFP) detector is newest addition in the far forward region [128, 130]. AFP is designed to measure proton scattered at small angles from the interaction point. The Zero Degree Calorimeter (ZDC) is located at ±140 m from the interaction point and plays an important role in heavy ion physics.

5.7 Trigger and Data Acquisition

With a collision rate of 40 MHz (i.e. bunch-crossing interactions every 25 ns) at design luminosity, recording all collisions events is not possible.[4] A sophisticated system of custom built hardware and dedicated software, the ATLAS Trigger and Data Acquisition (TDAQ), reduces the rate to more managable levels, keeping only the most interesting events for further processing. The trigger system was upgraded between Run I and Run II, in order to cope with the increased trigger rates when running at $\sqrt{s} = 13\,\text{TeV}$ and at a higher luminosity. Since the studies in this thesis utilize data from both Run I (chapter 8) and Run II (chapter 9), each system is briefly described below. More details about event reconstruction are described in chapter 6.

4. A single readout of the whole ATLAS detector results in over 1 MB of data [93], thus reading out all events would require a pipeline and storage capacity capable of handling a data rate of 40 TB/ s. Such a system would be extremely difficult to build.

5.7.1 Run I

In Run I (2009 to early 2013) the ATLAS trigger system [93, 131] consisted of three levels: the Level-1 (L1) trigger, the Level-2 (L2) trigger, and the Event Filter (EF). In order to cope with a collision rate of 40 MHz, the L1 trigger was implemented entirely in custom built hardware and firmware. Based on a limited set of trigger information from the calorimeter and the muon spectrometer only, the L1 trigger makes a decision whether or not to accept an even in less than 2.5 μs. The L1 trigger reduces the event rate from 40 MHz down to 75 kHz. Next, the L2 trigger uses all the detector information and further reduces the rate to 3.5 kHz. Finally, the EF reduces the event rate to about 200 Hz. Both the L2 and EF trigger are implemented in software.

5.7.2 Run II

The Run II trigger system consists of the L1 trigger and the HLT trigger [132], implemented in hardware and software, respectively. The L1 trigger reduces the rate from 40 MHz to about 100 kHz, and the HLT further reduces the rate to about 1 kHz. Exactly as in Run I, the L1 trigger accept information from the calorimeter and muon spectrometers. The L1 trigger decision is made by the Central Trigger Processor (CPT), based on inputs from the L1 calorimeter (L1Calo) and the L1 muon (L1Muon) subsystem. If a triggering decision is made by the CPT, a L1 accept signal is sent to the readout system, and the HLT receives regions-of-interest (ROIs) for local reconstruction. A schematic of the ATLAS Run II TDAQ system is shown in fig. 5.15.

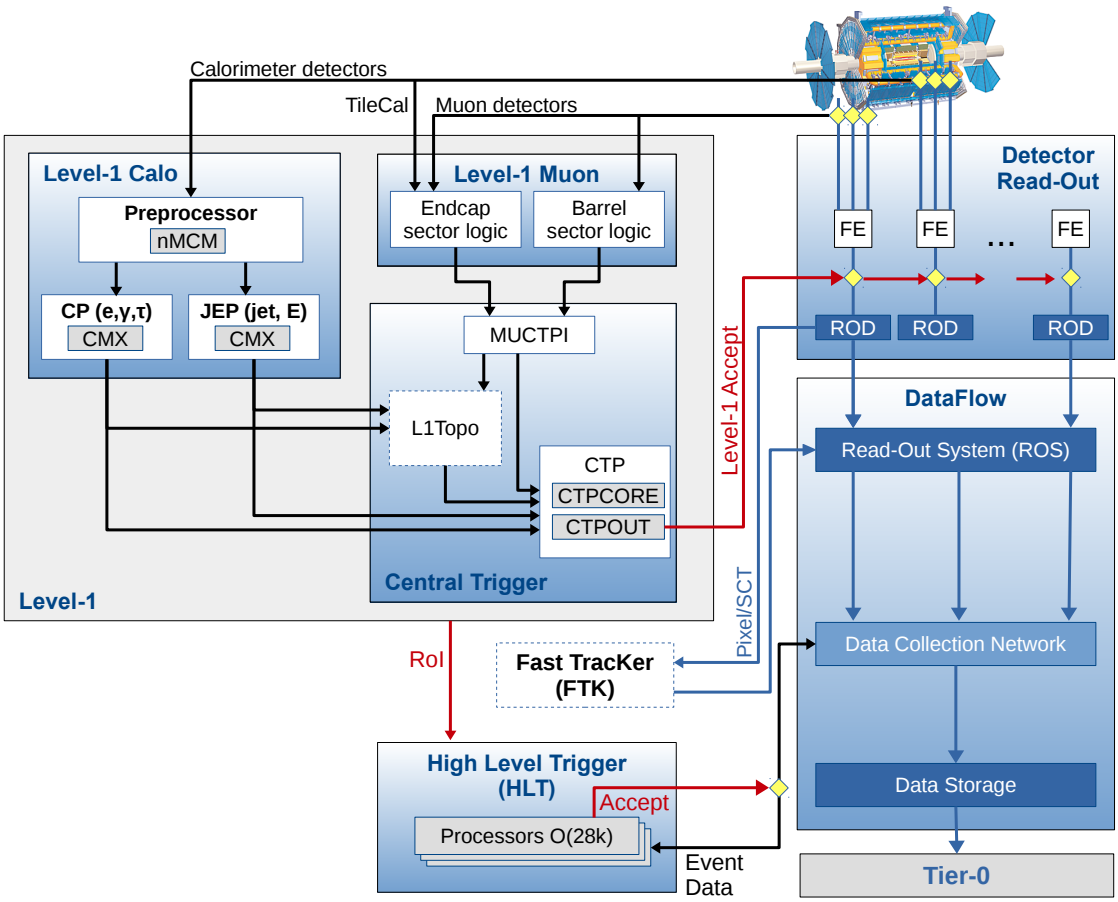

Figure 5.15: The ATLAS TDAQ system in Run II [132].

5.8 Conclusion

This chapter introduced the design principles of general purpose detectors, such as ATLAS and CMS, which consists of; an inner tracker for measuring the momentum of charged particles; a calorimeter system for measuring the energies of leptons, photons, and hadrons; and a muon spectrometer for identifying muons. The ATLAS detector is an incredible complicated piece of machinery, with over 100 million independent readout channels from its sub-detector systems. Its an engineering marvel, built by a collaboration of thousands of scientists and engineers for the purpose of exploring the nature of reality.

CHAPTER 6

EVENT SIMULATION AND RECONSTRUCTION

The goal of particle physics experiments—such as ATLAS and CMS—is to measure the outgoing particles resulting from the hard-scatter collisions, in order to reconstruct the intermediate states, e.g. Higgs bosons, top-quarks, etc. Such intermediate states are short lived, thus their properties can only be calculated based on their decay products, which are part of the measured final state particles.

This chapter provides a brief general introduction to the ATLAS Monte Carlo (MC) event simulation and event reconstruction. Event reconstruction is performed on both real data and MC simulation. The general workflow of an LHC search for new physics is introduced section 6.1. Section 6.2 provides an overview of the procedure for simulating physics events at ATLAS. Section 6.3 lists common data quality criteria, which are applied to most searches and SM measurements. Section 6.4 introduces the concept of a *jet*, which is *the* essential object for studying hadronic final states in the detector.

Since the two searches presented in this thesis were performed using datasets and event simulations from different LHC runs (8 TeV for the RPV stop search in chapter 8 and 13 TeV for the electroweak search in chapter 9), several things pertaining to the object reconstruction and the calibration procedures were slightly different. Also, the simulated SM background processes were different between the two searches. Because of these reasons, standalone sections describing the event reconstruction and the data and MC samples were written for each analysis in chapter 8 and chapter 9.

6.1 Analysis Workflow

In particle physics, we are often searching for phenomena that have been predicted but not yet seen. Usually this means that we have a theoretical model that predicts some new physical phenomena—such as new massive particles—that extents the SM. In order to compare the theory to data, particle physicists simulate both the predicted signal and dominant backgrounds, using the Monte Carlo method [133] (the physics event simulation is described in the next chapter), and compare the observations with the data. This can be summarized by the following steps (which are illustrated in fig. 6.1):

1. First, high-energy physics processes (for both signal and background) are simulated using MC generators at the parton level [134].

2. After that, the *soft physics* is simulated, i.e. how partons shower and decay and form bound states (pions, Kaons, protons, etc.).

3. Next, the whole ATLAS detector is simulated [135]. The propagation of particles through matter is simulated with GEANT4 [136]). All detector systems and sensors (such as calorimeter scintillators), defects (dead sensors, etc), electronic response, etc are included in the detector simulation.

4. At this stage the reconstruction of physics observables begin, using the available tracking and calorimeter sensor data. The process is essentially the same for both recorded and simulated data from here on. First, hits in the inner detector and energy deposits in calorimeter cells are reconstructed into tracks and calorimeter clusters, respectively. Tracks and clusters are then reconstructed into high level objects such as muons [137], electrons [138], photons [139], jets [140, 141], and missing transverse momentum [142]. As discussed in section 5.7, with an event rate of 40 MHz it is not feasible to record

all the data, thus good triggers to select events of high interest for searches and SM measurements are critical.

5. Now, we have reconstructed events for data and MC. Depending on what type of search or measurement is performed, different selections are made at the event level. However, certain selections are always made on in order to ensure good data quality, and efficient triggers (see section 6.3). A statistical analysis is then performed to separate signal from background[1].

6. Finally, an hypothesis test is performed, usually this means comparing the background only hypothesis, H_b, (i.e. processes predicted by the SM) to an hypothesis that includes background plus predicted signal, H_{s+b} (i.e. predictions of new SUSY particles). Hypothesis testing in searches for new physics is described in chapter 7.

6.2 Simulation of Physics Events at the LHC

The final-state *truth partons* are generated using a Monte Carlo (MC) event generator, which first calculates all the matrix elements relevant to the hard-scatter process. After generating the relevant diagrams, the generator samples the *phase space*, which spans all the degrees of freedom in the theory. The differential cross section (event weight), is calculated for many candidate events, and the average is taken as an approximation of $\int d\sigma$, which converges to the measured cross section [134]. The simplest way to implement this is to only consider *tree level* diagrams[2], which is referred to as leading order (LO). More complicated procedures involve computing all diagrams contributing up to a given order in the perturbation theory.

1. This could be a simple "cut-and-count" analysis, or make use of more sophisticated methods, such as (boosted) decision trees, neural networks, etc.

2. I.e. emission of real particles, and not taking higher order terms into account.

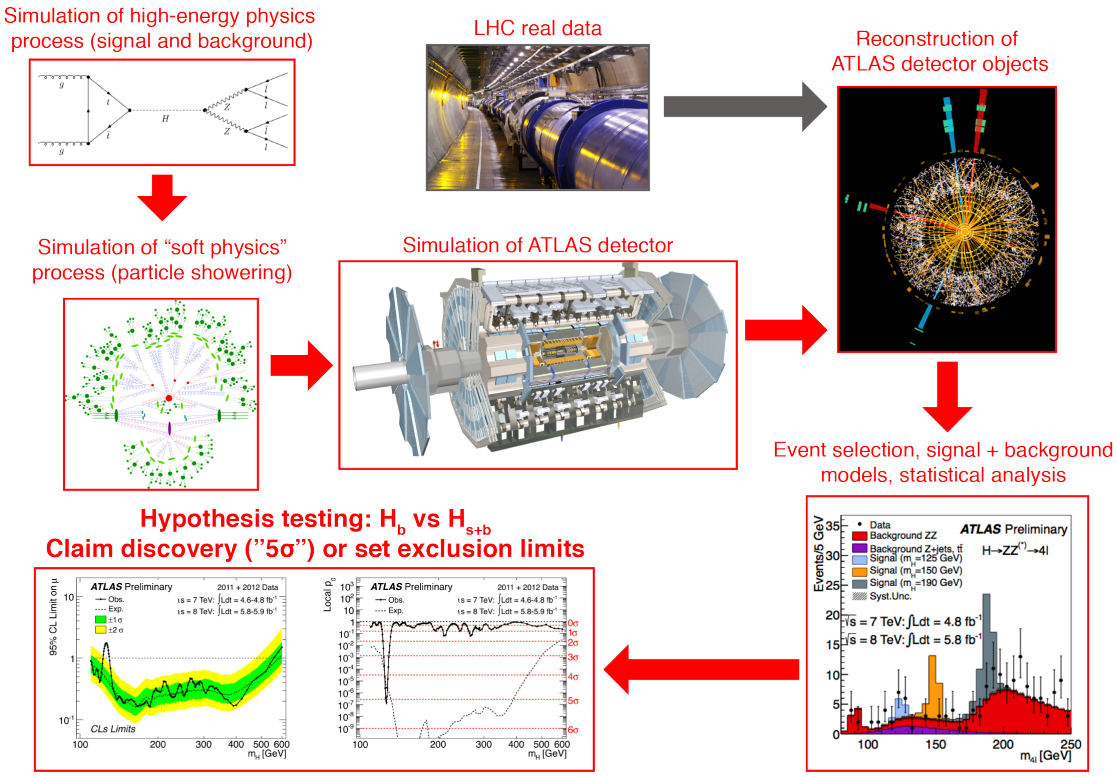

Figure 6.1: HEP analysis workflow. Example plots and event display are from the ATLAS 2012 Higgs discovery paper [12].

Modern event generators typically include next-to-leading order (NLO), and even next-to-next-to-leading order (NNLO) diagrams. The parton distribution functions mentioned in section 2.3.2 are critical for the event generation process. The outputs of the event generation process (i.e. the truth partons) are then passed on to undergo parton showering and hadronization. Next, the events are processed by full simulation of the ATLAS detector [135], which uses the GEANT4 [136] toolkit to simulate interaction between the stable final-state particles and the material in the detector[3]. The simulated events are reconstructed with the same algorithm as used for data. The specific details regarding the simulation (generator versions, tuning parameters, etc) pertaining to each analysis presented in this thesis is described in section 8.2 and section 9.2, for the RPV stop and electroweak search, respectively.

3. The simulation includes all material in the detector, not just the active material, which includes support structures, electronics, cabling, etc.

6.3 Standard Event and Data Quality Selections

- Good Runs List (GRL) [applied to data only]: During an ATLAS data run, events are organized into luminosity blocks (each spanning 1-2 minutes of data-taking). A GRL is an XML file that lists the luminosity blocks considered good for analysis from within the data runs. Separate GRLs are used for the 2012, 2015, and 2016 datasets. The 2012 dataset was used for the search presented in chapter 8. The 2015, and 2016 datasets were used for the search presented in chapter 9.

- TileCal, LAr, and SCT corrupted events [applied to data only]: Following the ATLAS recommendations, vetos are applied to reject events where Tile or LAr errors occur, as well as single event upsets in the SCT.

- Trigger [applied to both data and MC]: Different trigger strategies were applied in the two seaches presented in this thesis. The trigger strategy for the RPV stop and the electroweak searches are presented in chapter 8 and chapter 9, respectively.

- Jet cleaning [applied to both data and MC]: Non-collision backgrounds originating from calorimeter noise, beam halo interactions, or cosmic rays can lead to spurious calorimeter signals and the reconstruction of "bad" jets. This effect can be suppressed by applying a standard jet cleaning procedure, which has been developed for 2015 data to reject jets based on their shape and timing information [143]. Following these criteria, events are rejected if they contain at least one small radius jet (anti-k_T, with $R = 0.4$) with $p_{\mathrm{T}} > 20$ GeV classified as *bad-loose*.

- Muon cleaning [applied to both data and MC]: Fake muons can be reconstructed from high hit multiplicities in the muon spectrometer due to very energetic punch through jets, or from badly measured inner detector tracks in jets wrongly matched to muon spectrometer segments. Such fake muons are a potential source of fake $E_{\mathrm{T}}^{\mathrm{miss}}$. Events

containing these bad muons are rejected by vetoing any events satisfying the following cut: $\frac{\sigma(\frac{q}{p})}{|\frac{q}{p}|} > 0.2$. Events with muons arising from cosmic rays are rejected to avoid effects on the tails of the $E_{\mathrm{T}}^{\mathrm{miss}}$. Potential cosmic muons are identified after the muon-jet overlap removal as muons with large longitudinal and transverse impact parameters $|z_0| > 1$ mm and $|d_0| > 0.2$ mm, respectively.

- Primary vertex selection [applied to both data and MC]: Events are required to have at least one primary vertex with at least two tracks with $p_{\mathrm{T}} > 0.4$ GeV, selected as the vertex with the highest sum of transverse momentum of tracks associated with it.

6.4 Jets

Final state particles such as electrons, muons, and photons, can be measured directly through their interactions in the tracking, calorimeter, and muon systems. However, as was explained in section 2.3.1 there are no free quarks at the distance scale of the detector, due to *confinement*. Quarks and gluons originating from the proton-proton collisions in the LHC will shower (parton jet) and hadronize (particle jet) in to colorless objects which deposit their energy in the calorimeter (calorimeter jets). This process is illustrated in fig. 6.2.

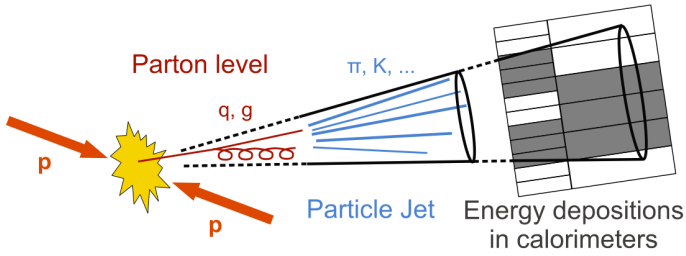

Figure 6.2: Illustration of the evolution of partons, which due to confinement results in a spray of particles in the calorimeter. [144]

6.4.1 Jet Reconstruction

Jets are reconstructed by a clustering algorithm, which determines the properties of the jet. The main goal of a good jet algorithm is to reconstruct jets which accurately represents the properties of the underlying parton(s). There have been many jet algorithms over the past decades, with cone-algorithms emerging as the most popular option among experimentalists [145, 146]. The standard jet clustering algorithm used within the ATLAS Collaboration is anti-k_t with a radius parameter of $R = 0.4$ [147], implemented in the FastJet software package [148]. Jets are reconstructed from three-dimensional topological energy clusters (topo-clusters) in the calorimeter. Topo-clusters have better noise suppression and energy resolution than cells, after being calibrated [149]. An event display, which includes several jets reconstructed with the anti-k_t $R = 0.4$ algorithm, is shown in fig. 6.3.

Topo-clusters are formed by the so-called "4-2-0" algorithm, where the basic observable controlling the cluster formation is the cell signal significance, defined as:

$$S = \frac{E^{\mathrm{EM}}_{\mathrm{cell}}}{\sigma^{\mathrm{EM}}_{\mathrm{noise,cell}}}, \tag{6.1}$$

where EM indicates that both the cell energy and cell noise are measured at the electromagnetic (EM) energy scale. Clusters are then formed according to the following algorithm:

1. Seed cells, defined as $S > 4$, form the initial topo-clusters.

2. Neighbouring cells that have $S > 2$ are added to expand the topo-clusters. If a neighbouring cell already belonged to another topo-cluster, the two topo-cluster are combined. This step is repeated until there are no more neighbouring cells that meet the $S > 2$ requirement.

3. Finally, all adjacent cells with $S > 0$ are added.

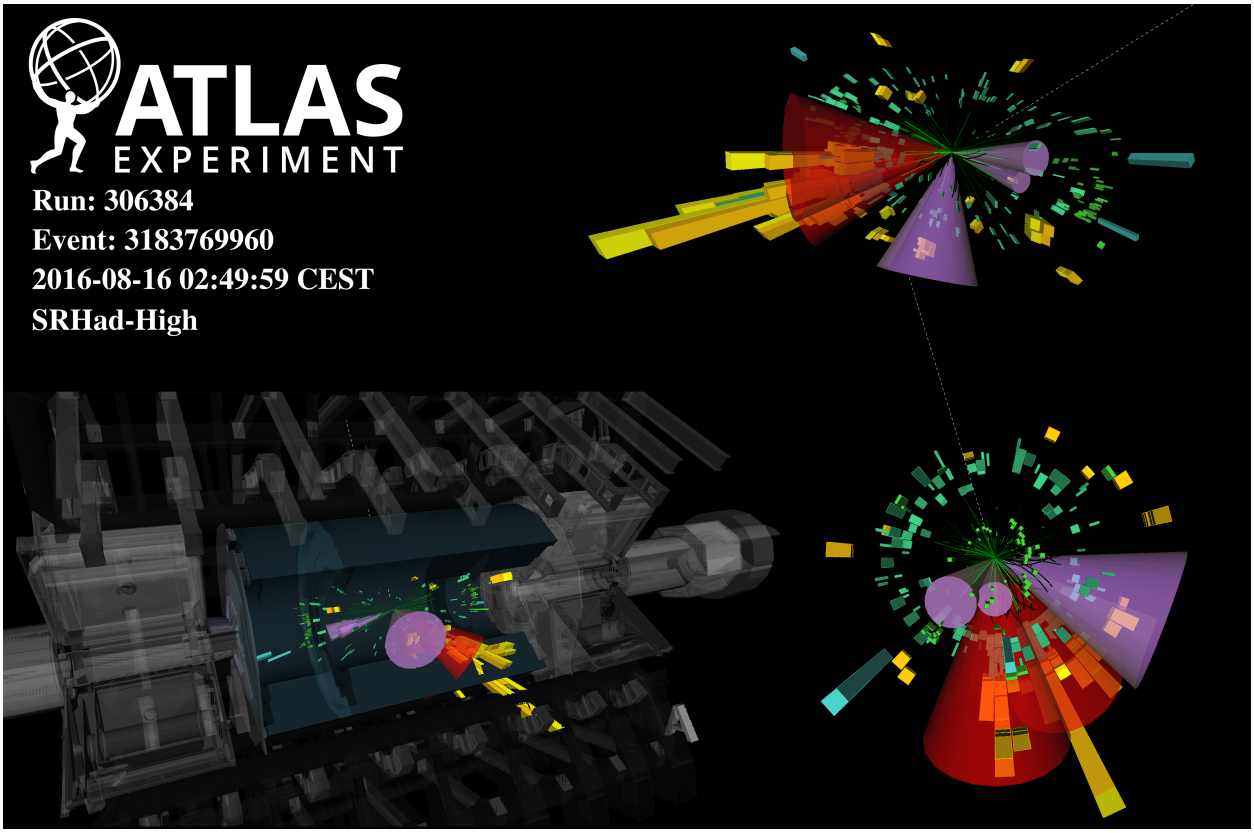

Figure 6.3: An event display using real data from the electroweak SUSY search presented in chapter 9. The event passes the selection criteria for SRHad-High in table 9.3. Jets reconstructed using the anti-k_t $R = 0.4$ algorithm are shown.

An example of this clustering algorithm is shown in fig. 6.4.

6.4.2 Tagging of b-hadrons

The lifetime of a typical b-hadron is of the order $1 - 1.5$ ps [19], which is significantly longer than the lifetime of most other hadrons, and long enough for b-hadrons to travel a few mm in the detector before decaying. This results in a *secondary vertex*, displaced from the primary hard-scatter vertex, as illustrated in fig. 6.5. To identify b-jets, a multivariate algorithm is used, which takes as its inputs the information about the impact parameters of charged-particle tracks, the parameters of reconstructed secondary vertices, and the topology of b- and c-hadron decays inside an anti-k_t $R = 0.4$ jet. Different versions of this algorithm were used in Run I (MV1 [150]) and Run II (MV2c10 [151, 152]).

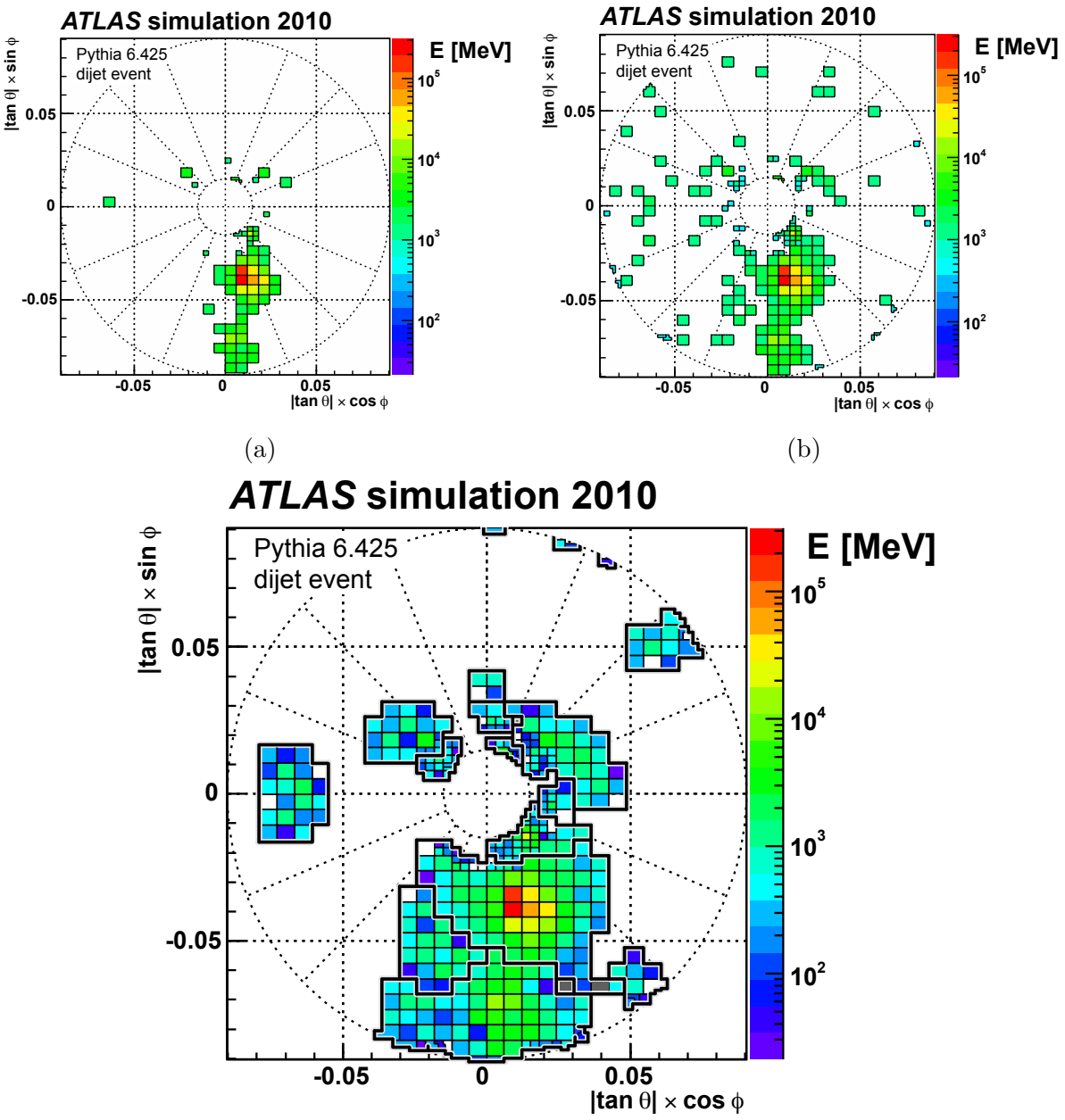

(a) (b)

(c)

Figure 6.4: Topo-clustering for simulated dijet events in the first module of the ATLAS Forward Calorimeter. [149]

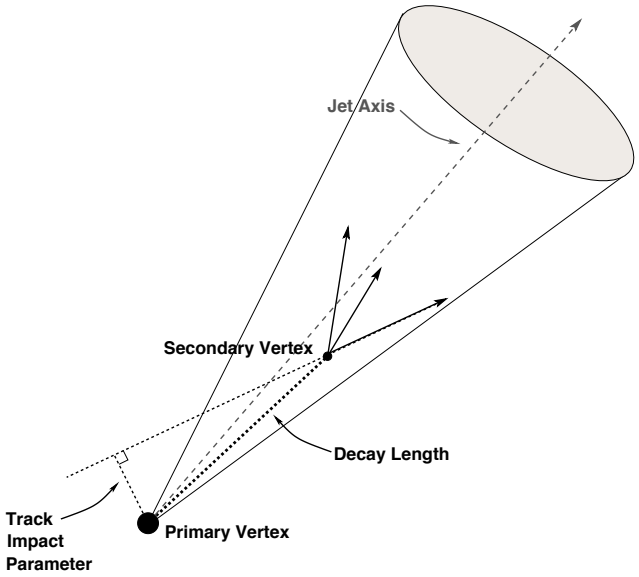

Figure 6.5: Long-lived particles are primarily identified by a secondary vertex, significantly displaced from the primary one. The secondary vertex is reconstructed from tracks with a large impact parameter significance relative to the primary vertex. [153]

CHAPTER 7

HYPOTHESIS TESTING IN SEARCHES FOR NEW PHYSICS

This chapter introduces common statistical terminology and methods for hypothesis testing when searching for new physics that are used by the particle physics community at large, and by ATLAS Collaboration in particular. These concepts are discussed both in the context of discovery and limit setting. Section 7.1 Introduces the concepts of signal-, control-, and validation regions. The specifics of the likelihood-based statistical test, which accounts for systematic uncertainties as variable nuisance parameters, used at the LHC experiments is described in section 7.2. A lot more information can be found in Refs. [154, 155, 156, 157, 158, 159].

7.1 Signal, Control, and Validation Regions

Many analyses typically involve defining signal regions (SR), where we expect high sensitivity for any potential signal, and control regions (CR), which are used to constrain the predicted background to the data. By construction, the signal contribution in the CR(s) is expected to be very small. The background estimate in the CR is then typically extrapolated to the SR. Often (especially for data-driven background estimation), validation regions (VR), with moderate signal contamination, are constructed to test the background estimate. The signal is often simulated for many different hypothesis (by varying a parameter, such as the mass of some new unknown particle). An illustration of the concept of signal, control-, and validation regions is shown in fig. 7.1.

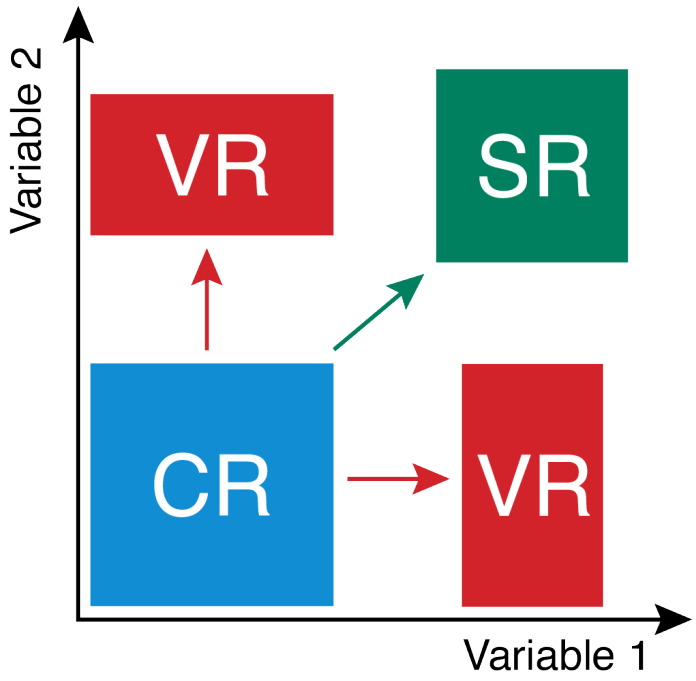

Figure 7.1: Illustration of signal-, control-, and validation-regions.

7.2 CLs and Limit Setting

When searching of new physics at the ATLAS experiment, hypothesis testing is generally performed by a frequentist statistical test [154]. Essentially we want to compare the probability, $P(\text{data}|H_b)$, of the observed data given a background only hypothesis, H_b, with the probability, $P(\text{data}|H_{s+b})$, of observation given the hypothesis of the background plus some predicted signal. For purposes of discovery, the background only hypothesis is taken as the null hypothesis, e.g. $H_0 = H_b$, which is tested against the alternative hypothesis, $H_1 = H_{s+b}$. When setting exclusion limits the roles are reversed, i.e. $H_0 = H_{s+b}$ and $H_1 = H_b$. The level of agreement between H and the data is quantified by the p-value, which is a probability of, under the assumption of H, finding data of equal or greater incompatibility with the predictions of H. It is common in particle physics to convert the p-value into an equivalent significance, $Z = \Phi^{-1}(1-p)$, i.e. a Gaussian distributed variable that is found Z standard deviations above its mean has an upper-tail probability of p (Φ^{-1} is the

quantile, i.e. the inverse of the cumulative distribution function of the standard Gaussian).

In the case of discovery, it is a "tradition" in the particle physics community to require a significance of at least $Z = 5$ (corresponding to $p = 2.87 \times 10^{-7}$) in order to claim a discovery. For example, this was indeed the case in the search for the Higgs boson [12]. As shown in fig. 7.2, there is a large deviation of about $Z \simeq 5$ around $m_H = 125$ GeV.

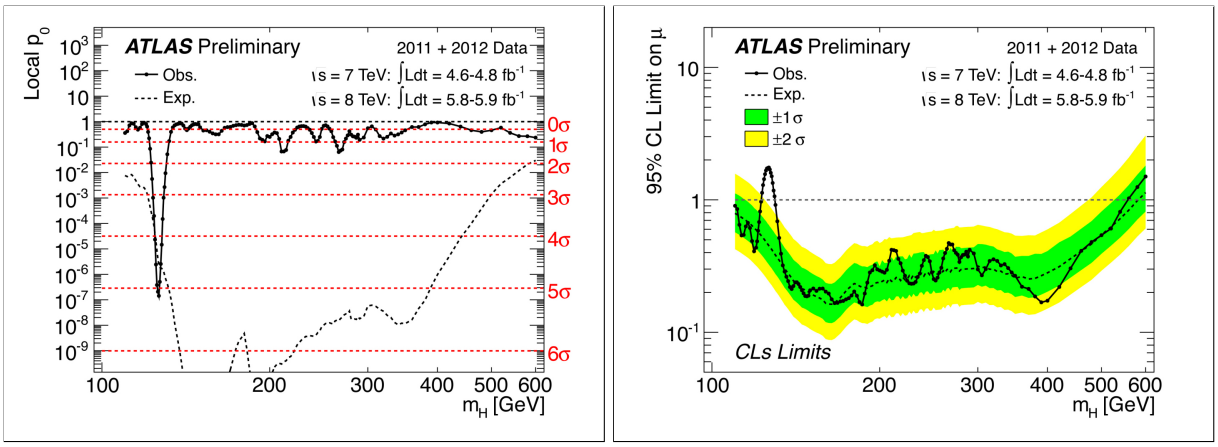

(a) (b)

Figure 7.2: Combined search results from the ATLAS 2012 Higgs discovery paper [12]. (a) The observed (solid) 95% CL limits on the signal strength as a function of m_H, and the expectation (dashed) under the background-only hypothesis. (b) The observed (solid) local p_0 as a function of m_H and the expectation (dashed) for a SM Higgs boson signal hypothesis ($\mu = 1$) at a specific mass.

In order to set exclusion limits on a signal hypothesis, particle physicists usually require a threshold p-value of 0.05, corresponding to a 95% confidence level ($Z = 1.64$). The reason for the significantly larger confidence level in rejecting the background hypothesis is motivated by the fact that the prevailing theory (usually the SM) has stood up to a lot of scrutiny, and in order to reject it, a very strong discrepancy is needed. Furthermore $3\sigma - 4\sigma$ fluctuations have appeared and later (usually when collecting more data) gone away several times in HEP experiments. In contrast, the signal hypothesis may be well motivated by theory, but it has yet to be observed. Of course, the 95% CL limits indeed imply that there is a 5% probability of having accepted the H_b hypothesis when H_{b+s} is true (a Type-II error).

It is also worth noting that "merely" a 5σ excess is only part of discovering a new phenomenon. The degree of belief in the new signal hypothesis, and the degree to which it can describe the data is also very important [154]. However, a p-value below the specified threshold to reject H_b is still regarded as a "discovery", even if that means that we still don't with certainty which signal model will replace it. In the case of the Higgs that meant that although a "Higgs-like" boson had been discovered, work still remained to measure if it was the Higgs boson predicted under the SM. This is why, at the CERN Higgs announcement presentation on July 4, 2012, the then CERN Director Rolf-Dieter Heuer said: "As a layman I would say, I think we have it!".

7.2.1 The likelihood function

The most common approach to establish a discovery (or set exclusion limits) in particle physics is based on a frequentist significance test using a log-likelihood ratio as a test statistic. To illustrate this approach, the RPV SUSY search [1] (which is presented in great detail in chapter 8) is used as an example.

As described above, an excess of signal over background is searched for in mass windows, by performing a counting experiment in each window. A likelihood function is constructed from a parametric model of the observed data, the nominal signal (s) and background (b) predictions, parametrized by the systematic uncertainty. Each systematic uncertainty, i, is described with a nuisance parameter, θ_i, that continuously interpolates between the systematic variations and the nominal values, e.g. $\theta_i = \pm 1$ for the $\pm\sigma$ variations, and $\theta_i = 0$ for the nominal (center) values. This likelihood function (in a specific mass window) can be written as

$$\mathcal{L}(n, \boldsymbol{\theta^0}|\mu, \boldsymbol{b}, \boldsymbol{\theta}) = \mathcal{L}_P\left(n|\nu(\mu, \boldsymbol{b}, \boldsymbol{\theta})\right) \times \prod_{i \in \text{ Syst}} G(\theta_i^0|\theta_i, \sigma_{\theta_i}), \tag{7.1}$$

where the Poisson expectation of observing n events is given by,

$$\mathcal{L}_P(n|\nu(\mu, \boldsymbol{b}, \boldsymbol{\theta})) = \frac{\nu^n}{n!}e^{-\nu}, \quad \nu(\mu, \boldsymbol{b}, \boldsymbol{\theta}) = \mu s + \theta_i b_i, \tag{7.2}$$

and the impact of systematic uncertainties is modelled by a product of Gaussian distributions, $G(\theta_i^0|\theta_i, \sigma_{\theta_i})$, usually of unity width ($\sigma_{\theta_i} = 1$). The number of expected events in the Poisson part of the likelihood, $\nu(\mu, \boldsymbol{b}, \boldsymbol{\theta})$, depends on the backgrounds, $\boldsymbol{b}$, nuisance parameters, $\boldsymbol{\theta}$, and the signal strength, μ. A signal strength of $\mu = 0$ corresponds to the background only hypothesis, H_b, and a signal strength of $\mu = 1$ corresponds to the signal plus background hypothesis, H_{s+b}, with a nominal cross-section, as predicted by theory.

The likelihood function is implemented using an ATLAS developed software package, HistFitter [159]. A fitting procedure is carried out using RooStats/RooFit (with Minuit as backend) [160], to minimize the negative log-likelihood (NLL) by varying the nuisance parameters, θ_j, the backgrounds $\boldsymbol{b}$, and signal strengths, μ (but keeping the number of events, n, and the central values, θ_j^0, constant). The minimum NLL corresponds to the model that best fits the data.

An example of the NLL is shown for the QCD background systematic uncertainty is shown in fig. 7.3.

7.2.2 The test statistic

To test an hypothesized value of μ we use the profile likelihood as a test statistic,

$$\lambda(\mu) = \frac{\mathcal{L}(n|\mu, \hat{\hat{\boldsymbol{\theta}}})}{\mathcal{L}(n|\hat{\mu}, \hat{\boldsymbol{\theta}})}, \tag{7.3}$$

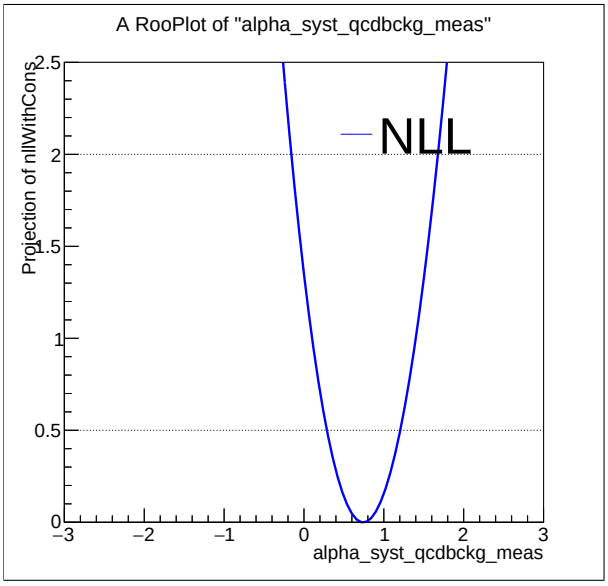

Figure 7.3: Example of minimized NLL for the QCD background systematics.

where $\hat{\mu}$ and $\hat{\boldsymbol{\theta}}$ maximize the (unconditional) likelihood function, and $\hat{\hat{\boldsymbol{\theta}}}$ in the numerator denotes the value of $\boldsymbol{\theta}$ that maximizes the likelihood function (eq. (7.1)) for a specific μ. Hence, $\hat{\hat{\boldsymbol{\theta}}}$ is the conditional maximum-likelihood (ML) estimator of $\boldsymbol{\theta}$, as a function of μ.

From (eq. (7.3)) it is clear that $0 \leq \lambda \leq 1$, where λ near 1 implies a very good agreement between the data and the hypothesized value of μ. It is common to use the (equivalent) profile log-likelihood ratio, as a test statistic,

$$q_\mu = -2 \log \lambda(\mu). \tag{7.4}$$

Higher values of q_μ correspond to increasing incompatibility between the data and signal model, as parametrized by μ. The level of disagreement is quantified by computing the p-value,

$$p_\mu = \int_{q_\mu,\text{obs}}^{\infty} f(q_\mu|\mu) dq_\mu \tag{7.5}$$

, where q_μ, obs is the value of the test statistic q_μ observed in the data. A set of μ values is rejected if the p-value is found to lie below some specified threshold, α. The pdf of q_μ is

given by $f(q_\mu|\mu)$, under the assumption of the signal strength μ. This pdf can be obtained by throwing multiple pseudo experiments that randomize the number of observed events, n, and the central values of the nuisance parameters, θ_i^0.

According to Wilks' theorem [161], the distribution of $f(q_\mu|\mu)$ is known in the case of large statistics in the data sample. For a single signal parameter, μ (such as in the RPV SUSY single bin counting experiment example), it follows a χ^2 distribution with one degree of freedom. The case of large statistics in the data sample is called *the asymptotic regime*. However, the approximation holds up reasonably well even for as few as $\mathcal{O}(10)$ events in the data [154].

For the test statistic, q_μ, one may obtain a low p-value either when the estimated signal strength $\hat{\mu}$ is found to be greater or less than the hypothesized value, μ. That is, the set of rejected μ values may lie on either side (i.e. $p < \alpha$) of the μ values not rejected, hence a two-sided confidence interval for μ is a possibility.

However, particle physicists usually are interested in a new signal that only can increase the mean event rate, beyond what is expected from the background. For a model where the data fluctuates such as the prediction is $\hat{\mu} < 0$, the best level of agreement between the data and any physical value of μ occurs for $\mu = 0$ [154].

In particular, in statistical tests when rejecting the null hypothesis ($H_0 = H_b$), i.e. $\mu = 0$, leads to the discovery of new physics, we have

$$q_0 = \begin{cases} -2\log\lambda(0) & \hat{\mu} \geq 0, \\ 0 & \hat{\mu} < 0, \end{cases} \tag{7.6}$$

where $\lambda(0)$ is the profile likelihood ratio for $\mu = 0$ (7.3).

This means that if there are fewer events in the data, than predicted by the background, i.e.

$\hat{\mu} < 0$, then $q_0 = 0$. From increasingly larger values of $\hat{\mu} > 0$, follow larger values of q_0. This corresponds to an increasing level of incompatibility between data and the $\mu = 0$ hypothesis. The level of disagreement is, as usual, quantified by the p-value, which is now given by

$$p_0 = \int_{q_0,\text{obs}}^{\infty} f(q_0|\mu) dq_0. \tag{7.7}$$

For the purposes of setting an upper limit on the strength parameter μ, a test statistic is commonly defined as

$$q_\mu = \begin{cases} -2\log\lambda(\mu) & \hat{\mu} \leq \mu, \\ 0 & \hat{\mu} < \hat{\mu} > \mu. \end{cases} \tag{7.8}$$

Since we here are interested in setting an upper limit on μ, data with $\hat{\mu} > \mu$ (i.e. $q_\mu = 0$ if the best prediction, $\hat{\mu}$, results in more events than what was observed for the signal plus background hypothesis, for a given signal strength μ) is not regarded as less compatible with μ than the data obtained.

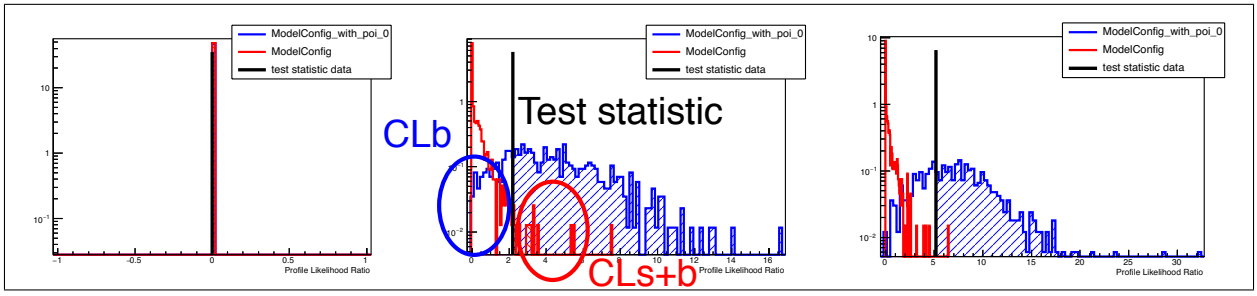

Figure 7.4: Distribution of the profile log-likelihood ratio, $f(q_\mu|\mu)$, generated from pseudo-experiments. The signal plus background and background only hypotheses are shown for different values of the signal strength μ.

7.2.3 Inverted hypothesis test

If we are unable to reject H_b, then we proceed to set exclusion limits (upper limits on μ, which often are converted into a cross-section). This is typically done by performing an inverted

hypothesis test, where the signal strength, μ, is increased step-by-step for a range of values. An hypothesis test is done at each value of μ, either by generating pseudo experiments to determine the distributions of the test statistic for the background only and the signal plus background models, or by using the asymptotic formula mentioned above (and described in detail in [154]). Distributions generated by pseudo experiments at different steps (i.e. for different μ values) are shown in fig. 7.4.

Exclusion limits on μ are set when the p-value goes below some determined threshold, typically $p < 0.05$ (corresponding to 95% CL). Examples of the inverse hypothesis scans, using both pseudo experiments and the asymptotic formula, are shown in 7.5. It common in particle physics, and the default procedure in ATLAS to use the CL_s as p-value when setting exclusion limits. The CL_s is given by

$$CL_s = CL_{s+b}/CL_b = p_{s+b}/(1 - p_b). \tag{7.9}$$

The agreement between data and the H_{s+b} (H_b) hypothesis is given by CL_{s+b} (CL_b). CL_b is the probability to get a result less compatible with the H_b hypothesis than the observed result. Similarly, CL_{s+b} is the probability to get a result which is less compatible with the H_{s+b} then the observation, under the assumption that the H_{s+b} hypothesis is true. The CL_s limits are more conservative than CL_{s+b}. In addition, CL_{s+b} has problems when the number of observed events is far below the number of expected events.

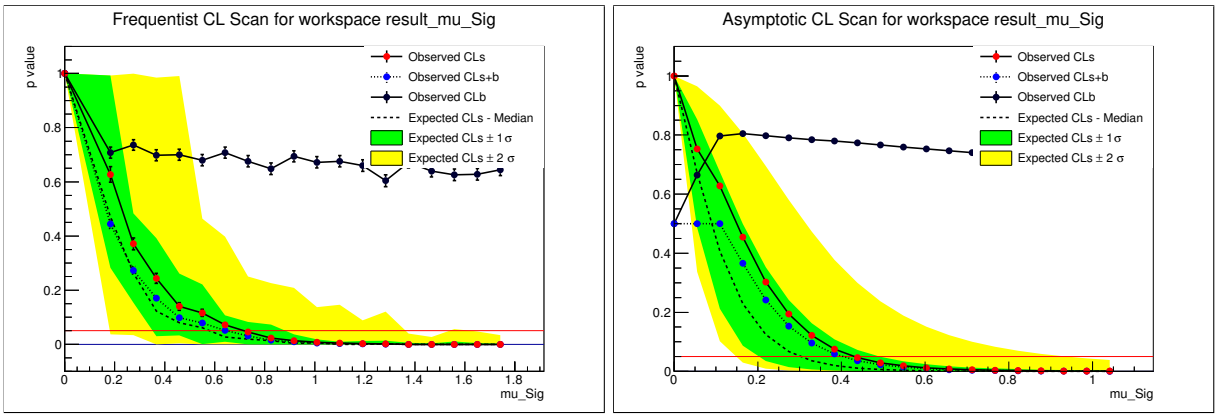

(a) (b)

Figure 7.5: Results for the inverted hypothesis test for (a) the frequentist approach (pseudo-experiments), and (b) using the asymptotic approximation.

CHAPTER 8

TOP SQUARKS WITH UDD R-PARITY-VIOLATING DECAYS AT 8 TEV

A search for the pair production of supersymmetric top squarks (stops), each with R-parity-violating decays into two Standard Model quarks, is performed using 17.4 fb^{-1} of $\sqrt{s} = 8$ TeV proton-proton collision data recorded by the ATLAS experiment at the LHC. Each top squark is assumed to decay to a b- and an s-quark, leading to four quarks in the final state. Background discrimination is achieved with the use of b-tagging and selections on the mass and substructure of large-radius jets, providing sensitivity to top squark masses as low as 100 GeV.

This chapter is structured as follows: An brief introduction and motivation of the search is presented in section 8.1. The data and MC samples used to simulate the dominant background processes, as well as the MC signal samples, are described section 8.2. Section 8.3 describes the kinematic variables used in the analysis and the event selection. Section 8.4 describes the background estimation strategy. Section 8.5 presents the dominant systematic uncertainties. Finally, the results are summarized in section 8.6.

8.1 Overview

For a general introduction to supersymmetry (SUSY) phenomenology, possible R-parity couplings, and how SUSY particles could possibly be produced in pp collisions at the LHC, see chapter 3. In RPC scenarios, SUSY particles are required to be produced in pairs and decay to the lightest supersymmetric particle (LSP), which is stable [76]. In R-parity-violating (RPV) models, decays to only SM particles are allowed, and generally relax the strong con-

straints now placed on standard RPC SUSY scenarios by the LHC experiments [162, 163]. It is therefore crucial to expand the scope of the SUSY search programme to include RPV models. Common signatures used for RPV searches include resonant lepton-pair production [164], exotic decays of long-lived particles with displaced vertices [165, 166, 167, 168], high lepton multiplicities [169, 170], and high-jet-multiplicity final states [171]. Scenarios which have stops of mass below 1 TeV are of particular interest as these address the hierarchy problem [172, 173, 174, 175].

SUSY RPV decays to SM quarks and leptons are controlled by three Yukawa couplings in the generic supersymmetric superpotential (see eq. (3.10)) [176, 177]. These couplings are represented by $\lambda_{ijk}, \lambda'_{ijk}, \lambda''_{ijk}$, where $i, j, k \in 1, 2, 3$ are generation indices that are sometimes omitted in the discussion that follows. The first two (λ, λ') are lepton-number-violating couplings, whereas the third (λ'') violates baryon number. It is therefore generally necessary that either of the couplings to quarks, λ' or λ'', be vanishingly small to prevent spontaneous proton decay [32]. It is common to consider non-zero values of each coupling separately. Scenarios in which $\lambda'' \neq 0$ are often referred to UDD scenarios because of the baryon-number-violating term that λ'' controls in the superpotential. Current indirect experimental constraints [178] on the sizes of each of the UDD couplings λ'' from sources other than proton decay are primarily valid for low squark mass and for first- and second-generation couplings. Those limits are driven by double nucleon decay [179] (for λ''_{112}), neutron oscillations [180] (for λ''_{113}), and Z-boson branching ratios [181].

This benchmark process considered in this chapter assumes the pair production of two stops[1], which then each decay to two SM quarks, using 17.4 fb^{-1} of $\sqrt{s} = 8$ TeV proton–proton (pp) collision data recorded by the ATLAS experiment at the Large Hadron Collider (LHC).

1. The superpartners of the left- and right-handed top quarks, $\tilde{t}_{\mathrm{L}}$ and $\tilde{t}_{\mathrm{R}}$, mix to form the two mass eigenstates $\tilde{t}_1$ and $\tilde{t}_2$, where $\tilde{t}_1$ is the lighter one. This analysis focuses on $\tilde{t}_1$, which is referred to hereafter as $\tilde{t}$.

This decay violates the UDD coupling. The search specifically targets low-mass stops in the range 100–400 GeV that decay via the λ''_{323} coupling, thus resulting in stop decays $\tilde{t} \to \bar{b}\bar{s}$ (assuming a 100% branching ratio) as shown in fig. 8.1. The motivation to focus on the third-generation UDD coupling originates primarily from the minimal flavour violation (MFV) hypothesis [182] and the potential for this decay channel to yield a possible signal of RPV SUSY with a viable dark-matter candidate [183]. The MFV hypothesis essentially requires that all flavour- and CP-violating interactions are linked to the known structure of Yukawa couplings, and has been used to argue for the importance of the λ'' couplings [184].

The process $\tilde{t}\tilde{t}^* \to \bar{b}\bar{s}bs$ represents an important channel in which to search for SUSY in scenarios not yet excluded by LHC data [184, 183, 185]. Some of the best constraints on this process are from the ALEPH Collaboration, which set lower bounds on the mass of the stop at $m_{\tilde{t}} \gtrsim 80$ GeV [186]. The CDF Collaboration extended these limits, excluding $50 \lesssim m_{\tilde{t}} \lesssim 90$ GeV [187]. In 2014, The CMS Collaboration released the results of a search that excludes $200 \lesssim m_{\tilde{t}} \lesssim 385$ GeV [188] in the case where heavy-flavour jets are present in the final state. In addition, two ATLAS searches have placed constraints on RPV stops that decay to $\bar{b}\bar{s}$ when they are produced in the decays of light gluinos ($m_{\tilde{g}} \lesssim$ 900–1000 GeV) [189, 190]. The search presented here specifically focuses on direct stop pair production and seeks to close the gap in excluded stop mass between $\sim$ 100–200 GeV. Contributions from RPV interactions at production – such as would be required for resonant single stop production – are neglected in this analysis. This approach is valid provided that the RPV interaction strength is small compared to the strong coupling constant, which is the case for $\lambda''_{323} \lesssim 10^{-2}$–$10^{-1}$ [191] and for the estimated size of $\lambda''_{323} \sim 10^{-4}$ from MFV in the model described in Ref. [184].

The reduced sensitivity of standard SUSY searches to RPV scenarios is primarily due to the limited effectiveness of the high missing transverse momentum requirements used in the event selection common to many of those searches, motivated by the assumed presence of

undetected LSPs. Consequently, the primary challenge in searches for RPV SUSY final states is to identify suitable substitutes for background rejection to the canonical large missing transverse momentum signature.

Backgrounds dominated by multijet final states typically overwhelm the signal in the four-jet topology. In order to overcome this challenge, new observables are employed to search for $\tilde{t}\tilde{t}^* \to \bar{b}\bar{s}bs$ in the low-$m_{\tilde{t}}$ regime [185]. For $m_{\tilde{t}} \approx 100$–$300$ GeV, the initial stop transverse momentum (p_{T}) spectrum extends significantly into the range for which $p_{\mathrm{T}} \gg m_{\tilde{t}}$. This feature is the result of boosts received from initial-state radiation (ISR) as well as originating from the parton distribution functions (PDFs). As the Lorentz boost of each stop becomes large, the stop decay products begin to merge with a radius roughly given by $\Delta R \approx 2m_{\tilde{t}}/p_{\mathrm{T}}$, and thus can be clustered together within a single large-radius (large-R) jet with a mass $m^{\mathrm{jet}} \approx m_{\tilde{t}}$. By focusing on such cases, the dijet and multijet background can be significantly reduced via selections that exploit this kinematic relationship and the structure of the resulting *stop jet*, in a similar way to boosted objects used in previous measurements and searches by ATLAS [192, 193, 194, 195, 196]. In this case, since the stop is directly produced in pairs instead of from the decay of a massive parent particle, the strategy is most effective at low $m_{\tilde{t}}$ where the boosts are the largest.

8.2 Dataset and MC Samples

Monte Carlo (MC) simulation is used to study the signal acceptance and systematic uncertainties, to test the background estimation methods used, and to estimate the $t\bar{t}$ background. In all cases, events are passed through the full GEANT4 [136] detector simulation of ATLAS [135] after the simulation of the parton shower and hadronisation processes. Following the detector simulation, identical event reconstruction and selection criteria are applied to both the MC simulation and to the data. Multiple pp collisions in the same and neighbour-

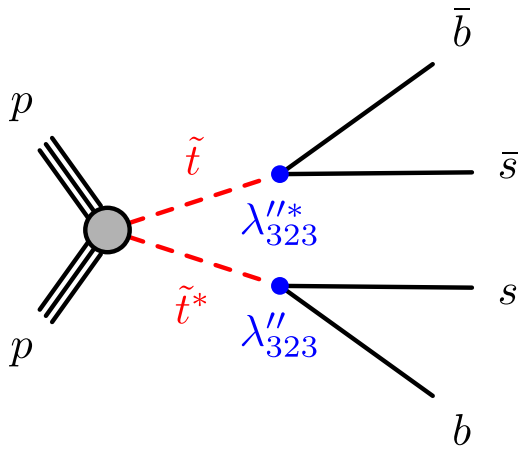

Figure 8.1: Benchmark signal process considered in this analysis. The solid black lines represent Standard Model particles, the dashed red lines represent the stops, and the blue points represent RPV vertices labelled by the relevant coupling for this diagram.

ing bunch crossings (pile-up) are simulated for all samples by overlaying additional soft pp collisions which are generated with PYTHIA 8.160 [197] using the ATLAS A2 set of tuned parameters (tune) in the MC generator [198] and the MSTW2008LO PDF set [199]. These additional interactions are overlaid onto the hard scatter and events are reweighted such that the MC distribution of the average number of pp interactions per bunch crossing matches the measured distribution in the full 8 TeV data sample.

The signal process is simulated using Herwig++ 2.6.3a [200] with the UEEE3 tune [201] for several stop-mass hypotheses using the PDF set CTEQ6L1 [202, 203]. All non-SM particles masses are set to 5 TeV except for the stop mass, which is scanned in 25 GeV steps from $m_{\tilde{t}} = 100$ GeV to $m_{\tilde{t}} = 400$ GeV. The signal cross-section used (shown in fig. 8.2) is calculated to next-to-leading order in the strong coupling constant, adding the resummation of soft gluon emission at next-to-leading-logarithmic accuracy (NLO+NLL) [204, 205, 206]. For the range of stop masses considered, the uncertainty on the cross-section is approximately 15% [207]. `MadGraph` 5.1.4.8 [208] is used to study the impact of ISR on the stop p_{T} spectrum. The `MadGraph` samples have one additional parton in the matrix element, which improves the modelling of a hard ISR jet. `MadGraph` is then interfaced to PYTHIA 6.426 with the

AUET2B tune [209] and the CTEQ6L1 PDF set for parton shower and hadronisation. The distribution of $p_{\mathrm{T}}(\widetilde{t\bar{t}}^{*})$ from the nominal Herwig++ signal sample is then reweighted to match that of the `MadGraph+PYTHIA` sample.

Dijet and multijet events, as well as top quark pair ($t\bar{t}$) production processes, are simulated in order to study the SM contributions and background estimation techniques. For optimisation studies, SM dijet and multijet events are generated using Herwig++ 2.6.3a with the CTEQ6L1 PDF set. Top quark pair events are generated with the `POWHEG`-BOX-r2129 [210, 211, 212] event generator with the CT10 NLO PDF set [213]. These events are then interfaced to PYTHIA 6.426 with the P2011C tune [214] and the same CTEQ6L1 PDF set as Herwig++. The $t\bar{t}$ production cross-section is calculated at next-to-next-to-leading order (NNLO) in QCD including resummation of next-to-next-to-leading logarithmic (NNLL) soft gluon terms with `top++2.0` [215, 216, 217, 218, 219, 220]. The value of the $t\bar{t}$ cross-section is $\sigma_{t\bar{t}} = 253^{+13}_{-15}$ pb.

8.3 Event Reconstruction, Observables, and Selection

The standard ATLAS event and data quality selections listed in section 6.3 were applied.

The anti-k_t algorithm [147], with a radius parameter of $R = 0.4$, is used for initial jet-finding using version 3 of FastJet [221]. The inputs to the jet reconstruction are three-dimensional topo-clusters [222]. This method first clusters together topologically connected calorimeter cells and classifies these clusters as either electromagnetic or hadronic. The classification uses a local cluster weighting calibration scheme based on cell-energy density and shower depth within the calorimeter [223]. Based on this classification, energy corrections are applied which are derived from single-pion MC simulations. Dedicated hadronic corrections are derived to account for the effects of differences in response to hadrons compared to electrons,

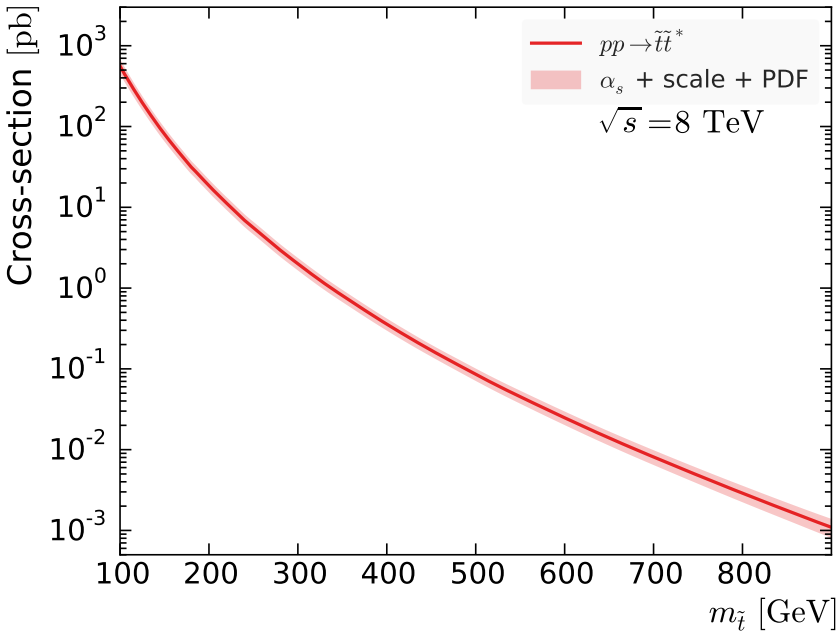

Figure 8.2: Cross-section for direct $\tilde{t}\tilde{t}^*$ pair production at the LHC centre-of-mass energy of $\sqrt{s} = 8$ TeV [204, 205, 206].

signal losses due to noise-suppression threshold effects, and energy lost in non-instrumented regions. The final jet energy calibration is derived from MC simulation as a correction relating the calorimeter response to the jet energy at generator level. In order to determine these corrections, the same jet definition used in the reconstruction is applied to stable (with lifetimes greater than 10 ps) generator-level particles, excluding muons and neutrinos. A subtraction procedure is also applied in order to mitigate the effects of pile-up [224]. Finally, the $R = 0.4$ jets are further calibrated with additional correction factors derived in situ from a combination of γ+jet, Z+jet, and dijet-balance methods [223].

All jets reconstructed with the anti-k_t algorithm using a radius parameter of $R = 0.4$ and a measured $p_{\mathrm{T}}^{\mathrm{jet}} > 20$ GeV are required to satisfy the quality criteria discussed in detail in Ref. [225]. These quality criteria selections for jets are extended to prevent contamination from detector noise through several detector-region-specific requirements. Jets contaminated

by energy deposits due to noise in the forward hadronic endcap calorimeter are rejected and jets in the central region ($|\eta| < 2.0$) that are at least 95% contained within the EM calorimeter are required to not exhibit any electronic pulse shape anomalies [226]. Any event with a jet that fails these requirements is removed from the analysis.

Identification of jets containing b-hadrons (so-called b-jets) is achieved through the use of a multivariate b-tagging algorithm referred to as MV1 [150]. This algorithm is based on an artificial neural-network algorithm that exploits the impact parameters of charged-particle tracks, the parameters of reconstructed secondary vertices, and the topology of b- and c-hadron decays inside an anti-k_t $R = 0.4$ jet. A working point corresponding to a 70% b-jet efficiency in simulated $t\bar{t}$ events is used. The corresponding mis-tag rates, defined as the fraction of jets originating from non-b-jets which are tagged by the b-tagging algorithm in an inclusive jet sample, for light jets and c-jets are approximately 1% and 20%, respectively. To account for differences with respect to data, data-derived corrections are applied to the MC simulation for the identification efficiency of b-jets and the probability to mis-identify jets resulting from light-flavour quarks, charm quarks, and gluons.

Initial jet-finding is extended using an approach called *jet re-clustering* [227]. This allows the use of larger-radius jet algorithms while maintaining the calibrations and systematic uncertainties associated with the input jet definition. Small-radius anti-k_t $R = 0.4$ jets with $p_{\mathrm{T}} > 20$ GeV and $|\eta| < 2.4$ are used as input without modification to an anti-k_t $R = 1.5$ large-R jet algorithm, to identify the hadronic stop decays. The small-R jets with $p_{\mathrm{T}} < 50$ GeV are required to have a jet vertex fraction (JVF) of at least 50%. After summing the p_{T} of charged-particle tracks matched to a jet, the JVF is the fraction due to tracks from the selected hard-scattering interaction and it provides a means by which to suppress jets from pile-up.

To further improve the background rejection, a splitting procedure is performed on each of

the two leading large-R jets. After jet-finding, the constituents of these large-R jets – the anti-k_t $R = 0.4$ input objects – are processed separately by the Cambridge–Aachen (C/A) algorithm [228, 229], as implemented in FastJet 3. The C/A final clustering is then undone by one step, such that there are two branches "a" and "b". The following *splitting* criteria are then applied to the branches "a" and "b" of each of the two leading large-R jets:[2]

- Both branches carry appreciable p_{T} relative to the large-R jet:

$$\frac{\min[p_{\mathrm{T}}(a), p_{\mathrm{T}}(b)]}{p_{\mathrm{T}}(\mathrm{large}{-}R)} > 0.1. \tag{8.1}$$

- The mass of each branch is small relative to its p_{T}:

$$\frac{m(a)}{p_{\mathrm{T}}(a)} < 0.3 \qquad \text{and} \qquad \frac{m(b)}{p_{\mathrm{T}}(b)} < 0.3. \tag{8.2}$$

If either of the leading two large-R jets fails these selections, the event is discarded.

Events must satisfy jet and H_{T}-selections applied in the trigger which require $H_{\mathrm{T}} = \sum p_{\mathrm{T}} >$ 500 GeV, calculated as the sum of level-2 trigger jets within $|\eta| < 3.2$, and a leading jet within $|\eta| < 3.2$ with $p_{\mathrm{T}} > 145$ GeV. This relatively low-threshold jet trigger came online part-way through the data-taking period in 2012 and collected 17.4 fb^{-1} of data. The corresponding offline selections require events to have at least one anti-k_t $R = 0.4$ jet with $p_{\mathrm{T}} > 175$ GeV and $|\eta| < 2.4$, as well as $H_{\mathrm{T}} > 650$ GeV, where the sum is over all anti-k_t $R = 0.4$ jets with $p_{\mathrm{T}} > 20$ GeV, $|\eta| < 2.4$, and JVF > 0.5 if $p_{\mathrm{T}} < 50$ GeV. The cumulative trigger selection efficiency is greater than 99% for these offline requirements. The offline event preselection further requires that at least two large-R jets with $p_{\mathrm{T}} > 200$ GeV and mass > 20 GeV be

2. This implementation is identical to Ref. [185], which is derived from the diboson-jet tagger [230]. This approach differs somewhat from that used in Ref. [231] in that no requirement is placed on the relative masses of the large-R and small-R jets.

present in each event. These requirements select a range of phase space for low stop masses in which the transverse momentum of the stops is often significantly greater than their mass.

The signal region (SR) is defined to suppress the large multijet background and to enhance the fraction of events that contain large-R jets consistent with the production of stop pairs, with each stop decaying to a light quark and a b-quark. Simulation studies indicate that three kinematic observables are particularly useful for background discrimination:

1. The mass asymmetry between the two leading large-R jets in the event (with masses m_1 and m_2, respectively), defined as

$$\mathcal{A} = \frac{|m_1 - m_2|}{m_1 + m_2}, \tag{8.3}$$

   differentiates signal from background since the two stop subjet-pair resonances are expected to be of equal mass.

2. The (absolute value of the cosine of the) stop-pair production angle, $|\cos\theta^*|$, with respect to the beam line in the centre-of-mass reference frame[3] distinguishes between centrally produced massive particles and high-mass forward-scattering events from QCD. It provides efficient discrimination and does not exhibit significant variation with the stop mass.

3. In addition, a requirement on the subjets is applied to each of the leading large-R jets in the event. The p_{T} of each subjet a and b relative to the other is referred to as the subjet $p_{\mathrm{T}2}/p_{\mathrm{T}1}$, defined by

$$\text{subjet } p_{\mathrm{T}2}/p_{\mathrm{T}1} = \frac{\min[p_{\mathrm{T}}(a), p_{\mathrm{T}}(b)]}{\max[p_{\mathrm{T}}(a), p_{\mathrm{T}}(b)]}. \tag{8.4}$$

3. This scattering angle, θ^*, is formed by boosting the two stop large-R jets to the centre-of-mass frame and measuring the angle of either stop large-R jet with respect to the beam line.

The $\mathcal{A}$, $|\cos\theta^*|$, and subjet $p_{\mathrm{T}2}/p_{\mathrm{T}1}$ variables provide good discrimination between signal and background and are motivated by an ATLAS search for scalar gluons at $\sqrt{s} = 7$ TeV [232] as well as by Refs. [185, 233].

In addition to the kinematic observables described above, b-tagging applied to anti-k_t $R = 0.4$ jets provides a very powerful discriminant for defining both the signal and the control regions, and one that is approximately uncorrelated with the kinematic features discussed above. Using these kinematic observables and the presence of at least two b-tagged jets per event, the signal region is defined by (for the leading two large-R jets)

$$\begin{aligned} \mathcal{A} &< 0.1, \\ |\cos\theta^*| &< 0.3, \\ \text{subjet } p_{\mathrm{T}2}/p_{\mathrm{T}1} &> 0.3. \end{aligned} \tag{8.5}$$

Distributions of the discriminating variables are shown in fig. 8.3. Insofar as the data points are dominated by background in these plots, even in the case of a potential signal, the data points should be understood to represent the background.

Following these selections, the distribution of the average mass of the leading two large-R jets, $m_{\mathrm{avg}}^{\mathrm{jet}} = (m_1^{\mathrm{jet}} + m_2^{\mathrm{jet}})/2$, is used to search for an excess of events above the background prediction. The search is done in regions of $m_{\mathrm{avg}}^{\mathrm{jet}}$ that are optimized to give the best significance. As shown in fig. 8.4, the stop signal is expected as a peak that would appear on top of a smoothly falling background spectrum. A Gaussian distribution is fitted to the stop signal $m_{\mathrm{avg}}^{\mathrm{jet}}$ peak. The mean of the fit, $\langle m_{\mathrm{avg}}^{\mathrm{jet}} \rangle$, is consistent with $m_{\tilde{t}}$ in each case. The resolution of the $m_{\mathrm{avg}}^{\mathrm{jet}}$ peak is given approximately $s/\langle m_{\mathrm{avg}}^{\mathrm{jet}} \rangle \sim 5-7\%$ (where s is the standard deviation of the fit), and has only a weak dependence on the stop mass in the range probed by this analysis. Mass *windows* in $m_{\mathrm{avg}}^{\mathrm{jet}}$ are determined by taking into account the effect of jet energy scale (JES) and jet energy resolution (JER) measurement uncertainties on the expected

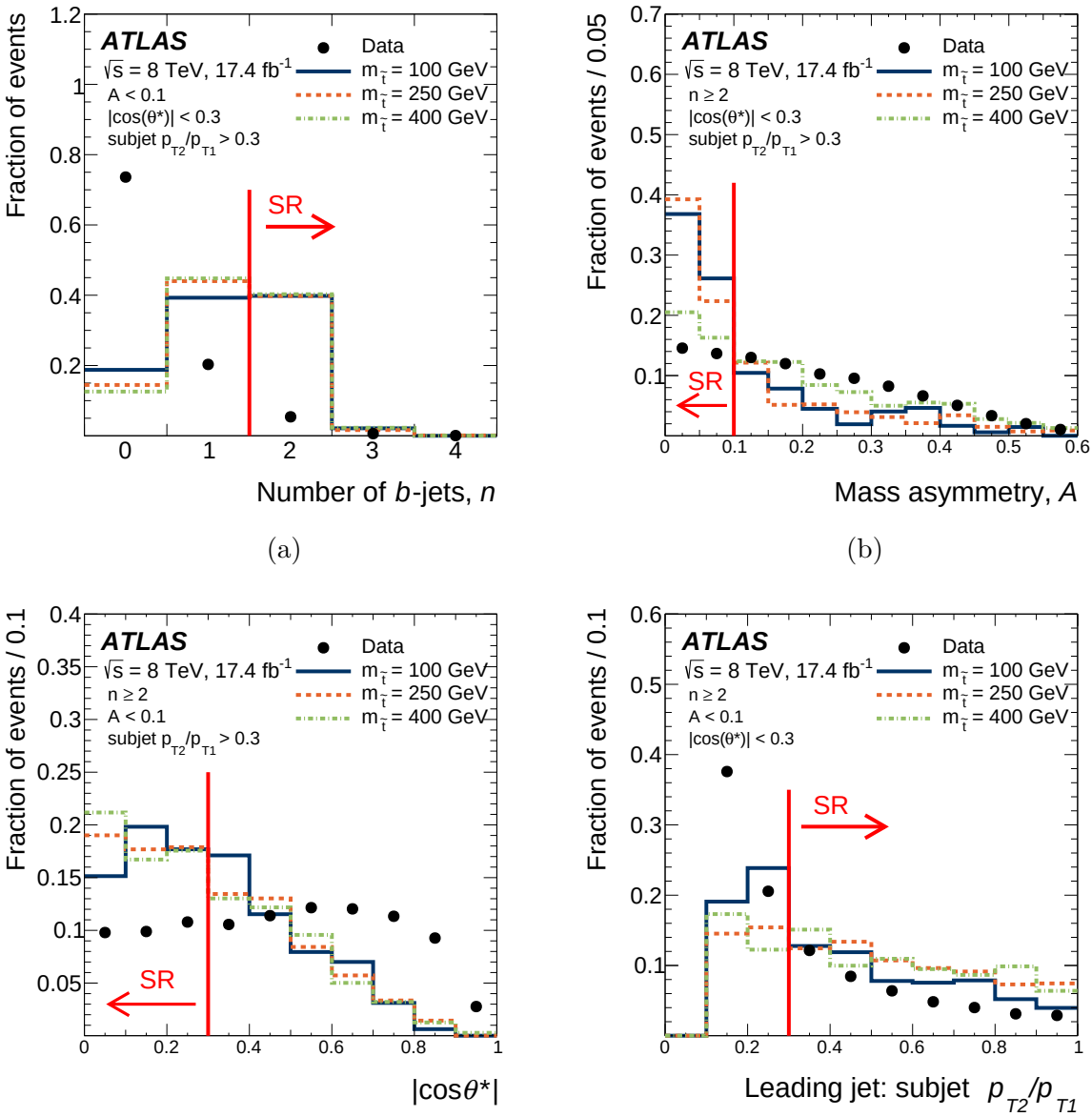

Figure 8.3: Distributions of the discriminating variables for events in which the other three selections are applied for each subfigure. The signal region is indicated with a red arrow. All distributions are normalized to unity. Overflows are included in the last bin for subfigures (a) and (b). (a) Number of b-tags/event, n. (b) Large-R jet mass asymmetry, $\mathcal{A}$. (c) Stop-pair centre-of-mass frame production angle, $|\cos\theta^*|$. (d) Subjet $p_{\mathrm{T}2}/p_{\mathrm{T}1}$ for the leading jet in each event.

signal $m_{\text{avg}}^{\text{jet}}$ distribution and the estimated background. The size of each mass window is defined to be equal to or larger than the full width of the $m_{\text{avg}}^{\text{jet}}$ mass spectrum for the $m_{\tilde{t}}$ model that best corresponds to that range. The definitions of these mass windows and the signal efficiency in each window are given in table 8.1. Figure 8.4a shows the mass windows overlaid on top of the signal $m_{\text{avg}}^{\text{jet}}$ distributions for a few stop masses. The efficiency of the mass windows (relative to the SR cuts of eq. (8.5)) varies from 79% at 100 GeV to 19% at 400 GeV. The low efficiency at high mass is due to the fact that the decay products are often not fully contained in the large-R jet, as can be seen in fig. 8.4b. Figure 8.5 shows the product of acceptance and efficiency, after the SR cuts and mass windows, as a function of $m_{\tilde{t}}$.

$m_{\tilde{t}}$ [GeV]	Window [GeV]	Selection efficiency in mass window
100	[95, 115]	79 %
125	[115, 135]	77 %
150	[135, 165]	83 %
175	[165, 190]	72 %
200	[185, 210]	68 %
225	[210, 235]	56 %
250	[235, 265]	55 %
275	[260, 295]	49 %
300	[280, 315]	44 %
325	[305, 350]	30 %
350	[325, 370]	29 %
375	[345, 395]	25 %
400	[375, 420]	19 %

Table 8.1: Definition of the signal mass windows and selection efficiency in each window relative to the SR cuts of eq. (8.5).

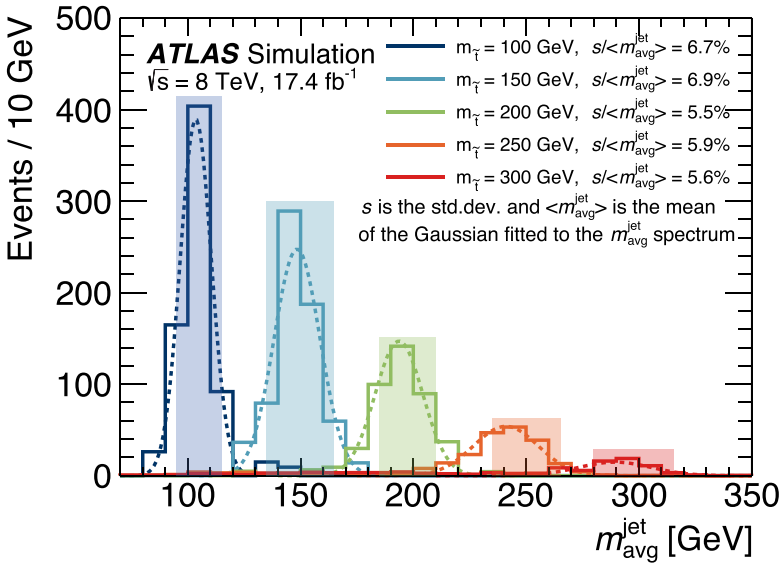

(a)

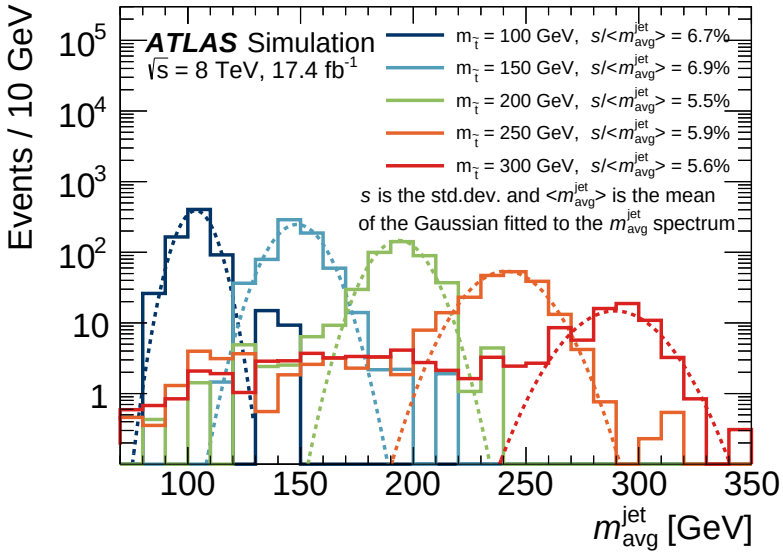

(b)

Figure 8.4: Distributions of the average jet mass $m_{\text{avg}}^{\text{jet}}$ for signal samples with $m_{\tilde{t}} = 100$, 150, 200, 250, and 300 GeV, in (a) linear and (b) logarithmic scales (solid lines). A Gaussian distribution is fitted to the mass peak of each sample (dashed lines). The resolution, $s/\langle m_{\text{avg}}^{\text{jet}} \rangle$, is quoted for each stop mass value. The mass windows are highlighted with the shaded rectangles in (a). The long tail peaking around $m_{\tilde{t}}/2$ for high-mass stops shown in (b) is due to events where not all stop decay products are clustered within the large-R jets.

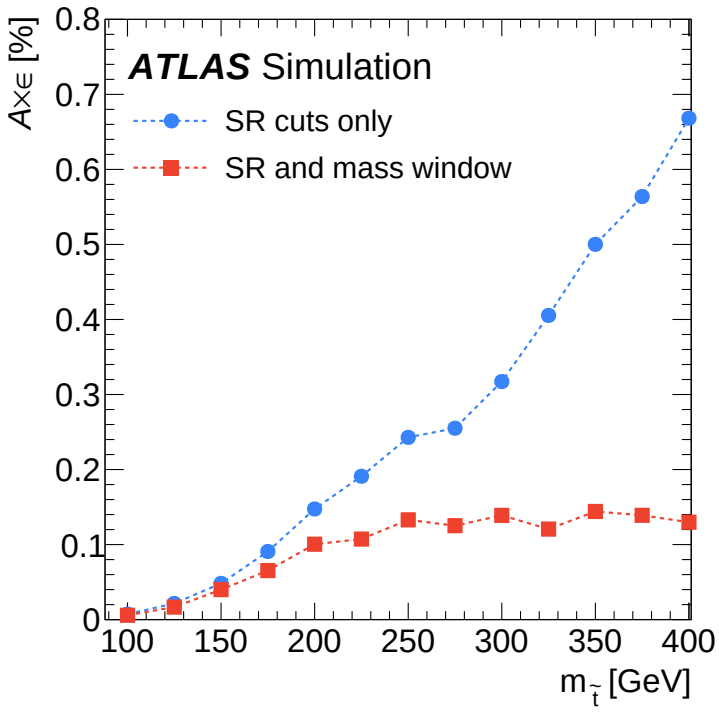

Figure 8.5: Total acceptance times efficiency ($A \times \epsilon$) of the SR cuts of eq. (8.5), and SR cuts combined with the mass window selection in table 8.1, as a function of $m_{\tilde{t}}$.

8.4 Background Estimation Strategy

The estimation of the dominant SM multijet background in the signal region, including both the expected number of events and the shape of the $m_{\text{avg}}^{\text{jet}}$ background spectrum, is performed directly from the data. MC simulations are used to study the background estimation method itself and to assess the contribution from $t\bar{t}$ production. For the background estimation, additional kinematic regions are defined by inverting the $\mathcal{A}$ and $|\cos\theta^*|$ selections as shown in table 8.2. These are labelled An, Bn, Cn, where n indicates the number of b-tags ($n = 0, = 1, \geq 2$). The signal region kinematic selection criteria of eq. (8.5) are comprised by the Dn requirements and summarized in the last row of table 8.2, where $SR \equiv D2$ with $n \geq 2$ b-tags, and $D1$ with $n = 1$ b-tag is a validation region. Signal event yields are summarized in table 8.3 for three stop masses.

Region	$\mathcal{A}$	$\lvert\cos\theta^*\rvert$	Subjet $p_{\text{T2}}/p_{\text{T1}}$	n
An	≥ 0.1	≥ 0.3	> 0.3	$= 0, = 1, \geq 2$
Bn	< 0.1	≥ 0.3	> 0.3	$= 0, = 1, \geq 2$
Cn	≥ 0.1	< 0.3	> 0.3	$= 0, = 1, \geq 2$
Dn	< 0.1	< 0.3	> 0.3	$= 0, = 1, \geq 2$

Table 8.2: Definitions of the kinematic regions defined by $\mathcal{A}$, $|\cos\theta^*|$, subjet $p_{\text{T2}}/p_{\text{T1}}$, and the b-tag multiplicity ($n = 0, = 1, \geq 2$). The letters A, B, C, and D label the $\mathcal{A}$ and $|\cos\theta^*|$ selections, whereas n indicates the number of b-tags. $D2 \equiv SR$ is the signal region of the analysis.

The method relies on the assumption that the shape of the $m_{\text{avg}}^{\text{jet}}$ spectrum is independent of the various b-tagging selections, as fig. 8.6a indicates, in each of the kinematic regions (An, Bn, Cn, and Dn) defined in table 8.2. The advantage of the approach adopted here is that events with fewer than two b-tagged jets can be used as control and validation regions for in situ studies of these kinematic regions. An estimation of the normalisation and shape of

Selection	$m_{\tilde{t}} = 100$ GeV	$m_{\tilde{t}} = 250$ GeV	$m_{\tilde{t}} = 400$ GeV
Total events	$(9.72 \pm 0.01) \times 10^6$	$(9.54 \pm 0.02) \times 10^4$	$(6.202 \pm 0.002) \times 10^3$
Jet + H_{T} trigger	$(5.47 \pm 0.08) \times 10^4$	$(2.07 \pm 0.01) \times 10^4$	$(5.98 \pm 0.02) \times 10^3$
Large-R jet tag	$(1.68 \pm 0.04) \times 10^4$	$(4.76 \pm 0.06) \times 10^3$	$(1.29 \pm 0.01) \times 10^3$
$n \geq 2$	$(6.35 \pm 0.23) \times 10^3$	$(1.70 \pm 0.03) \times 10^3$	515 ± 6
$A2$	416(58)	194(11)	68.7(22)
$B2$	639(71)	199(11)	33.3(16)
$C2$	419(62)	149(9)	71.2(22)
$D2$	711(74)	240(12)	41.5(18)

Table 8.3: The expected number of signal events in 17.4 fb^{-1} from MC simulation for each of the selections applied to the $n \geq 2$ region. Stop masses of $m_{\tilde{t}} = 100$ GeV, 250 GeV and 400 GeV are shown. The statistical uncertainty of the MC simulation is shown for each selection. The jet + H_{T} trigger selection includes the offline selection. The large-R jet tag includes both the kinematic preselections and the *splitting* criteria defined by eq. (8.1) and eq. (8.2). No selections are placed on the masses of the candidate stop jets. The region definitions of $A2$–$D2$ are summarised in table 8.2.

the spectrum in $D2$ can therefore be tested and validated using events with $n = 1$ as well as regions A and C. Region B is primarily used to evaluate shape differences in the predicted $m_{\mathrm{avg}}^{\mathrm{jet}}$ spectra (see section 8.5.1).

The $\mathcal{A}$ and $|\cos\theta^*|$ variables are found to have a correlation coefficient of at most 1% in data events for $n = 0$. In simulated multijet events, the correlation is also consistent with zero in events with $n \geq 2$, within the large statistical uncertainties. Consequently, the ratio of $n \geq 2$ (or $n = 1$) to $n = 0$ in regions A, B, and C should be approximately the same as the ratio in region D. The average jet mass spectrum, $m_{\mathrm{avg}}^{\mathrm{jet}}$, is compared across the various n selections for region A, as well as between each of the regions in events with $n = 0$. These comparisons are shown in fig. 8.6 along with the ratio of the spectrum in each region to that

which most closely matches the final signal region in each figure (region D for $n = 0$ and $n \geq 2$ for region A). The results demonstrate that the $m_{\text{avg}}^{\text{jet}}$ spectra in regions C and D are reliably reproduced by regions A and B, respectively, as shown in fig. 8.6b.

Region	N_{data}	$N_{t\bar{t}}$ ($\pm$ stat. $\pm$ syst.)			[95, 115] GeV		[135, 165] GeV		[165, 190] GeV		[375, 420] GeV	
					$\frac{N_S}{N_{\text{data}}}$	$\frac{N_{t\bar{t}}}{N_{\text{data}}}$	$\frac{N_S}{N_{\text{data}}}$	$\frac{N_{t\bar{t}}}{N_{\text{data}}}$	$\frac{N_S}{N_{\text{data}}}$	$\frac{N_{t\bar{t}}}{N_{\text{data}}}$	$\frac{N_S}{N_{\text{data}}}$	$\frac{N_{t\bar{t}}}{N_{\text{data}}}$
$n = 0$												
N_{A0}	296 226	390	± 10	$^{+100}_{-95}$	0.21 %	0.27 %	0.048 %	0.14 %	0.019 %	0.072 %	0.11 %	0.037 %
N_{B0}	115 671	176	± 7	$^{+50}_{-42}$	0.64 %	0.20 %	0.90 %	0.17 %	0.50 %	0.14 %	0.68 %	0.13 %
N_{C0}	114 186	221	± 8	$^{+59}_{-52}$	0.42 %	0.39 %	0.088 %	0.20 %	0.020 %	0.093 %	0.24 %	0.18 %
N_{D0}	44 749	110	± 6	$^{+27}_{-27}$	4.0 %	0.27 %	2.0 %	0.29 %	2.3 %	0.24 %	2.4 %	0. %
$n = 1$												
N_{A1}	79 604	1110	± 10	$^{+190}_{-180}$	1.2 %	2.6 %	0.46 %	1.5 %	0.48 %	0.74 %	0.22 %	0.71 %
N_{B1}	31 045	517	± 11	$^{+84}_{-83}$	14 %	1.9 %	9.7 %	2.3 %	8.0 %	1.9 %	10 %	0.089 %
N_{C1}	32 163	620	± 10	$^{+110}_{-100}$	4.8 %	3.4 %	1.6 %	2.1 %	1.3 %	0.99 %	0.28 %	0.76 %
N_{D1}	12 350	306	± 8	$^{+52}_{-45}$	29 %	2.3 %	31 %	3.6 %	21 %	3.7 %	43 %	0.000 10 %
$n \geq 2$												
N_{A2}	22 259	1050	± 10	$^{+190}_{-170}$	2.2 %	6.8 %	1.7 %	5.7 %	1.2 %	2.8 %	1.0 %	1.9 %
N_{B2}	8416	556	± 10	$^{+94}_{-86}$	50 %	7.2 %	29 %	10.0 %	24 %	8.8 %	26 %	0.24 %
N_{C2}	9384	570	± 10	$^{+100}_{-94}$	8.2 %	8.8 %	4.1 %	7.5 %	2.8 %	2.9 %	2.8 %	2.7 %
N_{D2}	3688	311	± 7	$^{+60}_{-47}$	120 %	8.4 %	73 %	14 %	72 %	11 %	160 %	0.51 %

Table 8.4: The observed event yields for 17.4 fb^{-1} in each of the regions for each b-tag multiplicity are shown, as well as the expected fractional signal contribution for the mass windows (as defined in table 8.1) corresponding to $m_{\tilde{t}} = 100$, 150, 175, and 400 GeV, and the $t\bar{t}$ contribution in the same mass windows. The $t\bar{t}$ systematic uncertainties include both the detector-level uncertainties and the theoretical uncertainties, as described in section 8.5.

The potential for events from $t\bar{t}$ production to contribute increases with the addition of b-tag-multiplicity selections. Table 8.4 presents the number of events in the data and the contribution from $t\bar{t}$, as determined by MC simulation, in regions A, B, C, and D for $n = 0$, $= 1$, ≥ 2. The expected signal and $t\bar{t}$ contributions are also given for a few mass windows. The $t\bar{t}$ contribution is at the few per-mille level in the events with $n = 0$. Contributions rise slightly in events with $n = 1$ to a maximum of $\lesssim 4\%$ in region $D1$. Lastly, regions $A2$ and

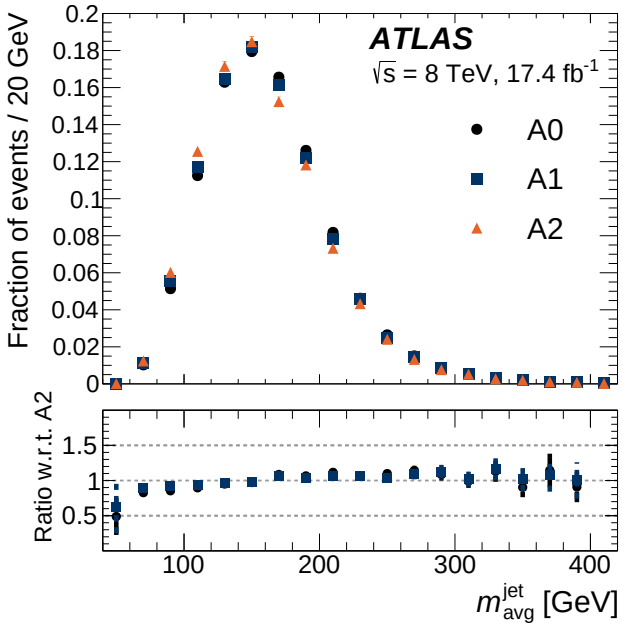

(a)

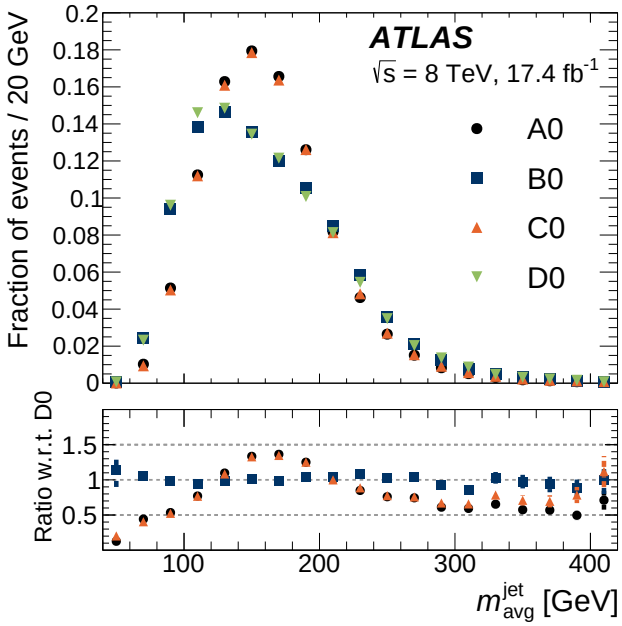

(b)

Figure 8.6: Shape comparisons of the $m_{\text{avg}}^{\text{jet}}$ spectrum for the data (a) in region A for events with $n = 0, = 1, \geq 2$ and (b) in regions A, B, C, D for events with $n = 0$. In each case, the lower panel shows the ratio of the spectrum in each region to that which most closely matches the final signal region ($n \geq 2$ for region A and region D for $n = 0$). Only statistical uncertainties are shown.

$C2$ have a maximum $t\bar{t}$ contribution of around $\lesssim 10\%$. Consequently, when validating the method and in the final background estimate, the contribution from $t\bar{t}$ is subtracted in each of the regions. The corrected number of events is defined as $N_{Xn} = N_{Xn}^{\text{data}} - N_{Xn}^{t\bar{t}}$ and the corrected $m_{\text{avg}}^{\text{jet}}$ spectrum is defined as $\vec{v}_{Xn} = \vec{v}_{Xn}^{\text{data}} - \vec{v}_{Xn}^{t\bar{t}}$ (where $X = A, B, C$, or D, and n refers to the number of b-tags), unless otherwise explicitly noted.

All regions used for the background estimation ($A0$, $C0$, $D0$, $A2$, and $C2$) exhibit potential signal contribution of less than 10%. Region $B2$ ($\mathcal{A} < 0.1$) is not used to derive the background estimate, since the expected signal contribution is much higher here than in $A2$ and $C2$ (for $m_{\tilde{t}} = 100$ GeV the signal contribution is 50% in $B2$, compared with 2.2% in $A2$ and 8.2% in $C2$). The expected signal contribution in the validation regions ($n = 1$) is only significant in $B1$ and $D1$. Due to this level of expected signal contribution, and the $m_{\text{avg}}^{\text{jet}}$ dependence of that contribution, the background estimation procedure obtains the $m_{\text{avg}}^{\text{jet}}$ spectrum from the $n = 0$ regions for the final background spectrum estimate. The background estimation procedure itself is summarized in the following steps:

1. The $m_{\text{avg}}^{\text{jet}}$ shape, $\vec{v}_{D0}$, and number of events, N_{D0}, are extracted from the $D0$ region.

2. A projection factor is derived between events with $n = 0$ and events with $n \geq 2$ for the signal-depleted regions A and C. As explained above, the number of $t\bar{t}$ events is subtracted in regions $A0, C0, A2$, and $C2$ before evaluating the projection factor $\langle k_{A,C} \rangle_2$:

$$\langle k_{A,C} \rangle_2 = (k_{A2} + k_{C2})/2, \quad \text{where} \quad k_{X2} = \frac{N_{X2}}{N_{X0}}, \quad X = A, C. \tag{8.6}$$

3. The projection factor is used to estimate the number of events,

$$N'_{D2} = \langle k_{A,C} \rangle_2 \times N_{D0} + N_{D2}^{t\bar{t}}, \tag{8.7}$$

and shape,

$$\vec{v}'_{D2} = \langle k_{A,C} \rangle_2 \times \vec{v}_{D0} + \vec{v}^{t\bar{t}}_{D2}, \tag{8.8}$$

in the signal region, $D2$ (where the contribution from $t\bar{t}$ in $D2$ has been added).

This procedure is performed in the entire mass range and the mass windows are then defined from the estimated background spectrum. The projection factors k_{A2} and k_{C2} are compatible at the level of about 4% (including the $t\bar{t}$ subtraction as in eq. (8.6)) and this difference is included as a systematic uncertainty on the background estimate (see section 8.5). The validity of the background estimation method can be demonstrated in the $n = 1$ regions by deriving a projection factor analogously to eq. (8.6) for $n = 0$ and $n = 1$,

$$\langle k_{A,C} \rangle_1 = (k_{A1} + k_{C1})/2. \tag{8.9}$$

The expected number of events in the full range of $D1$ is then estimated by

$$\begin{aligned} N'_{D1} &= \langle k_{A,C} \rangle_1 \times N_{D0} + N^{t\bar{t}}_{D1} \\ &= 12400 \pm 130. \end{aligned} \tag{8.10}$$

The same estimate for $D2$ gives

$$\begin{aligned} N'_{D2} &= \langle k_{A,C} \rangle_2 \times N_{D0} + N^{t\bar{t}}_{D2} \\ &= 3640^{+90}_{-80}. \end{aligned} \tag{8.11}$$

In eq. (8.9) and section 8.4 the uncertainty quoted includes the statistical uncertainty and the uncertainties related to the $t\bar{t}$ estimate (see section 8.5). These numbers should be compared with the observed numbers of events in table 8.4, 12350 in $D1$ and 3688 in $D2$. The observed numbers of events are consistent with the estimated values.

8.5 Systematic Uncertainties

Several sources of systematic uncertainty are considered when determining the estimated contributions from signal and background. The background estimate uncertainties pertain primarily to the method itself. The control and validation regions defined in section 8.4 are used to evaluate the size of these uncertainties. A description of the primary sources of uncertainty follows.

8.5.1 Background Estimation Shape Uncertainty

Events with $n = 1$ are used to test the validity of the background estimation method in data and to derive a systematic uncertainty on the approach. fig. 8.7 shows several results of this test by comparing three estimated spectra with the observed spectrum in each of the four regions. The estimated spectra of fig. 8.7 are determined using projection factors,

$$k_{X1} = N_{X1}/N_{X0}, \tag{8.12}$$

from events with $n = 0$ to those with $n = 1$, in each of the three regions $X = A$, B, and C in order to determine the extent to which the prediction varies with each choice. Region $D1$ was used to validate the systematic uncertainty derived from $A1$, $B1$, and $C1$. Because of the three projection factors (k_A, k_B, and k_C) there are three estimates ($\vec{v}_{Y1'_A}$, $\vec{v}_{Y1'_B}$, and $\vec{v}_{Y1'_C}$) of the $m^{\text{jet}}_{\text{avg}}$ spectrum in each of the regions $Y1 = A1$, $B1$, and $C1$. Thus, in total there are nine estimates of the actual spectra, these are written succinctly as

$$\vec{v}_{Y1'_X} = k_{X1} \times \vec{v}_{Y0}, \text{ where } X = \{A, B, C\} \text{ and } Y = \{A, B, C\}. \tag{8.13}$$

Note that the estimates $\vec{v}_{A1'_A}$, $\vec{v}_{B1'_B}$, and $\vec{v}_{C1'_C}$ are normalized to the data by construction,

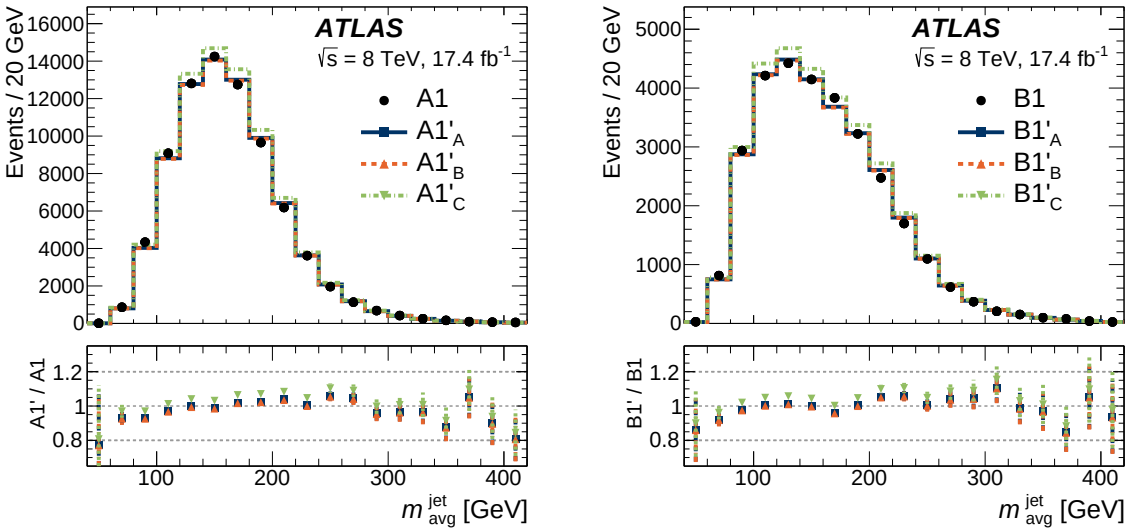

(a)

(b)

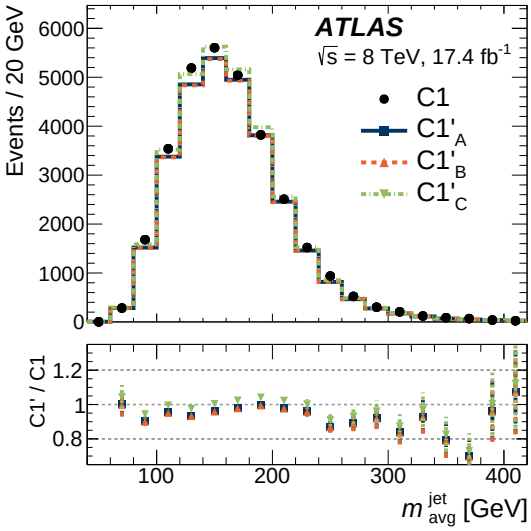

(c)

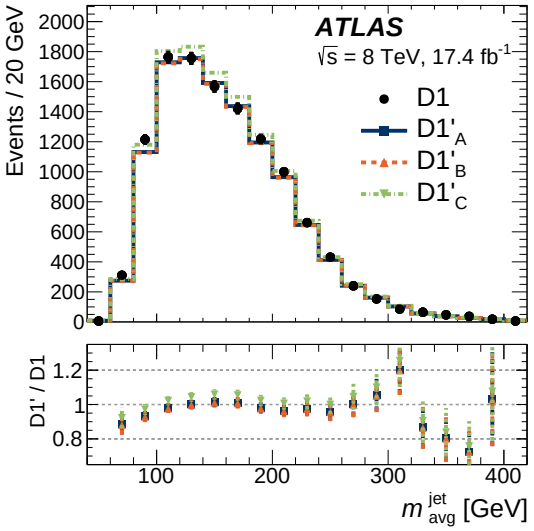

(d)

Figure 8.7: The $m_{\text{avg}}^{\text{jet}}$ distribution is shown in four validation regions with $n = 1$. In each case the data ($A1$, $B1$, $C1$, and $D1$) are compared to estimates based on projection factors derived between $n = 0$ and $n = 1$ in A, B, and C (see section 8.5.1).

so they test only the shape of the distribution in $n = 1$ compared to $n = 0$. A systematic uncertainty for the background projection is then derived by taking, bin-by-bin, the largest deviation of the ratio of estimated to actual yield from unity in the $m_{\text{avg}}^{\text{jet}}$ spectra in each of the regions A, B, and C according to

$$\Delta\vec{v}_{X,Y}(i) = |1 - \vec{v}_{Y1'_X}(i)/\vec{v}_{Y1}(i)|, \tag{8.14}$$

where $\vec{v}_{Y1}$ are the observed data points and $\vec{v}_{Y1'_X}$ are the estimated spectra defined by eq. (8.13). A fixed bin width of 50 GeV is used in order to reduce effects due to statistical uncertainties. The individual bins of the histograms are labelled i. Bin-by-bin, the largest ratio between the estimated and actual yield,

$$\sigma^{\text{bkg. syst.}}(i) = \max\left[\Delta\vec{v}_{X,Y}(i); X = \{A, B, C\}, Y = \{A, B, C\}\right], \tag{8.15}$$

is added in quadrature with the statistical uncertainty of that ratio in order to form the total systematic uncertainty for that particular bin. The size of the $m_{\text{avg}}^{\text{jet}}$ shape systematic uncertainty varies from less than 10% at low $m_{\text{avg}}^{\text{jet}} \approx 100$ GeV to 20% near $m_{\text{avg}}^{\text{jet}} \approx 400$ GeV. fig. 8.8 shows the $m_{\text{avg}}^{\text{jet}}$ shape systematic uncertainty as well as the total systematic uncertainty when combined with the constant systematic uncertainty due to the 4% difference between projection factors k_{A2} and k_{C2} mentioned in section 8.4, and the b-jet-multiplicity shape systematic uncertainty described below.

8.5.2 b-Jet-Multiplicity Shape Uncertainty

A systematic uncertainty based on the shape difference of the $m_{\text{avg}}^{\text{jet}}$ spectrum in the data between events with $n = 0$ and $n \geq 2$ is also considered. Regions A and C are used to directly compare the $m_{\text{avg}}^{\text{jet}}$ spectrum in the two b-tag regions. The final systematic uncertainty, due

to the shape difference between $n = 0$ and $n \geq 2$, is the maximum of the bin-by-bin difference of $A2$ compared to $A0$ (fig. 8.6a) and $C2$ compared to $C0$, is defined as

$$\sigma(i)^{b-\text{jet}-\text{multi. syst.}} = \max\left[|1 - \vec{v}_{A2}(i)/\vec{v}_{A0}(i)|, |1 - \vec{v}_{C2}(i)/\vec{v}_{C0}(i)|\right]. \tag{8.16}$$

This is then added in quadrature with the statistical uncertainty to form the total systematic uncertainty for that particular bin. A bin width of 50 GeV is used, just as above with the background estimation shape systematic uncertainty. The size of the $m_{\text{avg}}^{\text{jet}}$ shape systematic uncertainty varies from approximately 7–12% at low $m_{\text{avg}}^{\text{jet}}$ to 20% near $m_{\text{avg}}^{\text{jet}} \approx 300$ GeV, and to around 90% for $m_{\text{avg}}^{\text{jet}} \approx 400$ GeV. The large systematic uncertainty in the high-mass tail is due to the low number of events in the $n \geq 2$ regions. fig. 8.8 shows the b-jet-multiplicity shape systematic uncertainty as well as the total systematic uncertainty with the two above-mentioned systematic uncertainties.

8.5.3 $t\bar{t}$ Theory Uncertainty

Since POWHEG+PYTHIA MC simulation is used to determine the contribution from $t\bar{t}$ events in the signal region and each of the control regions, systematic uncertainties related to the MC simulation of the process itself are included in the total systematic uncertainty for the background estimation. The theoretical uncertainties include renormalisation and factorisation scale variations, parton distribution function uncertainties, the choice of MC generator using comparisons with MC@NLO [234], the choice of parton shower models using comparisons with Herwig [235], and initial- and final-state radiation (FSR) modelling uncertainties. The size of the theoretical systematic uncertainties for $t\bar{t}$ production vary from approximately 40% to 70% in the relevant kinematic regions and are dominated by the uncertainties from the MC generator and ISR/FSR variations. The detector-level uncertainties include the JES and JER uncertainties [223] as well as the b-tagging efficiency and mistag-rate uncertain-

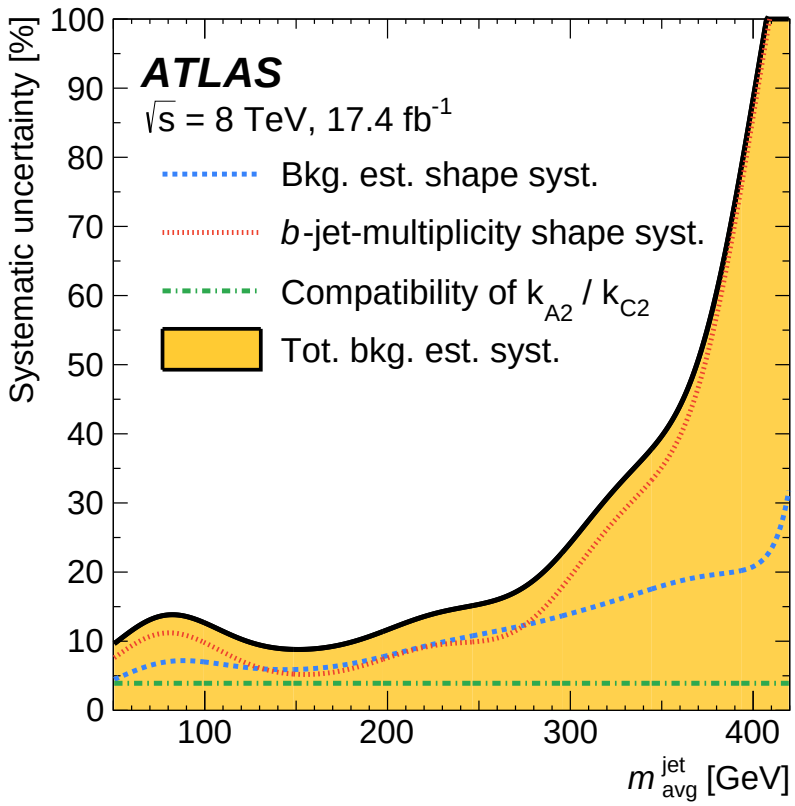

Figure 8.8: Systematic uncertainty for the data-driven multijet background estimation. The blue dashed line represents the background estimation systematic uncertainty estimated from comparisons of the predicted $m_{\text{avg}}^{\text{jet}}$ spectra in regions $A1$, $B1$, and $C1$ to the actual spectra. The red dotted line represents the estimated systematic uncertainty due to shape differences between events with $n = 0$ and $n \geq 2$. The green line represents a systematic uncertainty due to the level of compatibility of k_{A2} and k_{C2}. Finally, the black line with a filled yellow area shows the combined systematic uncertainty of all three contributions added in quadrature. The systematic uncertainty curves were smoothed with a Gaussian filter of spread 20 GeV.

ties [150]. Uncertainties associated with the large-R jet mass scale and resolution are taken into account by the JES and JER uncertainties of the input small-R jets [227].

The size of the total $t\bar{t}$ systematic uncertainty varies in the mass range $m_{\text{avg}}^{\text{jet}} = 100$–$200$ GeV from approximately 50% to 80%. In the range $m_{\text{avg}}^{\text{jet}} = 300$–$400$ GeV the $t\bar{t}$ systematic uncertainties are of the order of 100%, but the $t\bar{t}$ background is completely negligible in this range. Lastly, an uncertainty of 2.8% is applied to the measured integrated luminosity of 17.4 fb^{-1} following the methodology described in Ref. [236].

8.5.4 Signal Uncertainties

In addition to the systematic uncertainties associated with the background estimate, the MC simulation of the signal model is subject to systematic uncertainties. Much like the contribution from $t\bar{t}$, these uncertainties include experimental uncertainties as well as theoretical uncertainties. The detector-level uncertainties include the JES and JER uncertainties, and the b-tagging uncertainties as described for the estimate of $t\bar{t}$. The theoretical uncertainties include renormalisation and factorisation scale variations, parton distribution function uncertainties, and ISR and FSR modelling uncertainties. The nominal signal cross-section and its uncertainty are taken from an envelope of cross-section predictions using different PDF sets and factorisation and renormalisation scales, as described in Ref. [207]. Each signal model is varied according to these systematic uncertainties and the impact on the acceptance in each mass window is then propagated to the final result. The largest contribution to the total signal systematic uncertainty comes from the JES and b-tagging, both in the range 10–18%. The size of the theoretical uncertainty grows from around 5% for low-mass stops to around 10% for higher-mass stops.

To evaluate the ISR/FSR systematic uncertainty, separate samples of $\tilde{t}\tilde{t}^*$ pair events are

generated using `MadGraph` +PYTHIA, and the rate of ISR/FSR production is varied. These are used to reweight the $p_{\mathrm{T}}(\tilde{t}\tilde{t}^{*})$ distribution of the nominal signal samples to estimate the change in signal acceptance $\times$ efficiency. The effect ranges from 0–17%, with the largest impact at high $m_{\tilde{t}}$.

8.6 Results

Table 8.5 summarizes the observed and expected number of events that fall within each of the optimized mass windows in the signal region, $D2$. fig. 8.9 shows the observed $m_{\mathrm{avg}}^{\mathrm{jet}}$ distribution in the data, along with the estimated background spectrum, including both the systematic and statistical uncertainties. No excess over the background prediction is observed.

Model-independent upper limits at 95% confidence level (CL) on the number of beyond-the-SM (BSM) events for each signal region are derived using the CL_s prescription [237] and neglecting any possible contribution in the control regions. Dividing these by the integrated luminosity of the data sample provides upper limits on the visible BSM cross-section, $\sigma_{\mathrm{vis.}}$, which is defined as the product of acceptance (A), reconstruction efficiency (ϵ), branching ratio (BR), and production cross-section ($\sigma_{\mathrm{prod.}}$). This search specifically targets low-mass $\tilde{t} \to \bar{b}\bar{s}$ decays, assuming 100% BR. The resulting limits on the number of BSM events and on the visible signal cross-section are shown in table 8.6. The significance of an excess can be quantified by the probability (p_0) that a background-only experiment has at least as many events as observed. This p-value is also reported for each region in table 8.6, where $p_0 = 1 - \mathrm{CL}_b$ and CL_b is the confidence level observed for the background-only hypothesis. The p-value is truncated at 0.5 for any signal region where the observed number of events is less than the expected number.

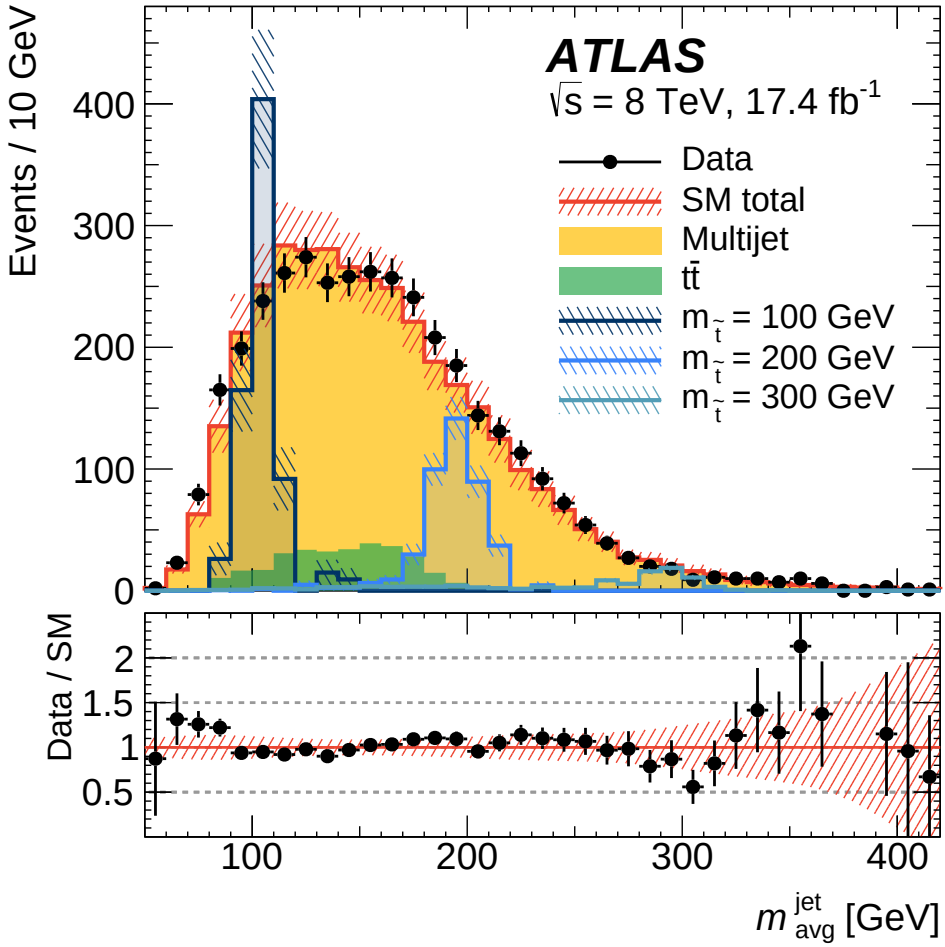

Figure 8.9: The observed $m_{\text{avg}}^{\text{jet}}$ spectrum in the signal region is shown as black points with statistical uncertainties. Also shown is the total SM background estimate, and the separate contributions from the data-driven multijet and MC $t\bar{t}$ backgrounds. The red hatched band represents the combined statistical and systematic uncertainty on the total SM background estimate. Signal mass spectra are shown with statistical uncertainties only. The bottom panel shows the ratio of the data relative to the total SM background estimate.

$m_{\tilde{t}}$ [GeV]	Window [GeV]	$N_B^{\text{data-driven est.}}$	$N_B^{t\bar{t}\text{ est.}}$	$N_B^{\text{tot. est.}}$	$N_{\text{data}}^{\text{obs.}}$	N_S
100	[95, 115]	465 ± 56	39 ± 26	504 ± 61	460	560 ± 140
125	[115, 135]	496 ± 49	68 ± 37	564 ± 61	555	570 ± 130
150	[135, 165]	680 ± 61	105 ± 49	785 ± 78	761	560 ± 110
175	[165, 190]	471 ± 46	63 ± 19	534 ± 50	583	421 ± 96
200	[185, 210]	395 ± 46	16.5 ± 9.6	412 ± 47	416	293 ± 50
225	[210, 235]	266 ± 37	2.4 ± 2.4	269 ± 37	283	178 ± 36
250	[235, 265]	176 ± 27	1.1 ± 1.1	177 ± 27	195	127 ± 29
275	[260, 295]	104 ± 19	0.59 ± 0.55	104 ± 19	96	71 ± 20
300	[280, 315]	69 ± 16	0.93 ± 0.29	70 ± 16	51	48 ± 10
325	[305, 350]	43 ± 14	0.73 ± 0.53	43 ± 14	44	29.4 ± 6.9
350	[325, 370]	26 ± 10	0.23 ± 0.15	26 ± 10	37	20.2 ± 4.3
375	[345, 395]	18.6 ± 9.8	0.076 ± 0.076	18.7 ± 9.8	22	12.6 ± 2.8
400	[375, 420]	9.5 ± 7.7	0.026 ± 0.026	9.5 ± 7.7	5	8.1 ± 1.8

Table 8.5: Summary of the observed number of events in the data and the estimated number of signal and background events with total uncertainties (i.e. all listed uncertainties are the combined statistical and systematic uncertainties) that fall within each of the optimised mass windows in region $D2$. The total number of estimated background events in each window is the sum of the estimated background from the data-driven method and the $t\bar{t}$ simulation. The columns, from left to right indicate: $N_B^{\text{data-driven est.}}$, the data-driven background estimate; $N_B^{t\bar{t}\text{ est.}}$, the background contribution from $t\bar{t}$; $N_B^{\text{tot. est.}}$, the total estimated background; $N_{\text{data}}^{\text{obs.}}$, the number of observed events in the data; and N_S, the number of expected signal events.

Exclusion limits are set on the signal model of interest. A profile likelihood ratio combining Poisson probabilities for signal and background is computed to determine the 95% CL for compatibility of the data with the signal-plus-background hypothesis (CL_{s+b}) [238]. A similar calculation is performed for the background-only hypothesis (CL_b). From the ratio of these two quantities, the confidence level for the presence of signal (CL_s) is determined [237]. Systematic uncertainties are treated as nuisance parameters assuming Gaussian distributions and pseudo-experiments are used to evaluate the results. This procedure is implemented using a software framework for statistical data analysis, HistFitter [239]. The observed and expected 95% CL upper limits on the allowed cross-section are shown in fig. 8.10. For each simulated stop mass, the optimal mass window is chosen and the expected background

Model-independent upper limits at 95% CL				
Window [GeV]	$\sigma_{\text{vis.}}$ [fb]	Observed N_{BSM}	Expected N_{BSM}	p_0
$[95, 115]$	5.8	101	$127\ ^{+50}_{-36}$	0.50
$[115, 135]$	7.0	122	$128\ ^{+50}_{-36}$	0.50
$[135, 165]$	8.4	145	$160\ ^{+40}_{-45}$	0.50
$[165, 190]$	8.4	146	$109\ ^{+43}_{-31}$	0.19
$[185, 210]$	5.9	103	$100\ ^{+39}_{-28}$	0.47
$[210, 235]$	5.1	89	$79\ ^{+31}_{-22}$	0.36
$[235, 265]$	4.2	73	$60\ ^{+24}_{-17}$	0.28
$[260, 295]$	2.2	38	$43\ ^{+17}_{-12}$	0.50
$[280, 315]$	1.4	25	$35\ ^{+14}_{-10}$	0.50
$[305, 350]$	1.7	30	$30\ ^{+12}_{-8}$	0.49
$[325, 370]$	1.8	31.8	$23.5\ ^{+9.4}_{-6.6}$	0.18
$[345, 395]$	1.4	23.8	$21.4\ ^{+8.4}_{-6.0}$	0.38
$[375, 420]$	0.57	10.0	$10.8\ ^{+3.2}_{-2.1}$	0.50

Table 8.6: Left to right: mass window range, 95% CL upper limits on the visible cross-section ($\sigma_{\text{vis.}} = \langle A \times \epsilon \times \text{BR} \times \sigma_{\text{prod.}} \rangle$) and on the number of signal events (Observed N_{BSM}). The fourth column (Expected N_{BSM}) shows the 95% CL upper limit on the number of signal events, given the expected number (and $\pm 1\sigma$ excursions on the expectation) of background events. The last column indicates the discovery p-value, $p_0 = 1 - \text{CL}_b$, where CL_b is the confidence level observed for the background-only hypothesis. The p-value is truncated at 0.5 for any mass window where the observed number of events is less than the expected number.

yield is compared to the observed number of events in the mass window. Any potential signal contribution in the control regions from which the background estimates are derived is included as a systematic uncertainty on the background estimate. Stops with masses between $100 \leq m_{\tilde{t}} \leq 315$ GeV are excluded at 95% confidence level[4]. All mass limits are quoted using the $\tilde{t}\tilde{t}^*$ signal production cross-section reduced by one standard deviation of the theory uncertainties.

4. These results were updated by ATLAS in 2017, using 36.7 fb^{-1} of 13 TeV data. The updated results excluded stops with masses between $100 \leq m_{\tilde{t}} \leq 470$ GeV and $480 \leq m_{\tilde{t}} \leq 610$ GeV. [240]

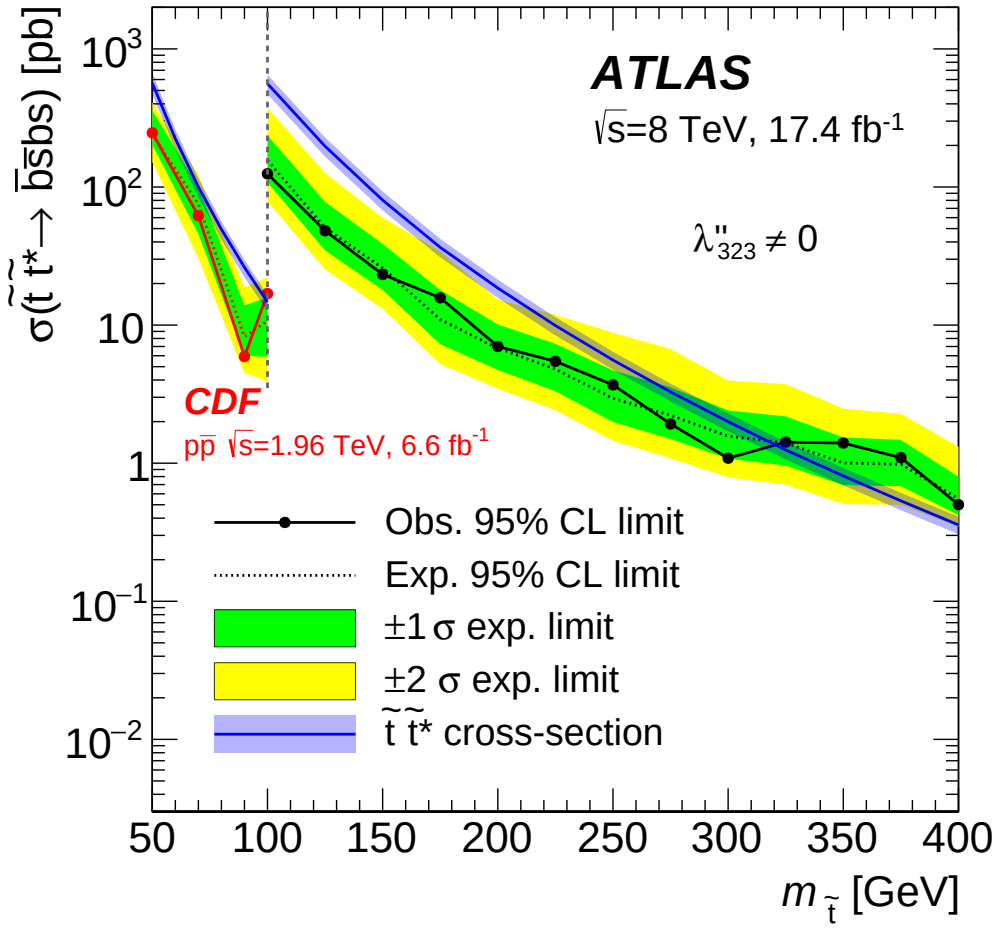

Figure 8.10: Observed and expected 95% CL upper limits on the stop pair production cross-section as function of the stop mass. The solid line with big round markers shows the observed limit, the dotted line shows the expected exclusion limit, and the green and yellow bands represent the uncertainties on this limit. Limits from the CDF Collaboration are shown in red for $m_{\tilde{t}} \leq 100$ GeV [187]. The blue line shows the theoretical signal cross-section and the blue band indicates the $\pm 1\sigma$ variations due to theoretical uncertainties on the signal production cross-section given by renormalisation and factorisation scale and PDF uncertainties. For this search the cross-section is calculated at NLO+NLL, whereas in the CDF paper the cross-section was calculated at NLO only.

8.7 Conclusion

A search for direct pair production of light top squarks, decaying via an R-parity-violating coupling to b- and s-quarks has been performed. The final state is characterized by two large-radius hadronic jets that each contain both decay products of the top squark. The search uses 17.4 fb^{-1} of $\sqrt{s} = 8$ TeV proton–proton collision data collected with the ATLAS detector at the LHC. No deviation from the background prediction is observed, and top squarks with masses between 100 and 315 GeV are excluded at 95% confidence level.

CHAPTER 9

ELECTROWEAK PAIR PRODUCTION WITH WH DECAYS AT 13 TEV

This chapter presents a search for electroweak pair production of the lightest chargino ($\tilde{\chi}_1^{\pm}$) the next-to-lightest neutralino ($\tilde{\chi}_2^0$), $pp \to \tilde{\chi}_1^{\pm}\tilde{\chi}_2^0$. The chargino decays to the lightest neutralino ($\tilde{\chi}_1^0$) and a $W^{\pm}$ boson, $\tilde{\chi}_1^{\pm} \to \tilde{\chi}_1^0 W^{\pm}$, and the next-to-lightest neutralino decays to the lightest neutralino and a Standard Model like 125 GeV Higgs boson, $\tilde{\chi}_2^0 \to \tilde{\chi}_1^0 h$. For the first time at the LHC a fully hadronic final state ($W \to q\bar{q}$ and $h \to b\bar{b}$) is considered for this model. The analysis is based on 36.1 fb^{-1} of $\sqrt{s} = 13$ TeV proton-proton collision data delivered by the Large Hadron Collider and recorded with the ATLAS detector.[1]

This chapter is organized as follows: Section 9.1 provides a brief overview and motivation for the simplified SUSY scenario targeted by this search. Section 9.2 describes the dataset and MC samples used to simulate the dominant background processes, as well as the MC samples used to simulate the signal model. Section 9.3 describes the event reconstruction, selection, and event level kinematic observables used for background rejection. Section 9.4 describes the strategy for estimating the dominant background processes and the procedure for optimizing the signal-to-background sensitivity. Section 9.5 describes the experimental and theoretical systematic uncertainties. Finally, the results are presented in section 9.6.

1. These results will be submitted for publication in Phys. Rev. D together with results from complementary ATLAS searches, with the same electroweak production and Wh decays, utilizing semi-leptonic final states [241].

9.1 Overview

In the simplified SUSY scenario considered as benchmark model in this chapter[2], R-parity conservation is assumed. Thus, the Lightest Supersymmetric Particle (LSP)—the lightest of the neutralinos ($\tilde{\chi}^0$)—is a stable particle. Together with the charginos ($\tilde{\chi}^{\pm}$), the neutralinos represent the mass eigenstates formed from the mixture of the γ, W, Z and Higgs bosons' gauge eigenstate superpartners (the higgsinos, winos and binos). The neutralinos and charginos are collectively referred to as *electroweakinos*. Specifically, the electroweakino mass eigenstates are designated in order of increasing mass as $\tilde{\chi}_i^{\pm}$ $(i = 1, 2)$ (charginos) and $\tilde{\chi}_j^0$ $(j = 1, 2, 3, 4)$ (neutralinos). In the benchmark model considered here, the compositions of the lightest chargino ($\tilde{\chi}_1^{\pm}$) and next-to-lightest neutralino ($\tilde{\chi}_2^0$) are wino-like and the two particles are nearly mass degenerate, whilst the lightest neutralino ($\tilde{\chi}_1^0$) is assumed to be bino-like.

Naturalness considerations [174, 175] suggest that the lightest of the charginos and neutralinos have masses near the electroweak scale. Their direct production may be the dominant one at the Large Hadron Collider (LHC) if the superpartners of the gluon and quarks are heavier than a few TeV. In SUSY models where the superpartners of the leptons have masses larger than those of the lightest chargino and next-to-lightest neutralino, the former might decay to the $\tilde{\chi}_1^0$ and a W boson ($\tilde{\chi}_1^{\pm} \to W\tilde{\chi}_1^0$), while the latter could decay to the $\tilde{\chi}_1^0$ and the lightest MSSM Higgs boson (h, SM-like) or Z boson ($\tilde{\chi}_2^0 \to h/Z\tilde{\chi}_1^0$) [242, 243, 76]. The decay via the Higgs boson is dominant when the mass splitting between the two lightest neutralinos is larger than the Higgs mass and the higgsinos are heavier than the winos. SUSY models of this kind, where sleptons are not too heavy although with masses above that of $\tilde{\chi}_1^{\pm}$ and $\tilde{\chi}_2^0$, could provide a possible explanation for the discrepancy between muon anomalous magnetic

2. For a general introduction to SUSY phenomenology, R-parity, and how SUSY particles could possibly be produced in pp collisions at the LHC, see chapter 3.

moment g-2 measurements and SM predictions [244, 245, 246, 247].

This chapter presents a search for the direct pair production of mass-degenerate charginos and next-to-lightest neutralinos assuming their prompt decays as $\tilde{\chi}_1^{\pm} \to W\tilde{\chi}_1^0$ and $\tilde{\chi}_2^0 \to h\tilde{\chi}_1^0$. The search targets a fully hadronic final state where $W \to q\bar{q}$ and $h \to b\bar{b}$, see fig. 9.1. Additional scenarios with the Higgs decaying to a pair of b-quarks, a pair of photons, a pair of W or Z bosons (where at least one of the $W/Z/\tau$ decays leptonically), or τ leptons are considered in a joint ATLAS paper [241]. Events are characterized by the presence of zero leptons ($\ell = e, \mu$), a large missing transverse momentum ($\vec{p}_{\mathrm{T}}^{\,\mathrm{miss}}$, with magnitude $E_{\mathrm{T}}^{\mathrm{miss}}$) from the neutralinos, and four jets (two originating from the fragmentation of the b-quarks). A simplified SUSY model [248, 249] is considered for the optimization of the search and the interpretation of results. The $\tilde{\chi}_1^{\pm} \to W\tilde{\chi}_1^0$ and $\tilde{\chi}_2^0 \to h\tilde{\chi}_1^0$ decays are assumed to have 100% branching ratio. The Higgs mass is set to 125 GeV, which is consistent with the measured value, and its branching fractions are assumed to be the same as in the SM. The Higgs (W) candidate can be fully reconstructed, by selecting the two leading b-tagged (non-b-tagged) jets. Previous searches for charginos and neutralinos at the LHC targeting decays through the Higgs in leptonic signatures have been reported by the ATLAS [250] and CMS [251] collaborations, whilst a search in the hadronic channel is reported for the first time in this thesis and in Ref. [241].

9.2 Dataset and MC Samples

The data used in this analysis were collected by the ATLAS detector in pp collisions at the LHC with a centre-of-mass energy of 13 TeV and a 25 ns proton bunch crossing interval during 2015 and 2016. The full dataset corresponds to an integrated luminosity of 36.1 fb^{-1} after requiring that all detector subsystems were operational during data recording. The uncertainty in the combined 2015+2016 integrated luminosity is 2.2%. It is derived following a

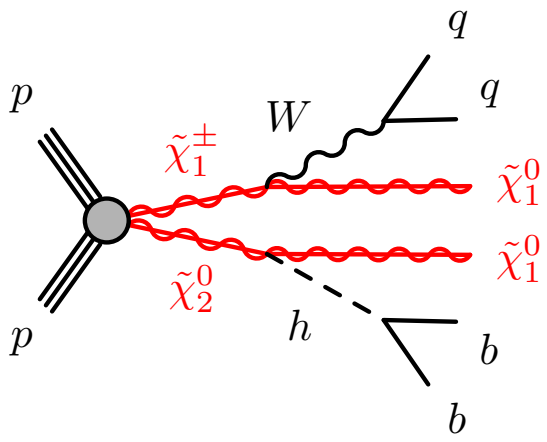

Figure 9.1: Diagram illustrating the simplified signal scenario considered in this chapter; pair production of the lighest chargino and the next-to-lightest neutralino, where the chargino decays into a W and an LSP, and the next-to-lighest neutralino decays into a Higgs boson and an LSP. The W and Higgs bosons then decay hadronically. The LSPs give rise to significant missing transverse momentum.

methodology similar to that detailed in Ref. [252] from a calibration of the luminosity scale using x–y beam-separation scans performed in August 2015 and May 2016. Each event includes on average 13.7 and 24.9 inelastic pp collisions (*pile-up*) in the same bunch crossing in the 2015 and 2016 datasets, respectively. Events are required to pass $E_{\mathrm{T}}^{\mathrm{miss}}$ triggers with period-dependent thresholds [253]. These triggers are fully efficient for events with offline reconstructed $E_{\mathrm{T}}^{\mathrm{miss}} > 200$ GeV.

Monte Carlo (MC) samples of simulated events are used to model the signal and to aid in the estimation of SM background processes, with the exception of multijet processes which are estimated from data only. All simulated samples were produced using the ATLAS simulation infrastructure [135] and GEANT4 [136], or a faster simulation based on a parameterization of the calorimeter response and GEANT4 for the other detector systems. The simulated events are reconstructed with the same algorithm as that used for data.

SUSY signal samples were generated with MadGraph5_aMC@NLO v2.3.3 [254] at leading order (LO) and interfaced to Pythia v8.212 [46] with the A14 [255] set of tuned parameters

(tune) for the modeling of the parton showering (PS), hadronization and underlying event. The matrix element (ME) calculation was performed at tree level and includes the emission of up to two additional partons. The ME–PS matching was done using the CKKW-L [256] prescription, with a matching scale set to one quarter of the chargino and next-to-lightest neutralino mass. The NNPDF23LO [257] parton distribution function (PDF) set was used. The cross-sections used to evaluate the signal yields are calculated to next-to-leading order (NLO) accuracy in the strong coupling constant, adding the resummation of soft gluon emission at next-to-leading-logarithmic accuracy (NLO+NLL) [204, 205, 206]. The nominal cross-section and uncertainty are taken as the midpoint and half-width of an envelope of cross-section predictions using different PDF sets and factorization and renormalization scales, as described in Ref. [258].

Background samples were simulated using different MC generator programs depending on the process. All background processes are normalized to the best available theoretical calculation for their respective cross-sections. The event generators, the accuracy of theoretical cross-sections, the underlying-event parameter tunes, and the PDF sets used for simulating the SM background processes are summarized in table 9.1. For all samples, except the ones generated using Sherpa [259], the EvtGen v1.2.0 [260] program was used to simulate the properties of the bottom- and charm-hadron decays. Several samples produced without detector simulation are employed to estimate systematic uncertainties associated with the specific configuration of the MC generators used for the nominal SM background samples. They include variations of the renormalization and factorization scales, the CKKW-L matching scale, as well as different PDF sets and fragmentation/hadronization models. Details of the MC modelling uncertainties are discussed in section 9.5.

Process	Generator + fragmentation/hadronization	Tune	PDF set	Cross-section order
W/Z + jets	Sherpa-2.2.0 [259]	Default	NNPDF3.0NNLO [257]	NNLO
$t\bar{t}$	Powheg-Box v2 [212, 211] + Pythia-6.428 [262]	PERUGIA2012 [261]	CT10 [213]	NNLO +NNLL
Single top	Powheg-Box v1 or v2 + Pythia-6.428	PERUGIA2012	CT10	NNLO +NNLL
Diboson WW, WZ, ZZ	Sherpa-2.2.1	Default	NNPDF3.0NNLO	NLO
$t\bar{t}+X$ $t\bar{t}W/Z$ 4 tops	MadGraph-2.2.2 [254] + Pythia-8.186 [46]	A14 [255]	NNPDF2.3	NLO
$t\bar{t}h$	MadGraph5_aMC@NLO-2.2.1 [263] + Herwig++-2.7.1	UEEE5 [264]	CT10	NLO
Wh, Zh	Pythia-8.186+EVTGEN [260]	A14	NNPDF2.3	LO

Table 9.1: List of generators used for the different processes. Information is given about the underlying-event tunes, the PDF sets and the pQCD highest-order accuracy (LO, NLO, next-to-next-to-leading order, NNLO, and next-to-next-to-leading-log, NNLL) used for the normalization of the different samples.

9.3 Event Reconstruction, Observables, and Selection

The standard ATLAS event and data quality selections listed in section 6.3 were applied. Kinematic variables, used to reject SM backgrounds, are described in section 9.3.1. Event preselections on the kinematic variables and data quality checks are described in section 9.3.2. Data/MC comparison plots at the preselection level are also shown in section 9.3.2.

Jets are reconstructed from three-dimensional topological energy clusters [265] in the calorimeter using the anti-k_t jet algorithm [147] with a radius parameter of 0.4. Each topological cluster is calibrated to the electromagnetic scale response prior to jet reconstruction. The reconstructed jets are then calibrated to the energy scale of stable final state particles[3] in the MC simulation by the application of a jet energy scale (JES) correction derived from $\sqrt{s} = 13\,\text{TeV}$ data and simulations [266]. Further selections are applied to reject jets within $|\eta| < 2.4$ that originate from pile-up interactions by means of a multivariate algorithm using information about the tracks matched to each jet [267, 266]. Candidate jets are required to have $p_{\text{T}} > 30$ GeV and $|\eta| < 2.8$.

A jet is tagged as a b-jet by means of a multivariate algorithm called MV2c10 using information about the impact parameters of inner detector tracks matched to the jet, the presence of displaced secondary vertices, and the reconstructed flight paths of b- and c-hadrons inside the jet [151, 152]. Jets tagged as b-jets must have $|\eta| < 2.5$. Several operating points are available, corresponding to various efficiencies obtained in $t\bar{t}$ simulated events. The 77% efficiency point was found to be optimal for most points in the phase space and is considered nominal for the results presented in this chapter. This configuration corresponds to a background rejection of 6 for c jets, 22 for τ leptons and 134 for light jets [151, 152], estimated using $t\bar{t}$ simulated events and assuming jets with $p_{\text{T}} = 20$ GeV.

3. Stable particles in the MC simulation event record are those that have a lifetime τ such that $c\tau > 10$ mm, and that originate from the hard-scatter interaction.

The $E_{\mathrm{T}}^{\mathrm{miss}}$ in the event is defined as the magnitude of the negative vector sum p_{T} of all selected and calibrated physics objects in the event, with an extra term added to account for soft energy in the event that is not associated to any of the selected objects. This soft term is calculated from inner detector tracks matched to the primary vertex to make it more resilient to pile-up contamination [268, 269].

Electron candidates are reconstructed from energy clusters in the electromagnetic calorimeter and inner detector tracks. They are required to pass the loose likelihood identification criteria and have B-layer hits (the so-called *loose* requirement) [270, 271]. These identification criteria simultaneously evaluate several properties of the electron candidates, including calorimeter-based shower shapes, inner detector track hits and impact parameters, and comparisons of calorimeter cluster energy to charged track p_{T}. Corrections for ambient energy contributions due to pile-up are included. Electrons are also required to have $p_{\mathrm{T}} > 20$ GeV and $|\eta| < 2.47$. These electrons are used in the overlap removal procedure that is described in detail below, and to apply lepton selections and vetoes in the various analysis channels, in some cases with additional selections applied.

Muon candidates are reconstructed from matching tracks in the inner detector and muon spectrometer. They are required to meet so-called *medium* quality and identification criteria, as described in Ref. [272], and to have $p_{\mathrm{T}} > 20$ GeV and $|\eta| < 2.5$. These muons are used in the overlap removal procedure and to apply lepton selections and vetoes in the various analysis channels, in some cases with additional selections applied. Events containing muons from calorimeter punch-through or poorly measured tracks are rejected if any muon has a large relative q/p error, or $\frac{\sigma(\frac{q}{p})}{|\frac{q}{p}|} > 0.2$, where q is the measure charge of the track. Cosmic ray muons are rejected after the muon-jet overlap removal by requiring the longitudinal and transverse impact parameters as $|z_0| \leq 1$ mm and $|d_0| \leq 0.2$ mm, respectively.

Overlaps between candidate objects are removed sequentially. Firstly, electron candidates

that lie within $\Delta R < 0.01$[4] from muon candidates are removed to suppress contributions from muon bremsstrahlung. Overlaps between electron and jet candidates are resolved next, and finally, overlaps between remaining jets and muon candidates are removed. Overlap removal between electron and jet candidates aims to remove jets that are formed primarily from the showering of a prompt electron and electrons that are produced in the decay chains of hadrons. Consequently, any non-b-tagged jet whose axis lies $\Delta R < 0.2$ from an electron is discarded. Electrons with $E_{\mathrm{T}} < 50$ GeV are discarded if lying within $\Delta R < 0.4$ to the axis of any remaining jet and the corresponding jet is kept. For higher-E_{T} electrons, the latter removal is performed using a threshold of $\Delta R = \min(0.4, 0.04 + 10 \text{ GeV}/p_{\mathrm{T}})$. The overlap removal procedure between muon and jet candidates is designed to remove those muons that are likely to have originated from the decay of hadrons and to retain the overlapping jet. Jets and muons may also appear in close proximity when the jet results from high-p_{T} muon bremsstrahlung, and in such cases the jet should be removed and the muon retained. Such jets are characterized by having very few matching inner detector tracks. Therefore, if the angular distance ΔR between a muon and a jet is lower than 0.2, the jet is removed if it is not b-tagged and has fewer than three matching inner detector tracks. As for the electrons, muons with p_{T} below (above) 50 GeV are subsequently discarded if they lie within $\Delta R = 0.4$ ($\Delta R = \min(0.4, 0.04 + 10 \text{ GeV}/p_{\mathrm{T}})$) of any remaining jet.

9.3.1 Event Variables

In order to target different signal mass hierarchies and reject SM backgrounds, signal regions (SRs) are defined based on optimized selections on the event variables defined below. The optimization procedure is described in section A.1.

4. $\Delta R = \sqrt{(\Delta y)^2 + (\Delta\phi)^2}$ defines the distance in rapidity y and azimuthal angle ϕ.

Object Multiplicity

Objects are ordered in descending order based on their p_{T}:

- N_{jet} is the number of jets with $|\eta| < 2.8$ and $p_{\mathrm{T}} > 30$ GeV.
- $N_{b-\mathrm{jet}}$ is the number of b-jets with $|\eta| < 2.5$ and $p_{\mathrm{T}} > 30$ GeV.
- N_{lepton} is the number of leptons (electrons or muons) with $|\eta| < 2.5$ and $p_{\mathrm{T}} > 20$ GeV. Leptons are used in some of the control regions, described in section 9.4.2.

Multijet Suppression

The minimum azimuthal angle $\Delta\phi^{4j}_{\mathrm{min}}$ between the $\vec{p}_{\mathrm{T}}^{\,\mathrm{miss}}$ and the $\vec{p}_{\mathrm{T}}$ of the four leading jets in the event is useful for rejecting events with mismeasured jet energies leading to $E_{\mathrm{T}}^{\mathrm{miss}}$ in the event, and is defined as:

$$\Delta\phi^{4j}_{\mathrm{min}} = \mathrm{min}_{i\leq 4}\Delta\phi\left(\vec{p}_{\mathrm{T}}^{\,\mathrm{miss}}, \vec{p}_{\mathrm{T,i}}^{\,\mathrm{jet}}\right). \tag{9.1}$$

This quantity typically has values close to zero for QCD processes due to jet mismeasurement or neutrinos emitted close to the jet axis. By requiring values $\Delta\phi^{4j}_{\mathrm{min}} > 0.4$ we suppress the multijet background, which can produce events with large $E_{\mathrm{T}}^{\mathrm{miss}}$ but small $\Delta\phi^{4j}_{\mathrm{min}}$.

Effective Mass

The effective mass, m_{eff}, is defined as the scalar sum of the p_{T} of jets, leptons and $E_{\text{T}}^{\text{miss}}$, which aids in establishing the mass scale of the processes being probed, and is defined as:

$$m_{\text{eff}} = \sum_{i}^{N_{\text{jet}}} p_{\text{T},i}^{\text{jet}} + \sum_{j}^{N_{\text{lepton}}} p_{\text{T},i}^{\ell} + E_{\text{T}}^{\text{miss}}. \tag{9.2}$$

where the first and second sums are over the selected jets (N_{jet}) and leptons (N_{lepton}), respectively. Since a lepton-veto is applied for all signal regions, the lepton term is only relevant for some of the control regions. It typically has a much higher value for the signal events than in background events.

Invariant Mass

- $m_{b\bar{b}}$ is the invariant mass of the two leading b-jets in the event, and serves as a selection criterion for dijet pairs to be considered as Higgs boson candidates.
- $m_{q\bar{q}}$ corresponds to the invariant mass of the two highest p_{T} jets in the event not identified as b-jets. This observable serves as a selection criterion for dijet pairs to be considered as W boson candidates.
- $m_{\ell\ell}$ is the invariant mass of the two leading same-flavor leptons (electrons or muons). Leptons are used in some of the control regions, described in section 9.4.2.

Contransverse mass

In order to further suppress $t\bar{t}$ background we utilize the contransverse mass variable, m_{CT} [273, 274], defined for the $b\bar{b}$ system as:

$$m_{\mathrm{CT}} = \sqrt{2p_{\mathrm{T}}^{b_1} p_{\mathrm{T}}^{b_2} (1 + \cos\Delta\phi_{bb})}, \tag{9.3}$$

where $p_{\mathrm{T}}^{b_1}$ and $p_{\mathrm{T}}^{b_2}$ are transverse momenta of the two leading b-jets and $\Delta\phi_{bb}$ is the azimuthal angle between them. It is one of the main discriminating variables in selections targeting Higgs bosons decaying into b-quarks and is effective in suppressing the top-quark pair production background. As is shown in Refs. [273, 274], the variable has a kinematic endpoint at $(m^2(\delta) - m^2(\alpha))/m^2(\delta)$, where δ is the pair produced heavy particle and a is the invisible particle produced in the decay. In the case of $t\bar{t}$ events, the kinematic endpoint corresponds to the top quark mass, while signal events tend to have higher values of m_{CT}.

Transverse b-jet Mass

Another useful transverse mass variable is m_{T}^{b}, the minimum transverse mass formed by $E_{\mathrm{T}}^{\mathrm{miss}}$ and up to two of the highest-p_{T} b-jets in the event, defined as:

$$m_{\mathrm{T}}^{b,\mathrm{min}} = \mathrm{min}_{i\leq 3}\left(\sqrt{2p_{\mathrm{T}}^{b\text{-jet}_i} E_{\mathrm{T}}^{\mathrm{miss}}\{1 - \cos[\Delta\phi(\vec{p}_{\mathrm{T}}^{\mathrm{miss}}, \vec{p}_{\mathrm{T}}^{b\text{-jet}_i})]\}}\right). \tag{9.4}$$

The variable has a kinematic endpoint near the top mass for $t\bar{t}$ backgrounds, while the value of m_{T}^{b} can be much larger in signal processes.

9.3.2 Event Preselection and Cleaning

The standard ATLAS event and data quality selections listed in section 6.3 were applied. Events are first selected online by missing transverse momentum triggers with an offline requirement of $E_{\mathrm{T}}^{\mathrm{miss}} > 200$ GeV. Specifically, `HLT_xe70` for 2015 data, and `HLT_xe100_mht_L1XE50` (`HLT_xe110_mht_L1XE50`) for early (late) 2016 data taking. The trigger remained unprescaled for all luminosity configurations in 2016. Additional preselections are applied based on the kinematic variables introduced in section 9.3.1, in order to further reject background, these are defined in section 9.3.2.

Loose and Tight Preselections

The *loose* and *tight* preselections listed in table 9.2 are applied to both data and MC samples in order to establish a baseline background rejection. The *loose* selection was used as a starting point when performing an optimization of the signal to background sensitivity, by cutting on the event variables defined in section 9.3.1. The optimization procedure is described in section A.1. The *tight* preselection is common to most of the signal-, control-, and validation-regions described in section 9.4, except for a few control regions where the zero lepton requirement is relaxed. Comparisons of data to SM predictions for the event variables defined in section 9.3.1 are shown with the *loose* and *tight* preselections fig. 9.2 and figs. 9.3 and 9.4. The uncertainty bands include statistical and systematic uncertainties described in section 9.5. As can be seen in these figures, the data is found to agree quite well with the prediction from the background MC. The distributions of two representative signal mass points are also shown. At the *tight* preselection level, the signal yields are still orders of magnitude smaller than the total background, thus a more refined selection is required in order to be sensitive to this benchmark SUSY signal model. The background estimation strategy s presented in section 9.4.

Variable	Loose	Tight
N_{lepton}	$= 0$	$= 0$
N_{jet} ($p_{\text{T}} > 30$ GeV)	≥ 4	$\in [4,\ 5]$
$N_{b-\text{jet}}$	–	$= 2$
$\Delta\phi^{4j}_{\text{min}}$	> 0.4	> 0.4
$E_{\text{T}}^{\text{miss}}$ [GeV]	> 200	> 200
m_{eff} [GeV]	> 700	> 700

Table 9.2: Definitions of the *loose*- and *tight* preselections.

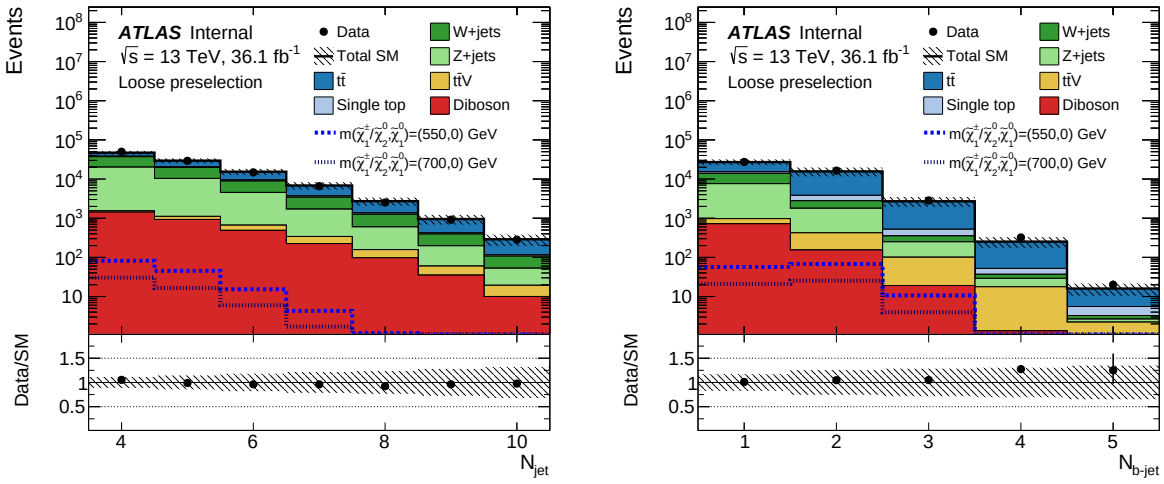

(a) N_{jet} (b) $N_{b-\text{jet}}$

Figure 9.2: Comparisons of data to SM predictions for (a) N_{jet} and (b) $N_{b-\text{jet}}$ after applying the *loose* preselection in table 9.2. The uncertainty bands include statistical and systematic uncertainties (see section 9.5).

9.4 Background Estimation Strategy

The dominant SM background processes and the event selection criteria designed to suppress these backgrounds (and enhance the benchmark signal models) are described in this section. The expected signal discovery reach is optimized in dedicated Signal Regions (SRs), targeting different mass hierarchies of the particles involved. The event selection is performed on the

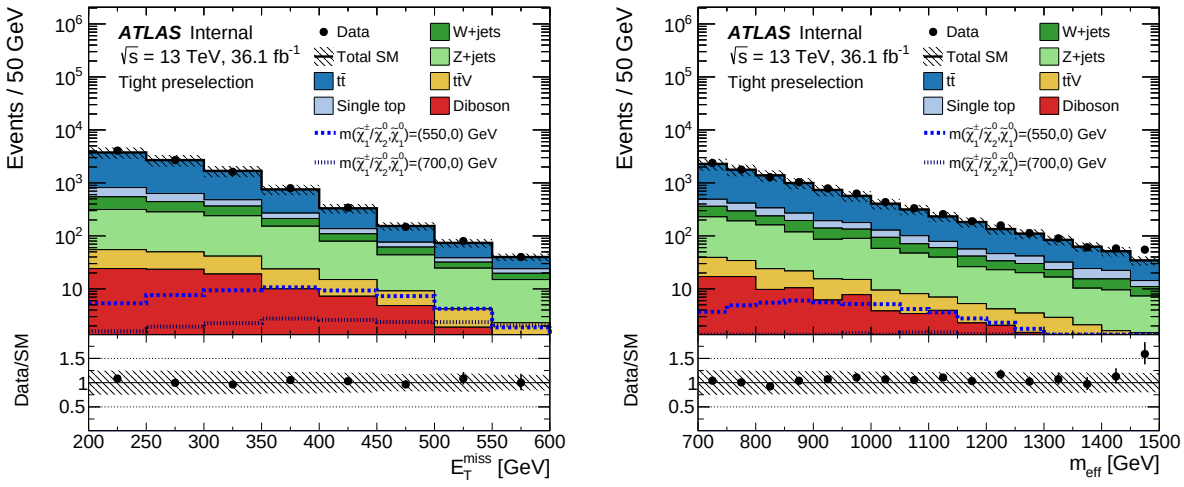

(a) $E_{\mathrm{T}}^{\mathrm{miss}}$ (b) m_{eff}

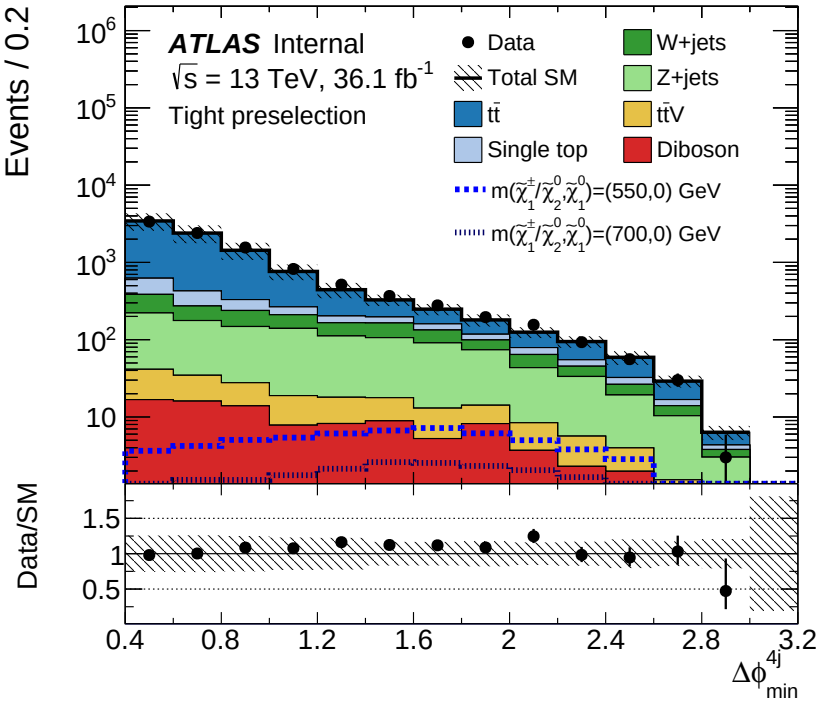

(c) $\Delta\phi_{\mathrm{min}}^{4j}$

Figure 9.3: Comparisons of data to SM predictions for (a) $E_{\mathrm{T}}^{\mathrm{miss}}$, (b) m_{eff}, (a), and (c) $\Delta\phi_{\mathrm{min}}^{4j}$ after applying the *tight* preselection in table 9.2. The uncertainty bands include statistical and systematic uncertainties (see section 9.5).

basis of the event variables defined in section 9.3.1.

The expected SM backgrounds are determined separately for each SR, with a profile likeli-

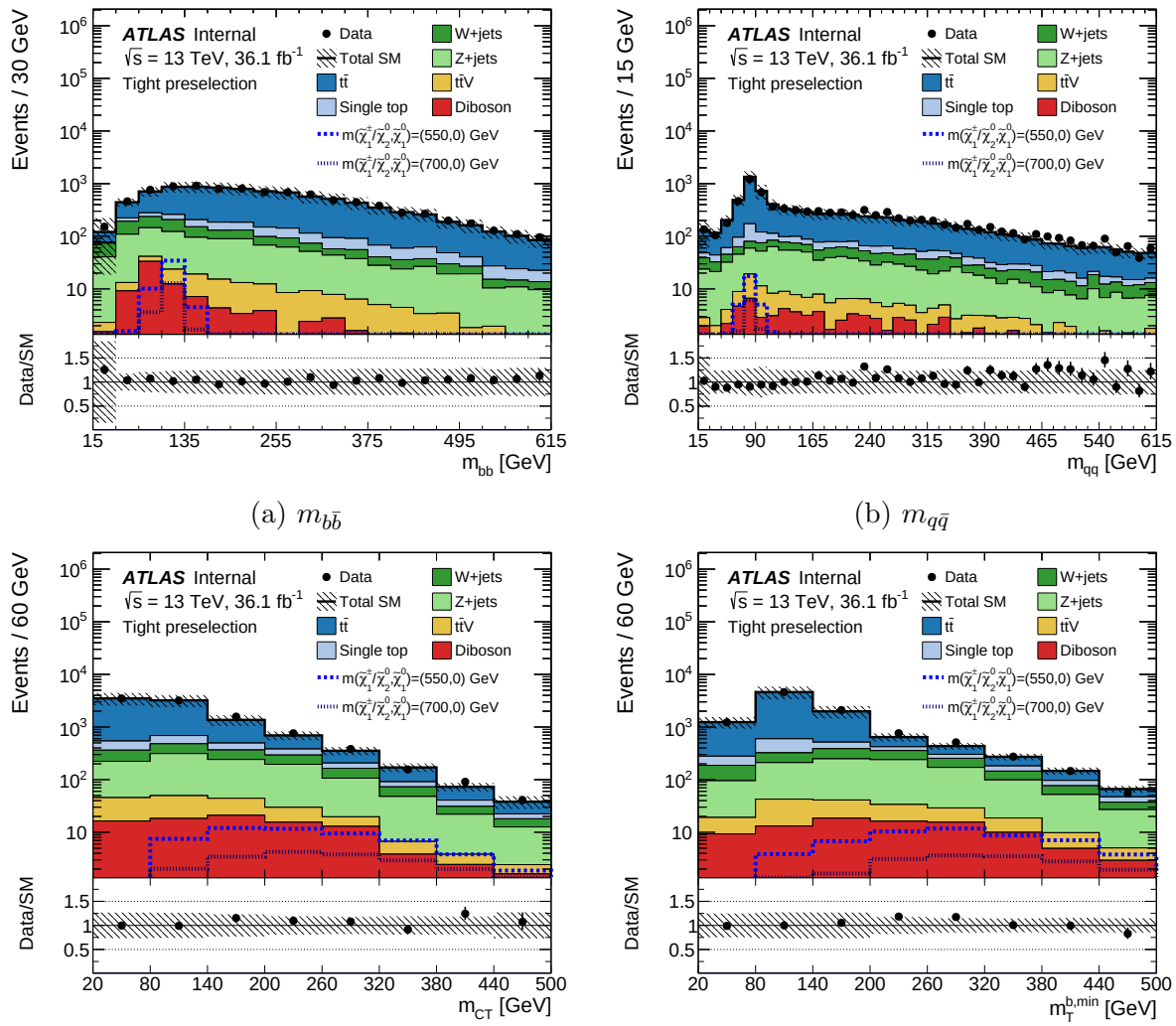

(a) $m_{b\bar{b}}$ (b) $m_{q\bar{q}}$

(c) m_{CT} (d) m_{T}^{b}

Figure 9.4: Comparisons of data to SM predictions for (a) $m_{b\bar{b}}$, (b) $m_{q\bar{q}}$, (c) m_{CT}, and (d) m_{T}^{b} after applying the *tight* preselection in table 9.2. The uncertainty bands include statistical and systematic uncertainties (see section 9.5).

hood fit [239], referred to as a *background-only fit* in the relevant CRs. The background-only fit uses the observed event yield in the associated CRs as a constraint to adjust the normalization of the dominant background processes assuming that no signal is present. CRs are designed to be enriched in specific background contributions relevant to the analysis, whilst minimising the signal contamination, and they are orthogonal to the SRs. The inputs to the background-only fit for each SR include the number of events observed in its associated CR

and the number of events predicted by simulation in each region for all background processes. They are both described by Poisson statistics. The systematic uncertainties, described in Section 9.5, are included in the fit as nuisance parameters. They are constrained by Gaussian distributions with widths corresponding to the sizes of the uncertainties and are treated as correlated, when appropriate, between the various regions. The product of the various probability density functions forms the likelihood, which the fit maximizes by adjusting the background normalization and the nuisance parameters. Finally, the reliability of the MC extrapolation of the SM background estimates outside of the control regions is evaluated in validation regions orthogonal to CRs and SRs.

The event selection, dominant backgrounds, and expected sensitivity in the SRs is presented in section 9.4.1. Background control and validation regions are defined insection 9.4.2.

9.4.1 Signal Region Event Selection

Signal regions are defined based on a multivariate optimization procedure by scanning over several of the kinematic variables defined in section 9.3.1. This optimization procedure is described in section A.1. The analysis exploits the large branching ratios for both $W \to q\bar{q}$ and $h \to b\bar{b}$ into hadronic final states. Stringent event selections based on the masses of both the W and Higgs bosons, the presence of exactly two b-jets, and the kinematic relationships of the final state jets and $E_{\mathrm{T}}^{\mathrm{miss}}$, are required in order to reduce the significant backgrounds from $t\bar{t}$, $Z+$jets, and single-top Wt production. Events are characterized by having 4 or 5 jets with $p_{\mathrm{T}} > 30$ GeV, exactly 2 of which are identified as b-jets, large m_{eff}, m_{CT}, and $m_{\mathrm{T}}^{b,\mathrm{min}}$. Two signal regions are defined, specifically targeting either high (HM) or low (LM) $\tilde{\chi}_2^0$ and $\tilde{\chi}_1^{\pm}$ masses (SRHad-High and SRHad-Low, respectively). The *tight* preselection defined in section 9.3.2 is common for both signal regions. The exact selections used are shown in table 9.3. The individual signal regions are not required to be orthogonal from one

another, but rather to provide a set of options from which to select the optimal set of selection for a given signal definition (based on whichever one has the best observed sensitivity, see fig. 9.15).

Variable	SRHad-High	SRHad-Low
N_{lepton}	$= 0$	$= 0$
N_{jet} ($p_{\text{T}} > 30$ GeV)	$\in [4,\ 5]$	$\in [4,\ 5]$
$N_{b-\text{jet}}$	$= 2$	$= 2$
$\Delta\phi^{4j}_{\text{min}}$	> 0.4	> 0.4
$E^{\text{miss}}_{\text{T}}$ [GeV]	> 250	> 200
m_{eff} [GeV]	> 900	> 700
$m_{b\bar{b}}$ [GeV]	$\in [105,\ 135]$	$\in [105,\ 135]$
$m_{q\bar{q}}$ [GeV]	$\in [75,\ 90]$	$\in [75,\ 90]$
m_{CT} [GeV]	> 140	> 190
$m^{b,\text{min}}_{\text{T}}$ [GeV]	> 160	> 180

Table 9.3: Signal region definitions.

The m_{eff} and $m^{b,\text{min}}_{\text{T}}$ selections are particularly effective at reducing the $t\bar{t}$ contributions, which is the dominant background for both signal regions. $Z+$jets and single top both contribute significantly as well, whereas the contribution from multijet production is found to be negligible. Figure 9.5 shows the background composition in both signal regions. The cause of the $t\bar{t}$ contribution increase in the low mass splitting signal region is a combination of the cuts differences, in particular applying a lower cut in m_{eff} increases this background. The background composition of single-top is mainly from Wt production with tau final states. The analysis is agnostic to jets induced by hadronic tau or quark/gluon decays. The background composition of $Z+$jets is mainly from neutrino decays. The $b\bar{b}$ invariant mass is required to be between $105 < m_{b\bar{b}} < 135$ GeV, consistent with the Higgs mass, for all

signal regions. All CRs and VRs select sidebands in the $m_{b\bar{b}}$ spectrum in order to remain orthogonal to the two SRs. These are further described in section 9.4.2.

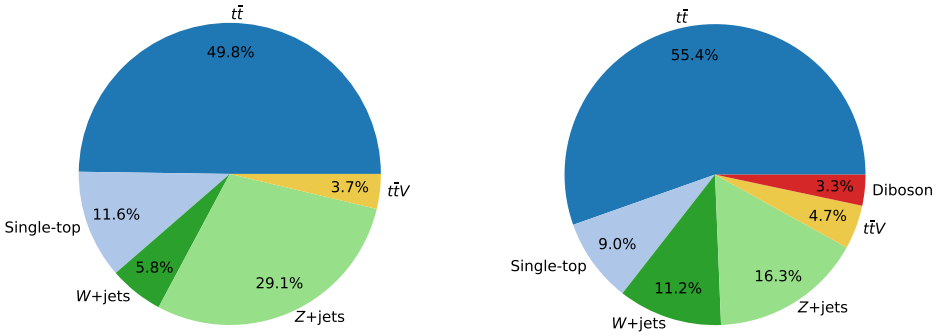

(a) (b)

Figure 9.5: Background composition in (a) SRHad-High and (b) SRHad-Low (based on pre-fit yields).

9.4.2 Background Control- and Validation Regions

Control regions are used to constrain the normalizations of the $t\bar{t}$, $Z+$jets, and Wt backgrounds with the data, while other processes are estimated using MC simulation studies. The background contributions to SRHad-High and SRHad-Low are estimated using fits to the data for $t\bar{t}$, $Z+$jets, and single-top in specially designed control regions. The three control regions used for estimating the $t\bar{t}$ (CRHad-TT), $Z+$jets (CRHad-Zj), and Wt (CRHad-ST) contributions are further divided into high-mass (HM) and low-mass (LM) categories in order to follow the design of the SRs. All CRs are required to be orthogonal from their respective signal regions. The control regions are defined primarily by inverting the selections on $m_{b\bar{b}}$, m_{CT}, $m_{\mathrm{T}}^{b,\mathrm{min}}$, and by requiring the presence of a lepton in some cases.

$t\bar{t}$ Control Regions

The $t\bar{t}$ background is estimated using $m_{\mathrm{CT}}, m_{\mathrm{T}}^{b,\mathrm{min}} < 140$ GeV and $m_{b\bar{b}} > 135$ GeV selections, while maintaining the other SR requirements. This approach isolates the $t\bar{t}$ contribution while suppressing single-top and $Z+$jets events, yielding an estimated 94% pure sample of $t\bar{t}$ events with negligible signal contamination. Figure 9.6 shows the distributions of two key observables, $E_{\mathrm{T}}^{\mathrm{miss}}$ for the $t\bar{t}$ high-mass control region, and m_{CT} for the $t\bar{t}$ low-mass control region. The inverted m_{CT} selection is critical for defining a pure $t\bar{t}$ control region, which is clear from Figure 9.6b.

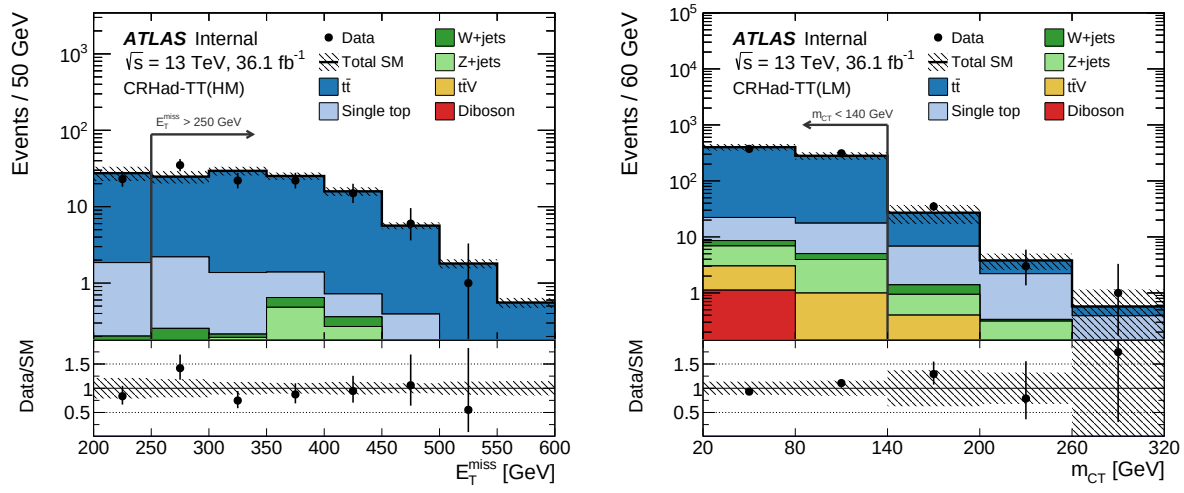

(a) (b)

Figure 9.6: Comparisons of data to SM prediction in $t\bar{t}$ control regions for representative kinematic distributions: (a) $E_{\mathrm{T}}^{\mathrm{miss}}$ for CRtt-Had(HM) and (b) m_{CT} for CRtt-Had(LM). Predictions from MC simulation are shown after the background-only fit. The arrow indicates the selection on that variable used to define the corresponding CRs. The uncertainty bands include statistical and systematic uncertainties.

Single-Top Control Regions

The dominant single-top contribution in the signal regions comes from Wt production with semi-leptonic decays into hadronic tau final states. Background events from Wt are estimated

by requiring exactly one lepton and $m_{\mathrm{CT}} > 200$ GeV, $m_{\mathrm{T}}^{b,\mathrm{min}} > 180$ GeV, and $m_{b\bar{b}} > 195$ GeV, while also relaxing the m_{eff} requirement for HM to $m_{\mathrm{eff}} > 700$ GeV. Figure 9.6 shows the m_{CT} and $m_{b\bar{b}}$ distributions in for the high- and low-mass single-top control regions, respectively. The $m_{b\bar{b}} > 195$ GeV selection is particularly effective, see fig. 9.7b.

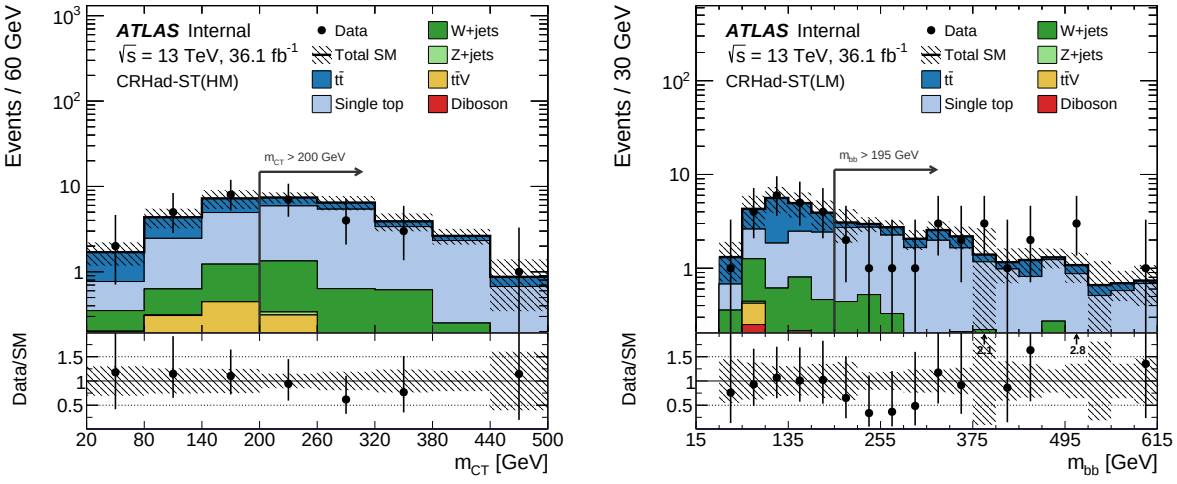

(a) (b)

Figure 9.7: Comparisons of data to SM prediction in single-top control regions for representative kinematic distributions: (a) m_{CT} for CRst-Had(HM) and (b) $m_{b\bar{b}}$ for CRst-Had(LM). Predictions from MC simulation are shown after the background-only fit. The arrow indicates the selection on that variable used to define the corresponding CRs. The uncertainty bands include statistical and systematic uncertainties.

$Z+$jets Control Regions

The dominant $Z+$jets decay in the signal regions is $Z(\nu\nu)+$jets. The $Z+$jets contribution is isolated using a same-sign, same-flavor ($e^{\pm}e^{\pm}$ or $\mu^{\pm}\mu^{\pm}$) high-p_{T} 2ℓ requirement with $p_{\mathrm{T},1}^{\ell} > 140$ GeV and $|m_{\ell\ell} - 90| < 15$ GeV, which reduces the $t\bar{t}$ contribution to this control region (see fig. 9.8). These leptons are then treated as invisible when calculating the $E_{\mathrm{T}}^{\mathrm{miss}}$. The kinematics of the matrix element that defines the $Z+$jets process can be studied independently of the decay channel of the Z boson, thus it is possible to study the modelling of events where the Z decays to two charged leptons as leptons are typically well-reconstructed

objects. In these events the leptons four momenta are added to the $E_{\mathrm{T}}^{\mathrm{miss}}$ in order to mimic the topology of the SRs, in which the Z boson decays to neutrinos, e.g. $E_{T,\mathrm{CRZ}}^{\mathrm{miss}} = E_{\mathrm{T}}^{\mathrm{miss}} + p_{\mathrm{T}}^{ll}$ (where Z is constructed from the 4-vectors of either 2 signal muons or 2 signal electrons). Figure 9.8 also shows the $m_{b\bar{b}}$ distribution for the low-mass $Z+$jets control region.

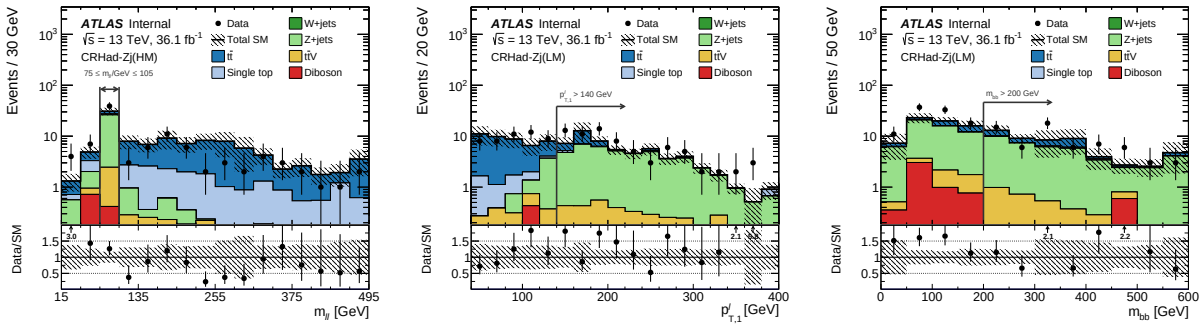

(a) (b) (c)

Figure 9.8: Comparisons of data to SM prediction in $Z+$jets control regions for representative kinematic distributions: (a) $m_{\ell\ell}$ for CRZj-Had(HM), (b) $p_{\mathrm{T},1}^{\ell}$ for CRZj-Had(LM), and (c) $p_{\mathrm{T},1}^{\ell}$ for CRZj-Had(LM). Predictions from MC simulation are shown after the background-only fit. The arrow indicates the selection on that variable used to define the corresponding CRs. The uncertainty bands include statistical and systematic uncertainties.

Validation Regions

To validate the background prediction, three sets of validation regions are defined to be similar, but orthogonal, to the SRs. The $t\bar{t}$ VRs for each SR (VRHad-TT, for HM or LM) reverse the m_{CT} selections, requiring $m_{\mathrm{CT}} < 140$ (190) GeV for HM (LM), selects the sideband $m_{b\bar{b}} > 135$ GeV (orthogonal to the SRs), but retain the SR selection on $m_{\mathrm{T}}^{b,\mathrm{min}}$. In order to validate the Wt and $Z+$jets estimates, VRs are defined using sideband regions in the $m_{b\bar{b}}$ and $m_{q\bar{q}}$ spectra, either by vetoing the SR range in both of these variables, $m_{b\bar{b}} \notin [105,\ 135]$ GeV and $m_{q\bar{q}} \notin [75,\ 90]$ GeV (VRHad-SB for HM and LM), or by selecting the $m_{b\bar{b}} > 135$ GeV sideband along with a W mass requirement on the non-b-tagged dijet invariant mass, $75 < m_{q\bar{q}} < 90$ GeV (VRHad-bbhigh, for HM or LM). Figure 9.9 show the

m_{T}^{b} and $m_{q\bar{q}}$ distributions in the $m_{b\bar{b}}$- and $m_{q\bar{q}}$-sideband validation regions.

An exhaustive list of the signal-, control-, and validation-region definitions can be found in table 9.4.

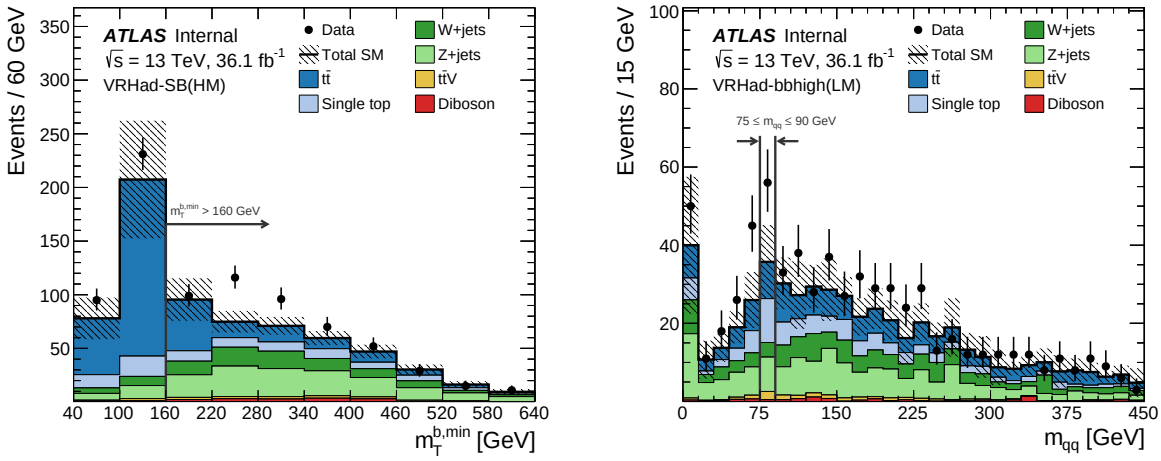

(a) (b)

Figure 9.9: Comparison of data to SM prediction in m_{T}^{b}- and $m_{q\bar{q}}$-sideband validation regions: (a) m_{T}^{b} in VRSB-Had(HM) and (a) $m_{q\bar{q}}$ in VRbbhigh-Had(LM).

Background-Only Fit

The yields estimated with the background-only fit are reported in table 9.5. The normalization factors (see bottom part of fig. 9.10) are found to be 0.88 ± 0.10 (0.85 ± 0.04), 1.47 ± 0.32 (1.22 ± 0.35), and 0.54 ± 0.25 (0.57 ± 0.22) for $t\bar{t}$, $Z+\text{jets}$, and Wt in the high-mass (low-mass) signal region, respectively. The errors include statistical and systematic uncertainties. No simulated diboson events are found to contribute to the CRHad-ST regions.

The number of events predicted by the background-only fit is compared to the data in the VRs in the upper panel of fig. 9.11. The pull, defined by the difference between the observed number of events (n_{obs}) and the predicted background yield (n_{pred}) divided by the total uncertainty (σ_{tot}), is shown for each region in the lower panel. No evidence of significant

	SRHad-High	CRHad-TT(HM)	CRHad-ST(HM)	CRHad-Zj(HM)	VRHad-TT(HM)	VRHad-SB(HM)	VRHad-bbhigh(HM)
N_{lepton}	$= 0$	$= 0$	$= 1$	$= 2$ (same flavour)	$= 0$	$= 0$	$= 0$
$p_{\text{T}}(l1, l2)$ [GeV]	–	–	$(> 20, -)$	$(> 140, > 20)$	–	–	–
m_Z [GeV]	–	–	–	$\in [75, 105]$	–	–	–
N_{jet}	$\in [4, 5]$	$\in [4, 5]$	$\in [4, 5]$	$\in [4, 5]$	$\in [4, 5]$	$\in [4, 5]$	$\in [4, 5]$
$N_{b-\text{jet}}$	$= 2$	$= 2$	$= 2$	$= 2$	$= 2$	$= 2$	$= 2$
$\Delta\phi^{4j}_{\text{min}}$	> 0.4	> 0.4	> 0.4	> 0.4	> 0.4	> 0.4	> 0.4
$E_{\text{T}}^{\text{miss}}$ [GeV]	> 250	> 250	> 250	> 250	> 250	> 250	> 250
m_{eff} [GeV]	> 900	> 900	> 700	> 900	> 900	> 900	> 900
$m_{b\bar{b}}$ [GeV]	$\in [105, 135]$	> 135	> 195	> 200	> 135	$\notin [105, 135]$	> 135
$m_{q\bar{q}}$ [GeV]	$\in [75, 90]$	$\in [75, 90]$	$\in [75, 90]$	–	$\in [75, 90]$	$\notin [75, 90]$	$\in [75, 90]$
m_{CT} [GeV]	> 140	< 140	> 200	–	< 140	> 140	> 140
$m_{\text{T}}^{b,\text{min}}$ [GeV]	> 160	< 140	> 180	–	> 160	> 160	> 160
	SRHad-Low	CRHad-TT(LM)	CRHad-ST(LM)	CRHad-Zj(LM)	VRHad-TT(LM)	VRHad-SB(LM)	VRHad-bbhigh(LM)
N_{lepton}	$= 0$	$= 0$	$= 1$	$= 2$ (same flavour)	$= 0$	$= 0$	$= 0$
$p_{\text{T}}(l1, l2)$ [GeV]	–	–	$(> 20, -)$	$(> 140, > 20)$	–	–	–
m_Z [GeV]	–	–	–	$\in [75, 105]$	–	–	–
N_{jet}	$\in [4, 5]$	$\in [4, 5]$	$\in [4, 5]$	$\in [4, 5]$	$\in [4, 5]$	$\in [4, 5]$	$\in [4, 5]$
$N_{b-\text{jet}}$	$= 2$	$= 2$	$= 2$	$= 2$	$= 2$	$= 2$	$= 2$
$\Delta\phi^{4j}_{\text{min}}$	> 0.4	> 0.4	> 0.4	> 0.4	> 0.4	> 0.4	> 0.4
$E_{\text{T}}^{\text{miss}}$ [GeV]	> 200	> 200	> 200	> 200	> 200	> 200	> 200
m_{eff} [GeV]	> 700	> 700	> 700	> 700	> 700	> 700	> 700
$m_{b\bar{b}}$ [GeV]	$\in [105, 135]$	> 135	> 195	> 200	> 135	$\notin [105, 135]$	> 135
$m_{q\bar{q}}$ [GeV]	$\in [75, 90]$	$\in [75, 90]$	$\in [75, 90]$	–	$\in [75, 90]$	$\notin [75, 90]$	$\in [75, 90]$
m_{CT} [GeV]	> 190	< 140	> 200	–	< 190	> 190	> 190
$m_{\text{T}}^{b,\text{min}}$ [GeV]	> 180	< 140	> 180	–	> 180	> 180	> 180

Table 9.4: Selection requirements for the signal, control, and validation regions.

background mismodelling is observed in the VRs.

9.5 Systematic Uncertainties

Several sources of experimental and theoretical systematic uncertainties in the signal and background estimates are considered in this analysis. Their impact is reduced through the normalization of the dominant backgrounds in the control regions defined with kinematic selections resembling those of the corresponding signal region (see table 9.4).

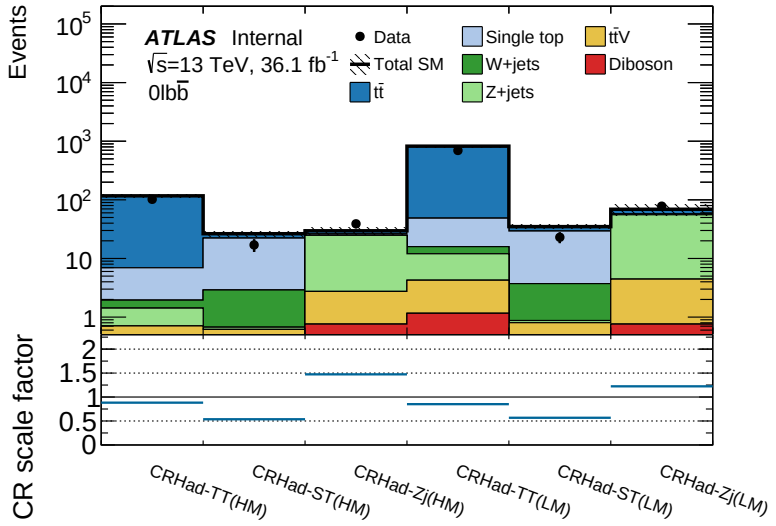

Figure 9.10: Comparison of the predicted backgrounds with the observed numbers of events in the CRs. The upper panel shows the observed number of events and the predicted background yield, *before* the fit to the CRs. All uncertainties defined in Section section 9.5 are included in the uncertainty band. The lower panel shows the scale factors obtained from the fit in each of the CRs.

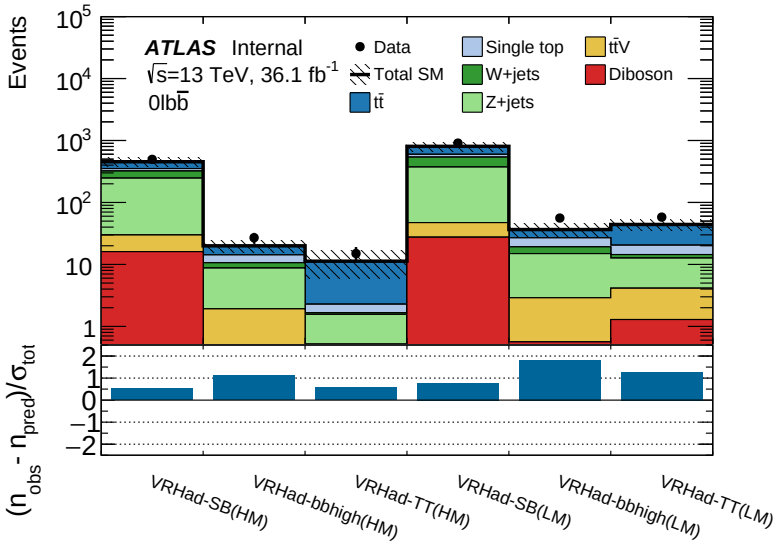

Figure 9.11: Comparison of the predicted backgrounds with the observed numbers of events in the VRs. The normalization of the backgrounds is obtained from the fit to the CRs. The upper panel shows the observed number of events and the predicted background yield. All uncertainties defined in Section section 9.5 are included in the uncertainty band. The lower panel shows the pulls in each VR.

CR channels	CRHad-TT(HM)	CRHad-ST(HM)	CRHad-Zj(HM)	CRHad-TT(LM)	CRHad-ST(LM)	CRHad-Zj(LM)
Observed events	102	17	39	695	23	78
Fitted bkg events	102 ± 10	17 ± 4	39 ± 6	695 ± 26	23 ± 5	78 ± 9
$t\bar{t}$	97 ± 11	3.7 ± 2.0	2.9 ± 2.4	659 ± 34	4.7 ± 2.3	10^{+12}_{-10}
Single top	$2.7^{+3.5}_{-2.7}$	10 ± 5	$0.8^{+0.9}_{-0.8}$	19 ± 19	15 ± 6	1.0 ± 0.9
$W+$jets	$0.5^{+0.6}_{-0.5}$	2.2 ± 1.1	0.0059 ± 0.0025	3.9 ± 3.1	2.8 ± 1.2	0.0059 ± 0.0026
$Z+$jets	1.1 ± 0.6	0.08 ± 0.07	32 ± 7	9.5 ± 3.2	0.09 ± 0.04	63 ± 17
$t\bar{t}V$	0.63 ± 0.14	0.62 ± 0.16	2.0 ± 0.4	3.1 ± 0.5	0.80 ± 0.17	3.7 ± 0.6
Diboson	$0.08^{+0.14}_{-0.08}$	–	0.8 ± 0.8	1.16 ± 0.34	–	0.8 ± 0.5

Table 9.5: Fit results in the control regions. The results are obtained from the control regions using the background-only fit. The errors shown are the statistical plus systematic uncertainties. Uncertainties on the fitted yields are symmetric by construction, where the negative error is truncated when reaching to zero event yield.

Following the procedure described in section 7.2, experimental and theoretical uncertainties are included as nuisance parameters with Gaussian constraints in the likelihood fits, taking into account correlations between different regions. Uncertainties due to the numbers of events in the CRs are also introduced in the fit for each region.

Theory uncertainties on the $t\bar{t}$ background processes dominate, up 50% in SRHad-Low region. Generator uncertainties are assessed by comparing Powheg+Pythia 6 to Sherpa 2.2.1, and the parton shower models are tested using Powheg+Pythia 6 compared to Powheg+Herwig++. Scale variations are evaluated by varying the h_{damp} parameter between m_{top} and $2 \times m_{\text{top}}$, and the renormalization and factorization scales up and down by a factor of two. Systematic uncertainties on the contributions from single top production also account for the impact of interference terms between single-resonant and double-resonant top production. Statistical uncertainties are included via the control regions in the data by which the processes are normalized and the finite MC simulation statistics available for evaluating some theoretical systematic uncertainties. Relaxed selections are used in order to improve the statistical precision of uncertainty estimates due to theory systematics on top contri-

butions. In particular, the m_{CT}, m_{T}^{b}, and m_{eff} selections are loosened for both SRs. The $Z+$jets and $W+$jets modelling uncertainties are estimated using the nominal SHERPA 2.2.1 samples by considering different merging (CKKW-L) and resummation scales, PDF variations from the NNPDF30NNLO replicas, as well as an envelope formed from seven-point scale variations of the renormalization and factorization scales. The various components are included as separate nuisance parameters in the likelihood fits.

Experimental uncertainties related to the jet energy scale play a significant role, uncertainties related to the jet energy scale contribute to approximately a 30% systematic uncertainty in the SRHad-High region. Uncertainties on the b-tagging efficiency and mis-tagging rates are sub-dominant for both regions, and are estimated by varying the η-, p_{T}- and flavour-dependent scale factors applied to each jet in the simulation within a range that reflects the systematic uncertainty in the measured tagging efficiency and mis-tag rates.

The dominant systematic uncertainties in both signal regions are summarized in table 9.6.

Uncertainty of region	SRHad-High	SRHad-Low
Total background expectation	2.49	7.76
Total background error	±1.28	±4.14
Systematic, experimental	±0.88	±1.17
Systematic, theoretical	±0.69	±3.82
Statistical, MC samples	±0.54	±0.84
Statistical, $\mu_{\mathrm{TT,ST,Zj}}$ scale-factors	±0.25	±0.52

Table 9.6: Dominant systematic uncertainties on background estimates in the signal regions. Individual uncertainties can be correlated, and do not necessarily add up quadratically to the total background uncertainty. The percentages show the size of the uncertainty relative to the total expected background.

9.6 Results

No significant deviations are observed between expected and observed yields in the search regions for each of the analysis channels considered. The results are also translated into upper limits on contributions from physics beyond the SM (BSM) for each signal region and are used to set exclusion limits at the 95% confidence level (CL) on the common mass of the charginos and next-to-lightest neutralinos for various values of the LSP mass in the simplified model considered in the analysis.

Table 9.7 provides the event yields and SM expectation in the SRHad-High and SRHad-Low signal regions after the background-only fit. The errors shown are the statistical plus systematic uncertainties. Good agreement is found between data and SM predictions for both signal regions.

SR channels	SRHad-High	SRHad-Low
Observed events	1	7
Fitted bkg events	2.5 ± 1.3	7.8 ± 4.1
$t\bar{t}$	1.1 ± 0.9	4.0 ± 3.9
Single top (Wt)	$0.2^{+0.2}_{-0.2}$	0.4 ± 0.3
$W+$jets	$0.1^{+0.3}_{-0.1}$	1.0 ± 0.7
$Z+$jets	1.0 ± 0.7	1.7 ± 1.0
$t\bar{t}V$	0.09 ± 0.03	0.4 ± 0.1
Diboson	–	$0.3^{+0.4}_{-0.3}$

Table 9.7: Event yields and SM expectation after background-only fit results for the SRHad-High and SRHad-Low regions. The errors shown are the statistical plus systematic uncertainties. Uncertainties on the fitted yields are symmetric by construction, where the negative error is truncated when reaching to zero event yield.

Table 9.8 summarizes the observed (S^{95}_{obs}) and expected (S^{95}_{exp}) 95% CL upper limits on

the number of BSM events and on the observed visible cross section, σ_{vis}, for both signal regions. Upper limits on contributions from new physics are estimated using the so-called model-independent fits. The CL_s method [275, 276] (see section 7.2) is used to derive the confidence level of the exclusion for a particular signal model; signal models with a CL_s value below 0.05 are said to be excluded at 95% CL. When normalized by the integrated luminosity of the data sample, results can be interpreted as corresponding observed upper limits on σ_{vis}, defined as the product of the BSM production cross section, the acceptance and the selection efficiency of a BSM signal. The p_0-values, which represent the probability of the SM background alone to fluctuate to the observed number of events or higher, are also provided.

Region	σ_{vis} [fb]	S^{95}_{obs}	S^{95}_{exp}	p_0-value
SRHad-Low	0.26	9.4	$9.5^{+3.3}_{-1.9}$	0.50
SRHad-High	0.10	3.6	$4.3^{+1.6}_{-1.0}$	0.50

Table 9.8: From left to right, the observed 95% CL upper limits on the visible cross sections σ_{vis}, the observed (S^{95}_{obs}) and expected (S^{95}_{exp}) 95% CL upper limits on the number of signal events with $\pm 1\sigma$ excursions of the expectation, and the discovery p-value (p_0), truncated at 0.5.

Figure 9.12 shows representative distributions of the data and SM predictions binned in $E_{\text{T}}^{\text{miss}}$, m_{eff}, m_{CT}, and $m_{b\bar{b}}$ in the SRs. The data agree well with the SM expectations in all distributions within the uncertainty bands, and no significant deviations are observed. The number of events predicted by the background-only fit is compared to the data in the SRs in the upper panel of fig. 9.13, the agreement is well within the estimated uncertainty bands, with a slight deficit observed in both SRHad-High and SRHad-Low.

fig. 9.14 shows the expected and observed exclusion for each of the signal regions separately, as well as a combination where either SRHad-High or SRHad-Low is used for each $\tilde{\chi}_1^{\pm}/\tilde{\chi}_2^0 - \tilde{\chi}_1^0$ mass hypothesis, depending on which one has the best expected sensitivity (see fig. 9.15). Experimental and theoretical systematic uncertainties, as described in section 9.5, are applied

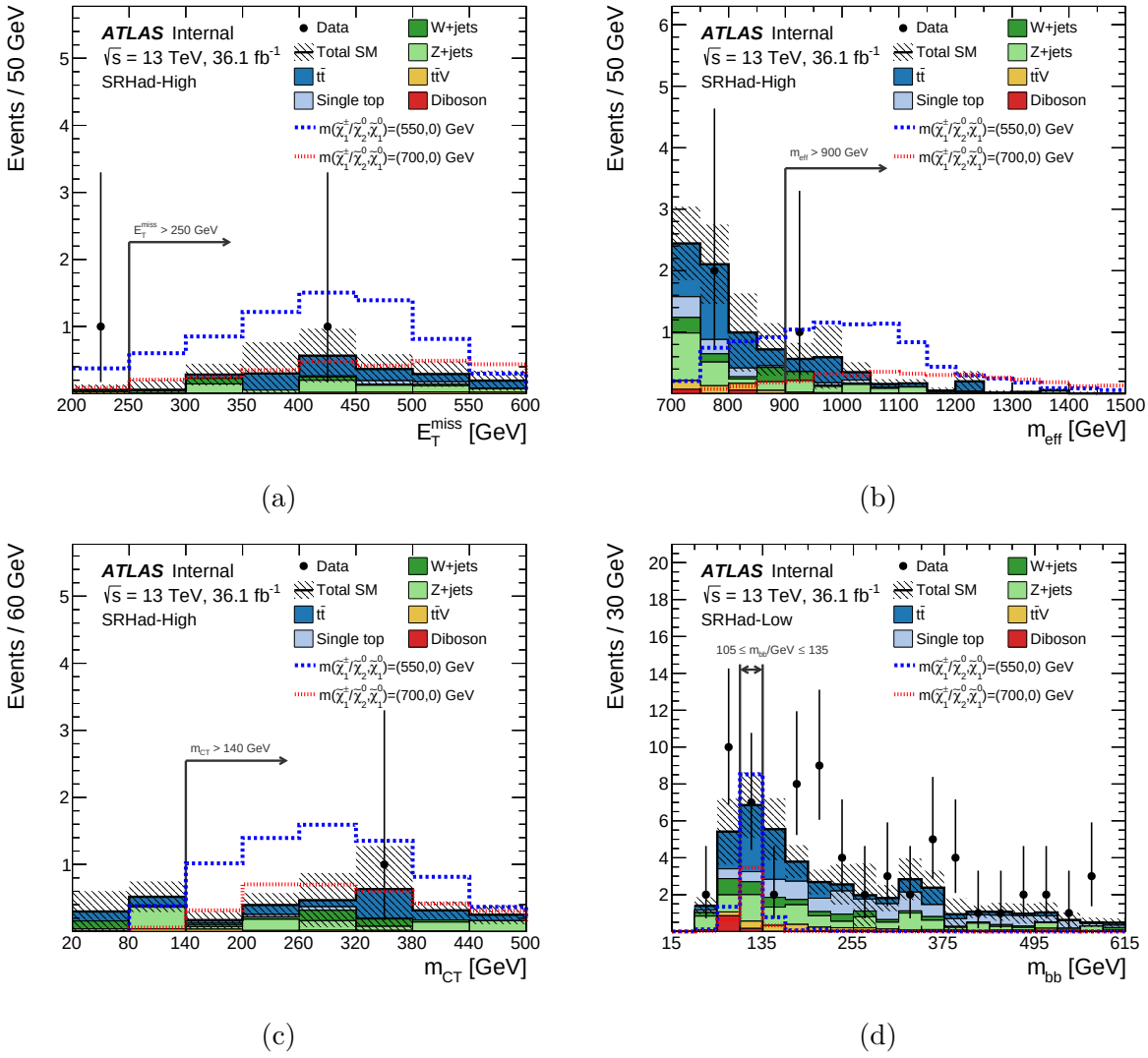

Figure 9.12: Data and SM predictions in SRs for (a) $E_{\mathrm{T}}^{\mathrm{miss}}$, (b) m_{eff}, and (c) m_{CT} in SRHad-High, and (d) $m_{b\bar{b}}$ in SRHad-Low. All SRs selections but the one on the quantity shown are applied. All uncertainties are included in the uncertainty band. Example SUSY models are superimposed for illustrative purposes.

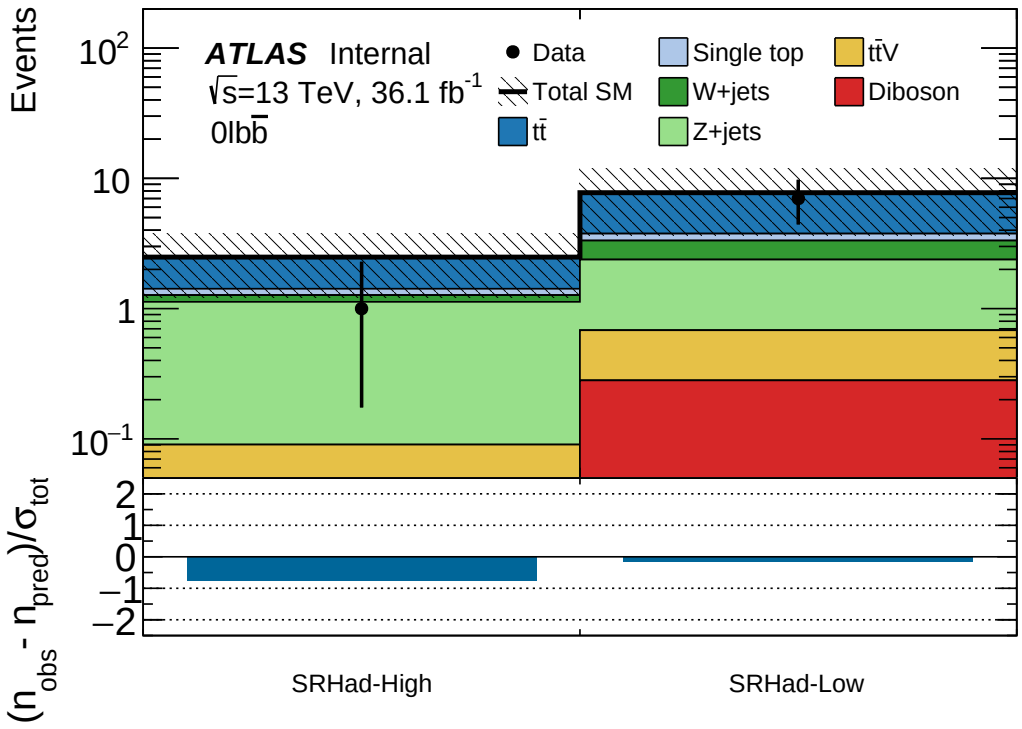

Figure 9.13: Comparison of the predicted backgrounds with the observed numbers of events in the SRs. The normalization of the backgrounds is obtained from the fit to the CRs for all channels. The upper panel shows the observed number of events and the predicted background yield. All uncertainties defined in Section 9.5 are included in the uncertainty band. The lower panel shows the pulls in each SR.

to background and signal samples. Thanks to the high branching ratio of the Higgs boson into b-quark pairs, the sensitivity is best at high masses of the chargino and next-to-lightest neutralinos and constraints up to 680 GeV are achieved for massless neutralinos.

A summary of the exclusion contours from all the channels included in the joint ATLAS publication in fig. 9.16 [241]. Expected and observed contours as obtained from each channel are shown, with the exception of the 3ℓ analysis which has no sensitivity. The overall expected sensitivity reaches from $m(\tilde{\chi}_1^{\pm}/\tilde{\chi}_2^0) = 150$ GeV to $m(\tilde{\chi}_1^{\pm}/\tilde{\chi}_2^0) = 635$ GeV, including significant improvements compared to previous results towards large $m(\tilde{\chi}_1^0)$ masses near the kinematic limit of the processes considered. These improvements are largely due to more highly optimized signal and control region definitions, as well as the addition of the $0\ell b\bar{b}$ analysis channel, which was the main contribution from the thesis work described in this report. The expected and observed cross section exclusion is shown in fig. 9.17 for all analyses presented in Ref. [241].

Finally, the acceptance and efficiency for both signal regions are shown in fig. 9.18. A summary cutflow table is included in section A.2.

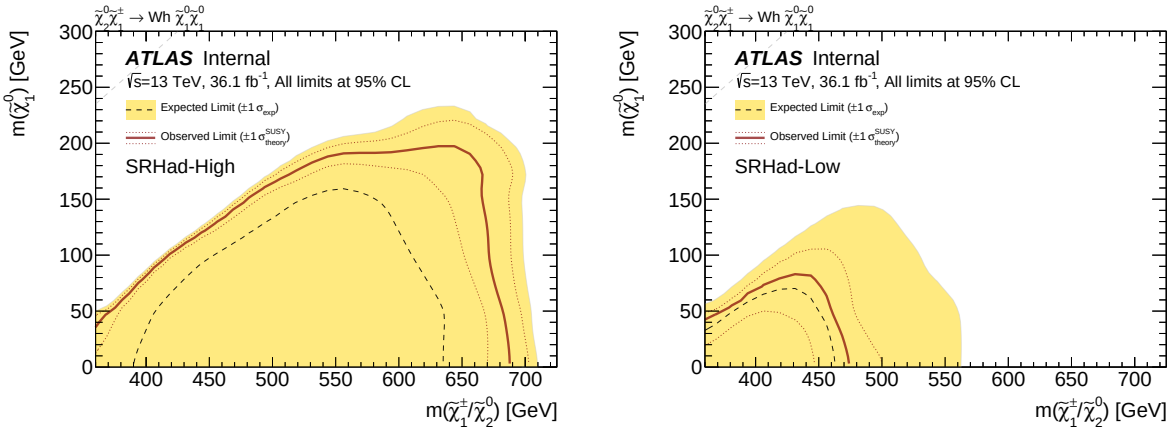

(a)

(b)

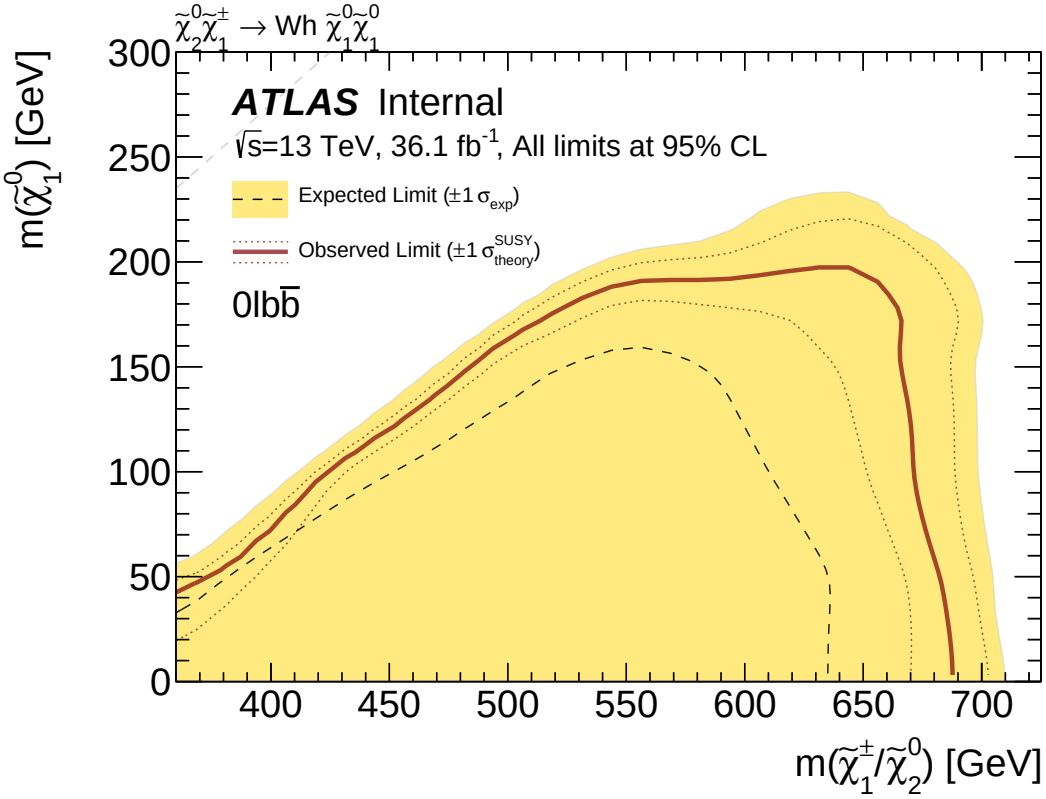

(c)

Figure 9.14: The expected and observed exclusion for (a) SRHad-High, (b) SRHad-Low, and (c) combination, i.e. choosing the region with best expected CLs for each mass point. Experimental and theoretical systematic uncertainties, as described in section 9.5, are applied to background and signal samples and illustrated by the yellow band and the red dotted contour lines, respectively. The red dotted lines indicate the ±1 sigma variation on the observed exclusion limit due to theoretical uncertainties on the signal cross section.

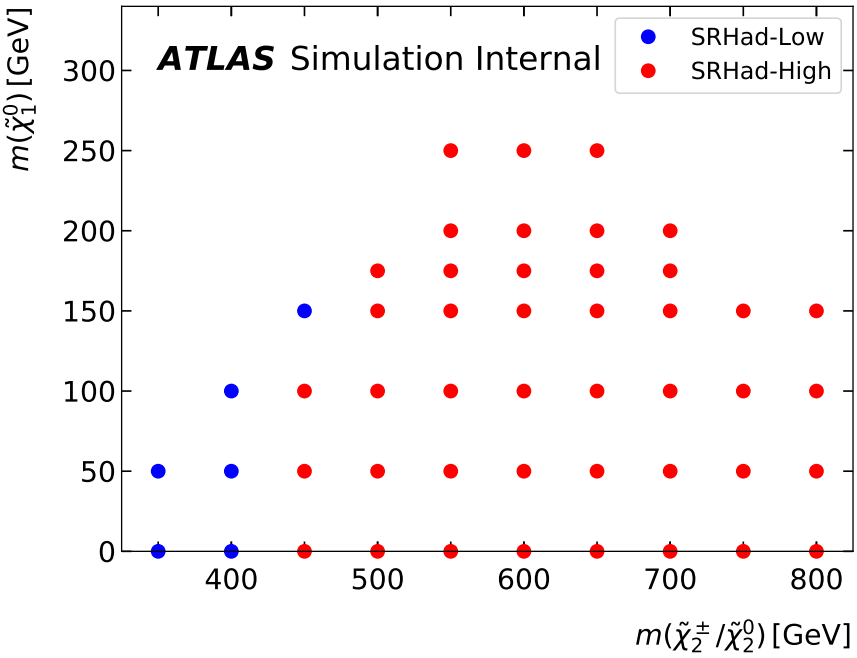

Figure 9.15: Signal region used for each of the $\tilde{\chi}_1^\pm/\tilde{\chi}_2^0$ and $\tilde{\chi}_1^0$ masses (determined based on the best expected sensitivity).

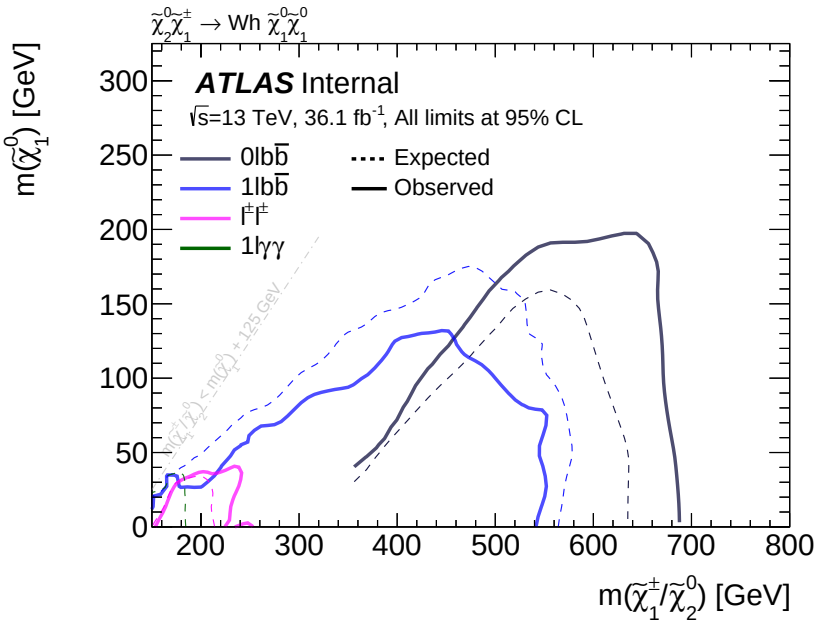

Figure 9.16: Comparison of the expected and observed exclusions for all channels in the ATLAS combination paper [241]. Only the expected exclusion is shown for the $1\ell\gamma\gamma$ channel since the observed exclusion does not appear due to the excess observed.

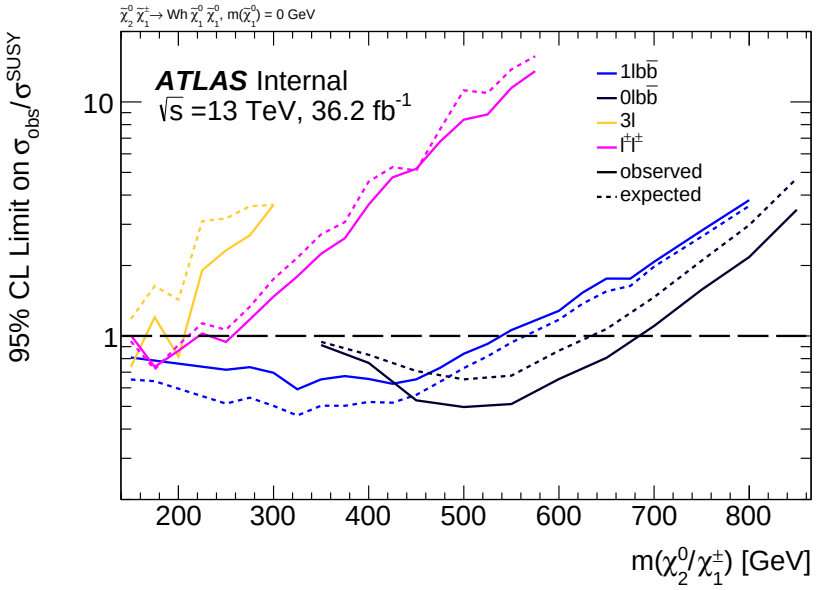

Figure 9.17: The expected and observed cross section exclusion as a function of $\tilde{\chi}_2^0/\tilde{\chi}_1^0$ masses for all channels in the ATLAS combination paper [241], assuming $m(\tilde{\chi}_1^0) = 0$ GeV.

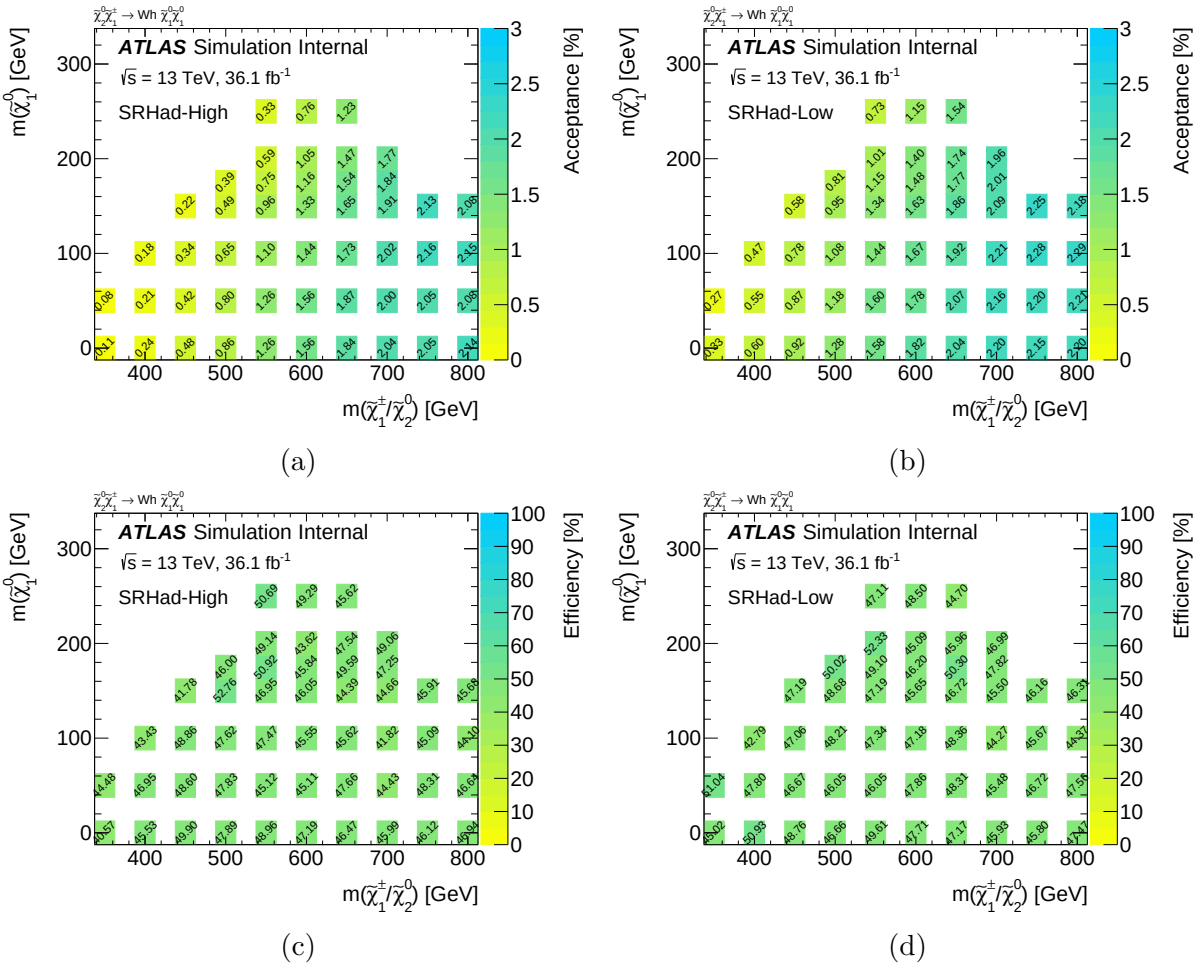

Figure 9.18: (a, b) Signal acceptance and (c, d) signal efficiency (for SRHad-High and SRHad-Low, respectively).

9.7 Conclusion

A search for electroweak pair production of a chargino and a neutralino, decaying via a W boson and a Standard Model like 125 GeV Higgs boson into a fully hadronic final state, has been performed. The Higgs boson in the final state is identified by two jets originating from bottom quarks. The analysis is based on 36.1 fb^{-1} of $\sqrt{s} = 13\,\text{TeV}$ pp collision data delivered by the LHC and recorded with the ATLAS detector. This is the first time a fully hadronic final state has been considered for this model, and the results are very promising. Observations are consistent with the Standard Model expectations, and 95% confidence level limits of up to 680 GeV in $\tilde{\chi}_1^{\pm}/\tilde{\chi}_2^0$ mass are set in the context of a simplified supersymmetric model.

CHAPTER 10

CONCLUDING REMARKS

The Large Hadron Collider (LHC) has enjoyed tremendous success, with over 100 fb^{-1} of 13 TeV data recorded by each of ATLAS and CMS to date [277], more than five times the LHC 8 TeV dataset, which was used in the Higgs boson discovery in 2012 [12]. The discovery of the Higgs boson was an astounding success, almost 50 years after it was first introduced as a mechanism for giving mass to the SM fermions and bosons. About six years has passed since the Higgs discovery, and if there is new physics beyond the SM around the TeV-scale, it has yet to show itself. However, as mentioned in the introduction, the LHC is only just getting started. Over the next couple of decades it is expected to collect more than an order of magnitude of additional data (about 4000 fb^{-1} is projected for the entire run of the high luminosity LHC), which will help significantly when searching for rare processes, such as electroweak SUSY (chapter 9). There should also be significant time available to go *back to the drawing board*, reflect on current analysis methods, and test new strategies and tools for physics analysis. I could hardly think of a more exciting time to have been a PhD student in experimental particle physics, and I am eager to find out what the future has in store. The next few years should be a particularly interesting time to analyze the full LHC 13 TeV dataset and to work on detector upgrades. Going forward, I intend to stay involved with searches for hadronic final states (at least until the end of Run II), however I am also interested to extend my scope beyond searches with hadronic final states; in particular Standard Model and Higgs precision measurements. I am also very interested in exploring new techniques for simulation, event reconstruction, and analysis, especially using Machine Learning. On the hardware front, I want to get more involved with the development efforts currently underway to prepare for the high luminosity LHC, which is scheduled to start collecting data in the mid/late-2020s. An interesting future lies ahead!

Glossary

AD Antiproton Decelerator. xii, 61

AFP ATLAS Forward Proton Detector. 89

ALFA Absolute Luminosity For ATLAS. 89

ALICE A Large Ion Collider Experiment. 60

ATLAS A Toroidal LHC ApparatuS. 60, 70

BSM beyond the Standard Model. 36

CEPC–SPPC Circular Electron Positron Collider – Super Proton-Proton Collider. 59

CERN the European Organization for Nuclear Research. 59

CKM Cabibbo-Kobayashi-Maskawa. 10, 28, 37

CLIC The Compact Linear Collider. 59

CMS Compact Muon Solenoid. 60

CNGS CERN Neutrinos to Gran Sasso. xii, 61

CP C-symmetry (charge conjugation symmetry) and P-symmetry (parity symmetry). 10

CPT Central Trigger Processor. 90

CSCs Cathode Strip Chambers. 73, 87

DM dark matter. 36

EF Event Filter. 90

electroweak theory The theory which describes both the electromagnetic force and the weak force. 8

EM electromagnetic. xiii, 72

FCal Forward Calorimeter. 73, 82, 84

FCC The Future Circular Collider. 59

GRL Good Runs List. 97

HE-LHC High-Energy LHC. 59

HEC Hadronic End-Cap. 73, 82, 84

Higgs mechanism The process which generates the proprety of mass for the gauge bosons. 8

HL-LHC High-Luminosity LHC. 59, 78

IBL Insertable B-Layer. 78

ID Inner Detector. 70, 77

ILC International e^+e^- Linear Collider. 59

ISOLDE On-Line Isotope Mass Separator. xii, 61

ITk Inner Tracker. 78

L1 Level-1. 90

L1Calo L1 calorimeter. 90

L1Muon L1 muon. 90

L2 Level-2. 90

LAr Liquid Argon Calorimeter. 72, 82, 97

LEP Large Electron Positron Collider. 59

LHC Large Hadron Collider. 59

LHCb The Large Hadron Collider beauty. 60

LHCf LHC forward. 60

Linac 2 Linear accelerator 2. 61

LSP Lightest Supersymmetric Particle. 149

LUCID LUminosity Cherenkov Integrating Detector. 87

MDTs Monitored Drift Tubes. 73, 87

MoEDAL Monopole and Exotics Detector at the LHC. 60

MSSM Minimal Supersymmetric Standard Model. 41

NLO Next-to-Next-to-Leading Order. 32

PDG Particle Data Group. x, 9, 10, 23

PMNS Pontecorvo-Maki-Nakagawa-Sakata. 28, 37

PMTs photomultiplier tubes. 85

PS Proton Synchrotron. 61

PSB Proton Synchrotron Booster. 61

QCD Quantum Chromodynamics. 8, 11

QED Quantum Electrodynamics. 10, 11

ROIs regions-of-interest. 90

RPCs Resistive Plate Chambers. 73, 87

SCT Semiconductor Tracker. 72, 77, 81, 97

SM Standard Model. 8

SPS Super Proton Synchrotron. 61

SRs Signal Regions. 161

SUSY supersymmetry. 114, 149

synchrotron An apparatus in which charged atomic and subatomic particles are accelerated by a magnetic field strength that increases with the energy of the particles in order to keep their orbital radius constant. 59

TDAQ Trigger and Data Acquisition. 89

TGCs Thin Gap Chambers. 73, 87

TileCal Tile Calorimeter. 73, 82, 84, 97

TOTEM TOTal Elastic and diffractive cross section Measurement. 60

TRT Transition Radiation Tracker. 72, 77, 81

ZDC Zero Degree Calorimeter. 89

Bibliography

[1] ATLAS Collaboration. "A search for top squarks with R-parity-violating decays to all-hadronic final states with the ATLAS detector in $\sqrt{s} = 8$ TeV proton-proton collisions". In: *JHEP* 06 (2016), p. 067. DOI: 10.1007/JHEP06(2016)067. arXiv: 1601.07453 [hep-ex] (cit. on pp. 1, 5, 107).

[2] David C. Lindberg. *The Beginnings of Western Science: The European Scientific Tradition in Philosophical, Religious, and Institutional Context, Prehistory to A.D. 1450, Second Edition*. The University of Chicago Press, 2008. URL: https://www.press.uchicago.edu/ucp/books/book/chicago/B/bo5550077.html (cit. on p. 2).

[3] Royal Society of Chemistry. *Development of the periodic table*. 2018. URL: http://www.rsc.org/periodic-table/history/about (visited on 09/03/2018) (cit. on p. 2).

[4] J. Clerk Maxwell. "On Faraday's Lines of Force". In: *Trans. Cambridge Philos. Soc.* 10 (1856), pp. 155–229. DOI: 10.1017/CBO9780511698095.011. URL: https://web.archive.org/web/20101215085100/http://blazelabs.com/On%20Faraday%27s%20Lines%20of%20Force.pdf (cit. on p. 3).

[5] F. R. S. J. Clerk Maxwell. "A dynamical theory of the electromagnetic field". In: *Phil. Trans. R. Soc. Lond.* 155 (1865), pp. 459–512. DOI: 10.1098/rstl.1865.0008 (cit. on p. 3).

[6] Albert A. Michelson and Edward W. Morley. "On the Relative Motion of the Earth and the Luminiferous Ether". In: *American Journal of Science* 34 (203) (1887), pp. 333–345. DOI: doi:10.2475/ajs.s3-34.203.333 (cit. on p. 3).

[7] Knt Sir Isaac Newton. *Opticks: Or, A Treatise of the Reflections, Refractions, Inflexions and Colours of Light. The Second Edition, with Additions*. 1718. URL: http://www.newtonproject.ox.ac.uk/view/texts/normalized/NATP00051 (cit. on p. 3).

[8] Translated by R. P. Hardie and R. K. Gaye. *Physics by Aristotle*. 350 B.C.E. URL: http://classics.mit.edu//Aristotle/physics.html (visited on 09/03/2018) (cit. on p. 3).

[9] Richard Stanley. *Einstein's Generation: Albert Michelson, the Velocity of Light, and the Ether Drift", Einstein's generation. The origins of the relativity revolution*. University of Chicago Press, 2009. URL: https://press.uchicago.edu/ucp/books/book/chicago/E/bo5924079.html (cit. on p. 3).

[10] Albert Einstein. "Zur Elektrodynamik bewegter Körper". In: *Annalen der Physik* 322 (10) (1905), pp. 891–921 (cit. on p. 3).

[11] Domenico Giulini and Norbert Straumann. "'...I Didn't reflect much on what I was doing...' how Planck discovered his radiation formula". In: *Submitted to: Phys. Bl.* (2000). arXiv: quant-ph/0010008 [quant-ph] (cit. on p. 3).

[12] ATLAS Collaboration. "Observation of a new particle in the search for the Standard Model Higgs boson with the ATLAS detector at the LHC". In: *Phys. Lett.* B716 (2012), pp. 1–29. DOI: 10.1016/j.physletb.2012.08.020. arXiv: 1207.7214 [hep-ex] (cit. on pp. 3, 10, 24, 39, 96, 106, 185).

[13] CMS Collaboration. "Observation of a new boson at a mass of 125 GeV with the CMS experiment at the LHC". In: *Phys. Lett.* B716 (2012), pp. 30–61. DOI: 10.1016/j.physletb.2012.08.021. arXiv: 1207.7235 [hep-ex] (cit. on pp. 3, 10, 24).

[14] Peter W. Higgs. "Broken Symmetries and the Masses of Gauge Bosons". In: *Phys.Rev.Lett.* 13 (1964), pp. 508–509. DOI: 10.1103/PhysRevLett.13.508 (cit. on pp. 4, 10).

[15] F. Englert and R. Brout. "Broken Symmetry and the Mass of Gauge Vector Mesons". In: *Phys.Rev.Lett.* 13 (1964), pp. 321–323. DOI: 10.1103/PhysRevLett.13.321 (cit. on pp. 4, 10).

[16] G.S. Guralnik, C.R. Hagen, and T.W.B. Kibble. "Global Conservation Laws and Massless Particles". In: *Phys.Rev.Lett.* 13 (1964), pp. 585–587. DOI: 10.1103/PhysRevLett.13.585 (cit. on pp. 4, 10).

[17] Till Tantau. "Graph Drawing in TikZ". In: *Proceedings of the 20th International Conference on Graph Drawing*. GD'12. Redmond, WA: Springer-Verlag, 2013, pp. 517–528. ISBN: 978-3-642-36762-5. DOI: 10.1007/978-3-642-36763-2_46 (cit. on pp. 9, 22, 40, 74, 75).

[18] Carsten Burgard. "A standard diagram of the current standard model of physics." Dec. 2016. URL: http://www.texample.net/tikz/examples/model-physics/ (visited on 09/03/2018) (cit. on p. 9).

[19] M. Tanabashi et al. "Review of Particle Physics". In: *Phys. Rev. D* 98 (3 Aug. 2018), p. 030001. DOI: 10.1103/PhysRevD.98.030001. URL: https://link.aps.org/doi/10.1103/PhysRevD.98.030001 (cit. on pp. 9, 12, 13, 23, 31, 39, 52, 101).

[20] S.L. Glashow. "Partial Symmetries of Weak Interactions". In: *Nucl.Phys.* 22 (1961), pp. 579–588. DOI: 10.1016/0029-5582(61)90469-2 (cit. on p. 10).

[21] Steven Weinberg. "A Model of Leptons". In: *Phys.Rev.Lett.* 19 (1967), pp. 1264–1266. DOI: 10.1103/PhysRevLett.19.1264 (cit. on p. 10).

[22] Abdus Salam and J.A. Strathdee. "On the Zero energy behavior of Regge poles and residues". In: *Conf.Proc.* C680519 (1968), pp. 59–103 (cit. on p. 10).

[23] Nobelprize.org. *The Nobel Prize in Physics 1979*. [Online; accessed 5-Sep-2018]. 2018. URL: https://www.nobelprize.org/prizes/physics/1979/summary/ (cit. on p. 10).

[24] Philip W. Anderson. "Plasmons, Gauge Invariance, and Mass". In: *Phys.Rev.* 130 (1963), pp. 439–442. DOI: 10.1103/PhysRev.130.439 (cit. on p. 10).

[25] C. Patrignani et al. "Review of Particle Physics". In: *Chin. Phys.* C40.10 (2016), p. 100001. DOI: 10.1088/1674-1137/40/10/100001 (cit. on p. 10).

[26] D. Hanneke, S. Fogwell, and G. Gabrielse. "New Measurement of the Electron Magnetic Moment and the Fine Structure Constant". In: *Phys. Rev. Lett.* 100 (12 Mar. 2008), p. 120801. DOI: 10.1103/PhysRevLett.100.120801. URL: https://link.aps.org/doi/10.1103/PhysRevLett.100.120801 (cit. on p. 10).

[27] ATLAS Collaboration. *Summary plots from the ATLAS Standard Model physics group*. https://atlas.web.cern.ch/Atlas/GROUPS/PHYSICS/CombinedSummaryPlots/SM/. [Online; accessed 1-Aug-2018]. 2018 (cit. on p. 11).

[28] M. Gell-Mann. *The Eightfold Way: A Theory of Strong Interaction Symmetry*. California Inst. of Tech., Pasadena. Synchrotron Lab. Mar. 1961. URL: https://www.osti.gov/servlets/purl/4008239 (cit. on p. 12).

[29] F. Halzen and Alan D. Martin. *Quarks and Leptons: An Introductory Course in Modern Particle Physics*. 1984. ISBN: 0471887412, 9780471887416 (cit. on pp. 12, 13, 31).

[30] Michael E. Peskin and Daniel V. Schroeder. *An Introduction to Quantum Field Theory*. Addison-Wesley Advanced Book Program (now Perseus Books), 1995. ISBN: 978-0201503975. URL: http://physics.weber.edu/schroeder/qftbook.html (cit. on pp. 12, 29, 30).

[31] Paul Langacker. "Introduction to the Standard Model and Electroweak Physics". In: (2009), pp. 3–48. arXiv: 0901.0241 [hep-ph] (cit. on pp. 12, 20, 21, 26, 38, 39, 41).

[32] Stephen P. Martin. "A Supersymmetry primer". In: (1997). [Adv. Ser. Direct. High Energy Phys.18,1(1998)], pp. 1–98. DOI: 10.1142/9789812839657_0001,10.1142/9789814307505_0001. arXiv: hep-ph/9709356 [hep-ph] (cit. on pp. 12, 39, 41–52, 56, 115).

[33] Murray Gell-Mann. "Symmetries of baryons and mesons". In: *Phys. Rev.* 125 (1962), pp. 1067–1084. DOI: 10.1103/PhysRev.125.1067 (cit. on p. 13).

[34] David J. Gross and Frank Wilczek. "Asymptotically Free Gauge Theories. I". In: *Phys. Rev. D* 8 (10 Nov. 1973), pp. 3633–3652. DOI: 10.1103/PhysRevD.8.3633. URL: https://link.aps.org/doi/10.1103/PhysRevD.8.3633 (cit. on p. 31).

[35] David J. Gross and Frank Wilczek. "Ultraviolet Behavior of Non-Abelian Gauge Theories". In: *Phys. Rev. Lett.* 30 (26 June 1973), pp. 1343–1346. DOI: 10.1103/PhysRevLett.30.1343. URL: https://link.aps.org/doi/10.1103/PhysRevLett.30.1343 (cit. on p. 31).

[36] Kenneth G. Wilson. "Confinement of quarks". In: *Phys. Rev. D* 10 (8 Oct. 1974), pp. 2445–2459. DOI: 10.1103/PhysRevD.10.2445. URL: https://link.aps.org/doi/10.1103/PhysRevD.10.2445 (cit. on p. 31).

[37] John C. Collins, Davison E. Soper, and George F. Sterman. "Factorization of Hard Processes in QCD". In: *Adv. Ser. Direct. High Energy Phys.* 5 (1989), pp. 1–91. DOI: 10.1142/9789814503266_0001. arXiv: hep-ph/0409313 [hep-ph] (cit. on p. 32).

[38] D. W. Duke and J. F. Owens. "Q^2-dependent parametrizations of parton distribution functions". In: *Phys. Rev. D* 30 (1 July 1984), pp. 49–54. DOI: 10.1103/PhysRevD.30.49. URL: https://link.aps.org/doi/10.1103/PhysRevD.30.49 (cit. on p. 32).

[39] Richard D. Ball et al. "Parton distributions from high-precision collider data". In: *Eur. Phys. J.* C77.10 (2017), p. 663. DOI: 10.1140/epjc/s10052-017-5199-5. arXiv: 1706.00428 [hep-ph] (cit. on p. 32).

[40] L. A. Harland-Lang et al. "Parton distributions in the LHC era: MMHT 2014 PDFs". In: *Eur. Phys. J.* C75.5 (2015), p. 204. DOI: 10.1140/epjc/s10052-015-3397-6. arXiv: 1412.3989 [hep-ph] (cit. on pp. 32, 33).

[41] Yuri L. Dokshitzer. "Calculation of the Structure Functions for Deep Inelastic Scattering and e+ e- Annihilation by Perturbation Theory in Quantum Chromodynamics." In: *Sov. Phys. JETP* 46 (1977). [Zh. Eksp. Teor. Fiz.73,1216(1977)], pp. 641–653 (cit. on p. 33).

[42] V. N. Gribov and L. N. Lipatov. "Deep inelastic e p scattering in perturbation theory". In: *Sov. J. Nucl. Phys.* 15 (1972). [Yad. Fiz.15,781(1972)], pp. 438–450 (cit. on p. 33).

[43] Guido Altarelli and G. Parisi. "Asymptotic Freedom in Parton Language". In: *Nucl. Phys.* B126 (1977), pp. 298–318. DOI: 10.1016/0550-3213(77)90384-4 (cit. on p. 33).

[44] B. R. Webber. "Fragmentation and hadronization". In: *Int. J. Mod. Phys.* A15S1 (2000). [eConfC990809,577(2000)], pp. 577–606. DOI: 10.1142/S0217751X00005334. arXiv: hep-ph/9912292 [hep-ph] (cit. on pp. 34, 36).

[45] Bo Andersson et al. "Parton Fragmentation and String Dynamics". In: *Phys. Rept.* 97 (1983), pp. 31–145. DOI: 10.1016/0370-1573(83)90080-7 (cit. on p. 34).

[46] Torbjorn Sjostrand, Stephen Mrenna, and Peter Z. Skands. "A Brief Introduction to PYTHIA 8.1". In: *Comput. Phys. Commun.* 178 (2008), pp. 852–867. DOI: 10.1016/j.cpc.2008.01.036. arXiv: 0710.3820 [hep-ph] (cit. on pp. 34, 151, 153).

[47] M. Bahr et al. "Herwig++ Physics and Manual". In: *Eur. Phys. J.* C58 (2008), pp. 639–707. DOI: 10.1140/epjc/s10052-008-0798-9. arXiv: 0803.0883 [hep-ph] (cit. on p. 34).

[48] Stefan Höche. "Introduction to parton-shower event generators". In: *Proceedings, Theoretical Advanced Study Institute in Elementary Particle Physics: Journeys Through the Precision Frontier: Amplitudes for Colliders (TASI 2014): Boulder, Colorado, June 2-27, 2014*. 2015, pp. 235–295. DOI: 10.1142/9789814678766_0005. arXiv: 1411.4085 [hep-ph] (cit. on p. 35).

[49] V. C. Rubin, W. K. Ford Jr., and N. Thonnard. "Rotational properties of 21 SC galaxies with a large range of luminosities and radii, from NGC 4605 /R = 4kpc/ to UGC 2885 /R = 122 kpc/". In: *ApJ* 238 (June 1980), pp. 471–487. DOI: 10.1086/158003 (cit. on pp. 37, 41).

[50] T. S. van Albada et al. "Distribution of dark matter in the spiral galaxy NGC 3198". In: *ApJ* 295 (Aug. 1985), pp. 305–313. DOI: 10.1086/163375 (cit. on pp. 37, 41).

[51] N. Kaiser and G. Squires. "Mapping the dark matter with weak gravitational lensing". In: *ApJ* 404 (Feb. 1993), pp. 441–450. DOI: 10.1086/172297 (cit. on pp. 37, 41).

[52] Richard Massey et al. "Dark matter maps reveal cosmic scaffolding". In: *Nature* 445 (2007), p. 286. DOI: 10.1038/nature05497. arXiv: astro-ph/0701594 [astro-ph] (cit. on pp. 37, 41).

[53] Planck Collaboration. "Planck 2013 results. I. Overview of products and scientific results". In: *A&A* 571 (2014), A1. DOI: 10.1051/0004-6361/201321529. URL: https://doi.org/10.1051/0004-6361/201321529 (cit. on pp. 37, 41).

[54] Katherine Garrett and Gintaras Duda. "Dark Matter: A Primer". In: *Adv. Astron.* 2011 (2011), p. 968283. DOI: 10.1155/2011/968283. arXiv: 1006.2483 [hep-ph] (cit. on p. 37).

[55] Gerard Jungman, Marc Kamionkowski, and Kim Griest. "Supersymmetric dark matter". In: *Phys. Rept.* 267 (1996), pp. 195–373. DOI: 10.1016/0370-1573(95)00058-5. arXiv: hep-ph/9506380 [hep-ph] (cit. on pp. 37, 43).

[56] Laurent Canetti, Marco Drewes, and Mikhail Shaposhnikov. "Matter and Antimatter in the Universe". In: *New J. Phys.* 14 (2012), p. 095012. DOI: 10.1088/1367-2630/14/9/095012. arXiv: 1204.4186 [hep-ph] (cit. on p. 37).

[57] Joseph D. Lykken. "Beyond the Standard Model". In: *CERN Yellow Report CERN-2010-002, 101-109*. 2010. arXiv: 1005.1676 [hep-ph]. URL: http://lss.fnal.gov/cgi-bin/find_paper.pl?conf-10-103 (cit. on p. 37).

[58] NASA/ESA and The Hubble Heritage Team (STScI/AURA). *Hubble mosaic of the majestic Sombrero Galaxy*. https://www.spacetelescope.org/images/opo0328a/. [Online; accessed 5-Sep-2018]. Oct. 2004 (cit. on p. 38).

[59] Izaak Neutelings. "University of Zurich, CMS Wiki Pages". July 2017. URL: https://wiki.physik.uzh.ch/cms/latex:tikz:timescales (visited on 09/03/2018) (cit. on p. 40).

[60] Yu. A. Golfand and E. P. Likhtman. "Extension of the Algebra of Poincare Group Generators and Violation of p Invariance". In: *JETP Lett.* 13 (1971). [Pisma Zh. Eksp. Teor. Fiz. **13** (1971) 452], pp. 323–326 (cit. on p. 41).

[61] D. V. Volkov and V. P. Akulov. "Is the Neutrino a Goldstone Particle?" In: *Phys. Lett. B* 46 (1973), pp. 109–110. DOI: 10.1016/0370-2693(73)90490-5 (cit. on p. 41).

[62] J. Wess and B. Zumino. "Supergauge Transformations in Four-Dimensions". In: *Nucl. Phys. B* 70 (1974), pp. 39–50. DOI: 10.1016/0550-3213(74)90355-1 (cit. on p. 42).

[63] J. Wess and B. Zumino. "Supergauge Invariant Extension of Quantum Electrodynamics". In: *Nucl. Phys. B* 78 (1974), p. 1. DOI: 10.1016/0550-3213(74)90112-6 (cit. on p. 42).

[64] S. Ferrara and B. Zumino. "Supergauge Invariant Yang-Mills Theories". In: *Nucl. Phys. B* 79 (1974), p. 413. DOI: 10.1016/0550-3213(74)90559-8 (cit. on p. 42).

[65] Abdus Salam and J. A. Strathdee. "Supersymmetry and Nonabelian Gauges". In: *Phys. Lett. B* 51 (1974), pp. 353–355. DOI: 10.1016/0370-2693(74)90226-3 (cit. on p. 42).

[66] ATLAS Collaboration. "Observation of a new particle in the search for the Standard Model Higgs boson with the ATLAS detector at the LHC". In: *Phys. Lett. B* 716 (2012), p. 1. DOI: 10.1016/j.physletb.2012.08.020. arXiv: 1207.7214 [hep-ex] (cit. on p. 42).

[67] CMS Collaboration. "Observation of a new boson at a mass of 125 GeV with the CMS experiment at the LHC". In: *Phys. Lett. B* 716 (2012), p. 30. DOI: 10.1016/j.physletb.2012.08.021. arXiv: 1207.7235 [hep-ex] (cit. on p. 42).

[68] ATLAS and CMS Collaborations. "Combined Measurement of the Higgs Boson Mass in pp Collisions at $\sqrt{s} = 7$ and 8 TeV with the ATLAS and CMS Experiments". In: *Phys. Rev. Lett.* 114 (2015), p. 191803. DOI: 10.1103/PhysRevLett.114.191803. arXiv: 1503.07589 [hep-ex] (cit. on p. 42).

[69] ATLAS and CMS Collaborations. "Measurements of the Higgs boson production and decay rates and constraints on its couplings from a combined ATLAS and CMS analysis of the LHC pp collision data at $\sqrt{s} = 7$ and 8 TeV". In: *JHEP* 08 (2016), p. 045. DOI: 10.1007/JHEP08(2016)045. arXiv: 1606.02266 [hep-ex] (cit. on p. 42).

[70] N. Sakai. "Naturalness in Supersymmetric Guts". In: *Z. Phys. C* 11 (1981), p. 153. DOI: 10.1007/BF01573998 (cit. on pp. 42, 43).

[71] S. Dimopoulos, S. Raby, and Frank Wilczek. "Supersymmetry and the Scale of Unification". In: *Phys. Rev. D* 24 (1981), pp. 1681–1683. DOI: 10.1103/PhysRevD.24.1681 (cit. on pp. 42, 43).

[72] Luis E. Ibanez and Graham G. Ross. "Low-Energy Predictions in Supersymmetric Grand Unified Theories". In: *Phys. Lett. B* 105 (1981), p. 439. DOI: 10.1016/0370-2693(81)91200-4 (cit. on pp. 42, 43).

[73] Savas Dimopoulos and Howard Georgi. "Softly Broken Supersymmetry and SU(5)". In: *Nucl. Phys. B* 193 (1981), p. 150. DOI: 10.1016/0550-3213(81)90522-8 (cit. on pp. 42, 43).

[74] H. Goldberg. "Constraint on the Photino Mass from Cosmology". In: *Phys. Rev. Lett.* 50 (1983). [Erratum: Phys. Rev. Lett.103,099905(2009)], p. 1419. DOI: 10.1103/PhysRevLett.50.1419 (cit. on p. 43).

[75] John R. Ellis et al. "Supersymmetric Relics from the Big Bang". In: *Nucl. Phys. B* 238 (1984), pp. 453–476. DOI: 10.1016/0550-3213(84)90461-9 (cit. on p. 43).

[76] Glennys R. Farrar and Pierre Fayet. "Phenomenology of the Production, Decay, and Detection of New Hadronic States Associated with Supersymmetry". In: *Phys. Lett. B* 76 (1978), p. 575. DOI: 10.1016/0370-2693(78)90858-4 (cit. on pp. 43, 114, 149).

[77] Hitoshi Murayama. "Supersymmetry phenomenology". In: *Proceedings, Summer School in Particle Physics: Trieste, Italy, June 21-July 9, 1999*. 2000, pp. 296–335. arXiv: hep-ph/0002232 [hep-ph] (cit. on p. 43).

[78] Asimina Arvanitaki et al. "The Last Vestiges of Naturalness". In: *JHEP* 03 (2014), p. 022. DOI: 10.1007/JHEP03(2014)022. arXiv: 1309.3568 [hep-ph] (cit. on p. 46).

[79] Herbert K. Dreiner. "An Introduction to explicit R-parity violation". In: (1997). [Adv. Ser. Direct. High Energy Phys.21,565(2010)], pp. 462–479. DOI: 10.1142/9789814307505_0017. arXiv: hep-ph/9707435 [hep-ph] (cit. on pp. 51, 52).

[80] Ian Hinchliffe and Thomas Kaeding. "B- and L-violating couplings in the minimal supersymmetric standard model". In: *Phys. Rev. D* 47 (1 Jan. 1993), pp. 279–284.

DOI: 10.1103/PhysRevD.47.279. URL: https://link.aps.org/doi/10.1103/PhysRevD.47.279 (cit. on p. 52).

[81] Daniele Alves. "Simplified Models for LHC New Physics Searches". In: *J. Phys.* G39 (2012). Ed. by Nima Arkani-Hamed et al., p. 105005. DOI: 10.1088/0954-3899/39/10/105005. arXiv: 1105.2838 [hep-ph] (cit. on p. 53).

[82] E. Halkiadakis, G. Redlinger, and D. Shih. "Status and Implications of Beyond-the-Standard-Model Searches at the LHC". In: *Annual Review of Nuclear and Particle Science* 64 (Oct. 2014), pp. 319–342. DOI: 10.1146/annurev-nucl-102313-025632 (cit. on p. 55).

[83] ATLAS Collaboration. *ATLAS Supersymmetry Physics Results*. https://twiki.cern.ch/twiki/bin/view/AtlasPublic/SupersymmetryPublicResults. [Online; accessed 8-September-2018]. 2018 (cit. on pp. 54, 57).

[84] CMS Collaboration. *CMS Supersymmetry Physics Results*. https://twiki.cern.ch/twiki/bin/view/CMSPublic/PhysicsResultsSUS. [Online; accessed 8-September-2018]. 2018 (cit. on p. 54).

[85] Lyndon Evans and Philip Bryant. "LHC Machine". In: *JINST* 3 (2008), S08001. DOI: 10.1088/1748-0221/3/08/S08001 (cit. on pp. 59, 60, 64).

[86] Oliver S. Bruning et al. "LHC Design Report Vol.1: The LHC Main Ring". In: (2004) (cit. on p. 59).

[87] Thomas Sven Pettersson and P Lefèvre. *The Large Hadron Collider: conceptual design*. Tech. rep. CERN-AC-95-05-LHC. Oct. 1995. URL: https://cds.cern.ch/record/291782 (cit. on p. 59).

[88] "LHC Guide". Mar. 2017. URL: https://cds.cern.ch/record/2255762 (cit. on p. 59).

[89] Vladimir Shiltsev. "Considerations On Energy Frontier Colliders After LHC". In: *Proceedings, 2nd North American Particle Accelerator Conference (NAPAC2016): Chicago, Illinois, USA, October 9-14, 2016*. 2017, TUPOB07. DOI: 10.18429/JACoW-NAPAC2016-TUPOB07. arXiv: 1705.02011 [physics.acc-ph]. URL: https://inspirehep.net/record/1598293/files/arXiv:1705.02011.pdf (cit. on p. 59).

[90] *LEP design report*. Copies shelved as reports in LEP, PS and SPS libraries. Geneva: CERN, 1984. URL: http://cds.cern.ch/record/102083 (cit. on pp. 59, 64).

[91] Panagiota Foka and Malgorzata Anna Janik. "An overview of experimental results from ultra-relativistic heavy-ion collisions at the CERN LHC: Hard probes". In: *Rev. Phys.* 1 (2016), pp. 172–194. DOI: 10.1016/j.revip.2016.11.001. arXiv: 1702.07231 [hep-ex] (cit. on p. 60).

[92] K. Aamodt et al. "The ALICE experiment at the CERN LHC". In: *JINST* 3 (2008), S08002. DOI: 10.1088/1748-0221/3/08/S08002 (cit. on p. 60).

[93] ATLAS Collaboration. "The ATLAS Experiment at the CERN Large Hadron Collider". In: *JINST* 3 (2008), S08003. DOI: 10.1088/1748-0221/3/08/S08003 (cit. on pp. 60, 70, 74–79, 81–90).

[94] S. Chatrchyan et al. "The CMS Experiment at the CERN LHC". In: *JINST* 3 (2008), S08004. DOI: 10.1088/1748-0221/3/08/S08004 (cit. on pp. 60, 70).

[95] A. Augusto Alves Jr. et al. "The LHCb Detector at the LHC". In: *JINST* 3 (2008), S08005. DOI: 10.1088/1748-0221/3/08/S08005 (cit. on p. 60).

[96] O. Adriani et al. "The LHCf detector at the CERN Large Hadron Collider". In: *JINST* 3 (2008), S08006. DOI: 10.1088/1748-0221/3/08/S08006 (cit. on p. 60).

[97] G. Anelli et al. "The TOTEM experiment at the CERN Large Hadron Collider". In: *JINST* 3 (2008), S08007. DOI: 10.1088/1748-0221/3/08/S08007 (cit. on p. 60).

[98] J. L. Pinfold. "The MoEDAL Experiment at the LHC – a New Light on the Terascale Frontier". In: *J. Phys. Conf. Ser.* 631.1 (2015), p. 012014. DOI: 10.1088/1742-6596/631/1/012014 (cit. on p. 60).

[99] CERN Service graphique. "Overall view of the LHC". June 2014. URL: https://cds.cern.ch/record/1708849 (cit. on p. 60).

[100] CERN. *The accelerator complex*. 2012. URL: http://cds.cern.ch/record/1997193 (visited on 05/02/2018) (cit. on pp. 61, 62).

[101] M. A. Fraser et al. "Status of the HIE-ISOLDE project at CERN". In: *Proceedings, 12th Heavy Ion Accelerator Technology Conference (HIAT2012): Chicago, IL, USA, June 18-21, 2012*. 2012, WEC02. arXiv: 1707.05129 [physics.acc-ph]. URL: https://inspirehep.net/record/1610355/files/arXiv:1707.05129.pdf (cit. on p. 61).

[102] M. Hori and J. Walz. "Physics at CERN's Antiproton Decelerator". In: *Prog. Part. Nucl. Phys.* 72 (2013), pp. 206–253. DOI: 10.1016/j.ppnp.2013.02.004. arXiv: 1304.3721 [physics.atom-ph] (cit. on p. 61).

[103] R. Acquafredda et al. "First events from the CNGS neutrino beam detected in the OPERA experiment". In: *New J. Phys.* 8 (2006), p. 303. DOI: 10.1088/1367-2630/8/12/303. arXiv: hep-ex/0611023 [hep-ex] (cit. on p. 61).

[104] CERN Christiane Lefèvre. "The CERN accelerator complex". Dec. 2008. URL: https://cds.cern.ch/record/1260465 (cit. on p. 61).

[105] CERN Maximilien Brice. "3d view photo of the LHC Machine". Nov. 2009. URL: http://cds.cern.ch/record/1223589 (cit. on p. 62).

[106] Helmut Wiedemann. *Particle accelerator physics I*. Berlin, Germany: Springer, 1999. ISBN: 9783540490432, 9783662038277. DOI: 10.1007/978-3-662-03827-7. URL: http://www.springer.com/us/book/9783662038277 (cit. on p. 63).

[107] Stephen Holmes, Ronald S Moore, and Vladimir Shiltsev. "Overview of the Tevatron collider complex: goals, operations and performance". In: *Journal of Instrumentation* 6.08 (2011), T08001. URL: http://stacks.iop.org/1748-0221/6/i=08/a=T08001 (cit. on p. 64).

[108] CERN Jean-Luc Caron. "LHC Layout". Sept. 1997. URL: https://cds.cern.ch/record/841573 (cit. on p. 65).

[109] ATLAS Collaboration. *ATLAS Luminosity Public Results Run 2*. https://twiki.cern.ch/twiki/bin/view/AtlasPublic/LuminosityPublicResultsRun2. [Online; accessed 12-April-2018]. 2016 (cit. on pp. 67, 68).

[110] ATLAS Collaboration. *ATLAS detector and physics performance: Technical Design Report, 1*. Technical Design Report ATLAS. Geneva: CERN, 1999. URL: https://cds.cern.ch/record/391176 (cit. on p. 70).

[111] ATLAS Collaboration. "Studies of the performance of the ATLAS detector using cosmic-ray muons". In: *Eur. Phys. J.* C71 (2011), p. 1593. DOI: 10.1140/epjc/s10052-011-1593-6. arXiv: 1011.6665 [physics.ins-det] (cit. on p. 70).

[112] ATLAS Collaboration. "The ATLAS Inner Detector commissioning and calibration". In: *Eur. Phys. J.* C70 (2010), pp. 787–821. DOI: 10.1140/epjc/s10052-010-1366-7. arXiv: 1004.5293 [physics.ins-det] (cit. on p. 70).

[113] ATLAS Collaboration. "Performance of the ATLAS Detector using First Collision Data". In: *JHEP* 09 (2010), p. 056. DOI: 10.1007/JHEP09(2010)056. arXiv: 1005.5254 [hep-ex] (cit. on p. 70).

[114] T. S. Pettersson and P Lefèvre. *The Large Hadron Collider: conceptual design*. Tech. rep. CERN-AC-95-05-LHC. Oct. 1995. URL: https://cds.cern.ch/record/291782 (cit. on p. 70).

[115] CERN Joao Pequenao. "Computer generated image of the whole ATLAS detector". Mar. 2008. URL: https://cds.cern.ch/record/1095924 (cit. on p. 73).

[116] ATLAS Collaboration. *ATLAS muon spectrometer: Technical Design Report*. Technical Design Report ATLAS. Geneva: CERN, 1997. URL: https://cds.cern.ch/record/331068 (cit. on p. 76).

[117] S Haywood et al. *ATLAS inner detector: Technical Design Report, 2*. Technical Design Report ATLAS. Geneva: CERN, 1997. URL: http://cds.cern.ch/record/331064 (cit. on p. 77).

[118] ATLAS Collaboration. "The Phase-II ATLAS ITk pixel upgrade". In: *JINST* 12.07 (2017), p. C07023. DOI: 10.1088/1748-0221/12/07/C07023 (cit. on p. 78).

[119] ATLAS Collaboration. "Study of the material of the ATLAS inner detector for Run 2 of the LHC". In: *JINST* 12.12 (2017), P12009. DOI: 10.1088/1748-0221/12/12/P12009. arXiv: 1707.02826 [hep-ex] (cit. on p. 80).

[120] G. Aad et al. "ATLAS pixel detector electronics and sensors". In: *JINST* 3 (2008), P07007. DOI: 10.1088/1748-0221/3/07/P07007 (cit. on pp. 78, 80).

[121] *ATLAS Insertable B-Layer Technical Design Report*. Tech. rep. CERN-LHCC-2010-013. ATLAS-TDR-19. Sept. 2010. URL: http://cds.cern.ch/record/1291633 (cit. on p. 80).

[122] ATLAS Collaboration. "Operation and performance of the ATLAS semiconductor tracker". In: *JINST* 9 (2014), P08009. DOI: 10.1088/1748-0221/9/08/P08009. arXiv: 1404.7473 [hep-ex] (cit. on p. 81).

[123] E. Abat et al. "The ATLAS TRT electronics". In: *JINST* 3 (2008), P06007. DOI: 10.1088/1748-0221/3/06/P06007 (cit. on p. 81).

[124] "Particle Identification Performance of the ATLAS Transition Radiation Tracker". In: (2011) (cit. on p. 81).

[125] ATLAS Collaboration. "Readiness of the ATLAS Liquid Argon Calorimeter for LHC Collisions". In: *Eur. Phys. J.* C70 (2010), pp. 723–753. DOI: 10.1140/epjc/s10052-010-1354-y. arXiv: 0912.2642 [physics.ins-det] (cit. on p. 83).

[126] G. Aad et al. "Readiness of the ATLAS Tile Calorimeter for LHC collisions". In: *Eur. Phys. J.* C70 (2010), pp. 1193–1236. DOI: 10.1140/epjc/s10052-010-1508-y. arXiv: 1007.5423 [physics.ins-det] (cit. on p. 84).

[127] ATLAS Collaboration. "ATLAS muon spectrometer: Technical design report". In: (1997) (cit. on p. 87).

[128] Nitesh Soni. "ATLAS Forward Detectors and Physics". In: *25th Lake Louise Winter Institute: Celebrating 25 years (LLWI 2010) Lake Louise, Alberta, Canada, February 15-20, 2010*. 2010. arXiv: 1006.5426 [hep-ex]. URL: https://inspirehep.net/record/859613/files/arXiv:1006.5426.pdf (cit. on pp. 87, 89).

[129] S. Abdel Khalek et al. "The ALFA Roman Pot Detectors of ATLAS". In: *JINST* 11.11 (2016), P11013. DOI: 10.1088/1748-0221/11/11/P11013. arXiv: 1609.00249 [physics.ins-det] (cit. on p. 89).

[130] ATLAS Collaboration. "Beam tests of an integrated prototype of the ATLAS Forward Proton detector". In: *JINST* 11.09 (2016), P09005. DOI: 10.1088/1748-0221/11/09/P09005. arXiv: 1608.01485 [physics.ins-det] (cit. on p. 89).

[131] ATLAS Collaboration. "Performance of the ATLAS Trigger System in 2010". In: *Eur. Phys. J.* C72 (2012), p. 1849. DOI: 10.1140/epjc/s10052-011-1849-1. arXiv: 1110.1530 [hep-ex] (cit. on p. 90).

[132] ATLAS Collaboration. "Performance of the ATLAS Trigger System in 2015". In: *Eur. Phys. J.* C77.5 (2017), p. 317. DOI: 10.1140/epjc/s10052-017-4852-3. arXiv: 1611.09661 [hep-ex] (cit. on pp. 90, 91).

[133] Stefan Weinzierl. "Introduction to Monte Carlo methods". In: (2000). arXiv: hep-ph/0006269 [hep-ph] (cit. on p. 94).

[134] M. A. Dobbs et al. "Les Houches guidebook to Monte Carlo generators for hadron collider physics". In: *Physics at TeV colliders. Proceedings, Workshop, Les Houches, France, May 26-June 3, 2003*. 2004, pp. 411–459. arXiv: hep-ph/0403045 [hep-ph]. URL: http://lss.fnal.gov/cgi-bin/find_paper.pl?conf-04-183 (cit. on pp. 94, 95).

[135] ATLAS Collaboration. "The ATLAS simulation infrastructure". In: *Eur. Phys. J. C* 70 (2010), p. 823. DOI: 10.1140/epjc/s10052-010-1429-9. arXiv: 1005.4568 [physics.ins-det] (cit. on pp. 94, 96, 117, 151).

[136] S. Agostinelli et al. "GEANT4: A Simulation toolkit". In: *Nucl. Instrum. Meth.* A506 (2003), pp. 250–303. DOI: 10.1016/S0168-9002(03)01368-8 (cit. on pp. 94, 96, 117, 151).

[137] ATLAS Collaboration. "Muon reconstruction performance of the ATLAS detector in proton-proton collision data at $\sqrt{s}$ =13 TeV". In: *Eur. Phys. J.* C76.5 (2016), p. 292. DOI: 10.1140/epjc/s10052-016-4120-y. arXiv: 1603.05598 [hep-ex] (cit. on p. 94).

[138] Morad Aaboud et al. "Electron efficiency measurements with the ATLAS detector using 2012 LHC proton-proton collision data". In: *Eur. Phys. J.* C77.3 (2017), p. 195. DOI: 10.1140/epjc/s10052-017-4756-2. arXiv: 1612.01456 [hep-ex] (cit. on p. 94).

[139] Morad Aaboud et al. "Measurement of the photon identification efficiencies with the ATLAS detector using LHC Run-1 data". In: *Eur. Phys. J.* C76.12 (2016), p. 666. DOI: 10.1140/epjc/s10052-016-4507-9. arXiv: 1606.01813 [hep-ex] (cit. on p. 94).

[140] M. Aaboud et al. "Jet energy scale measurements and their systematic uncertainties in proton-proton collisions at $\sqrt{s} = 13$ TeV with the ATLAS detector". In: *Phys. Rev.* D96.7 (2017), p. 072002. DOI: 10.1103/PhysRevD.96.072002. arXiv: 1703.09665 [hep-ex] (cit. on p. 94).

[141] Morad Aaboud et al. "Identification and rejection of pile-up jets at high pseudorapidity with the ATLAS detector". In: *Eur. Phys. J.* C77.9 (2017). [Erratum: Eur. Phys. J.C77,no.10,712(2017)], p. 580. DOI: 10.1140/epjc/s10052-017-5081-5, 10.1140/epjc/s10052-017-5245-3. arXiv: 1705.02211 [hep-ex] (cit. on p. 94).

[142] Morad Aaboud et al. "Performance of missing transverse momentum reconstruction with the ATLAS detector using proton-proton collisions at $\sqrt{s} = 13$ TeV". In: (2018). arXiv: 1802.08168 [hep-ex] (cit. on p. 94).

[143] ATLAS Collaboration. "Selection of jets produced in 13 TeV proton-proton collisions with the ATLAS detector". In: (2015) (cit. on p. 97).

[144] Henning Kirschenmann. *Jets at CMS and the determination of their energy scale*. http://cms.web.cern.ch/news/jets-cms-and-determination-their-energy-scale. [Online; accessed 5-Sep-2018]. July 2012 (cit. on p. 98).

[145] John E. Huth et al. "Toward a standardization of jet definitions". In: *1990 DPF Summer Study on High-energy Physics: Research Directions for the Decade (Snowmass 90) Snowmass, Colorado, June 25-July 13, 1990*. 1990, pp. 0134–136. URL: http://lss.fnal.gov/cgi-bin/find_paper.pl?conf-90-249 (cit. on p. 99).

[146] Gavin P. Salam. "Towards Jetography". In: *Eur. Phys. J.* C67 (2010), pp. 637–686. DOI: 10.1140/epjc/s10052-010-1314-6. arXiv: 0906.1833 [hep-ph] (cit. on p. 99).

[147] Matteo Cacciari, Gavin P. Salam, and Gregory Soyez. "The anti-k_t jet clustering algorithm". In: *JHEP* 04 (2008), p. 063. DOI: 10.1088/1126-6708/2008/04/063. arXiv: 0802.1189 [hep-ph] (cit. on pp. 99, 119, 154).

[148] Matteo Cacciari and Gavin P. Salam. "Dispelling the N^3 myth for the k_t jet-finder". In: *Phys. Lett.* B641 (2006), pp. 57–61. DOI: 10.1016/j.physletb.2006.08.037. arXiv: hep-ph/0512210 [hep-ph] (cit. on p. 99).

[149] Georges Aad et al. "Topological cell clustering in the ATLAS calorimeters and its performance in LHC Run 1". In: *Eur. Phys. J.* C77 (2017), p. 490. DOI: 10.1140/epjc/s10052-017-5004-5. arXiv: 1603.02934 [hep-ex] (cit. on pp. 99, 102).

[150] ATLAS Collaboration. "Performance of b-Jet Identification in the ATLAS Experiment". In: *Submitted to JINST* (2015). arXiv: 1512.01094 [hep-ex] (cit. on pp. 101, 121, 140).

[151] ATLAS Collaboration. "Performance of b-jet identification in the ATLAS experiment". In: *JINST* 11 (2016), P04008. DOI: 10.1088/1748-0221/11/04/P04008. arXiv: 1512.01094 [hep-ex] (cit. on pp. 101, 154).

[152] ATLAS Collaboration. *Optimisation of the ATLAS b-tagging performance for the 2016 LHC Run*. ATL-PHYS-PUB-2016-012. 2016. URL: https://cds.cern.ch/record/2160731 (cit. on pp. 101, 154).

[153] *Performance of the ATLAS Secondary Vertex b-tagging Algorithm in 7 TeV Collision Data*. Tech. rep. ATLAS-CONF-2010-042. Geneva: CERN, July 2010. URL: https://cds.cern.ch/record/1277682 (cit. on p. 103).

[154] Glen Cowan et al. "Asymptotic formulae for likelihood-based tests of new physics". In: *Eur. Phys. J.* C71 (2011). [Erratum: Eur. Phys. J.C73,2501(2013)], p. 1554. DOI: 10.1140/epjc/s10052-011-1554-0,10.1140/epjc/s10052-013-2501-z. arXiv: 1007.1727 [physics.data-an] (cit. on pp. 104, 105, 107, 110, 112).

[155] Louis Lyons. "Discovering the Significance of 5 sigma". In: (2013). arXiv: 1310.1284 [physics.data-an] (cit. on p. 104).

[156] Louis Lyons. "Statistical Issues in Searches for New Physics". In: 2014. arXiv: 1409.1903 [hep-ex]. URL: https://inspirehep.net/record/1315329/files/arXiv:1409.1903.pdf (cit. on p. 104).

[157] A L Read. "Presentation of search results: the CL s technique". In: *Journal of Physics G: Nuclear and Particle Physics* 28.10 (2002), p. 2693. URL: http://stacks.iop.org/0954-3899/28/i=10/a=313 (cit. on p. 104).

[158] Diego Casadei. "Statistical methods used in ATLAS for exclusion and discovery". In: CERN. Geneva: CERN, 2011, pp. 94–99. DOI: 10.5170/CERN-2011-006.94. arXiv: 1108.2288 [physics.data-an]. URL: https://inspirehep.net/record/922978/files/arXiv:1108.2288.pdf (cit. on p. 104).

[159] M. Baak et al. "HistFitter software framework for statistical data analysis". In: *Eur. Phys. J.* C75 (2015), p. 153. DOI: 10.1140/epjc/s10052-015-3327-7. arXiv: 1410.1280 [hep-ex] (cit. on pp. 104, 108).

[160] Kyle Cranmer et al. Tech. rep. CERN-OPEN-2012-016. New York: New York U., Jan. 2012. URL: https://cds.cern.ch/record/1456844 (cit. on p. 108).

[161] S. S. Wilks. "The Large-Sample Distribution of the Likelihood Ratio for Testing Composite Hypotheses". In: *Annals Math. Statist.* 9.1 (1938), pp. 60–62. DOI: 10.1214/aoms/1177732360 (cit. on p. 110).

[162] ATLAS Collaboration. "ATLAS Run 1 searches for direct pair production of third-generation squarks at the Large Hadron Collider". In: *Eur. Phys. J. C* 75 (2015), p. 510. DOI: 10.1140/epjc/s10052-015-3726-9. arXiv: 1506.08616 [hep-ex] (cit. on p. 115).

[163] CMS Collaboration. "Searches for third-generation squark production in fully hadronic final states in proton-proton collisions at $\sqrt{s} = 8$ TeV". In: *JHEP* 1506 (2015), p. 116. DOI: 10.1007/JHEP06(2015)116. arXiv: 1503.08037 [hep-ex] (cit. on p. 115).

[164] ATLAS Collaboration. "Search for a Heavy Neutral Particle Decaying to $e\mu$, $e\tau$, or $\mu\tau$ in pp Collisions at $\sqrt{s} = 8$ TeV with the ATLAS Detector". In: *Phys. Rev. Lett.* 115 (2015), p. 031801. DOI: 10.1103/PhysRevLett.115.031801. arXiv: 1503.04430 [hep-ex] (cit. on p. 115).

[165] ATLAS Collaboration. "Search for long-lived stopped R-hadrons decaying out-of-time with pp collisions using the ATLAS detector". In: *Phys. Rev. D* 88 (2013), p. 112003. DOI: 10.1103/PhysRevD.88.112003. arXiv: 1310.6584 [hep-ex] (cit. on p. 115).

[166] ATLAS Collaboration. "Searches for heavy long-lived charged particles with the ATLAS detector in proton–proton collisions at $\sqrt{s} = 8$ TeV". In: *JHEP* 01 (2015), p. 068. DOI: 10.1007/JHEP01(2015)068. arXiv: 1411.6795 [hep-ex] (cit. on p. 115).

[167] ATLAS Collaboration. "Search for massive, long-lived particles using multitrack displaced vertices or displaced lepton pairs in pp collisions at $\sqrt{s} = 8$ TeV with the ATLAS detector". In: *Phys. Rev. D* 92 (2015), p. 072004. DOI: 10.1103/PhysRevD.92.072004. arXiv: 1504.05162 [hep-ex] (cit. on p. 115).

[168] ATLAS Collaboration. "Search for metastable heavy charged particles with large ionisation energy loss in pp collisions at $\sqrt{s} = 8$ TeV using the ATLAS experiment". In: *Eur. Phys. J. C* 75 (2015), p. 407. DOI: 10.1140/epjc/s10052-015-3609-0. arXiv: 1506.05332 [hep-ex] (cit. on p. 115).

[169] ATLAS Collaboration. "Search for supersymmetry in events with four or more leptons in $\sqrt{s} = 8$ TeV pp collisions with the ATLAS detector". In: *Phys. Rev. D* 90 (2014), p. 052001. DOI: 10.1103/PhysRevD.90.052001. arXiv: 1405.5086 [hep-ex] (cit. on p. 115).

[170] CMS Collaboration. "Search for top squarks in R-parity-violating supersymmetry using three or more leptons and b-tagged jets". In: *Phys. Rev. Lett.* 111 (2013), p. 221801. DOI: 10.1103/PhysRevLett.111.221801. arXiv: 1306.6643 [hep-ex] (cit. on p. 115).

[171] Georges Aad et al. "Search for massive supersymmetric particles decaying to many jets using the ATLAS detector in pp collisions at $\sqrt{s} = 8$ TeV". In: *Phys. Rev.* D91.11 (2015). [Erratum: Phys. Rev.D93,no.3,039901(2016)], p. 112016. DOI: 10.1103/PhysRevD.93.039901,10.1103/PhysRevD.91.112016. arXiv: 1502.05686 [hep-ex] (cit. on p. 115).

[172] Kenzo Inoue et al. "Aspects of Grand Unified Models with Softly Broken Supersymmetry". In: *Prog. Theor. Phys.* 68 (1982). [Erratum: Prog. Theor. Phys.70,330(1983)], p. 927. DOI: 10.1143/PTP.68.927 (cit. on p. 115).

[173] John R. Ellis and Serge Rudaz. "Search for Supersymmetry in Toponium Decays". In: *Phys. Lett. B* 128 (1983), p. 248. DOI: 10.1016/0370-2693(83)90402-1 (cit. on p. 115).

[174] Riccardo Barbieri and G. F. Giudice. "Upper Bounds on Supersymmetric Particle Masses". In: *Nucl. Phys. B* 306 (1988), p. 63. DOI: 10.1016/0550-3213(88)90171-X (cit. on pp. 115, 149).

[175] B. de Carlos and J. A. Casas. "One loop analysis of the electroweak breaking in supersymmetric models and the fine tuning problem". In: *Phys. Lett. B* 309 (1993), pp. 320–328. DOI: 10.1016/0370-2693(93)90940-J. arXiv: hep-ph/9303291 [hep-ph] (cit. on pp. 115, 149).

[176] Herbert K. Dreiner. "An introduction to explicit R-parity violation". In: *Pramana* 51 (1998), pp. 123–133. DOI: 10.1007/BF02827485. arXiv: hep-ph/9707435 [hep-ph] (cit. on p. 115).

[177] B.C. Allanach, A. Dedes, and H.K. Dreiner. "R parity violating minimal supergravity model". In: *Phys. Rev. D* 69 (2004), p. 115002. DOI: 10.1103/PhysRevD.69.115002, 10.1103/PhysRevD.72.079902. arXiv: hep-ph/0309196 [hep-ph] (cit. on p. 115).

[178] B.C. Allanach, A. Dedes, and Herbert K. Dreiner. "Bounds on R-parity violating couplings at the weak scale and at the GUT scale". In: *Phys. Rev. D* 60 (1999), p. 075014. DOI: 10.1103/PhysRevD.60.075014. arXiv: hep-ph/9906209 [hep-ph] (cit. on p. 115).

[179] Marc Sher and J. L. Goity. "Bounds on Delta B = 1 Couplings in the Supersymmetric Standard Model". In: *Phys. Lett. B* 346 (1995), p. 69. DOI: 10.1016/0370-2693(96)01076-3. arXiv: hep-ph/9503472 [hep-ph] (cit. on p. 115).

[180] F. Zwirner. "Observable $\Delta B = 2$ transitions without nucleon decay in a minimal supersymmetric extension of the Standard Model". In: *Phys. Lett. B* 132 (1983), p. 103. DOI: 10.1016/0370-2693(83)90230-7 (cit. on p. 115).

[181] Gautam Bhattacharyya. "A Brief review of R-parity violating couplings (Invited talk presented at 'Beyond the Desert', Castle Ringberg, Tegernsee, Germany, 8-14 June 1997)". In: (1997). arXiv: hep-ph/9709395 [hep-ph] (cit. on p. 115).

[182] G. D'Ambrosio et al. "Minimal flavor violation: An Effective field theory approach". In: *Nucl. Phys. B* 645 (2002), pp. 155–187. DOI: 10.1016/S0550-3213(02)00836-2. arXiv: hep-ph/0207036 [hep-ph] (cit. on p. 116).

[183] Brian Batell, Tongyan Lin, and Lian-Tao Wang. "Flavored Dark Matter and R-Parity Violation". In: *JHEP* 1401 (2014), p. 075. DOI: 10.1007/JHEP01(2014)075. arXiv: 1309.4462 [hep-ph] (cit. on p. 116).

[184] Csaba Csaki, Yuval Grossman, and Ben Heidenreich. "MFV SUSY: A Natural Theory for R-Parity Violation". In: *Phys. Rev. D* 85 (2012), p. 095009. DOI: 10.1103/PhysRevD.85.095009. arXiv: 1111.1239 [hep-ph] (cit. on p. 116).

[185] Yang Bai, Andrey Katz, and Brock Tweedie. "Pulling Out All the Stops: Searching for RPV SUSY with Stop-Jets". In: *JHEP* 1401 (2014), p. 040. DOI: 10.1007/JHEP01(2014)040. arXiv: 1309.6631 [hep-ph] (cit. on pp. 116, 117, 122, 124).

[186] A. Heister et al. "Search for supersymmetric particles with R parity violating decays in e^+e^- collisions at $\sqrt{s}$ up to 209-GeV". In: *Eur. Phys. J. C* 31 (2003). DOI: 10.1140/epjc/s2003-01311-5. arXiv: hep-ex/0210014 [hep-ex] (cit. on p. 116).

[187] T. Aaltonen et al. "Search for Pair Production of Strongly Interacting Particles Decaying to Pairs of Jets in $p\bar{p}$ Collisions at $\sqrt{s} = 1.96$ TeV". In: *Phys. Rev. Lett.* 111 (2013), p. 031802. DOI: 10.1103/PhysRevLett.111.031802. arXiv: 1303.2699 [hep-ex] (cit. on pp. 116, 146).

[188] CMS Collaboration. "Search for pair-produced resonances decaying to jet pairs in proton-proton collisions at $\sqrt{s} = 8$ TeV". In: *Phys. Lett. B* 747 (2015), p. 98. DOI: 10.1016/j.physletb.2015.04.045. arXiv: 1412.7706 [hep-ex] (cit. on p. 116).

[189] ATLAS Collaboration. "Search for new phenomena in final states with large jet multiplicities and missing transverse momentum at $\sqrt{s} = 8$ TeV proton–proton collisions using the ATLAS experiment". In: *JHEP* 10 (2013), p. 130. DOI: 10.1007/JHEP10(2013)130. arXiv: 1308.1841 [hep-ex] (cit. on p. 116). Erratum: in: *JHEP* 01 (2014), p. 109. DOI: 10.1007/JHEP01(2014)109.

[190] ATLAS Collaboration. "Search for supersymmetry at $\sqrt{s} = 8$ TeV in final states with jets and two same-sign leptons or three leptons with the ATLAS detector". In: *JHEP* 06 (2014), p. 035. DOI: 10.1007/JHEP06(2014)035. arXiv: 1404.2500 [hep-ex] (cit. on p. 116).

[191] R. Barbier et al. "R-parity violating supersymmetry". In: *Phys. Rept.* 420 (2005), p. 1. DOI: 10.1016/j.physrep.2005.08.006. arXiv: hep-ph/0406039 [hep-ph] (cit. on p. 116).

[192] ATLAS Collaboration. "Jet mass and substructure of inclusive jets in $\sqrt{s} = 7$ TeV pp collisions with the ATLAS experiment". In: *JHEP* 05 (2012), p. 128. DOI: 10.1007/JHEP05(2012)128. arXiv: 1203.4606 [hep-ex] (cit. on p. 117).

[193] ATLAS Collaboration. "ATLAS measurements of the properties of jets for boosted particle searches". In: *Phys. Rev. D* 86 (2012), p. 072006. DOI: 10.1103/PhysRevD.86.072006. arXiv: 1206.5369 [hep-ex] (cit. on p. 117).

[194] ATLAS Collaboration. "A search for $t\bar{t}$ resonances in lepton+jets events with highly boosted top quarks collected in pp collisions at $\sqrt{s} = 7$ TeV with the ATLAS detector". In: *JHEP* 09 (2012), p. 041. DOI: 10.1007/JHEP09(2012)041. arXiv: 1207.2409 [hep-ex] (cit. on p. 117).

[195] ATLAS Collaboration. "Performance of jet substructure techniques for large-R jets in proton–proton collisions at $\sqrt{s} = 7$ TeV using the ATLAS detector". In: *JHEP* 09 (2013), p. 076. DOI: 10.1007/JHEP09(2013)076. arXiv: 1306.4945 [hep-ex] (cit. on p. 117).

[196] ATLAS Collaboration. "Measurement of the cross-section of high transverse momentum vector bosons reconstructed as single jets and studies of jet substructure in pp collisions at $\sqrt{s} = 7$ TeV with the ATLAS detector". In: *New J. Phys.* 16 (2014), p. 113013. DOI: 10.1088/1367-2630/16/11/113013. arXiv: 1407.0800 [hep-ex] (cit. on p. 117).

[197] Torbjorn Sjostrand, Stephen Mrenna, and Peter Z. Skands. "A Brief Introduction to PYTHIA 8.1". In: *Comput. Phys. Commun.* 178 (2008), pp. 852–867. DOI: 10.1016/j.cpc.2008.01.036. arXiv: 0710.3820 [hep-ph] (cit. on p. 118).

[198] ATLAS Collaboration. *Further ATLAS tunes of* PYTHIA *6 and Pythia 8*. ATL-PHYS-PUB-2011-014. 2011. URL: https://cds.cern.ch/record/1400677 (cit. on p. 118).

[199] G. Watt and R.S. Thorne. "Study of Monte Carlo approach to experimental uncertainty propagation with MSTW 2008 PDFs". In: *JHEP* 1208 (2012), p. 052. DOI: 10.1007/JHEP08(2012)052. arXiv: 1205.4024 [hep-ph] (cit. on p. 118).

[200] M. Bähr et al. "Herwig++ physics and manual". In: *Eur. Phys. J. C* 58 (2008), p. 639. DOI: 10.1140/epjc/s10052-008-0798-9. arXiv: 0803.0883 [hep-ph] (cit. on p. 118).

[201] Stefan Gieseke, Christian Röhr, and Andrzej Siödmok. "Colour reconnections in Herwig++". In: *Eur. Phys. J. C* 72 (2012), p. 2225. DOI: 10.1140/epjc/s10052-012-2225-5. arXiv: 1206.0041 [hep-ph] (cit. on p. 118).

[202] J. Pumplin et al. "New generation of parton distributions with uncertainties from global QCD analysis". In: *JHEP* 0207 (2002), p. 012. DOI: 10.1088/1126-6708/2002/07/012. arXiv: 0201195 [hep-ph] (cit. on p. 118).

[203] Pavel M. Nadolsky et al. "Implications of CTEQ global analysis for collider observables". In: *Phys. Rev. D* 78 (2008), p. 013004. DOI: 10.1103/PhysRevD.78.013004. arXiv: 0802.0007 [hep-ph] (cit. on p. 118).

[204] W. Beenakker et al. "Stop production at hadron colliders". In: *Nucl. Phys. B* 515 (1998), pp. 3–14. DOI: 10.1016/S0550-3213(98)00014-5. arXiv: hep-ph/9710451 [hep-ph] (cit. on pp. 118, 120, 152).

[205] Wim Beenakker et al. "Supersymmetric top and bottom squark production at hadron colliders". In: *JHEP* 08 (2010), p. 098. DOI: 10.1007/JHEP08(2010)098. arXiv: 1006.4771 [hep-ph] (cit. on pp. 118, 120, 152).

[206] W. Beenakker et al. "Squark and gluino hadroproduction". In: *Int. J. Mod. Phys. A* 26 (2011), pp. 2637–2664. DOI: 10.1142/S0217751X11053560. arXiv: 1105.1110 [hep-ph] (cit. on pp. 118, 120, 152).

[207] Michael Krämer et al. "Supersymmetry production cross sections in pp collisions at sqrts = 7 TeV". In: (2012). arXiv: 1206.2892 [hep-ph] (cit. on pp. 118, 140).

[208] Johan Alwall et al. "MadGraph 5 : Going Beyond". In: *JHEP* 1106 (2011), p. 128. DOI: 10.1007/JHEP06(2011)128. arXiv: 1106.0522 [hep-ph] (cit. on p. 118).

[209] ATLAS Collaboration. *ATLAS tunes of* PYTHIA *6 and Pythia 8 for MC11*. ATL-PHYS-PUB-2011-009. 2011. URL: https://cds.cern.ch/record/1363300 (cit. on p. 119).

[210] Paolo Nason. "A New method for combining NLO QCD with shower Monte Carlo algorithms". In: *JHEP* 0411 (2004), p. 040. DOI: 10.1088/1126-6708/2004/11/040. arXiv: hep-ph/0409146 [hep-ph] (cit. on p. 119).

[211] Stefano Frixione, Paolo Nason, and Carlo Oleari. "Matching NLO QCD computations with Parton Shower simulations: the POWHEG method". In: *JHEP* 11 (2007), p. 070. DOI: 10.1088/1126-6708/2007/11/070. arXiv: 0709.2092 [hep-ph] (cit. on pp. 119, 153).

[212] Simone Alioli et al. "A general framework for implementing NLO calculations in shower Monte Carlo programs: the POWHEG BOX". In: *JHEP* 06 (2010), p. 043. DOI: 10.1007/JHEP06(2010)043. arXiv: 1002.2581 [hep-ph] (cit. on pp. 119, 153).

[213] Hung-Liang Lai et al. "New parton distributions for collider physics". In: *Phys. Rev. D* 82 (2010), p. 074024. DOI: 10.1103/PhysRevD.82.074024. arXiv: 1007.2241 [hep-ph] (cit. on pp. 119, 153).

[214] Peter Zeiler Skands. "Tuning Monte Carlo Generators: The Perugia Tunes". In: *Phys. Rev. D* 82 (2010), p. 074018. DOI: 10.1103/PhysRevD.82.074018. arXiv: 1005.3457 [hep-ph] (cit. on p. 119).

[215] Paul Czakon Michałand Fiedler and Alexander Mitov. "Total Top-Quark Pair-Production Cross Section at Hadron Colliders Through $\mathcal{O}(\alpha_S^4)$". In: *Phys. Rev. Lett.* 110 (2013), p. 252004. DOI: 10.1103/PhysRevLett.110.252004. arXiv: 1303.6254 [hep-ph] (cit. on p. 119).

[216] Michal Czakon and Alexander Mitov. "NNLO corrections to top pair production at hadron colliders: the quark-gluon reaction". In: *JHEP* 1301 (2013), p. 080. DOI: 10.1007/JHEP01(2013)080. arXiv: 1210.6832 [hep-ph] (cit. on p. 119).

[217] Michal Czakon and Alexander Mitov. "NNLO corrections to top-pair production at hadron colliders: the all-fermionic scattering channels". In: *JHEP* 1212 (2012), p. 054. DOI: 10.1007/JHEP12(2012)054. arXiv: 1207.0236 [hep-ph] (cit. on p. 119).

[218] Peter Bärnreuther, Michal Czakon, and Alexander Mitov. "Percent Level Precision Physics at the Tevatron: First Genuine NNLO QCD Corrections to $q\bar{q} \to t\bar{t} + X$". In: *Phys. Rev. Lett.* 109 (2012), p. 132001. DOI: 10.1103/PhysRevLett.109.132001. arXiv: 1204.5201 [hep-ph] (cit. on p. 119).

[219] Matteo Cacciari et al. "Top-pair production at hadron colliders with next-to-next-to-leading logarithmic soft-gluon resummation". In: *Phys. Lett. B* 710 (2012), pp. 612–622. DOI: 10.1016/j.physletb.2012.03.013. arXiv: 1111.5869 [hep-ph] (cit. on p. 119).

[220] Michal Czakon and Alexander Mitov. "Top++: A Program for the Calculation of the Top-Pair Cross-Section at Hadron Colliders". In: *Comput. Phys. Commun.* 185 (2014), p. 2930. DOI: 10.1016/j.cpc.2014.06.021. arXiv: 1112.5675 [hep-ph] (cit. on p. 119).

[221] Matteo Cacciari, Gavin P. Salam, and Gregory Soyez. "FastJet User Manual". In: *Eur. Phys. J. C* 72 (2012), p. 1896. DOI: 10.1140/epjc/s10052-012-1896-2. arXiv: 1111.6097 [hep-ph] (cit. on p. 119).

[222] W. Lampl et al. *Calorimeter clustering algorithms: description and performance.* ATL-LARG-PUB-2008-002. 2008. URL: http://cdsweb.cern.ch/record/1099735 (cit. on p. 119).

[223] ATLAS Collaboration. "Jet energy measurement and its systematic uncertainty in proton–proton collisions at $\sqrt{s} = 7$ TeV with the ATLAS detector". In: *Eur. Phys. J. C* 75 (2015), p. 17. DOI: 10.1140/epjc/s10052-014-3190-y. arXiv: 1406.0076 [hep-ex] (cit. on pp. 119, 120, 138).

[224] M. Cacciari and G. P. Salam. "Pileup subtraction using jet areas". In: *Phys. Lett. B* 659 (2008), p. 119. DOI: 10.1016/j.physletb.2007.09.077. arXiv: 0707.1378 [hep-ph] (cit. on p. 120).

[225] ATLAS Collaboration. "Characterisation and mitigation of beam-induced backgrounds observed in the ATLAS detector during the 2011 proton–proton run". In: *JINST* 8 (2013), P07004. DOI: 10.1088/1748-0221/8/07/P07004. arXiv: 1303.0223 [hep-ex] (cit. on p. 120).

[226] ATLAS Collaboration. "Monitoring and data quality assessment of the ATLAS liquid argon calorimeter". In: *JINST* 9 (2014), P07024. DOI: 10.1088/1748-0221/9/07/P07024. arXiv: 1405.3768 [hep-ex] (cit. on p. 121).

[227] Benjamin Nachman et al. "Jets from Jets: Re-clustering as a tool for large radius jet reconstruction and grooming at the LHC". In: *JHEP* 02 (2015), p. 075. DOI: 10.1007/JHEP02(2015)075. arXiv: 1407.2922 [hep-ph] (cit. on pp. 121, 140).

[228] Yuri L. Dokshitzer et al. "Better jet clustering algorithms". In: *JHEP* 9708 (1997), p. 001. DOI: 10.1088/1126-6708/1997/08/001. arXiv: hep-ph/9707323 [hep-ph] (cit. on p. 122).

[229] M. Wobisch and T. Wengler. "Hadronization corrections to jet cross-sections in deep inelastic scattering". In: *Monte Carlo generators for HERA physics. Proceedings,*

Workshop, Hamburg, Germany, 1998-1999. 1998. arXiv: hep-ph/9907280 [hep-ph] (cit. on p. 122).

[230] Minho Son, Christian Spethmann, and Brock Tweedie. "Diboson-Jets and the Search for Resonant Zh Production". In: *JHEP* 1208 (2012), p. 160. DOI: 10.1007/JHEP08(2012)160. arXiv: 1204.0525 [hep-ph] (cit. on p. 122).

[231] J. M. Butterworth et al. "Jet substructure as a new Higgs search channel at the LHC". In: *Phys. Rev. Lett.* 100 (2008), p. 242001. DOI: 10.1103/PhysRevLett.100.242001. arXiv: 0802.2470 [hep-ph] (cit. on p. 122).

[232] ATLAS Collaboration. "Search for Massive Colored Scalars in Four-Jet Final States in $\sqrt{s} = 7$ TeV proton-proton collisions with the ATLAS Detector". In: *Eur. Phys. J. C* 71 (2011), p. 1828. DOI: 10.1140/epjc/s10052-011-1828-6. arXiv: 1110.2693 [hep-ex] (cit. on p. 124).

[233] Steffen Schumann, Adrien Renaud, and Dirk Zerwas. "Hadronically decaying color-adjoint scalars at the LHC". In: *JHEP* 1109 (2011), p. 074. DOI: 10.1007/JHEP09(2011)074. arXiv: 1108.2957 [hep-ph] (cit. on p. 124).

[234] Stefano Frixione and Bryan R. Webber. "Matching NLO QCD computations and parton shower simulations". In: *JHEP* 0206 (2002), p. 029. DOI: 10.1088/1126-6708/2002/06/029. arXiv: hep-ph/0204244 [hep-ph] (cit. on p. 138).

[235] G. Corcella et al. "HERWIG 6: An Event generator for hadron emission reactions with interfering gluons (including supersymmetric processes)". In: *JHEP* 0101 (2001), p. 010. DOI: 10.1088/1126-6708/2001/01/010. arXiv: hep-ph/0011363 [hep-ph] (cit. on p. 138).

[236] ATLAS Collaboration. "Improved luminosity determination in pp collisions at $\sqrt{s} = 7$ TeV using the ATLAS detector at the LHC". In: *Eur. Phys. J. C* 73 (2013), p. 2518.

DOI: 10.1140/epjc/s10052-013-2518-3. arXiv: 1302.4393 [hep-ex] (cit. on p. 140).

[237] Alexander L. Read. "Presentation of search results: The CL_s technique". In: *J. Phys. G* 28 (2002), p. 2693. DOI: 10.1088/0954-3899/28/10/313 (cit. on pp. 141, 143).

[238] Glen Cowan et al. "Asymptotic formulae for likelihood-based tests of new physics". In: *Eur. Phys. J.* C71 (2011). [Erratum: Eur. Phys. J. C73, 2501 (2013)], p. 1554. DOI: 10.1140/epjc/s10052-011-1554-0,10.1140/epjc/s10052-013-2501-z. arXiv: 1007.1727 [physics.data-an] (cit. on p. 143).

[239] M. Baak et al. "HistFitter software framework for statistical data analysis". In: *Eur. Phys. J.* C75.4 (2015), p. 153. DOI: 10.1140/epjc/s10052-015-3327-7. arXiv: 1410.1280 [hep-ex] (cit. on pp. 143, 163).

[240] Morad Aaboud et al. "A search for pair-produced resonances in four-jet final states at $\sqrt{s} = 13$ TeV with the ATLAS detector". In: *Eur. Phys. J.* C78.3 (2018), p. 250. DOI: 10.1140/epjc/s10052-018-5693-4. arXiv: 1710.07171 [hep-ex] (cit. on p. 145).

[241] ATLAS Collaboration. "Search for chargino and neutralino production in final states with a Higgs boson and missing transverse momentum at $\sqrt{s} = 13$ TeV with the ATLAS detector". In: *To be submitted to: Phys. Rev. D.* (2018). arXiv: xxxx.yyyyy [hep-ex] (cit. on pp. 148, 150, 179, 181, 182).

[242] Pierre Fayet. "Supersymmetry and Weak, Electromagnetic and Strong Interactions". In: *Phys. Lett. B* 64 (1976), p. 159. DOI: 10.1016/0370-2693(76)90319-1 (cit. on p. 149).

[243] Pierre Fayet. "Spontaneously Broken Supersymmetric Theories of Weak, Electromagnetic and Strong Interactions". In: *Phys. Lett. B* 69 (1977), p. 489. DOI: 10.1016/0370-2693(77)90852-8 (cit. on p. 149).

[244] Siba Prasad Das, Monoranjan Guchait, and D. P. Roy. "Testing SUSY models for the muon g-2 anomaly via chargino-neutralino pair production at the LHC". In: *Phys. Rev. D* 90.5 (2014), p. 055011. DOI: 10.1103/PhysRevD.90.055011. arXiv: 1406.6925 [hep-ph] (cit. on p. 150).

[245] M. Adeel Ajaib et al. "Neutralinos and sleptons at the LHC in light of muon $(g-2)_\mu$". In: *Phys. Rev. D* 92.7 (2015), p. 075033. DOI: 10.1103/PhysRevD.92.075033. arXiv: 1505.05896 [hep-ph] (cit. on p. 150).

[246] Manimala Chakraborti et al. "Reduced LHC constraints for higgsino-like heavier electroweakinos". In: *JHEP* 11 (2015), p. 050. DOI: 10.1007/JHEP11(2015)050. arXiv: 1507.01395 [hep-ph] (cit. on p. 150).

[247] Motoi Endo et al. "Probing minimal SUSY scenarios in the light of muon $g-2$ and dark matter". In: *JHEP* 06 (2017), p. 031. DOI: 10.1007/JHEP06(2017)031. arXiv: 1704.05287 [hep-ph] (cit. on p. 150).

[248] Johan Alwall, Philip Schuster, and Natalia Toro. "Simplified Models for a First Characterization of New Physics at the LHC". In: *Phys. Rev. D* 79 (2009), p. 075020. DOI: 10.1103/PhysRevD.79.075020. arXiv: 0810.3921 [hep-ph] (cit. on p. 150).

[249] Daniele Alves. "Simplified Models for LHC New Physics Searches". In: *J. Phys. G* 39 (2012). Ed. by Nima Arkani-Hamed et al., p. 105005. DOI: 10.1088/0954-3899/39/10/105005. arXiv: 1105.2838 [hep-ph] (cit. on p. 150).

[250] ATLAS Collaboration. "Search for the electroweak production of supersymmetric particles in $\sqrt{s} = 8$ TeV pp collisions with the ATLAS detector". In: *Phys. Rev. D* 93 (2016), p. 052002. DOI: 10.1103/PhysRevD.93.052002. arXiv: 1509.07152 [hep-ex] (cit. on p. 150).

[251] CMS Collaboration. "Combined search for electroweak production of charginos and neutralinos in proton-proton collisions at $\sqrt{s} = 13$ TeV". In: *JHEP* 03 (2018), p. 160. DOI: 10.1007/JHEP03(2018)160. arXiv: 1801.03957 [hep-ex] (cit. on p. 150).

[252] ATLAS Collaboration. "Luminosity determination in pp collisions at $\sqrt{s} = 8$ TeV using the ATLAS detector at the LHC". In: *Eur. Phys. J. C* 76 (2016), p. 653. DOI: 10.1140/epjc/s10052-016-4466-1. arXiv: 1608.03953 [hep-ex] (cit. on p. 151).

[253] ATLAS Collaboration. *2015 start-up trigger menu and initial performance assessment of the ATLAS trigger using Run-2 data*. ATL-DAQ-PUB-2016-001. 2016. URL: https://cds.cern.ch/record/2136007 (cit. on p. 151).

[254] J. Alwall et al. "The automated computation of tree-level and next-to-leading order differential cross sections, and their matching to parton shower simulations". In: *JHEP* 1407 (2014), p. 079. DOI: 10.1007/JHEP07(2014)079. arXiv: 1405.0301 [hep-ph] (cit. on pp. 151, 153).

[255] ATLAS Collaboration. *ATLAS Pythia 8 tunes to 7 TeV data*. ATL-PHYS-PUB-2014-021. 2014. URL: https://cds.cern.ch/record/1966419 (cit. on pp. 151, 153).

[256] Leif Lönnblad and Stefan Prestel. "Merging Multi-leg NLO Matrix Elements with Parton Showers". In: *JHEP* 03 (2013), p. 166. DOI: 10.1007/JHEP03(2013)166. arXiv: 1211.7278 [hep-ph] (cit. on p. 152).

[257] Richard D. Ball et al. "Parton distributions with LHC data". In: *Nucl. Phys. B* 867 (2013), pp. 244–289. DOI: 10.1016/j.nuclphysb.2012.10.003. arXiv: 1207.1303 [hep-ph] (cit. on pp. 152, 153).

[258] Christoph Borschensky et al. "Squark and gluino production cross sections in pp collisions at $\sqrt{s} = 13$, 14, 33 and 100 TeV". In: *Eur. Phys. J. C* 74 (2014), p. 3174. DOI: 10.1140/epjc/s10052-014-3174-y. arXiv: 1407.5066 [hep-ph] (cit. on p. 152).

[259] T. Gleisberg et al. "Event generation with SHERPA 1.1". In: *JHEP* 02 (2009), p. 007. DOI: 10.1088/1126-6708/2009/02/007. arXiv: 0811.4622 [hep-ph] (cit. on pp. 152, 153).

[260] D. J. Lange. "The EvtGen particle decay simulation package". In: *Nucl. Instrum. Meth. A* 462 (2001), pp. 152–155. DOI: 10.1016/S0168-9002(01)00089-4 (cit. on pp. 152, 153).

[261] Peter Zeiler Skands. "Tuning Monte Carlo Generators: The Perugia Tunes". In: *Phys. Rev. D* 82 (2010), p. 074018. DOI: 10.1103/PhysRevD.82.074018. arXiv: 1005.3457 [hep-ph] (cit. on p. 153).

[262] Torbjorn Sjöstrand, Stephen Mrenna, and Peter Z. Skands. "PYTHIA 6.4 Physics and Manual". In: *JHEP* 05 (2006), p. 026. DOI: 10.1088/1126-6708/2006/05/026. arXiv: hep-ph/0603175 [hep-ph] (cit. on p. 153).

[263] Johan Alwall et al. "The automated computation of tree-level and next-to-leading order differential cross sections, and their matching to parton shower simulations". In: *JHEP* 07 (2014), p. 079. DOI: 10.1007/JHEP07(2014)079. arXiv: 1405.0301 [hep-ph] (cit. on p. 153).

[264] Stefan Gieseke, Christian Rohr, and Andrzej Siodmok. "Colour reconnections in Herwig++". In: *Eur. Phys. J. C* 72 (2012), p. 2225. DOI: 10.1140/epjc/s10052-012-2225-5. arXiv: 1206.0041 [hep-ph] (cit. on p. 153).

[265] ATLAS Collaboration. "Topological cell clustering in the ATLAS calorimeters and its performance in LHC Run 1". In: *Eur. Phys. J. C* 77 (2017), p. 490. DOI: 10.1140/epjc/s10052-017-5004-5. arXiv: 1603.02934 [hep-ex] (cit. on p. 154).

[266] ATLAS Collaboration. "Jet energy scale measurements and their systematic uncertainties in proton–proton collisions at $\sqrt{s} = 13$ TeV with the ATLAS detector". In:

Phys. Rev. D 96 (2017), p. 072002. DOI: 10.1103/PhysRevD.96.072002. arXiv: 1703.09665 [hep-ex] (cit. on p. 154).

[267] ATLAS Collaboration. "Performance of pile-up mitigation techniques for jets in pp collisions at $\sqrt{s} = 8$ TeV using the ATLAS detector". In: *Eur. Phys. J. C* 76 (2016), p. 581. DOI: 10.1140/epjc/s10052-016-4395-z. arXiv: 1510.03823 [hep-ex] (cit. on p. 154).

[268] ATLAS Collaboration. *Expected performance of missing transverse momentum reconstruction for the ATLAS detector at $\sqrt{s} = 13$ TeV*. ATL-PHYS-PUB-2015-023. 2015. URL: https://cds.cern.ch/record/2037700 (cit. on p. 155).

[269] ATLAS Collaboration. *Performance of missing transverse momentum reconstruction with the ATLAS detector in the first proton–proton collisions at $\sqrt{s} = 13$ TeV*. ATL-PHYS-PUB-2015-027. 2015. URL: https://cds.cern.ch/record/2037904 (cit. on p. 155).

[270] ATLAS Collaboration. "Electron and photon energy calibration with the ATLAS detector using LHC Run 1 data". In: *Eur. Phys. J. C* 74 (2014), p. 3071. DOI: 10.1140/epjc/s10052-014-3071-4. arXiv: 1407.5063 [hep-ex] (cit. on p. 155).

[271] ATLAS Collaboration. *Electron efficiency measurements with the ATLAS detector using the 2015 LHC proton–proton collision data*. ATLAS-CONF-2016-024. 2016. URL: https://cds.cern.ch/record/2157687 (cit. on p. 155).

[272] ATLAS Collaboration. "Muon reconstruction performance of the ATLAS detector in proton–proton collision data at $\sqrt{s} = 13$ TeV". In: *Eur. Phys. J. C* 76 (2016), p. 292. DOI: 10.1140/epjc/s10052-016-4120-y. arXiv: 1603.05598 [hep-ex] (cit. on p. 155).

[273] Daniel R. Tovey. "On measuring the masses of pair-produced semi-invisibly decaying particles at hadron colliders". In: *JHEP* 04 (2008), p. 034. DOI: 10.1088/1126-6708/2008/04/034. arXiv: 0802.2879 [hep-ph] (cit. on p. 159).

[274] Giacomo Polesello and Daniel R. Tovey. "Supersymmetric particle mass measurement with the boost-corrected contransverse mass". In: *JHEP* 03 (2010), p. 030. DOI: 10.1007/JHEP03(2010)030. arXiv: 0910.0174 [hep-ph] (cit. on p. 159).

[275] Thomas Junk. "Confidence level computation for combining searches with small statistics". In: *Nucl. Instrum. Meth. A* 434 (1999), pp. 435–443. DOI: 10.1016/S0168-9002(99)00498-2. arXiv: hep-ex/9902006 [hep-ex] (cit. on p. 176).

[276] Alexander L. Read. "Presentation of search results: The CL(s) technique". In: *J. Phys. G* 28 (2002). [,11(2002)], pp. 2693–2704. DOI: 10.1088/0954-3899/28/10/313 (cit. on p. 176).

[277] ATLAS Collaboration. *ATLAS Experiment Luminosity Public Results Run2*. https://twiki.cern.ch/twiki/bin/view/AtlasPublic/LuminosityPublicResultsRun2. [Online; accessed 9-September-2018]. 2018 (cit. on p. 185).

[278] Lorenzo Moneta et al. "The RooStats Project". In: *PoS* ACAT2010 (2010), p. 057. DOI: 10.22323/1.093.0057. arXiv: 1009.1003 [physics.data-an] (cit. on p. 227).

[279] CERN. *RooStats TWiki*. 2018. URL: https://twiki.cern.ch/twiki/bin/view/RooStats/WebHome (visited on 08/29/2018) (cit. on p. 227).

Appendices

APPENDIX A

SUPPLEMENTAL MATERIAL FOR THE ELECTROWEAK WH SEARCH

A.1 Signal Region Optimization

A multivariate optimization process was performed[1] by scanning over several of the kinematic variables defined in section 9.3.1, using the *loose* selection as defined in table 9.2 as a starting point. A flat uncertainty of 30% was used for the optimization. A scan over N_{jet}, $E_{\text{T}}^{\text{miss}}$, m_{eff}, m_{CT}, and m_{T}^{b} (with fixed cuts: $N_{b-\text{jet}} \geq 2$, $\Delta\phi_{\text{min}}^{4j} > 0.4$, $105 < m_{b\bar{b}} < 135$ GeV, and $75 < m_{q\bar{q}} < 90$), indicated that low-$m(\tilde{\chi}_1^{\pm}/\tilde{\chi}_2^0)$ regions profits from a looser m_{eff} cut while high-$m(\tilde{\chi}_1^{\pm}/\tilde{\chi}_2^0)$ regions benefits from a higher cut on m_{eff} as can be seen in fig. A.1. Therefore two different optimizations were run; one with $m_{\text{eff}} > 700$ GeV, and another one with $m_{\text{eff}} > 900$ GeV. For each, the following variables were optimized:

- $4 \leq N_{\text{jet}} \leq x$, where $x = 4, 5, 6$
- $2 \leq N_{b-\text{jet}} \leq x$, where $x = 2, 3, 4$
- $E_{\text{T}}^{\text{miss}} > x$, where x was scanned between $200 - 400$ GeV in 50 GeV steps
- $m_{\text{T}}^{b,\text{min}} > x$, where x was scanned between $80 - 400$ GeV in 20 GeV steps
- $m_{\text{CT}} > x$, where x was scanned between $100 - 300$ GeV in 10 GeV steps

The optimal cuts at different mass points are shown in fig. A.2 and fig. A.3, for the optimization with a fixed m_{eff} cut of $m_{\text{eff}} > 900$ GeV and $m_{\text{eff}} > 700$ GeV, respectively. Separate

1. using $Z_n = \text{RooStats.NumberCountingUtils.BinomialExpZ}(N_S, N_B, 0.3)$ [278, 279] as a figure of merit, where N_S and N_B are the number of signal and total background events, respectively.

optimizations of the $m_{b\bar{b}}$ and $m_{q\bar{q}}$ variables indicated that selections of $105 < m_{b\bar{b}} < 135$ GeV and $75 < m_{q\bar{q}} < 90$ were quite optimal. Two SRs where defined, SRHad-High and SRHad-Low, corresponding roughly to the optimal selection for $(m(\tilde{\chi}_1^{\pm}/\tilde{\chi}_2^0) = 600, m(\tilde{\chi}_1^0) = 50)$ and $(m(\tilde{\chi}_1^{\pm}/\tilde{\chi}_2^0) = 350, m(\tilde{\chi}_1^0) = 50)$, respectively[2] The signal-to-background significance in SRHad-High and SRHad-Low resulting from the optimization is shown in fig. A.4.

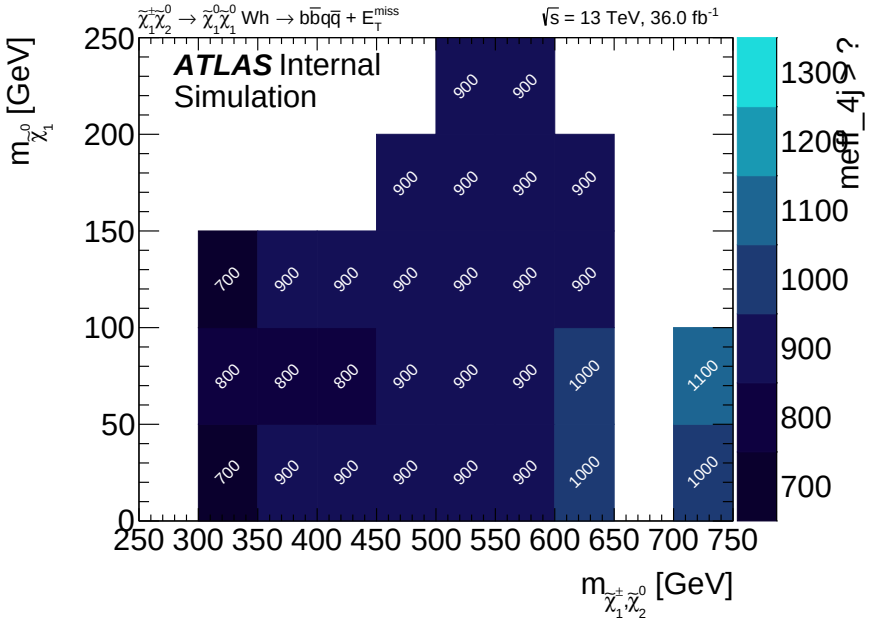

Figure A.1: Optimal cut on m_{eff} for each mass point.

2. The optimization studies described in this section where performed using an early batch of privately generated signal MC samples. These samples had a bug in the job options which affected the branching ratios of the W and Higgs bosons. The optimization was later re-done using ATLAS officially generated signal samples, where the bug in the job option had been corrected, however the re-optimization didn't yield any significant improvement and due to time constraints on the analysis the signal region selections defined from the initial optimization were kept.

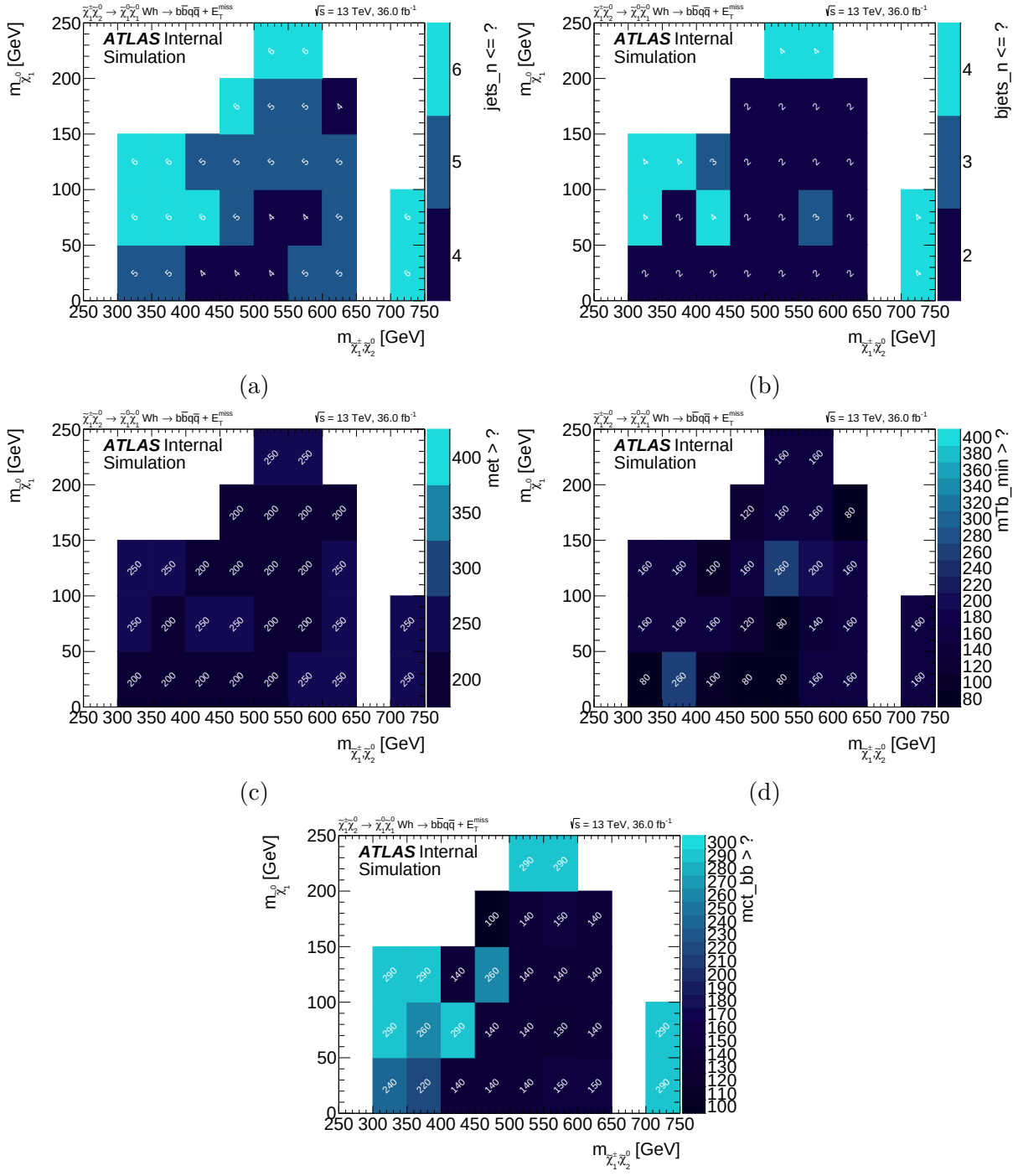

Figure A.2: Optimal cuts on (a) N_{jet}, (b) $N_{b-\text{jet}}$, (c) $E_{\text{T}}^{\text{miss}}$, (d) $m_{\text{T}}^{b,\text{min}}$, and (e) m_{CT} for the optimization with fixed $m_{\text{eff}} > 900$ GeV.

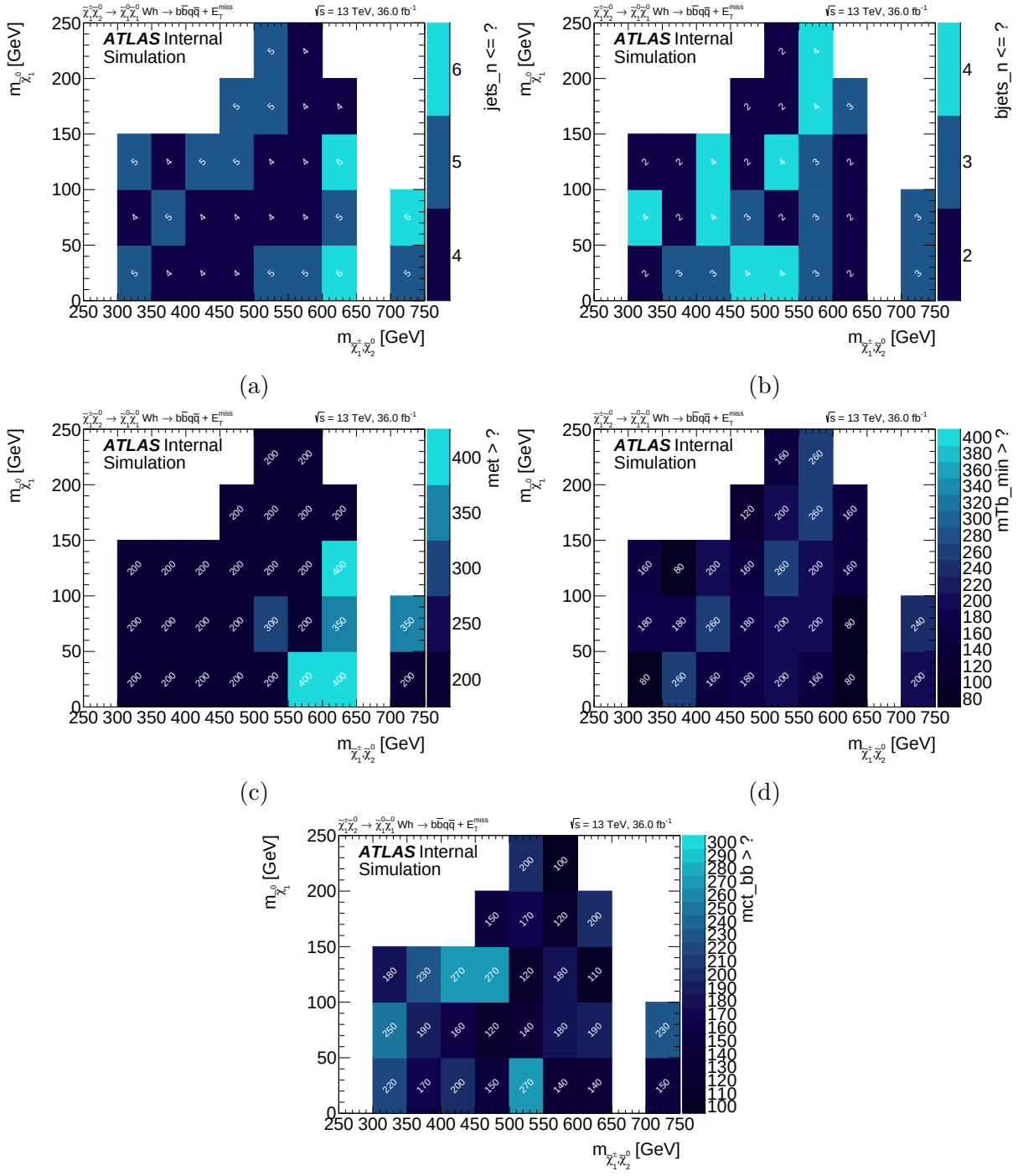

Figure A.3: Optimal cuts on (a) N_{jet}, (b) $N_{b-\text{jet}}$, (c) $E_{\text{T}}^{\text{miss}}$, (d) $m_{\text{T}}^{b,\text{min}}$, and (e) m_{CT} for the optimization with fixed $m_{\text{eff}} > 700$ GeV.

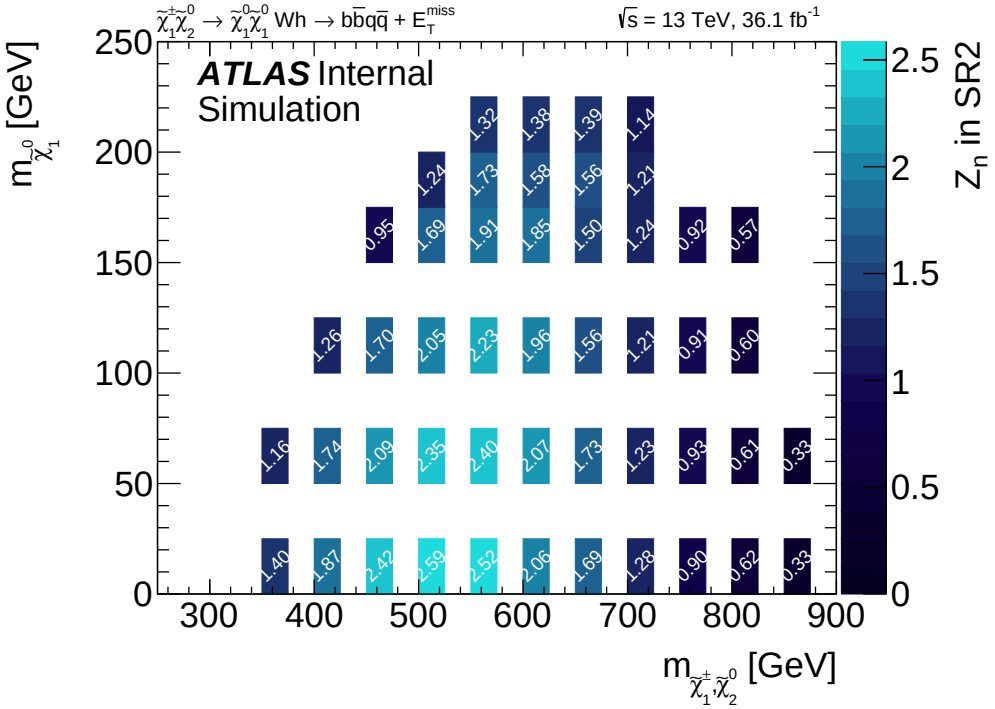

(a)

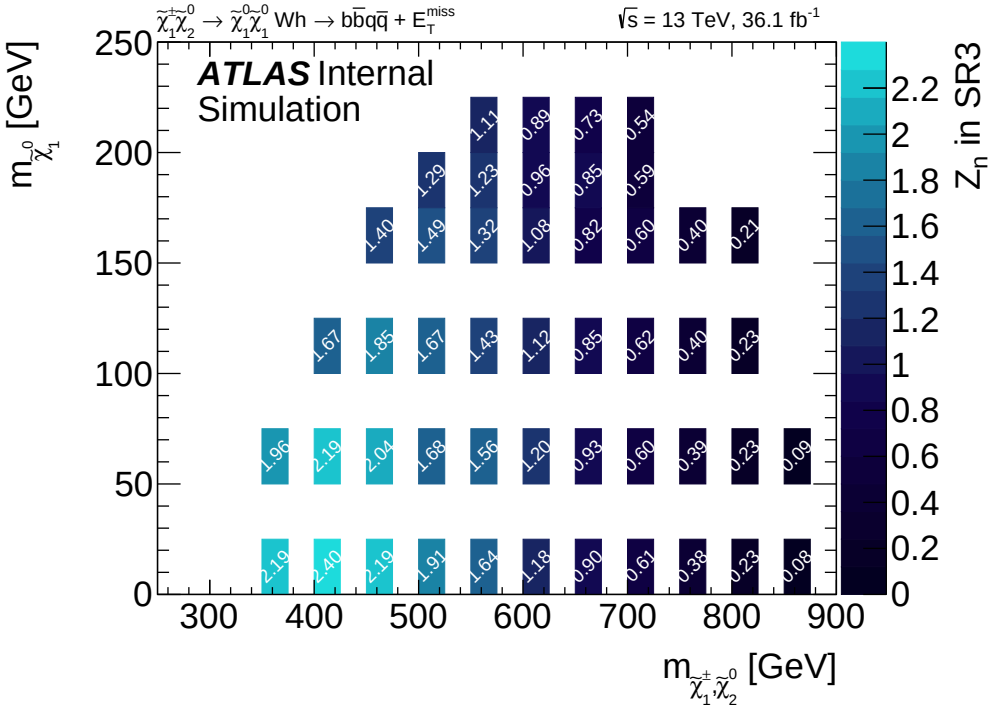

(b)

Figure A.4: Sensitivity estimates for (a) SRHad-High and (b) SRHad-Low. The optimization was performed using $Z_n = \text{BinomialExpZ}(N_S, N_B, 0.3)$ as a figure of merit.

A.2 Summary Cutflow

Cut	Total Background	Wh(550,0)	Wh(700,0)
All events	2834780000 ± 270000	427.2 ± 1.9	134.7 ± 0.6
Preselection+Cleaning	20046000 ± 32000	336.9 ± 2.0	109.6 ± 0.7
$N_{\text{lepton}} = 0$	5697000 ± 24000	334.7 ± 2.0	108.8 ± 0.7
N_{jet} ($p_{\text{T}} > 30$ GeV) $\in [4,\ 5]$	2267000 ± 6000	205.1 ± 1.6	65.2 ± 0.5
$N_{b-\text{jet}} = 2$	398900 ± 1400	92.4 ± 1.1	29.3 ± 0.4
$\Delta\phi^{4j}_{\text{min}} > 0.4$	272500 ± 900	79.6 ± 1.0	25.38 ± 0.33
$E_{\text{T}}^{\text{miss}} > 200$ GeV	24980 ± 100	65.9 ± 0.9	22.42 ± 0.31
$m_{\text{eff}} > 700$ GeV	9540 ± 50	57.7 ± 0.8	21.35 ± 0.31
$m_{b\bar{b}} \in [105, 135]$ GeV	873 ± 15	34.5 ± 0.6	12.84 ± 0.24
$m_{q\bar{q}} \in [75, 90]$ GeV	92 ± 4	12.4 ± 0.4	4.28 ± 0.13
SRHad-Low			
$m_{\text{CT}} > 190$ GeV	9.4 ± 1.0	8.91 ± 0.30	3.60 ± 0.12
$m_{\text{T}}^{b,\text{min}} > 180$ GeV	8.5 ± 0.9	8.52 ± 0.29	3.47 ± 0.12
SRHad-High			
$E_{\text{T}}^{\text{miss}} > 250$ GeV	73.2 ± 2.5	11.2 ± 0.4	3.94 ± 0.13
$m_{\text{eff}} > 900$ GeV	6.5 ± 0.6	7.37 ± 0.28	3.38 ± 0.12
$m_{\text{CT}} > 140$ GeV	2.7 ± 0.5	6.88 ± 0.28	3.25 ± 0.11
$m_{\text{T}}^{b,\text{min}} > 160$ GeV	2.4 ± 0.5	6.75 ± 0.28	3.22 ± 0.11

Table A.1: Event selection cutflow for signal and total background. Only statistical uncertainties are shown.